Parametric study of the current limit within a single driver-scale

transport beam line of an induction Linac for Heavy Ion Fusion

by

Lionel Robert Prost


Diplôme d'Ingénieur (Ecole Nationale Supérieure de Mécanique et
des Microtechniques, France) 1997


A dissertation submitted in partial satisfaction of the

requirements for the degree of

Doctor of Philosophy
in

Engineering-Nuclear Engineering

in the

GRADUATE DIVISION

of the

UNIVERSITY OF CALIFORNIA, BERKELEY

Committee in charge:

Professor Edward C. Morse, Chair
Professor Donald R. Olander
Professor Stanley A. Berger
Doctor Peter A. Seidl

Fall 2004

The dissertation of Lionel Robert Prost is approved:

_____

Chair                                                                   Date

_____

                                                                        Date

_____

                                                                        Date

_____

                                                                        Date

University of California, Berkeley

Fall 2004

# Abstract

Parametric study of the current limit within a single driver-scale

transport beam line of an induction Linac for Heavy Ion Fusion[*]

by

Lionel Robert Prost

Doctor of Philosophy in Nuclear Engineering

University of California, Berkeley

Professor Edward C. Morse, Chair

The High Current Experiment (HCX) at Lawrence Berkeley National Laboratory is part of the US program that explores heavy-ion beam as the driver option for fusion energy production in an Inertial Fusion Energy (IFE) plant. The HCX is a beam transport experiment at a scale representative of the low-energy end of an induction linear accelerator driver. The primary mission of this experiment is to investigate aperture fill factors acceptable for the transport of space-

1

charge-dominated heavy-ion beams at high intensity (line charge density ~0.2 µC/m) over long pulse durations (4 µs) in alternating gradient focusing lattices of electrostatic or magnetic quadrupoles. This experiment is testing transport issues resulting from nonlinear space-charge effects and collective modes, beam centroid alignment and steering, envelope matching, image charges and focusing field nonlinearities, halo and, electron and gas cloud effects.

We present the results for a coasting 1 MeV $K^+$ ion beam transported through ten electrostatic quadrupoles. The measurements cover two different fill factor studies (60% and 80% of the clear aperture radius) for which the transverse phase-space of the beam was characterized in detail, along with beam energy measurements and the first halo measurements. Electrostatic quadrupole transport at high beam fill factor (≈80%) is achieved with acceptable emittance growth and beam loss. We achieved good envelope control, and re-matching may only be needed every ten lattice periods (at 80% fill factor) in a longer lattice of similar design. We also show that understanding and controlling the time dependence of the envelope parameters is critical to achieving high

fill factors, notably because of the injector and matching section dynamics.

---

Professor Edward C. Morse

Dissertation Committee Chair

## List of figures

# List of tables

## Acknowledgements

# Chapter I - Introduction

With the world population growing, the many developing countries entering the industrialization process and the increasing needs for electrical power from developed countries, providing enough energy to the world for the years to come has become a concern. The depletion of global fossil fuel reserves and environmental issues associated with their use (e.g.: greenhouse effect, global warming), the inefficiency of renewable sources of energy (e.g.: solar, wind), and the radioactive waste management and proliferation problems of nuclear fission power plants make nuclear fusion the premier choice for producing safe and clean energy [1,2,3].

## I.1 - Fusion principle

Fusion is the process of combining light nuclei such as isotopes of hydrogen to form heavier ones [4]. As a result, a large amount of energy is released and carried away by the product particles. In order to overcome the Coulomb forces between the nuclei, the fuel must be heated to approximately $10^8$ K or about 10 keV, which forms a plasma. The reaction rate is proportional to the reaction rate parameter, $\langle \sigma v \rangle$, which is the product of the cross section $\sigma$ and velocity $v$ averaged over a Maxwellian velocity distribution. Because it has the largest peak rate parameter in the range of attainable temperature [5], the most common reaction usually considered is the fusion of deuterium and tritium (Figure I-1),

$$D + T \rightarrow {}^{4}He\ (3.5\,MeV) + n\ (14.1\,MeV),$$　　　　(Eq. I-1)
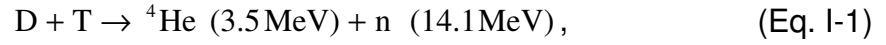
which produces an alpha particle and a neutron.
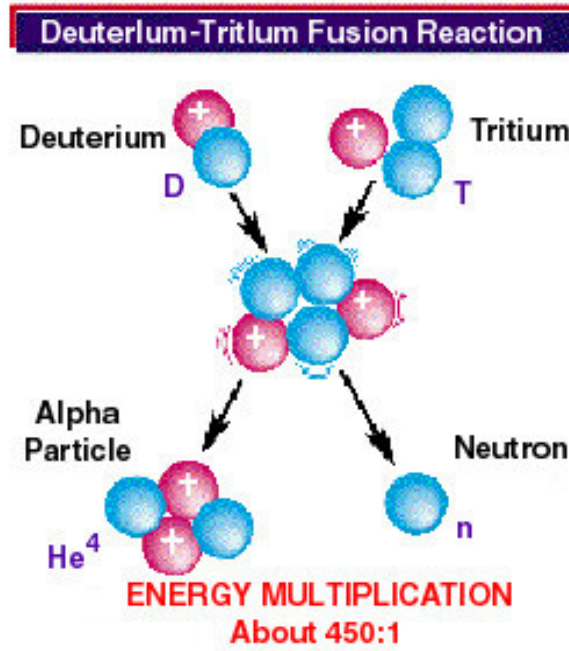


**Figure I-1**: D-T fusion reaction.

The neutron has a long range and is used to heat a coolant that will eventually lead to electricity generation and the alpha particle provides heat to the remaining of the fuel and contributes to sustaining the fusion reaction. If we define the burnup fraction, $f$, as $n = n_0\ (1 - f)$, where $n_0$ is the initial fuel density, we can obtain, for an equal mixture of deuterium and tritium

$$\frac{f}{1 - f} = \frac{\langle \sigma v \rangle}{2} n_0 \tau,$$　　　　(Eq. I-2)

where $\tau$ is the burnup time. From (Eq. I-2), typically referred to as the Lawson Criterion [6], we see that the burn fraction increases with the $n_0\tau$ product (i.e. confinement). The two approaches for fusion try to maximize one term or the other in the product. In magnetic confinement fusion, the plasma density is rather low but the burnup time is expected to be on the order of several seconds or minutes. In inertial confinement fusion, the very short reaction time is compensated by the large density that results from compressing the fuel.

In magnetic fusion energy (MFE) [7,8], a burning plasma is confined using strong magnetic fields, which are created by external coils as well as electric currents flowing in the fusion plasma itself. The most advanced concept relies on a toroidally shaped fusion reactor (tokamak) such as shown in the conceptual drawing of ITER ("The way" in Latin) (Figure I-2), the largest such device to be built in the near future [9].
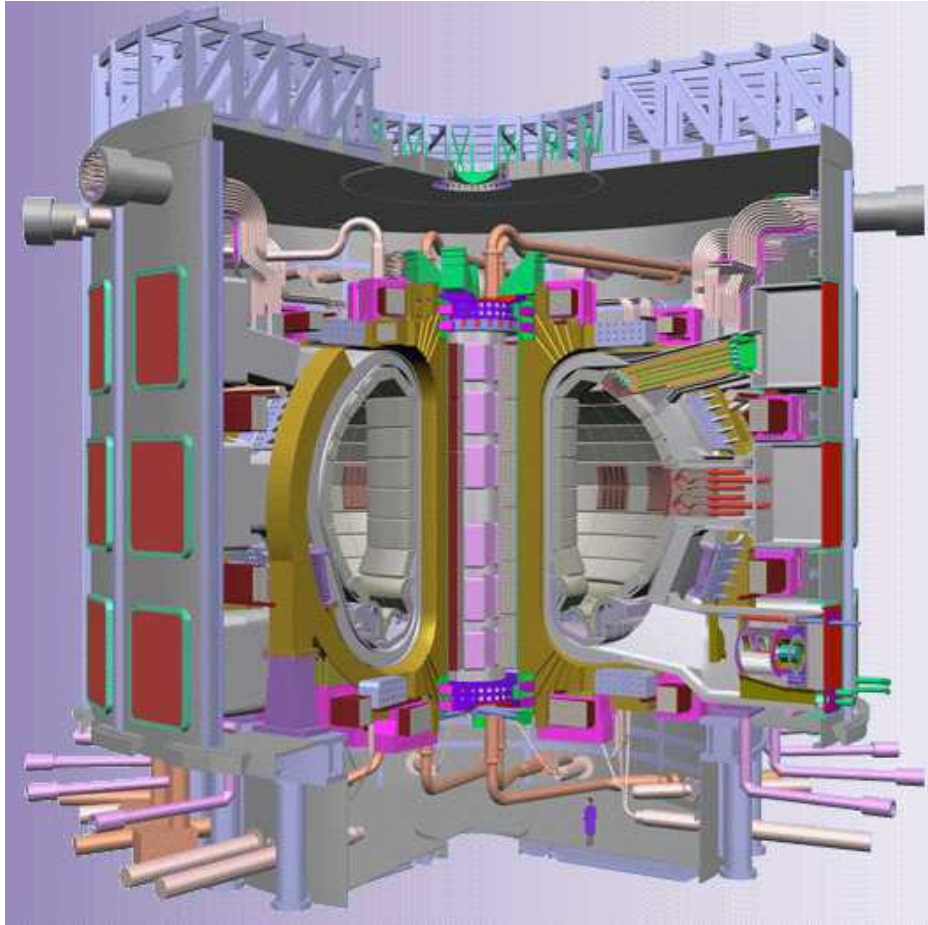
**Figure I-2**: ITER conceptual drawing [9]. Note the person at the bottom for scale.

ITER will be the first fusion device to produce thermal energy at the level of an electricity-producing power station.

In Inertial Fusion Energy (IFE) [10,11], a small pellet (a few millimeters in diameter) of DT fuel (a few milligrams) is compressed to very high densities by heating it with a laser or ion beam (i.e. the driver). During compression, a hot spot at the center reaches the required 5-10 keV for the fusion reaction to occur which ignites the fuel. Then, the alpha particles produced in the reaction heat up

the fuel surrounding the hot spot enabling the fusion burn wave to propagate outward. During radial compression, the inertia of the fuel overcomes the outward pressure due to the rapid increase in density. Once compressed and heated to a plasma state, the fuel mass limits its own disassembly until a significant fraction has undergone the reaction. By igniting pellets several times per second, sufficient fusion energy can be released for commercial electricity production. The National Ignition Facility (NIF), the largest laser system in the world, is in the final stage of construction. Its mission is to achieve controlled ignition at the laboratory scale, the proof of principle that inertial fusion can meet the energy balance requirements [12].

## I.2 - Inertial Fusion Energy (IFE) power plant concept

An inertial confinement fusion power plant is shown schematically in Figure I-3. It consists of a driver, a target factory a fusion chamber and a steam plant.
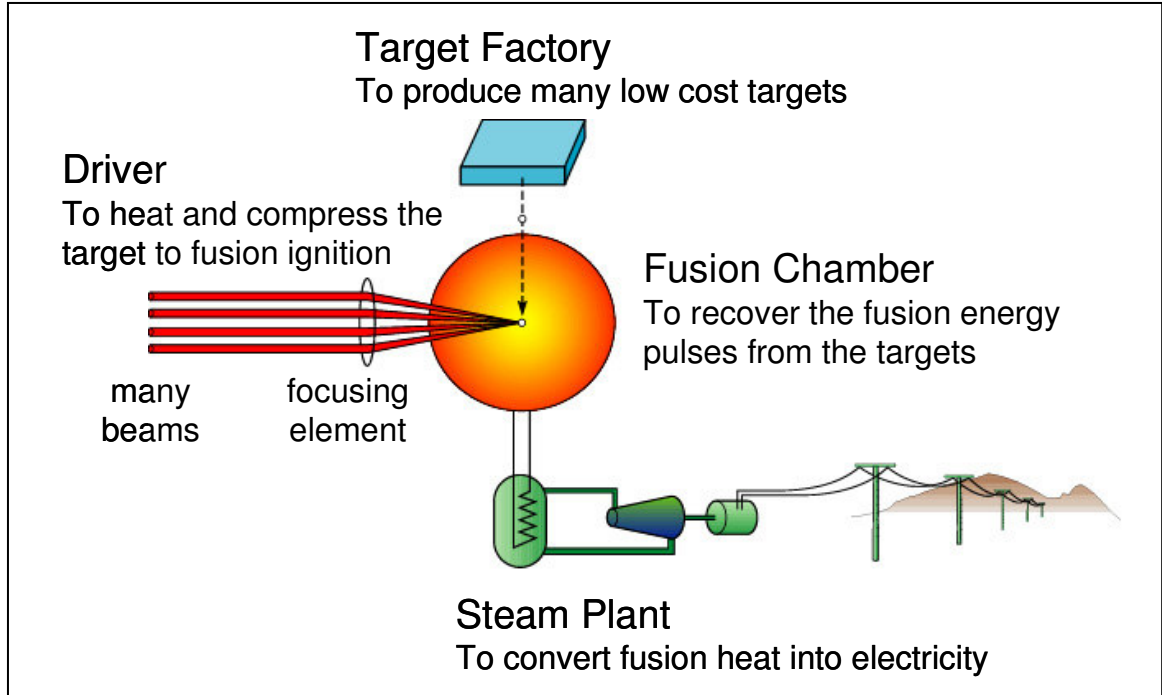
**Figure I-3**: Simplified schematic of an IFE power plant.

For the concept to be viable, a simple fusion reactor power balance analysis [13] shows that

$$f_p \eta_{Th} G \eta_D = 1,$$ (Eq. I-3)

where, $f_p$ is the fraction of the generated electricity recycled to the driver, $\eta_{Th}$ is the conventional steam cycle efficiency, $G$ is the target gain (i.e. the ratio of the yield to the required driver energy) and $\eta_D$ is the driver efficiency. Assuming $f_p$ = 0.25, $\eta_{Th}$ = 0.4, we find that the effectiveness of the driver-target combination, $G\eta_D$, should be at least 10. Since the efficiency of the driver is typically less than 25% (laser or ion beam), the target gain must be ≈50 or more and is determined by the physics of the compression [14,15].

Inertial fusion micro-explosions can be driven directly or indirectly. In the direct drive scenario, the laser or ion beams impinge onto the DT fuel itself and compress it. In the indirect drive scenario, the DT fuel pellet is placed inside a cylindrical casing referred to by its German term *holraum* (Figure I-4) [16].
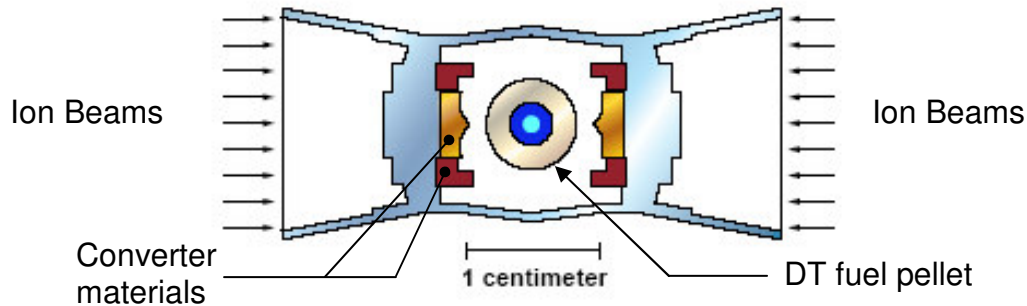


**Figure I-4**: Conceptual design of a *hohlraum* for heavy-ion driven IFE, showing a DT fuel pellet inside a cylindrical casing lined with metal [16].

The role of the *holraum* is to convert the incident energy of the laser or particle beam into a uniform x-ray radiation field inside the *holraum*, which then compresses the fuel pellet. The indirect drive approach has the advantage that spherically uniform compression can be achieved using only a limited number of beams.

In contrast with MFE, the IFE concept has the advantage of decoupling the driver from the reaction chamber. In this simpler geometry, the first wall can be a liquid metal or molten salt, minimizing radiation damage to the reaction chamber structural elements as well as a coolant collecting the energy released from the fusion reaction [17].

7

## I.3 - Heavy-Ion Fusion (HIF)

### I.3.1 - Generalities

As mentioned previously, the driver of an inertial power plant can either be laser or particle beams and in case of ion beams, both light and heavy ions can be used [18]. In the heavy ion inertial fusion concept, the DT target is driven by beams of heavy ions with ion kinetic energy $3 \leq E_{Beam} \leq 10$ GeV. Heavy Ion Fusion (HIF) has several advantages over laser driven fusion. First, the accelerator technology, which was developed primarily for high energy physics research has now reached an advanced stage of engineering maturity, resulting in high reliability over long period of times. Additionally, accelerators have relatively high efficiencies ($\approx 30\%$) and repetition rates of several per second are easily achievable, which have not been demonstrated for high-intensity lasers. On the other hand, charged particle beams are more difficult to focus than lasers, especially at the large currents required in this application.

Since the final cost of electricity is greatly influenced by the efficiency of the fusion reaction in the DT fuel, the target design sets the beam energy and currents requirements for the driver as well as the spot size to be achieved. In most target designs for HIF, the driver must be able to deliver 3-7 MJ in $\approx$10 ns. For efficient conversion to x-rays, it is desirable that the incident ions deposit their energy in a very short distance into the *holraum* converter materials. Typical targets produce highest gain for incident ion ranges between 0.02 and 0.2 g cm$^{-2}$ [19]. Together with the power requirement, we then find that heavy ions (mass $\approx$ 200 amu) need to be accelerated to a few GeV for a total beam current

of ≈ 100 kA divided into 10 to 100 beam lines. Because of their longer range, light ions must operate at a lower energy and therefore a much higher total beam current.

High current beams can be produced and accelerated very efficiently in an induction linear accelerator (i.e. linac) and is therefore the acceleration technology of choice for HIF (as opposed to radiofrequency linacs) [20]. In induction linacs, the beam passes through pulsed toroidal cores of magnetic material by which a long pulse accelerating field is generated [54]. The beam is transversely confined with electrostatic and magnetic quadrupole lenses, while the longitudinal beam velocity is increased in a sequence of accelerating induction cells between those lenses. The diagram in Figure I-5 shows a typical heavy ion driver.
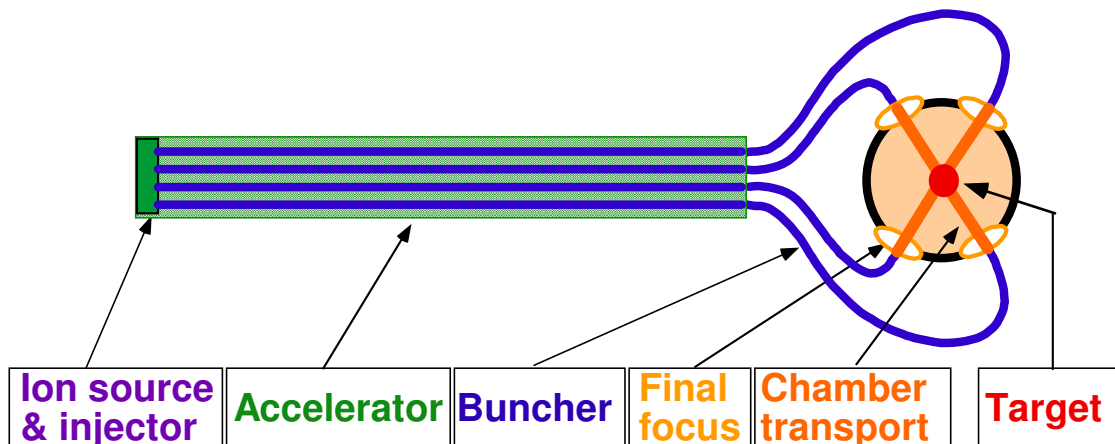


**Figure I-5**: Conceptual diagram of a heavy-ion linear accelerator for IFE.

Each beam line may consist of an ion source and injector that produces a 1-2 MeV beam, an accelerator (electrostatic focusing up to ~100 MeV then

magnetic focusing) that brings the beam energy to its final energy (3-10 GeV), a 'buncher' or 'drift compression' section where the beam is longitudinally compressed to reduce the pulse duration to tens of nanoseconds (and increase the beam current) and the final focus section where the beam is focused onto a spot with a radius of a few millimeters. The final focus region may employ neutralization techniques to achieve smaller spot sizes on target.

### I.3.2 - *Overview of an updated conceptual heavy ion fusion power plant based on an induction linac: the Robust Point Design (RPD)*

Typical power plant reactors produce electrical power of 800 to 1500 MWe. Conceptual designs for heavy-ion driven inertial fusion power plants are usually based an electrical output of about 1000 MWe though the cost of producing electricity scales favorably for higher output. We present here a recently updated self-consistent point design for a heavy ion fusion power plant based on an induction linac driver, indirect-drive targets, and a thick liquid wall chamber [21]. Previous advanced designs for a power plant include the HIBALL-II [22] and the HYLIFE-II [23] designs. The main power plant parameters for all three designs are summarized in Table I.

**Table I**: Plant parameters of the HYBALL-II, HYLIFE-II and RPD conceptual power plant designs [22,23,21]. Quantities in parentheses indicate the number per reactor chamber.

|                                   | HIBALL-II    | HYLIFE-II | RPD  |
| --------------------------------- | ------------ | --------- | ---- |
| Number of reactor chambers        | 4            | 1         | 1    |
| Fusion power, MW                  | 8000 (2000)  | 2835      | 2400 |
| Net electrical output, MW         | 3784 (946)   | 1083      | 1058 |
| Driver energy, MJ                 | 5.0          | 5.0       | 7.0  |
| Target Gain                       | 80           | 70        | 57   |
| Fusion yield, MJ                  | 400          | 350       | 400  |
| Driver efficiency                 | 0.27         | 0.20      | 0.38 |
| Thermal-to-electrical efficiency  | 0.42         | 0.412     | 0.44 |
| Repetition rate, Hz               | 20 (5)       | 8.2       | 6.0  |

The RPD is based on conservative parameters such that each design area can meet its functional requirements in a robust manner. It starts with a target design which is a variation of the distributed radiator target (DRT) discussed in Ref [24,25]. This new design allows beams to come in from a larger angle, up to 24 degrees off axis instead of 12 degrees for the original DRT design, and spot sizes (i.e. RMS radius) of 2.3 mm and 1.8 mm for the foot and main pulse, respectively. Two-dimensional integrated simulations of target ignition (using the hydro code LASNEX [26]) predict that it will yield 400 MJ of fusion power at 7.0 MJ driver energy, a gain of 57. Note that simulations have produced a gain of 130 for a driving beam energy of 3.3 MJ for the closed-coupled version of the distributed radiator design [27], in which the case-to-capsule ratio was decreased by about 25% with respect to the DRT design.

The pulse is delivered using 120 beams, 48 for the foot pulse (3.3 GeV, 1.76 MJ) and 72 for the main pulse (4.0 GeV, 5.28 MJ) in a multiple-beam superconducting magnet array arrangement, which consists of 1835 focusing units, excluding the final focus magnets, where each unit is an array of 120 superconducting magnets. During transport and acceleration, the beam fills 66% (at final energy) to 72% (at injection) of the magnet aperture, with a peak magnetic field of 4 T (at windings). The induction linac driver uses $Bi^+$ (A = 209 amu), is 2.9 km long with accelerating gradients ranging from 0.026 MV/m at injection to 1.5 MV/m close to the final energy. The peak beam current per beam is 94 A at final energy.

As for the HYLIFE-II chamber, the RPD chamber uses thick liquid wall of molten salt (Flinabe, which chemical composition is $LiNaBeF_4$, instead of Flibe, $Li_2BeF_4$) as a coolant but also for the additional purposes of tritium breeding and neutron shielding. One of the main differences with the HYLIFE-II chamber design is the vortices that shield the beam line penetration as shown on Figure I-6 [28].
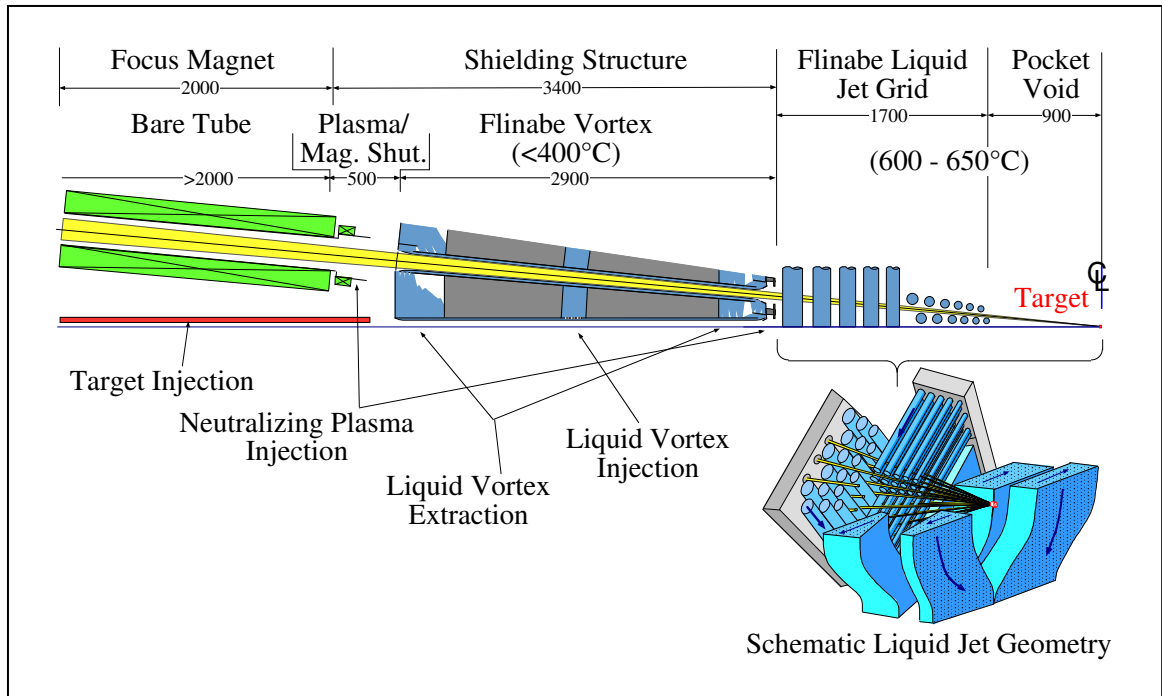
**Figure I-6**: Schematic of the RPD beam line [28]. Lengths are in millimeters.

For the robust assumptions of this design point, the resulting cost of electricity is near the optimum at 7.2 ¢/kWeh [21].

### I.4 - Overview of previous scaled experiments

Several low current and low kinetic energy experiments have been recently completed [29]. In these experiments, the physical dimensions, the generalized perveance (measure of the ratio of space-charge potential energy to kinetic energy) and the emittance of the beam were scaled appropriately to explore beam dynamics in a regime relevant for the HIF mission. They mainly address transverse beam dynamics, where the phase-space evolution due to the beam manipulations is the primary experimental result. These experiments

include recirculation and bending of an ion beam, four-to-one beam merging, scaled beam focusing, beam current amplification and single beam transport.

The recirculator experiment [30] was aimed at studying the feasibility of building a space-charge-dominated, ion induction circular machine as an alternative concept for heavy-ion fusion and demonstrating the ability to coordinate bending and acceleration while maintaining good beam control and brightness. It was designed to accelerate 2 mA $K^+$ ions from 80keV to 300 keV in 15 laps. However, only one 90° bend was completed. Still, results from this experiment indicated that bending and acceleration were possible with acceptable beam degradation.

The beam merging (i.e. combiner) experiment [31] addressed designs scenarios in which several beams are merged into a single beam line while making a transition from electrostatic focusing to magnetic focusing at ≈100 MeV [32]. The combiner system consisted in of four 3 mA $Cs^+$ sources, each followed by a 160 kV diode and a focusing transport channel. Once combined, the merged beam was transported (without acceleration) and diagnosed in the remaining 31 lattice periods of the transport channel. The results indicate that the phase-space dilution from merging may be acceptable for some HIF designs.

The Final Focus Scaled Experiment (FFSE) [33] studied vacuum ballistic focusing (and some neutralizing schemes) at the one-tenth scale of the then-proposed HYBALL-II final focus design. In this experiment, up to ≈100 μA, 160 keV $Cs^+$ was first transported through 10 electrostatic quadrupoles in preparation for the focusing section that consisted of six pulsed magnetic

quadrupoles. The expected emittance-dominated (scaled) focal spot was achieved as well as smaller focal spots when a hot filament was placed after the last focusing magnet and emitted enough low-energy electrons for space-charge neutralization of the beam.

Current amplification as explored in the MBE-4 accelerator [34] is an integral feature of the induction linac approach to heavy-ion fusion. In a driver, the current amplification is achieved by a smooth and controlled temporal compression of the beam by a factor of ~100. One out of the four available beam lines was used and produced a 10 mA, 200 keV $Cs^+$ beam followed by a matching section and the electrostatic-quadrupole-based transport channel (30 lattice periods, 24 acceleration gaps). The results indicate that ≈3:1 current amplification factors for both drifting and accelerated beams are accompanied by little or no transverse normalized emittance growth.

Finally, the Single Beam Transport Experiment (SBTE) [35] studied extensively the stability limits associated with the transport of space-charge-dominated ion beams in long alternating gradient (AG) transport channels. The beam line consisted of five matching electrostatic quadrupoles with independent voltages followed by 82 electrostatic quadrupoles with equal voltages alternating in sign. An alumino-silicate cesium source produced the ions, which were further accelerated through a four-electrode injector to an energy of 120 to 200 keV. Attenuators mounted on a rotating wheel at the exit of the injector provided a means of controlling the beam current to be transported (from 1 to 15.2 mA at 120 keV), thus the space-charge intensity of the beam. By varying the focusing

15

strength of the quadrupoles and the beam current, the quantities $\sigma_0$ and $\sigma$, respectively the betatron phase advance of a particle in the lattice without and with space-charge were parametrically scanned within the limits accessible in the experiment. Total beam current and emittance measurements made at the beginning and the end of the transport channel determined if the transport conditions were stable (no emittance growth nor beam loss) or unstable (emittance growth and/or beam loss). It was found that the beam behavior was always stable for $\sigma_0 \leq 90°$ and unstable for $\sigma_0 \geq 90°$ if a sufficiently high current was injected.

From all these experiments, no "show stopper" was revealed in any of the main beam manipulations envisioned in a heavy ion fusion driver.

## I.5 - The High Current Transport Experiment (HCX)

Scaled experiments cannot address non ideal effects associated with a full-scale driver, due to the much higher absolute magnitude of the space-charge intensity in a driver. Such non ideal effects include background gas bursts and secondary electrons induced by lost halo particles, instabilities and space-charge nonlinearities induced by trapped and streaming electrons in the self field potential well of the ion beam, and unanticipated material limits that might lead to degraded vacuum or voltage breakdown [36].

The High Current Experiment (HCX) [37] located at Lawrence Berkeley National Laboratory and carried out by the HIF-VNL[1] is designed to explore the physics of intense beams and test non-scalable issues in beam transport at driver-scale line-charge density. Earlier quadrupole transport experiments (such as the ones described in Section - I.4 -) have had beam currents (or line-charge densities) that were an order of magnitude (or more) smaller than those envisioned for a fusion driver.

**Table II**: Comparison of the main beam parameters for a heavy ion fusion driver (at injection) and the High Current Experiment (achievable parameters).

|  | HIF driver | HCX |
| --- | --- | --- |
| Number of beams | ≈ 100 | 1 |
| Ion mass, amu | > 100 | 39 ($K^+$) |
| Beam current per beam, A | ~ 0.5 | ~ 0.5 |
| $\Delta I / I$ during pulse, % | ±0.2 | ±1.0 |
| Injector voltage, MV | ~ 1.5 - 2.0 | 1.8 |
| $\Delta V / V$ during pulse, % | ±0.1 | ±0.1 |
| Line charge density per beam, μC/m | ≥ 0.2 | ≥ 0.2 |
| Pulse length, μs | ≈ 10 - 20 | > 4 |
| Rise time, μs | < 1 | < 1 |
| Emittance per beam, π mm mrad | < 1 | ≤ 1 |
| Life time, pulses | $1.6 \times 10^8$ | $\sim 3 \times 10^5$ |

At an injection energy of 1-1.8 MeV, a line-charge density, $\lambda$, of 0.1-0.2 μC m$^{-1}$ and a pulse duration of >4 μs, the HCX main beam parameters are in the range

of interest for a fusion driver front-end (see Table II). At 1 MeV where we report most of our results, the generalized beam perveance is

$$K = \frac{1}{4\pi\varepsilon_0} \frac{\lambda}{E_B} = 8 \times 10^{-4},$$ (Eq. I-4)

where $E_B$ .is the beam energy in eV and $\lambda$ is in C m$^{-1}$. In this regime space-charge forces strongly influence the beam properties during its transport, but image charges induced on metallic structures of the machine aperture play an important role. For comparison, the beam line charge density and generalized perveance of large accelerator facilities such as the Spallation Neutron Source (SNS) Front End [38,39,40] and Fermilab's Linac Experimental Facility [41,42,43] are one to two orders of magnitude lower than the HCX parameters. Also, in both cases, the beam is rapidly accelerated to energies where space-charge effects are diminished. For heavy-ion inertial fusion, where the line-charge density increases from ≈0.2 μC m$^{-1}$ at injection to ≈1.7 μC m$^{-1}$ at the end of the accelerator (4.0 GeV, Bi$^+$ beam) and ≈30 μC m$^{-1}$ at the end of the drift compression at the D-T target [21], the perveance is increased by beam bunch compression as part of the acceleration schedule, which optimizes the induction linear accelerator efficiency.

Moreover, even in SBTE mentioned in the previous section, the maximum generalized perveance was 2.2 x 10$^{-3}$ - higher than generally envisioned for a fusion driver, but the line charge density remained about one order of magnitude lower (at a maximum of ≈0.03 μC m$^{-1}$) than for the HCX or a fusion driver front end. Finally, The University of Maryland Electron Ring (UMER) [44,45], which

was designed for studying the transport of high intensity electron beams in a strong focusing lattice, can also produce highly tune-depressed beams but with a line charge density of $\lambda \approx 1.5 \times 10^{-3}$ µC m$^{-1}$ [46].

### I.5.1 - HCX mission statement

A principal goal of the experiment is to evaluate the maximum acceptable beam fill factor, or the radial extent of the beam within the physical aperture (i.e. $r_{beam}/r_{ap}$, where $r_{beam}$ is the maximum envelope excursion of a matched beam propagating in a transport channel of radius $r_{ap}$ as illustrated in Figure I-7), addressing the question of how compact a multiple-beam focusing lattice may be to accommodate the transport and acceleration of the heavy ion beams.
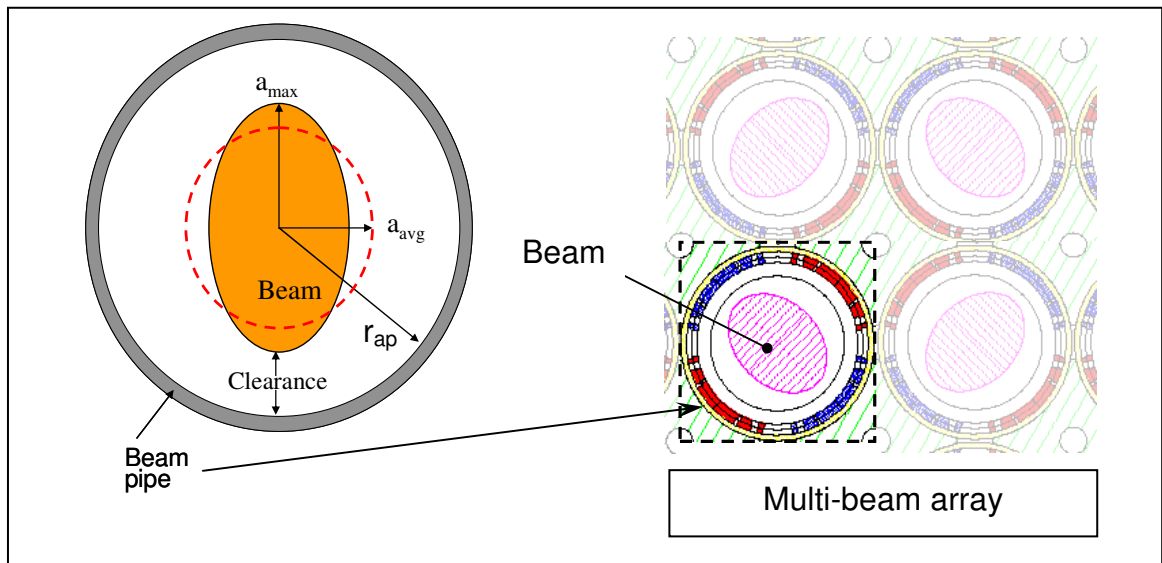


**Figure I-7**: Sketches showing schematically the definition of 'fill factor' and a multi-beam lattice arrangement.

Higher fill factors are desirable because they make more economically efficient use of material structures. For example, cost savings of 50% have been projected in multi-beam drivers if the fill factor can be increased from 60% to 80% as illustrated in Figure I-8 that shows results from the IBEAM system code [47,48].
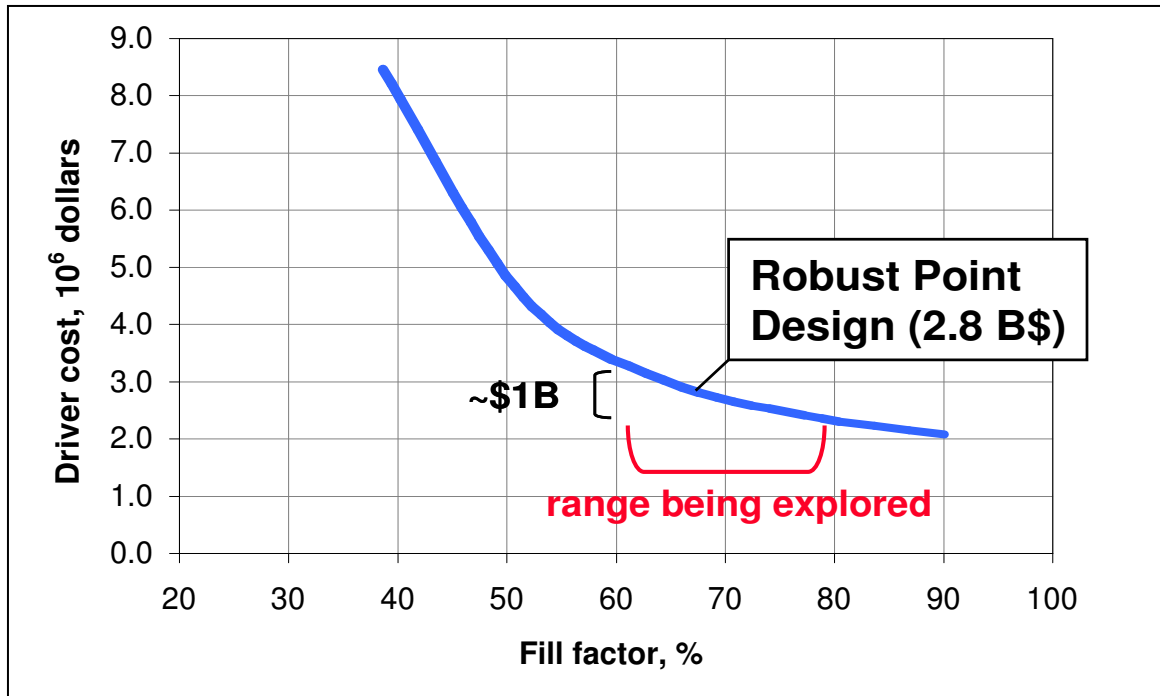


**Figure I-8**: Results from a system study (using the system code IBEAM) assuming a fixed number of beams, initial pulse length, and quadrupole field strength (*courtesy of Wayne Meier*).

The fill factor study on HCX addresses the more fundamental issue of how much charge can be transported in a single channel without degrading the beam quality. Greater fill factors enhance non ideal physics effects resulting from imperfect focusing optics, images charge and halo impacting material structures

and releasing desorbed gases that interact with long-pulse beams creating possible electron-cloud effects. These are intense beam physics issues that may be relevant to other accelerator applications requiring high intensity, such as spallation neutron sources and the production of rare isotopes. Design and engineering issues such as the frequency at which the beam coherent oscillation (i.e. centroid) must be corrected for, or the alignment tolerances for the focusing elements, are also less favorable the greater the fill factor and are also addressed.

### I.5.2 - Experimental configuration

The present HCX configuration consists of the $K^+$ ion source and injector, an electrostatic quadrupole matching section (six quadrupoles), the first ten electrostatic transport quadrupoles and four room-temperature pulsed magnetic quadrupoles. A multi-purpose diagnostic station (D-end) is at the end of the beam line (Figure I-9).
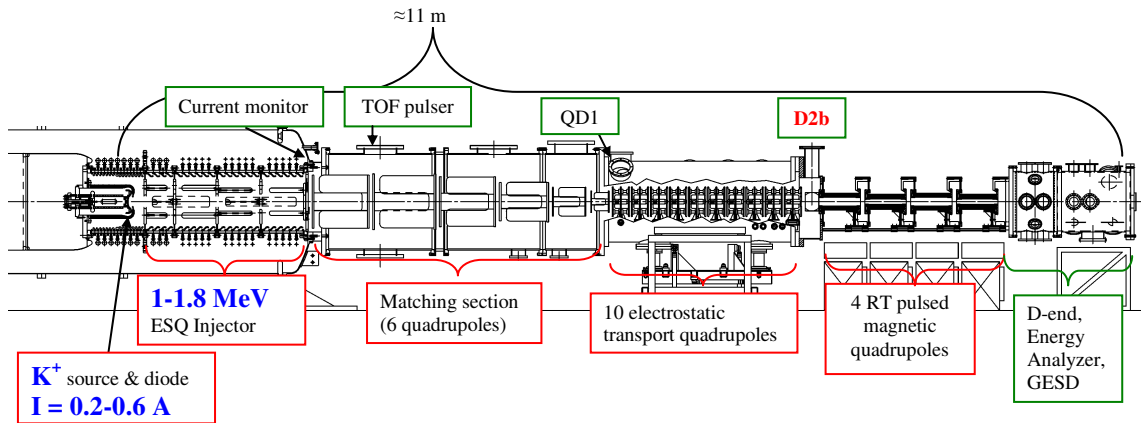


**Figure I-9**: Layout of the HCX (elevation view), after March 24th, 2003.

Beam diagnostics are also located at the interface of the matching section and the ten transport quadrupoles section (QD1) and after the last transport quadrupole in the periodic lattice (D2).At the early stages of the experiment (prior to March 24th, 2003), the apparatus did not include the magnetic quadrupoles. Instead, the electrostatic lattice was directly coupled to the multi-purpose diagnostics tank (Figure I-10).
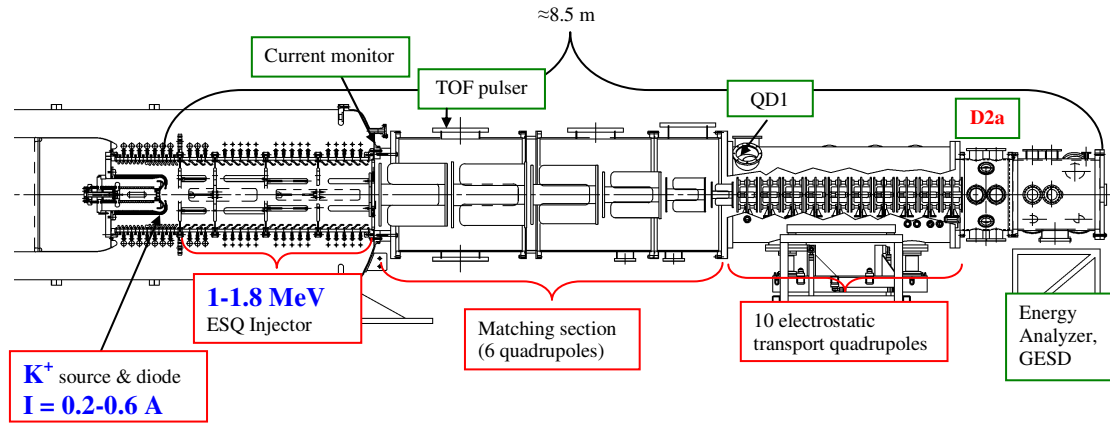


**Figure I-10**: Layout of the HCX (elevation view), before March 24th, 2003.

As a result of the two different setups, the drift distances to the measuring planes for the data taken at the exit of the electrostatic transport section prior to March 24th, 2003 (D2a) differ from the ones for the data taken after March 24th, 2003 (D2b). These drift distances are summarized in Table III.

**Table III**: Drift distances for the emittance slit-scanner measuring planes at the exit of the electrostatic transport section for the experimental setups shown in Figure I-9 (after March 24th, '03, D2b configuration) and Figure I-10 (before March 24th, '03, D2a configuration).

|  | D2a (*through March '03*) | D2b (*after March '03*) |
|---|---|---|
| QI10[2] end plate to horizontally driven slit, cm | 8.6 | 3.1 |
| QI10[2] end plate to vertically driven slit, cm | 11.1 | 2.5 |
| Horizontally driven slit to slit-cup drift, cm | 15.7 | 7.2 |
| Vertically driven slit to slit-cup drift, cm | 15.2 | 7.8 |

Note that the measuring planes for the D2b configuration are upstream of the D2a configuration measuring planes.

When making measurements at QD1, the first quadrupole of the electrostatic transport section is moved out of the beam path via a vacuum feedthrough and the lead screw assembly and the selected diagnostics are moved in. There is no quadrupole at D2 (merely a 15.2 cm drift through the diagnostics vacuum box to the first magnetic quadrupole). All diagnostics stations include transverse slit scanners and Faraday cups (with an additional current transformer at QD1). A large current transformer at the exit of the injector monitors the total beam current.

The various sections of the beam line (source-injector, matching section and electrostatic transport section) will be described in more detail as well as all the diagnostics used to characterize the beam distribution. The Gas Electron

---

[2] Nomenclature is described in Section - VIII.1 -

23

Source Diagnostic (GESD) is located at the end of the diagnostics tank (D-end) and is used to measure electron emission and gas desorption yields from ions incident on targets at near-grazing incident ion angles. These data, reported by *A. W. Molvik et al.* [49] (and not discussed in this thesis), are intended for calibration of the signal intensities collected on the flush-probe electrodes in the magnetic quadrupoles so that the beam loss and the gas desorption rate can be inferred. The GESD can also be used to study mitigation techniques of such undesirable effects. The GESD can be removed and replaced with an Electrostatic Energy Analyzer (EA) used for direct beam energy measurements (Section - XI.2 -).

### I.5.3 - *Results reported in this thesis*

The remainder of this thesis is organized as follows: In Chapter II, we review the principal notions of beam dynamics relevant for the understanding of the data presented in later chapters; in Chapter III, all the diagnostics used to acquire the data are described; Chapter IV gives an overview of the tools employed for numerical simulations of the experiment and Chapter V introduces the experimental agenda and summarizes the beam main parameters. Then, we report the steps undertaken to produce a high brightness (i.e. high current, low emittance) beam adequate for the HCX mission (Chapter VI). Then, we show the results of the beam matching procedure, and beam control issues associated with it (Chapter VII). Two fill factor measurements are reported for which the transverse phase-space of the beam was characterized in detail (Chapter VIII), along with beam energy measurements (Chapter XI) and preliminary halo

measurements (Chapter IX). Comparisons of the measurements to envelope models and Particle-In-Cell simulations are made (in Chapters VIII and IX). In addition, a study of the sensitivity of the main beam parameters to beam current variations is presented (Chapter X).

Based on these measurements, preliminary conclusions are drawn on the issues raised in the HCX mission statement, namely fill factor limits and future designs trade-offs for a heavy ion fusion linear accelerator (or any high current linac) with electrostatic focusing elements (Chapter XII). However, definitive answers to these questions require additional measurements and a longer transport channel, as originally planned.

A Glossary of specialized terms can be found in Appendix B.

# Chapter II -    Relevant notions of beam dynamics

This chapter is intended to outline the relevant theories of beam dynamics and define the relevant quantities that will be of some interest for the experimentalist in the context of this work. Extensive treatments of the topics presented below can be found in several references [50,51,52,53,54,55,84].

## II.1 -    Transverse charged particle beam dynamics

### II.1.1 -    Zero-current limit

Consider an ensemble of particles with charge $q$ and rest-mass $m$ propagating in the positive $z$-direction. The transverse equation of motion for a single particle, without acceleration, is

$$\frac{d^2 \vec{r}_\perp}{dt^2} = \frac{q}{m\gamma} \left( \vec{E} + \vec{v} \times \vec{B} \right)_\perp ,$$  (Eq. II-1)

where $\vec{E}$ and $\vec{B}$ are the electric and magnetic fields, $\vec{v} \equiv \vec{\beta} c$ is the particle velocity, $\gamma \equiv (1 - \beta^2)^{-1/2}$ is the relativistic factor and $\vec{r}_\perp$ is the position transverse to $\hat{z}$. The electromagnetic field acting on the particle consists of an externally applied field and the collective interaction due to the space-charge repulsion. In the low current limit, the space-charge repulsion is ignored. It is convenient to express the transverse motion of the particle as a function of the longitudinal dimension $z$. Then, (Eq. II-1) becomes

$$\vec{r}_{\perp}^{\,''} = \frac{q}{m\gamma\beta_z^2 c^2}\left(\vec{E} + \vec{v} \times \vec{B}\right)_{\perp},$$ 
(Eq. II-2)

using
$$\frac{d}{dt} = \beta_z c \frac{d}{dz}.$$ 
(Eq. II-3)

The prime denotes differentiation with respect to $z$. If the transverse velocity is much smaller than the forward velocity, we can apply the paraxial approximation, in which the transverse motion is effectively decoupled from the longitudinal motion [56]. In this approximation, $\beta_z c = \beta c$ and (Eq. II-2) becomes

$$\vec{r}_{\perp}^{\,''} = \frac{q}{m\gamma\beta^2 c^2}\left(\vec{E}_{\perp} + \beta c \hat{z} \times \vec{B}\right).$$ 
(Eq. II-4)

Assuming quadrupole focusing (as in alternating-gradient (AG) accelerators, in which focusing and defocusing lenses alternate), the external fields are proportional to $\|\vec{r}\|$ (i.e. n = 2, ν = 0 in a multipole expansion of the fields [57]) and the focusing strengths can be expressed as

(electrostatic focusing) $\quad k_{x,y}(z) = \pm\dfrac{q}{m\gamma\beta^2 c^2} E'(z),$ 
(Eq. II-5)

(magnetic focusing) $\quad k_{x,y}(z) = \mp\dfrac{q}{m\gamma\beta c} B'(z),$ 
(Eq. II-6)

where $E'$ and $B'$ are the field gradients. Note that for a positive gradient, the forces are focusing in the horizontal ($x$) direction and defocusing in the vertical ($y$) direction for an electrostatic quadrupole and have opposite signs for a

magnetic quadrupole. Then the equation of motion, (Eq. II-4), can be expressed in the form of Hill's equations:

$$x'' + k_x(z)x = 0 \,, \tag{Eq. II-7}$$

$$y'' + k_y(z)y = 0 \,. \tag{Eq. II-8}$$

A beam particle in a transverse focusing force as described by (Eq. II-7) and (Eq. II-8) experiences an alternating sequence of focusing and defocusing forces (i.e. FODO lattice) as it propagates through the accelerator. Since the particle orbits in such an alternating-gradient lattice deviate farther from the axis in focusing lenses than in defocusing lenses, on average the particle experiences a focusing force.

### II.1.2 - *The Courant-Snyder invariant and definition of emittance*

Based on Floquet's theorem, and for a periodic lattice, one can express any solution of the Hill's equation in a phase-amplitude form (for instance in the horizontal direction, (Eq. II-7)):

$$x(z) = A_x w(z)\cos[\psi(z) + \phi] \,, \tag{Eq. II-9}$$

where $A_x$ and $\phi$ are constants determined by the initial conditions and the constraint that $w(z)$ and $\psi(z)$ need to satisfy

$$\psi'(z) = \frac{1}{w^2(z)} \,. \tag{Eq. II-10}$$

Substituting (Eq. II-9) into (Eq. II-7) and using (Eq. II-10) yields the differential equation

$$w''(z) + k_x(z)w(z) - \frac{1}{w^3} = 0 \qquad \text{(Eq. II-11)}$$

for the amplitude function $w(z)$.

Taking the derivative of the phase-amplitude form of the particle trajectory and eliminating $\psi + \phi$, one finds the Courant-Snyder invariant, which can be expressed as

$$\hat{\gamma} x^2 + 2\hat{\alpha} x x' + \hat{\beta} x'^2 = A_x^2, \qquad \text{(Eq. II-12)}$$

by using the definitions

$$\hat{\beta}(z) = w^2(z), \qquad \text{(Eq. II-13)}$$

$$\hat{\alpha}(z) = -w(z)w'(z), \qquad \text{(Eq. II-14)}$$

$$\hat{\gamma}(z) = \frac{1}{w^2(z)} + w'^2(z) = \frac{1 + \hat{\alpha}^2(z)}{\hat{\beta}(z)}. \qquad \text{(Eq. II-15)}$$

Thus, (Eq. II-12) defines an ellipse in the $x - x'$ phase space which area is $\pi A_x^2$. The emittance of the beam in this plane, $\varepsilon_x$, can then be defined as the area of the ellipse that is formed by the outermost particle orbits (and that corresponds to the maximum value of $A_x$) such that

$$\varepsilon_x = A_{x,Max}^2. \qquad \text{(Eq. II-16)}$$

The same derivation applies for the vertical (y) direction.

### II.1.3 -   *The effect of space charge and the K-V envelope equation*

In the zero-current limit, all particles in the beam move independently of each other. To self-consistently include the beam self-repulsion due to its space-charge, we need to consider the evolution of the beam distribution in the transverse $x$, $x'$, $y$, $y'$ phase space. The Kapchinskij-Vladimirskij (K-V) distribution is the only known repeating distribution that self-consistently describes beam propagation in an alternating gradient focusing lattice [58]. It is used to derive the so-called 'K-V envelope equation', which gives the trajectory of the edge of the beam as a function of the self and applied fields and the emittance. A quick outline of one derivation is given here.

Consider a uniform density beam filling an elliptical cross-section with semi-axes $a$ and $b$. Then, the space-charge fields inside the ellipse are given by

$$\vec{E}_{sc} = \frac{\lambda}{\pi\varepsilon_0} \frac{1}{a+b}\left(\frac{x}{a}\hat{x} + \frac{y}{b}\hat{y}\right) \qquad\qquad \text{(Eq. II-17)}$$

$$\vec{B}_{sc} = \frac{\mu_0\lambda}{\pi}\beta c\frac{1}{a+b}\left(-\frac{y}{b}\hat{x} + \frac{x}{a}\hat{y}\right) \qquad\qquad \text{(Eq. II-18)}$$

in which $\lambda$ is the line charge density of the beam [59]. If we combine the space-charge repulsion and the external forces, we find from (Eq. II-4), (Eq. II-7) and (Eq. II-17):

$$x'' + k_x(z)x = \frac{2K}{(a+b)}\frac{x}{a}, \qquad\qquad \text{(Eq. II-19)}$$

And similarly in the $y$-direction

$$y'' + k_y(z)y = \frac{2K}{(a+b)}\frac{y}{b},$$ (Eq. II-20)

where $K$ is the generalized perveance as defined in (Eq. I-4). These are linear equations of motion (Hill's equations). Therefore, if $a(z)$ and $b(z)$ are regarded as specified functions, Floquet's theorem can be applied, Courant-Snyder invariants can be identified and phase-amplitude solutions can be constructed. Then, a distribution constructed from the Courant-Snyder invariants must be found that generates the needed uniform beam $\rho = q\hat{n}$ to produce a fully self-consistent model.

Similar to the results from Section - II.1.2 -, one can find that the beam-edge is given by:

$$a(z) = \sqrt{\varepsilon_x} w_x(z),$$ (Eq. II-21)

$$b(z) = \sqrt{\varepsilon_y} w_y(z),$$ (Eq. II-22)

and the equations for the envelope radii are derived from the equations for $w_x(z)$ and $w_y(z)$:

$$a'' + k_x a - \frac{2K}{(a+b)} - \frac{\varepsilon_x^2}{a^3} = 0,$$ (Eq. II-23)

$$b'' + k_y b - \frac{2K}{(a+b)} - \frac{\varepsilon_y^2}{b^3} = 0.$$ (Eq. II-24)

These are the so-called RMS envelope equations or K-V envelope equations. To complete the derivation, one must show that a distribution formed from the

31

constants of motion yields the correct, consistent density projections. This distribution is the K-V distribution, which is defined as:

$$f_\perp(x, y, x', y', z) = \frac{\hat{n}\,ab}{\pi\,\varepsilon_x\,\varepsilon_y}\,\delta\left[\frac{(x/w_x)^2 + (w_x x' - w'_x x)^2}{\varepsilon_x}\right.$$

$$\left. + \frac{(y/w_y)^2 + (w_y y' - w'_y y)^2}{\varepsilon_y} - 1\right], \qquad \text{(Eq. II-25)}$$

where $\delta(x)$ is the Dirac-delta function.

### II.1.4 - *Concept of equivalent beams and RMS emittance*

Laboratory beams usually differ from the K-V distribution described above or any other theoretical, stationary particle distributions. However, according to the concept of equivalent beams developed by Lapostolle and Sacherer [60,61], "two beams composed of the same particle species and having the same current and kinetic energy are *equivalent* in an approximate sense if the second moments of the distribution are the same" [62]. It is therefore customary to define the projected beam widths and emittances in terms of their RMS definitions when comparing different distributions. The second moment in the particle coordinates $x$ is defined by

$$< x^2 > = \int\int\int\int x^2 f(x, y, x', y')\, dx\, dy\, dx'\, dy', \qquad \text{(Eq. II-26)}$$

and the RMS beam width in the $x$-direction is then given by

$$x_{RMS} = \sqrt{< x^2 >}, \qquad \text{(Eq. II-27)}$$

and similarly for the other second moments.

32

In the limit of a K-V distribution, one can show that the edge measures are simply related to the statistical RMS measures. With $x_{max} = a$, the maximum $x$-position (radius or envelope) and $x'_{max} = a'$, the maximum slope in the particle distribution, we find that

$$< x^2 >= \frac{a^2}{4}.$$  (Eq. II-28)

The first two derivatives of (Eq. II-28) with respect to the direction of propagation are:

$$a' = \frac{4 < x x' >}{a},$$  (Eq. II-29)

$$a'' = \frac{4}{a}\left(< x'^2 > + < x x'' >\right) - \frac{16}{a^3} < x x' >^2,$$  (Eq. II-30)

where (Eq. II-29) has been used to eliminate $a'$ from (Eq. II-30). To eliminate $x''$ from (Eq. II-30), we use (Eq. II-19), which combined with (Eq. II-28) gives

$$a'' = \frac{16 < x'^2 >< x^2 >}{a^3} + k_x a + \frac{2K}{(a+b)} - \frac{16 < x x' >^2}{a^3}.$$  (Eq. II-31)

Finally, comparing (Eq. II-31) to (Eq. II-23), we can define an 'edge' emittance that is equivalent to the transverse phase space area of the beam in terms of RMS quantities:

$$\varepsilon_{x,edge} = 4\varepsilon_{RMS} = 4\sqrt{< x'^2 >< x^2 > - < x x' >^2}.$$  (Eq. II-32)

Again, we have the same definitions in the $y$-direction.

33

Because the second moments and cross moments are easily obtained from the experimental measurements, the emittance (and all other beam parameters) quoted in this work are calculated using (Eq. II-32).

### II.1.5 - *Smooth approximation*

From the phase-amplitude formulation of the solutions of the equation of motion, it is apparent that the trajectories of the particles consist of a fast oscillation at a frequency corresponding to the period of the focusing lattice and of a slower oscillation extending over several lattice periods. The slower, smooth oscillatory behavior is called the betatron oscillation [55]. In the smooth approximation, the trajectories are taken to be cosines and sines and one obtains the smooth beam envelope equations:

$$a_0'' + \left(\frac{\sigma_0}{2L}\right)^2 a_0 = \frac{\varepsilon_x^2}{a_0^3} + \frac{2K}{a_0 + b_0} , \qquad \text{(Eq. II-33)}$$

$$b_0'' + \left(\frac{\sigma_0}{2L}\right)^2 b_0 = \frac{\varepsilon_y^2}{b_0^3} + \frac{2K}{a_0 + b_0} , \qquad \text{(Eq. II-34)}$$

where $a_0(z)$ and $b_0(z)$ define the smooth beam envelope, $\sigma_0$ is the undepressed tune or phase advance per lattice period and $L$ is a half-lattice period. The undepressed phase advance can be calculated exactly from the properties of the focusing lattice using the transfer matrix approach [55]. An approximate formulation for $\sigma_0$ in the smooth-limit for a FODO lattice is used [63]:

$$\sigma_0 = k_{max} \ell_{eff} L. \tag{Eq. II-35}$$

Here, $k_{max}$ is the peak quadrupole strength and $\ell_{eff}$ is the effective length of a quadrupole. From (Eq. II-33) or (Eq. II-34), we can find an expression for the average beam radius, $R_0$, assuming $\varepsilon_x = \varepsilon_y = \varepsilon$:

$$\left(\frac{\sigma_0}{2L}\right)^2 R_0 = \frac{\varepsilon^2}{R_0^3} + \frac{K}{R_0}. \tag{Eq. II-36}$$

This expression leads to the definition of the depressed tune or phase – advance $\sigma$ as

$$\left(\frac{\sigma}{2L}\right)^2 \equiv \left(\frac{\sigma_0}{2L}\right)^2 - \frac{K}{R_0^2}. \tag{Eq. II-37}$$

Finally, we define the tune depression [64] as the ratio $\sigma/\sigma_0$, which is a measure of the space charge intensity of the beam.

More approximate relations can be derived between the depressed and undepressed tune and the lattice and beam properties by taking expansions in $k_{max} L^2$ [65].

## II.1.6 - *Electrostatic focusing line charge density limit scaling*

If we neglect the emittance in (Eq. II-36) and express $\sigma_0$ in terms of the lattice period $L$, the quadrupole's peak voltage $V_q$, the longitudinal quadrupole

occupancy (i.e. $l_{eff}/L$), $r_{ap}$ and $E_B$, we can write the maximum transportable line charge density per beam as

$$\lambda_B = 0.9 \frac{\mu C}{m} \left( \frac{V_q}{80 \text{ kV}} \right) \left( \frac{\sigma_0}{1.4} \right) \left( \frac{R_0/r_{ap}}{0.7} \right)^2 \left( \frac{\eta}{0.7} \right).$$  (Eq. II-38)

Although an ideal case, (Eq. II-38) shows the importance of the fill factor, which enters quadratically. This is also true for magnetic quadrupole focusing or solenoid focusing systems.

### II.1.7 -  *Envelope mismatch modes in a FODO transport channel*

When the beam is matched to the lattice, the beam envelope undergoes periodic oscillations (one full oscillation every two quadrupoles) and its average radius over a lattice period, $R_0$ (Eq. II-36), is constant. When the beam is not matched, the envelope radius becomes a periodically varying function of distance $z$, with a periodicity different from the lattice. There are many reasons that can cause the beam to be mismatched: errors in the determination of the beam energy, beam current, quadrupole voltages and so on. The following analysis considers envelope mismatches that are the result of small errors in the beam initial dimensions.

II.1.7.1 -  Continuous focusing

Starting with a continuous focusing model (i.e. smooth approximation) of the lattice ((Eq. II-33) and (Eq. II-34)) and taking the initial conditions to be

$$a = R_0 + \delta a ; \qquad |\delta a|/R_0 \ll 1,$$  (Eq. II-39)

$$b = R_0 + \delta b \, ; \qquad\qquad |\delta b| / R_0 \ll 1 \, , \qquad\qquad \text{(Eq. II-40)}$$

one obtains two coupled linearized differential equations which exhibit two independent solutions that lead to two fundamental oscillation modes [66]:

$$a = R_0 + \delta R \cos(k_B z + \psi_B) \, , \qquad\qquad \text{(Eq. II-41)}$$

Breathing mode

$$b = R_0 + \delta R \cos(k_B z + \psi_B) \, , \qquad\qquad \text{(Eq. II-42)}$$

$$a = R_0 + \delta R \cos(k_Q z + \psi_Q) \, , \qquad\qquad \text{(Eq. II-43)}$$

Quadrupole mode

$$b = R_0 - \delta R \cos(k_Q z + \psi_Q) \, , \qquad\qquad \text{(Eq. II-44)}$$

where

$$k_B = \sqrt{2k_{\beta_0}^2 + 2k_\beta^2} \, , \qquad\qquad \text{(Eq. II-45)}$$

$$k_Q = \sqrt{k_{\beta_0}^2 + 3k_\beta^2} \, , \qquad\qquad \text{(Eq. II-46)}$$

and

$$k_{\beta_0} \equiv \frac{\sigma_0}{2L} \, , \qquad\qquad \text{(Eq. II-47)}$$

$$k_\beta \equiv \sqrt{k_{\beta_0}^2 - \frac{K}{R_0^2}} \, , \qquad\qquad \text{(Eq. II-48)}$$

and with $\delta R$, $\psi_B$ and $\psi_Q$ being constants. In one case, the quadrupole mode, the two oscillations in the $x$ and $y$ directions are 180° out of phase. In the other, the breathing mode, both oscillations are in phase. Any other envelope oscillation can then be expressed as a combination of these two modes.

37

II.1.7.2 - Alternating Gradient (AG) focusing

For an AG channel, described by (Eq. II-23) and (Eq. II-24), the same analysis can be carried out. The perturbation is now applied around the matched beam radii, $a_0$ and $b_0$, which gives the following initial conditions:

$$a(z) = a_0(z) + \delta a(z); \qquad |\delta a|/a_0 << 1, \qquad \text{(Eq. II-49)}$$

$$b(z) = b_0(z) + \delta b(z); \qquad |\delta b|/b_0 << 1. \qquad \text{(Eq. II-50)}$$

The results are similar to the continuous focusing analysis in that two fundamental modes equivalent to the breathing and quadrupole modes above describe all possible envelope mismatch oscillations [67]. Note that the frequency of these modes is slightly smaller. A lengthier discussion of these modes and their stability regimes can be found in Ref. [68] (e.g.: the modes phase advances are given by $\sigma_{B,Q} = 2\arg\lambda$, where $\lambda$ is a complex eigenvalue depending on $\sigma_0$, the free-drift between two subsequent thin-lens quadrupoles, the beam size and the perveance $K$ and is defined in Equation G21 of Ref. [68]). Also in Ref. [68], quadrupole excitation prescriptions have been derived for launching pure modes in a middle of a drift within the lattice, using 'HCX-like' parameters. From an experimental point of view, these prescriptions give another knob to control the beam maximum excursion, making it possible to purposely fill more of the aperture locally. With two mode frequencies, it is harder to understand where the excursions occur, which in turn may impair the interpretation of the data. Also, both modes have different symmetry properties and whether one mode may be doing more harm than the other with regard to effects outside the envelope

model is being studied. For example, the higher frequency breathing mode appears to generate a higher amplitude beam halo.

### II.1.8 -    *Implications of electrostatic charge-density oscillations for intense beams*

Equilibrium and stability properties of intense beams are complex problems and discussions are presented in Refs [53,69 ,134]. Here, we are interested in the case of electrostatic charge-density oscillations. This was first treated by Gluckstern [70] and by Davidson and Krall [71] for a K-V distribution in a continuous focusing channel. Local perturbations in a beam can produce collective modes of oscillations, which Gluckstern described in terms of the oscillations of the space-charge potential associated with the density fluctuations. Solving the perturbed linearized Vlasov equation leads to solution of the perturbed potentials $V_n \propto e^{i\omega t} G(r,\phi)$, where the time $t$ can be related to the propagation distance and $G(r,\phi)$ describes the geometric dependence of the potentials on the cylindrical coordinates ($r$ and $\phi$). $G(r,\phi)$ consists of a sum of $r^n \cos m\phi$ and $r^n \sin m\phi$ terms, where $n$, the 'order' of the mode and $m \leq n$, the azimuthal variation, are integers [72]. Hoffman *et al.* [164] treated the alternating gradient channel problem with solenoid and quadrupole focusing, which leads to similar perturbed potentials but where the coefficients are more difficult to obtain and require numerically solving sets of differential and integral equations.

More recently, Lund and Davidson [73] employed a warm-fluid model to investigate the equilibrium and stability properties of unbunched, continuously

focused intense ion beams. They find that the radial eigenfunction describing axisymmetric flute perturbations about a K-V equilibrium is identical to the eigenfunction derived from the full kinetic treatment. The warm-fluid stability properties for axisymmetric flute perturbations about a K-V beam equilibrium is of some particular interest because, at first approximation, it helps explain features that are seen in the HCX beam current-density distribution (see Section -IX.1 -). The transverse fluid mode structure for perturbations about a warm K-V beam equilibrium is described by the radial eigenfunction expansion of the perturbed potential

$$\delta\phi_n(r) = \begin{cases} \dfrac{A_n}{2}\left[ P_{n-1}\left(1-2\dfrac{r^2}{r_b^2}\right) + P_n\left(1-2\dfrac{r^2}{r_b^2}\right)\right], & 0 \le r \le r_b, \\ 0, & 0 < r \le r_{ap}, \end{cases}$$
(Eq. II-51)

where $P_n(x)$ denotes the $n$ th-order Legendre polynomial, $A_n = const$ denotes the linear mode amplitude and $r_b$ is the beam edge radius, an by the dispersion relation

$$\omega = \omega_p^2 + 4\left(\omega_r - \frac{\omega_c}{2}\right)^2 + \frac{8T_\perp}{mr_b^2}n^2,$$
(Eq. II-52)

where $\omega_r = const$ is the equilibrium angular rotation velocity, $\omega_c$ is the cyclotron frequency, $T_\perp = const$ is the effective perpendicular temperature in energy units on axis ($r = 0$), $\omega_p = const$ is the plasma frequency and $n$ is an integer. In the case of pure electric focusing appropriate to model alternating gradient transport channels, (Eq. II-52) can be expressed as

$$\left(\frac{\omega}{v_0}\right)^2 = 2 + 2\left(\frac{v}{v_0}\right)^2\left(2n^2 - 1\right).$$  (Eq. II-53)

Here,

$$v^2 \equiv \omega_f^2 - \frac{\omega_p^2}{2} = \frac{2T_\perp}{mr_b^2},$$  (Eq. II-54)

$$v_0^2 \equiv \omega_f^2 = \frac{2T_\perp}{mr_b^2} + \frac{\omega_p^2}{2}$$  (Eq. II-55)

are the squares of the depressed and undepressed single-particle oscillations frequencies in the equilibrium field. From the Poisson equation and (Eq. II-51), one obtains the body-wave component of the perturbed density $\delta_n(r)$. Figure II-1 shows the radial potential and density eigenfunctions for oscillations modes one to five. These modes are used (Section -IX.1 -) to characterize perturbations in the beam density.
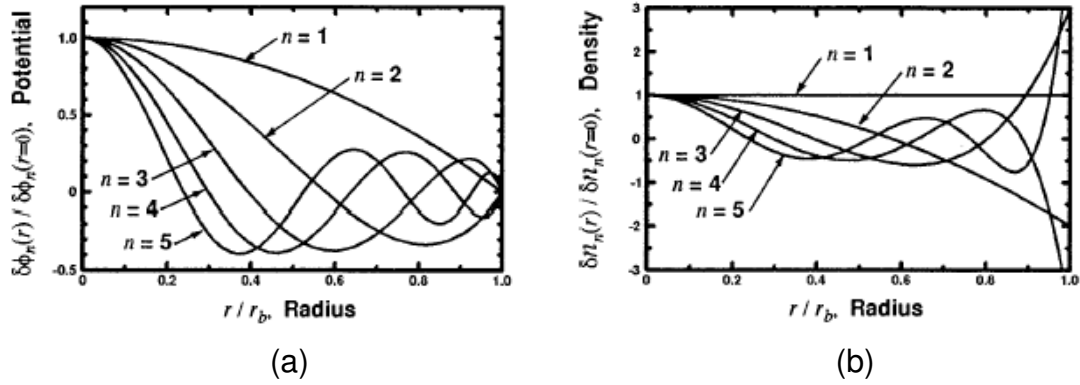
**Figure II-1**: Solutions for the normalized radial eigenfunction of axisymmetric flute perturbations are plotted as a function of normalized radial coordinate $r/r_b$ for a warm K-V beam equilibrium in the electrostatic approximation. The eigenfunction is plotted in terms of (a) the normalized potential $\delta\phi_n / \delta\phi_n(r=0)$, and (b) the normalized density $\delta n_n / \delta n_n(r=0)$ for radial mode numbers $n =1,2,...,$ and 5 [73].

### II.1.9 -   Non-linear effects

All the derivations above were treated with assumptions leading to linear sets of equations. Nonideal effects that are present in actual accelerators are highly nonlinear and tend to increase the RMS emittance. Some of these effects are discussed below.

II.1.9.1 - Fringe fields

Fringe fields near the ends of the focusing elements generate third-order aberrations (i.e. spherical aberrations [74]) that arise from the longitudinal

42

variation of the quadrupolar field. These third order terms appear in the equation of motion through the first and second derivatives of the focusing field gradient with respect to the direction of propagation [75, 76]. To calculate the longitudinal field and the higher-order multipoles the shape of the fringe field and all its derivatives need to be known and can be approximated by:

$$G(z) = \frac{1}{2} G_0 \left\{ \left[ 1 + \tanh\left( \frac{\pi z}{L_f} \right) \right] \right\},$$

(Eq. II-56)

where $G_0$ is the quadrupole field gradient in the center of the quadrupole, and $L_f$ is the length of the fringe field. (Eq. II-56) is plotted on Figure II-2 along with the hard-edge equivalent quadrupole field.
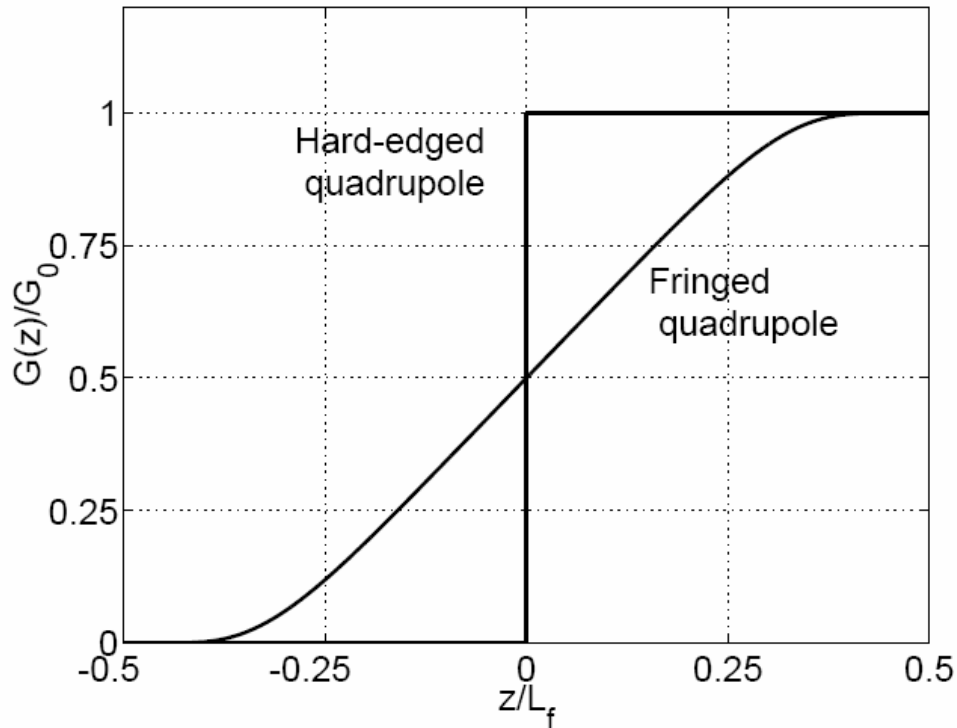


**Figure II-2**: Quadrupole field gradient $G(z)$ as a function of distance $z$ in the fringe field region of a quadrupole. The length of the fringe field is $L_f$. [75]

43

II.1.9.2 -  Misalignment

If a focusing element is not perfectly aligned with respect to the beam centroid, the beam experiences a dipole-like field as it passes through and will be kicked transversely. The coherent motion of the beam is then simply described by the single particle equation of motion. As the beam passes through a number of displaced quadrupoles, it oscillates and the oscillation amplitude average grows. Even if all quadrupoles are perfectly aligned, an initial beam misalignment will also cause the beam centroid to oscillate [77].

II.1.9.3 -  Image charges

When close to conducting surfaces, the presence of charged particles will induce image charges on these surfaces such that the electric fields in these conductors are zero. The first-order effect of these forces on the coherent motion of the beam (i.e. centroid) is linear and proportional to the centroid displacement, assuming a cylindrical geometry (for instance, beam in a drift tube) for small displacements with respect to the tube radius [77]. The effect of image forces becomes more important when the beam approaches to one of the conductors or when the cylindrical geometry is absent. The image forces affect significantly the beam dynamics because the field generated by these images will in general contain higher-order multipole fields, which act nonlinearly on the beam. For instance, a semi-analytical calculation of the image-charge-induced field for a uniformly-charged elliptical beam within four hyperbolic surfaces (as in an

electrostatic quadrupole) [78] showed a pronounced contribution of the 4th order term of the image field potential function and consequent 3rd order nonlinearity in the components of the image field proper.

II.1.9.4 - Higher-order multipole fields

When designing and manufacturing electrostatic and magnetic quadrupoles, one tries to eliminate all nonlinear fields. Nevertheless, a certain level of higher-order multipoles always remain but are usually small enough to be ignored when the beam particles do not approach too close to the focusing elements. For example, for the quadrupoles used on the HCX, a multipole decomposition of the calculated electrostatic field based on the mechanical design was obtained and showed very good field quality (see Section - VIII.1 -). However, with the beam filling most of the aperture, higher order multipoles will be sampled and will lead to phase-space distortions and some emittance growth.

II.1.9.5 - Realistic transverse beam distributions

Space-charge forces discussed in Section - II.1.3 - are linear because the current-density distribution is taken to be uniform within an ellipse. Also, it remains uniform as the beam propagates only for the highly idealized K-V distribution. In reality, beam distributions are neither of the K-V type nor exactly uniform. Space charge wave oscillations due small-amplitude perturbations were treated in Section - II.1.8 - by linearizing the initial problem. But more generally, nonlinear space charge forces will appear and an analytic treatment is no longer possible. Space-charge nonlinearities will affect the beam dynamics and detailed

particle-in-cell simulations are required to analyze their effect. In particular, some of the non-linear charge potential energy may thermalize and contribute to emittance growth.

II.1.9.6 - Presence of background gas and electrons

The beam will interact with the residual gas present in the system. Scattering, background ionization and beam stripping may occur. These effects account for indirect beam loss during transport to the target. Additionally, if beam ions or secondary ions are lost to the walls of the channel, a cascade of secondary electrons, neutrals and gas molecules will be produced and likely cross the beam path, generating more losses as secondary particles build up. Although this mechanism can potentially lead to loss of beam control, its time evolution is determined by the drift velocities for neutrals and gas molecules which are relatively slow and make this process an issue for long pulses (> 5 µs) only. Moreover, the secondary electrons may not be as problematic in an electrostatic quadrupole, where they will be swept out of the beam path due to the large electric fields that exist, as in a magnetic quadrupole, where they can be trapped in the beam potential [79].

## II.1.10 - *Beam halo*

Halos are loosely defined as a cluster of particles surrounding a dense core in any of the particle distribution projections. They contribute to emittance growth (reducing focusability of the beam) and can increase beam loss significantly (causing accelerator activation and increasing electron/gas

desorption). The halo is thought to be the result of the transformation of excess or free energy to particle thermal energy through the action of nonlinear space-charge fields [80]. In particular, beam mismatch is believed to be a primary mechanism for halo formation although other, more complicated mechanisms may play an important role and simulations reveal chaotic behavior at high space-charge depressions [81]. Gluckstern [82] developed an analytic model for halo formation in which the driving term, the envelope breathing mode oscillation, leads to growth of ion amplitudes in the core through the parametric resonance. It is however only an approximation of a much more complicated situation.

Halos are most likely to be produced at transition locations, such as discontinuities in frequency, structure geometry, transverse focusing pattern accelerating gradient and phase [82].

## II.2 - Longitudinal charged particle beam dynamics

There are several ways to look at the longitudinal beam dynamics according to the type of the system and the goal of the theoretical description: formation of the ion beam in the diode region of the injector system (steady state described by the Child-Langmuir law, i.e. space-charge limited flow in between the ion source and the extraction electrode, the transient beam head formation is more complex), the description of accelerating gaps and their consequences on the beam longitudinal, the effect of space-charge on the beam bunch or longitudinal-transverse energy transfers.

### II.2.1 - *Longitudinal envelope equation for linear rf fields systems*

As for the transverse directions, it is possible to describe the evolution of the beam envelope along its direction of propagation, with the rf accelerating fields being homologous to the focusing fields of Section - II.1 -. Without going into the details of a fairly lengthy derivation, it can be shown that the displacement $z_m$ of the particles from the bunch center with parabolic line-charge density profile (i.e. 'linear beam' model) follows [83]:

$$z_m'' + \kappa_{z0} z_m - \frac{K_L}{z_m^2} - \frac{\varepsilon_{zz'}^2}{z_m^3} = 0 \qquad \text{(Eq. II-57)}$$

where $K_L$ is the longitudinal perveance (with unit of length in contrast with the dimensionless perveance of the transverse case) defined as

$$K_L = \frac{3}{2} \frac{gNr_c}{\beta_0^2 \gamma_0^5} \qquad \text{(Eq. II-58)}$$

$\kappa_{z0}$ is the longitudinal focusing function (induced by the accelerating field) and $\varepsilon_{zz'}$ represents the unnormalized total longitudinal emittance of the bunch in the moving frame. $z_m$ and usually $\kappa_{z0}$ are functions of the distance $s$ as in the transverse case. In (Eq. II-58), $N$ is the total number of particles, $g$ is the geometry factor (often simply called the 'g-factor') that appears in the derivation of the longitudinal self-field of beam bunches) and $r_c$ is the classical particle radius.

As for the transverse envelope equation, very few self-consistent distribution functions actually meet the assumptions made in the calculation

leading to (Eq. II-57) and probably no real distribution seen on the various beam lines around the world either. Then, the use of this envelope equation resides in its RMS formulation:

$$\tilde{z}'' + \kappa_{z0}\tilde{z} - \frac{K_L}{5\sqrt{5}\tilde{z}^2} - \frac{\tilde{\varepsilon}_{zz'}^2}{\tilde{z}^3} = 0 \qquad \text{(Eq. II-59)}$$

which is appropriate for comparison between different distributions.

It should be noted that this envelope equation does not apply to single bunch linear accelerators where the acceleration is provided by induction cores. In these systems, the parabolic bunch model would not apply nor would the linear approximation of the accelerating field. However, in the drift compression region of a fusion driver, the beam longitudinal profile would become parabolic. The above formulation, with some adjustments, would then be adequate. The longitudinal dynamics of induction linacs are better described by the fluid equations (Section - II.2.3 -) and the evolution of space-charge waves or rarefaction waves (at the beam head and tail).

## II.2.2 -    The 'g-factor' model

The 'g-factor' approach [84] deals with deriving the beam longitudinal self electric field induced by line charge density perturbations.

We start with the model of a drifting beam taken as an infinite cylinder with constant radius, $a$, and constant charge density, $\rho_0$, traveling within a grounded pipe of radius $r_{ap}$ In this case, the line charge density of the beam as a function

of the transverse distance, $r$, with respect to the center line of the beam is given

by:

$$\lambda(r) = \lambda_0 \left(\frac{r}{a}\right)^2, \qquad r \leq a, \qquad \text{(Eq. II-60)}$$

$$\lambda(r) = \lambda_0, \qquad r > a. \qquad \text{(Eq. II-61)}$$

where $\lambda_0$ is the total line charge density, and the radial electric field is given by

(Gauss's law)

$$E_r = -\frac{\partial \varphi}{\partial r} = \frac{\lambda(r)}{2\pi\varepsilon_0 r} \qquad \text{(Eq. II-62)}$$

Integrating (Eq. II-62) from the grounded pipe to some distance $r$ from the center

line, and substituting $\lambda(r)$ with (Eq. II-60) and (Eq. II-61), gives the beam radial

potential $\varphi(r)$ :

$$\varphi(r) = \begin{cases} \dfrac{\lambda_0}{2\pi\varepsilon_0}\left[\dfrac{1}{2}\left(1-\dfrac{r^2}{a^2}\right)+\ln\left(\dfrac{r_{ap}}{a}\right)\right], & 0 \leq r \leq a, \\[4mm] \dfrac{\lambda_0}{2\pi\varepsilon_0}\ln\left(\dfrac{r_{ap}}{r}\right), & a \leq r \leq r_{ap}. \end{cases} \qquad \text{(Eq. II-63)}$$

We then look at the effect of small variations of the line charge density and

beam radius as a function of the direction of propagation of the beam, $z$ .

Differentiating the beam potential with respect to $\lambda_0$ and $a$ , gives:

$$\frac{\partial \varphi}{\partial z} = \frac{1}{2\pi\varepsilon_0}\left\{\left[\frac{1}{2}\left(1-\frac{r^2}{a^2}\right)+\ln\left(\frac{r_{ap}}{a}\right)\right]\frac{\partial \lambda_0}{\partial z} - \left[\left(1-\frac{r^2}{a^2}\right)\frac{\lambda_0}{a}\right]\frac{\partial a}{\partial z}\right\} \qquad \text{(Eq. II-64)}$$

Noting that for constant charge density we can write

$$\frac{\lambda_0}{a^2} = const \qquad\qquad \text{(Eq. II-65)}$$

which in turn gives a direct relationship in between the line charge density and the beam radius perturbations,

$$\frac{\partial \lambda_0}{\partial z} = -\frac{2\lambda_0}{a}\frac{\partial a}{\partial z} \qquad\qquad \text{(Eq. II-66)}$$

and we finally obtain for the longitudinal self electric field of the beam:

$$E_z = -g\frac{\partial \lambda_0}{\partial z} \qquad\qquad \text{(Eq. II-67)}$$

where

$$g = \frac{1}{4\pi\varepsilon_0} 2\ln\left(\frac{r_{ap}}{a}\right) \qquad\qquad \text{(Eq. II-68)}$$

The coupling of the beam radius perturbation with the line charge density perturbation can be interpreted as the propagation of a wave at the 'surface' of the beam distribution and is consistent with the space-charge dominated regime.

Another typical assumption, relevant for emittance-dominated regime, is to consider line charge density perturbation only (since space-charge forces are negligible for determining the radius of the beam, line charge density perturbations will not affect the beam radius). This would then be equivalent to waves propagating through the 'body' (or core) of the beam instead of on its surface. With $a = const$, (Eq. II-64) becomes:

$$\frac{\partial \varphi}{\partial z} = \frac{1}{4\pi\varepsilon_0}\left[\left(1-\frac{r^2}{a^2}\right)+2\ln\left(\frac{r_{ap}}{a}\right)\right]\frac{\partial \lambda_0}{\partial z} \qquad\qquad \text{(Eq. II-69)}$$

To make use of these assumptions in the wave calculations, the average electric self field is averaged over the beam radius. Calculation of the integral then gives:

$$\overline{E_z} = -\overline{g}\frac{\partial \lambda_0}{\partial z}$$

(Eq. II-70)

with

$$\overline{g} = \frac{1}{4\pi\varepsilon_0}\left[\frac{1}{2} + 2\ln\left(\frac{r_{ap}}{a}\right)\right]$$

(Eq. II-71)

The description of the self electric field of the beam through the 'g-factor' model is the first step towards the discussion of longitudinal wave propagation of Section - II.2.4 -. The values derived here are only approximations of real, more complex systems. In practice, the 'g-factor' is often used as an independent fitting parameter.

### II.2.3 -    1-D Fluid equations

To obtain the 1-D fluid equations, we start from the Vlasov equilibrium description of the ion beam [84]:

$$\frac{df}{ds} = 0$$

(Eq. II-72)

where $f$ is a single-particle distribution function in space, momentum and time variables, and $s$ is the axial coordinate of the beam particle, defined as $v_B\, dt = ds$, with $v_B$ being the beam-average longitudinal velocity. If we integrate (Eq. II-72) over the transverse space and momentum variables, a more detailed 1-D representation of the Vlasov equation emerges:

52

$$\frac{\partial \tilde{f}}{\partial s} + z' \frac{\partial \tilde{f}}{\partial z} + z'' \frac{\partial \tilde{f}}{\partial z'} = 0 \qquad \text{(Eq. II-73)}$$

where we defined $\tilde{f}$ to be:

$$\tilde{f}(z, z', s) = \iiint f \, dx \, dx' \, dy \, dy' \qquad \text{(Eq. II-74)}$$

With the following notation,

$$\lambda \equiv \int \tilde{f} \, dz' \qquad \text{(Eq. II-75)}$$

$$\lambda \overline{z'} \equiv \int \tilde{f} \, z' \, dz' \qquad \text{(Eq. II-76)}$$

$$\lambda \overline{z'^2} \equiv \int \tilde{f} \, z'^2 \, dz' \qquad \text{(Eq. II-77)}$$

$$\Delta z'^2 \equiv \overline{z'^2} - \left(\overline{z'}\right)^2 \qquad \text{(Eq. II-78)}$$

integration over $z'$ gives the 'continuity equation':

$$\frac{\partial \lambda}{\partial s} + \frac{\partial}{\partial z}\left(\lambda \overline{z'}\right) = 0 \qquad \text{(Eq. II-79)}$$

Multiplying the 1-D Vlasov equation by $z'$, integrating the result over $z'$ again, then dividing by $\lambda$ and using the continuity equation and the definition of $\Delta z'^2$ eventually leads to the 'momentum equation':

$$\frac{\partial \overline{z'}}{\partial s} + \overline{z'} \frac{\partial \overline{z'}}{\partial z} + \frac{1}{\lambda} \frac{\partial}{\partial z}\left(\lambda \Delta z'^2\right) = \overline{z''} \qquad \text{(Eq. II-80)}$$

In (Eq. II-80), the first two terms on the left-hand side are the inertial terms, the 3$^{rd}$ term on the left-hand side is the pressure term and the right-hand side represents the forces.

## II.2.4 - *Space-charge waves in the context of the 1-D incompressible cold fluid model*

Space-charge waves are a concern in the drift compression region of the accelerator, where the beam head is decelerated and its tail is accelerated in order to reduce the length of the beam pulse. As the beam is compressed, space-charge waves could result in the undesirable effect of degrading the focusability of the beam on the target. Also, any acceleration voltage perturbations (or ripples) along the accelerator will introduce such waves. In the context of the HCX experiment, these waves are used as a time stamp for time-of-flight (TOF) measurements of the beam energy (see Sections - III.2 - and - XI.3 -).

### II.2.4.1 - General problem of space-charge wave propagation

Simply put, space-charge waves are the result of localized fluctuations in the line charge density of the beam, which in turn modifies the self field configuration of the bunch. Below is one analytical treatment of the propagation of such waves relevant to TOF measurement techniques.

The space-charge wave model comes from combining the 'g-factor' model with the 1-D fluid equations. The continuity and momentum equations derived in Section - II.2.3 -can be rewritten as [85]:

$$\frac{\partial \lambda}{\partial t} + \frac{\partial (\lambda v)}{\partial z} = 0 \qquad \text{(Eq. II-81)}$$

$$\frac{\partial v}{\partial t} + v \frac{\partial v}{\partial z} = \frac{q}{m} E_z \qquad \text{(Eq. II-82)}$$

where $q$ is the ion charge, $m$ the ion mass , $v$ the ion velocity and $E_z$ is the longitudinal self electric field produced by fluctuations in the line charge density $\lambda$, as described in Section - II.2.2 - by (Eq. II-67) and (Eq. II-68) or (Eq. II-70) and (Eq. II-71). The pressure term of (Eq. II-80) has been neglected since we assume space-charge dominated beams. The subscript '0' has been dropped for simplicity (and to avoid confusion later on). In addition, the time variable is employed instead of the axial coordinate, $s$.

After linearization and transformation into the co-moving frame, we can combine (Eq. II-81) and (Eq. II-82) into

$$\frac{\partial^2 \lambda_1}{\partial t'^2} - \frac{q}{m} g \lambda_0 \frac{\partial^2 \lambda_1}{\partial z'^2} = 0 \qquad \text{(Eq. II-83)}$$

where the 'primes' refer to the co-moving frame coordinates, the 0 subscripts refer to equilibrium quantities and the 1 subscripts refer to perturbed quantities. By defining a space charge wave speed

$$c_s \equiv \sqrt{\frac{q g \lambda_0}{m}} \qquad \text{(Eq. II-84)}$$

we identify (Eq. II-83) as the wave equation, with general solution (in the lab frame)

$$\lambda_1 = \lambda_0 \left[ f_R(z - (v_0 + c_s)t) + f_L(z - (v_0 - c_s)t) \right] \qquad \text{(Eq. II-85)}$$

$$v_1 = c_s \left[ f_R(z - (v_0 + c_s)t) - f_L(z - (v_0 - c_s)t) \right] \qquad \text{(Eq. II-86)}$$

55

where $f_R(x)$ and $f_L(x)$ are arbitrary functions of the argument $x$ representing right and left traveling waves in the beam frame, and $v_0$ is the unperturbed beam velocity.

For the particular problem of a voltage variation across an induction gap, we need to set boundary conditions. In this case, because of charge conservation, the instantaneous current must be the same on both side of the gap, so that $\dfrac{I_1}{I_0} = 0$. However, there is a velocity perturbation satisfying $\dfrac{v_1}{v_0} = \dfrac{1}{2}\dfrac{V_1}{V_0}$ and therefore $\dfrac{\lambda_1}{\lambda_0} = -\dfrac{1}{2}\dfrac{V_1}{V_0}$. If we let $\dfrac{V_1(z=0,t)}{V_0} \equiv h(t)$, then the boundary conditions become:

$$v_1 = \frac{v_0}{2} h(t) \qquad\qquad \text{(Eq. II-87)}$$

$$\lambda_1 = -\frac{\lambda_0}{2} h(t) \qquad\qquad \text{(Eq. II-88)}$$

So the solution for all $z$ and $t$ can be written as:

$$\frac{\lambda_1}{\lambda_0} = \frac{1}{4}\left(\frac{v_0}{c_S}-1\right)h\left(t-\frac{z}{v_0+c_S}\right) - \frac{1}{4}\left(\frac{v_0}{c_S}+1\right)h\left(t-\frac{z}{v_0-c_S}\right) \qquad \text{(Eq. II-89)}$$

$$\frac{v_1}{c_S} = \frac{1}{4}\left(\frac{v_0}{c_S}-1\right)h\left(t-\frac{z}{v_0+c_S}\right) + \frac{1}{4}\left(\frac{v_0}{c_S}+1\right)h\left(t-\frac{z}{v_0-c_S}\right) \qquad \text{(Eq. II-90)}$$

$$\frac{I_1}{I_0} = \frac{1}{4}\frac{v_0}{c_S}\left[1-\left(\frac{c_S}{v_0}\right)^2\right]h\left(t-\frac{z}{v_0+c_S}\right) - \frac{1}{4}\frac{v_0}{c_S}\left[1-\left(\frac{c_S}{v_0}\right)^2\right]h\left(t-\frac{t}{v_0-c_S}\right) \qquad \text{(Eq. II-91)}$$

II.2.4.2 - Specific considerations for time-of-flight measurements on HCX

The goal here is to purposely induce space-charge waves and use them as a time reference further downstream when evaluating the time-of-flight of the beam traveling from the point at which the perturbation was produced and the point where the beam current is measured [94]. For an applied step function within a drift tube, particles are accelerated by the voltage $\Delta V$, resulting in velocity perturbations $\dfrac{\Delta v}{v} = \dfrac{1}{2}\dfrac{\Delta V}{V_0}$.

Modifying slightly the formalism used in the previous section, we can write:

$$\frac{v^+}{v_0} = \frac{v^-}{v_0} = \frac{1}{4}\frac{\Delta V}{V_0} \qquad \text{(Eq. II-92)}$$

where $v^+$ is the velocity of the right traveling wave (called the 'fast' wave) and $v^-$ the velocity of the left traveling wave (the 'slow' wave). Then, (Eq. II-89) and (Eq. II-91) can respectively be broken up into a fast wave and a slow wave notation, which gives

$$\lambda^+ = \frac{1}{4}\frac{\Delta V}{V_0}\left(\frac{v_0}{c_S}-1\right)\lambda_0 \qquad \text{(Eq. II-93)}$$

$$\lambda^- = -\frac{1}{4}\frac{\Delta V}{V_0}\left(\frac{v_0}{c_S}+1\right)\lambda_0 \qquad \text{(Eq. II-94)}$$

for the line charge density perturbations and

$$I^+ = -I^- = \frac{1}{4}\frac{v_0}{c_S}\left[1-\left(\frac{c_S}{v_o}\right)^2\right]\frac{\Delta V}{V_0}I_0 \qquad \text{(Eq. II-95)}$$

for the current variations.

If we now consider HCX beam parameters, at 1 MeV, the beam potential is $\Phi$ = 1.50 kV, implying a bunch velocity wave-speed ratio $\dfrac{v_0}{c_S}$ of 36.5. The beam current $I_0$ is 175 mA. Using (Eq. II-95),

$$I^+ = -I^- \cong 1596 \frac{\Delta V}{V_0} \, \text{mA} \qquad\qquad \text{(Eq. II-96)}$$

Thus, a 1 kV perturbation would result in a ±1.6 mA current perturbation wave drifting apart at a velocity $c_S$ = 6.1 cm μs$^{-1}$. If a Faraday cup is collecting the beam current 5 m downstream of the excitation, the separation between the fast and slow waves is 123 ns.

## II.2.4.3 - Beam-end erosion

The longitudinal space-charge fields of a bunched beam inside a conducting pipe cause the ends of the bunch to move outwards and, in the absence of restoring forces, to erode the bunch [86] (i.e. elongation of the bunch). It is interesting to look at the 1-D evolution of pulse with a monoenergetic longitudinal distribution and constant line-charge density that ends with a step function.

Starting with (Eq. II-81) and (Eq. II-82) and making use of (Eq. II-67) and (Eq. II-68), the solution for the initially square profile in energy and line charge density is:

$$\frac{\lambda}{\lambda_0} = \begin{cases} 1, & z < -c_S t \\ \left(\frac{2}{3} - \frac{z}{3c_S t}\right)^2, & -c_S t < z < 2c_S t, \\ 0, & z > 2c_S t \end{cases} \qquad \text{(Eq. II-97)}$$

$$\frac{v}{c_S} = \begin{cases} 0, & z < -c_S t \\ \frac{2}{3}\left(1 + \frac{z}{c_S t}\right), & -c_S t < z < 2c_S t, \end{cases} \qquad \text{(Eq. II-98)}$$

where $c_S$ is given by (Eq. II-84), and $z$ and $v$ are measured backward in the beam frame. From the limits in (Eq. II-97) and (Eq. II-98), one can see that the beam end expands at twice the space-charge wave speed and the rarefaction wave propagates inward at the space-charge wave speed. For typical HCX parameters at 1 MeV, the space-charge wave velocity is 6.1 cm $\mu s^{-1}$ resulting in an expected ≈200 ns increase in the rise and fall times of the beam pulse after 5.5 m (matching section plus transport section). Because the beam pulse is never perfectly square, the above calculation should be viewed as an upper limit to the beam-end erosion.

59

# Chapter III - Beam diagnostics description

## III.1 - Beam current

The beam current is the most routinely measured quantity on all beam lines. It gives the very first assessment of the functionality of the beam line. Faraday cups and current monitors (or Rogowski coils) are the standard diagnostics.

### III.1.1 - Faraday cup

The Faraday cup [87] is a cylindrical, shielded container that measures the beam electrical charges. When the beam enters the Faraday cup, the charge induced on the inner electrode, the collector, is determined by an electrometer [88]. Except for dynamic Faraday cups, this is a destructive measurement since the collector is closed at one end. The electrical signal results from the particles' field entering or leaving the region within the electrode, not when they hit a surface. Because the interpretation of the signal is straightforward in the configuration where particles are collected, the closed (i.e. cup) configuration is preferred and most widely used. However, the design must insure that secondary electrons and the dense partially ionized gas cloud that result from the ions hitting the electrode surfaces do not escape the collecting region, which would alter the measurement accuracy.

All Faraday cups on the HCX have two electrodes (a suppressor ring upstream of the collector) encased in a common grounded case (also cylindrical in shape) and electrically insulated from it (Figure III-1).
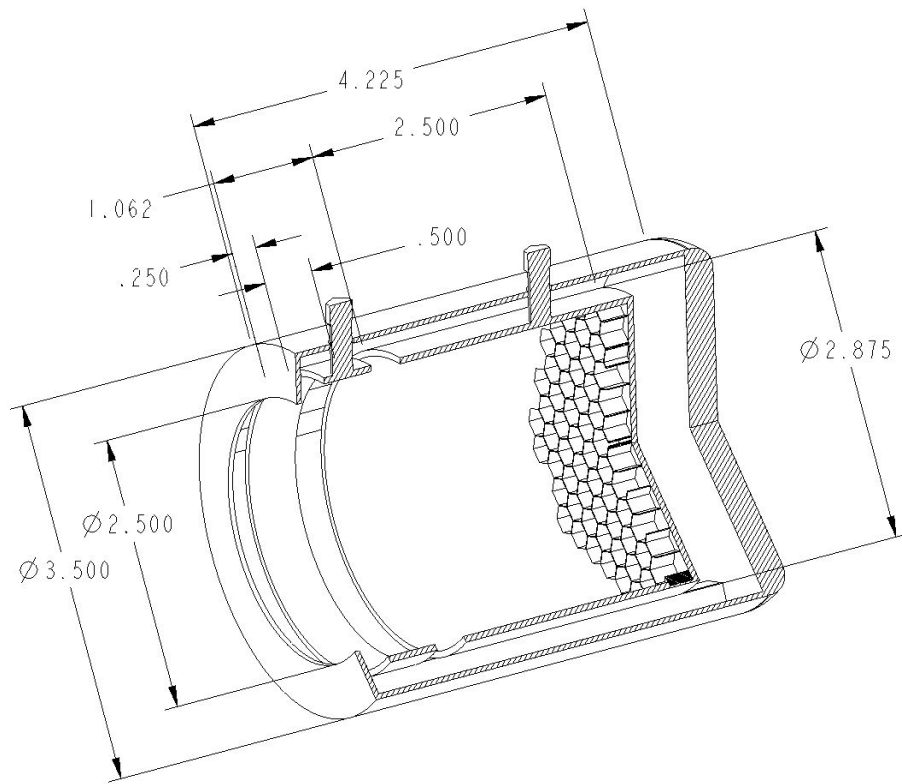
**Figure III-1**: Typical Faraday cup mechanical drawing at QD1. Dimensions are in inches.

The collector is shaped to receive the incoming ion beam. The ratio of its depth to its aperture radius is equal to or greater than two ('deep' Faraday cup) unless it would not fit at the location of the measurement in the beam line. The deep Faraday cup design has the double purpose of helping keep the gas cloud generated at the bottom inside the cup region and establishing an effective bias on the axis.

The excess charge on the collector has a path to ground through a coupling circuit that allows the application of a bias voltage as well as monitoring

the collected charge. The cup is biased positive and the suppressor ring negative to prevent secondary electrons from leaving the collector. The suppressor voltage also helps to reject incoming low energy electrons that may travel with the ion beam. Additionally, a metallic honeycomb structure (Figure III-2) is placed at the bottom of the cup such that the bias and beam fields are reduced at the point of impact, thereby preventing electrons- and beam-generated gaseous ions from being accelerated and expelled [89].
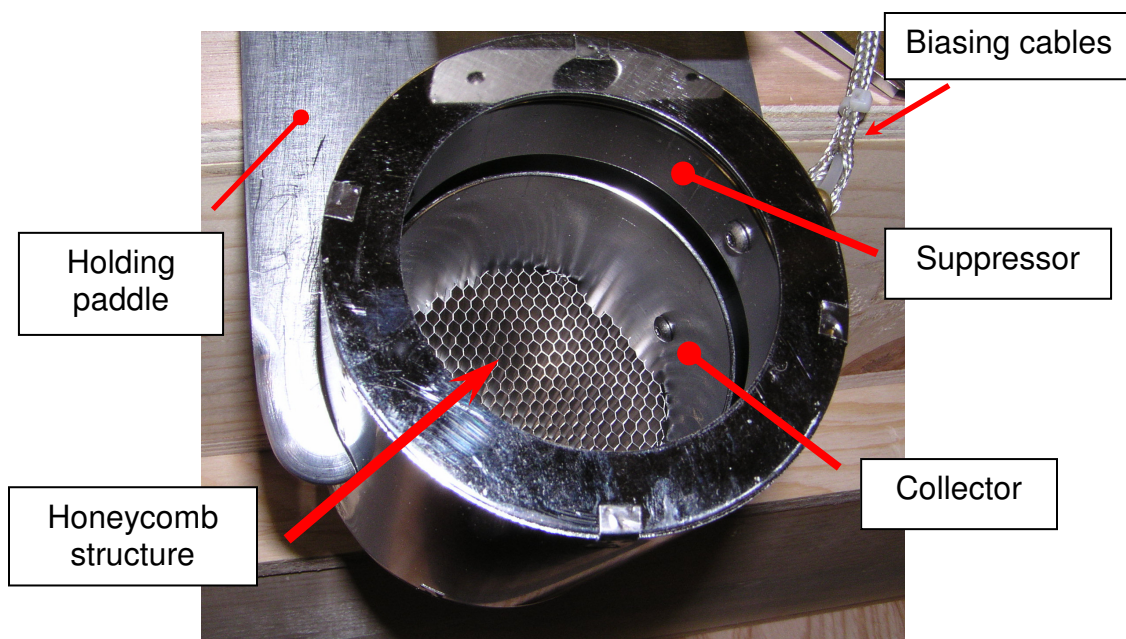


**Figure III-2**: Photograph a small Faraday cup showing the honeycomb structure at the bottom.

The voltage applied to the collector and the suppressor is typically a few hundred volts when the Faraday cup is preceded by a negatively-biased focusing quadrupole. A few kilovolts may be required in a field-free region. After

installation on the beam line, current versus biasing calibration curves are measured to ensure effective suppression of secondary particle effects (Figure III-3).
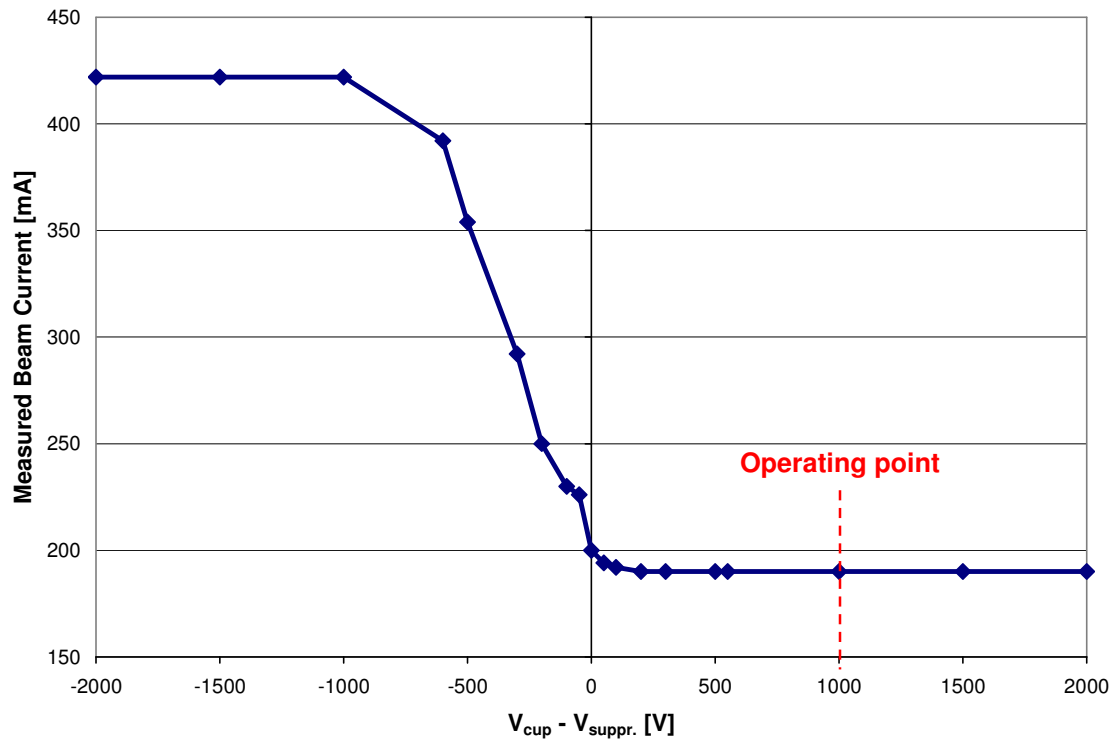


**Figure III-3**: I-V calibration curve for a standard Faraday cup used on the HCX beam line.

### III.1.2 -    *Beam current monitor (a.k.a. Rogowski coil or current transformer)*

Current monitors are relatively simple devices that consist of winding a coil around a core (magnetic core or not) as illustrated in Figure III-4 [90]. They measure the beam magnetic field (and therefore the beam current). They are non-destructive but usually have a lower detection threshold than Faraday cups.

Some relevant dimensions for a design are $a$ the minor mean radius of the coil (to the center of the winding), $r$ the major mean radius of the coil, $N$ the number of turns on the coil and $\mu$ the magnetic permeability of the core. Others (like the windings pitch and wire diameter) may be needed if one wants to evaluate the self inductance of the coil. Detailed discussions of Rogowski coil theory and designs can be found in Refs. [90,91].
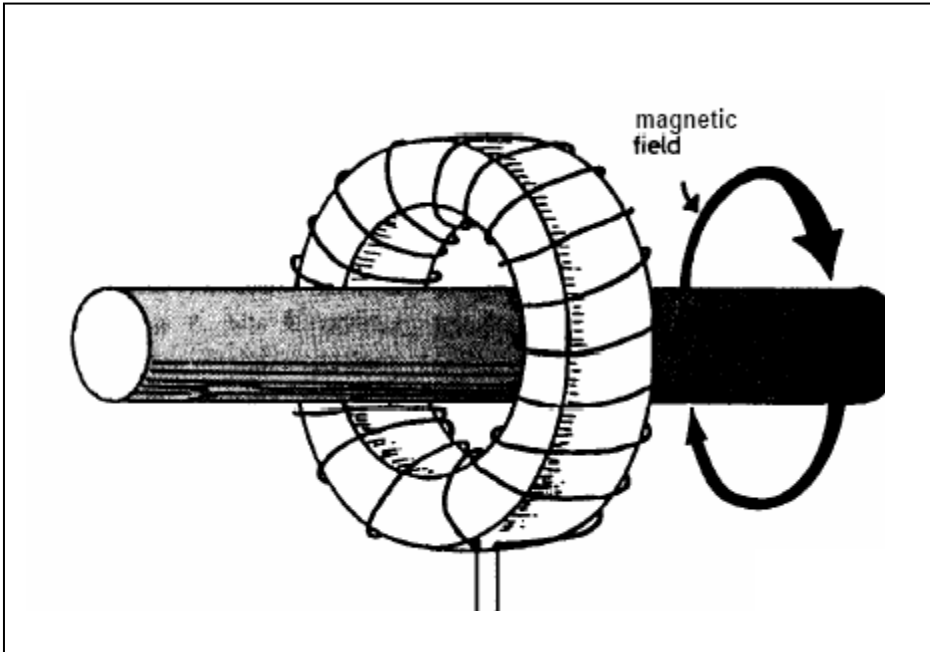


**Figure III-4**: Simplified current transformer sketch [90].

At first approximation, the current transformer's equivalent circuit is simply an inductor $L$ in parallel with a resistor $R$, where

$$R = R_{CVR} + Z_S$$

(Eq. III-1)

with $R_{CVR}$ being a current-viewing resistor impedance and $Z_S$ the skin-effect resistance. When a time-varying current, in our case the beam current $I_{Beam}$, threads the coil, its flux

$$\phi \cong \frac{\mu I_{Beam} N a^2}{2r}$$ (Eq. III-2)

induces a voltage in it, represented by the circuit equation

$$\frac{1}{L}\frac{d\phi}{dt} = \frac{dI_c}{dt} + \frac{R}{L}I_c$$ (Eq. III-3)

where $I_c$ is the coil current. If the coil is configured such that $L/R$ is greater than the pulse width, the coil is 'self-integrating' and the coil current is proportional to $\phi$ and therefore $I_{Beam}$.

We have two current monitors on our beam line. One is a commercial Pearson monitor [92]; the other is a large custom-made current transformer. Both are calibrated by passing a known square current pulse through them and measuring the voltage output. This gives both the gain (or sensitivity) of the coil and the $L/R$ decay constant. For the commercial monitor, the decay of the output pulse is such that the error due to the voltage droop is less than 0.5% over a 4 μs pulse. For the large current transformer, the decay constant was measured to be 80 μs, which leads to a 5% voltage drop over a 4 μs pulse, which needs to be corrected for when analyzing the beam current waveform in detail. In order to apply the correction, one needs to integrate (Eq. III-3). We then obtain the prescription that

$$I_{Beam} = \kappa \left( v_0 + \frac{R}{L} \int v_0 \, dt \right) \hspace{2cm} \text{(Eq. III-4)}$$

where

$$v_0 = R \, I_c \hspace{2cm} \text{(Eq. III-5)}$$

is the measured output voltage pulse and $\kappa$ is a calibration constant determined by the details of the circuit (i.e. the gain of the coil). The second term in (Eq. III-4) is numerically applied when reading in saved current waveforms.

Because back streaming electrons may lead to erroneous beam current readings it is sometimes necessary to install an electron suppressor in the vicinity of the current monitor. This is particularly important when the beam loss occurs in an otherwise field-free region.

## III.2 - Beam energy

In order to measure the absolute beam energy and its time distribution (longitudinal profile), we have chosen two approaches: a 90° Electrostatic Energy Analyzer (EA) (Section - III.2.1 -) and a time-of-flight (TOF) technique (Section - III.2.2 -).

### III.2.1 - The Electrostatic Energy Analyzer (EA)

The Energy Analyzer [93] used on the HCX beam line to perform the beam energy measurements was originally designed and built for use on the Single Beam Transport Experiment (SBTE) [35] and the Multiple Beam Experiment-4 (MBE-4) [34], with a maximum diagnosed beam energy of 0.9 MeV. Its functionality above this limit had not been demonstrated. The EA is

a cylindrical sector field analyzer for with a linear relationship between the applied potential difference on the electrodes and the energy of the beam. The geometry of the EA is illustrated in Figure III-5, which shows a preliminary CAD drawing of a new, higher-resolution but very similar analyzer currently being designed.
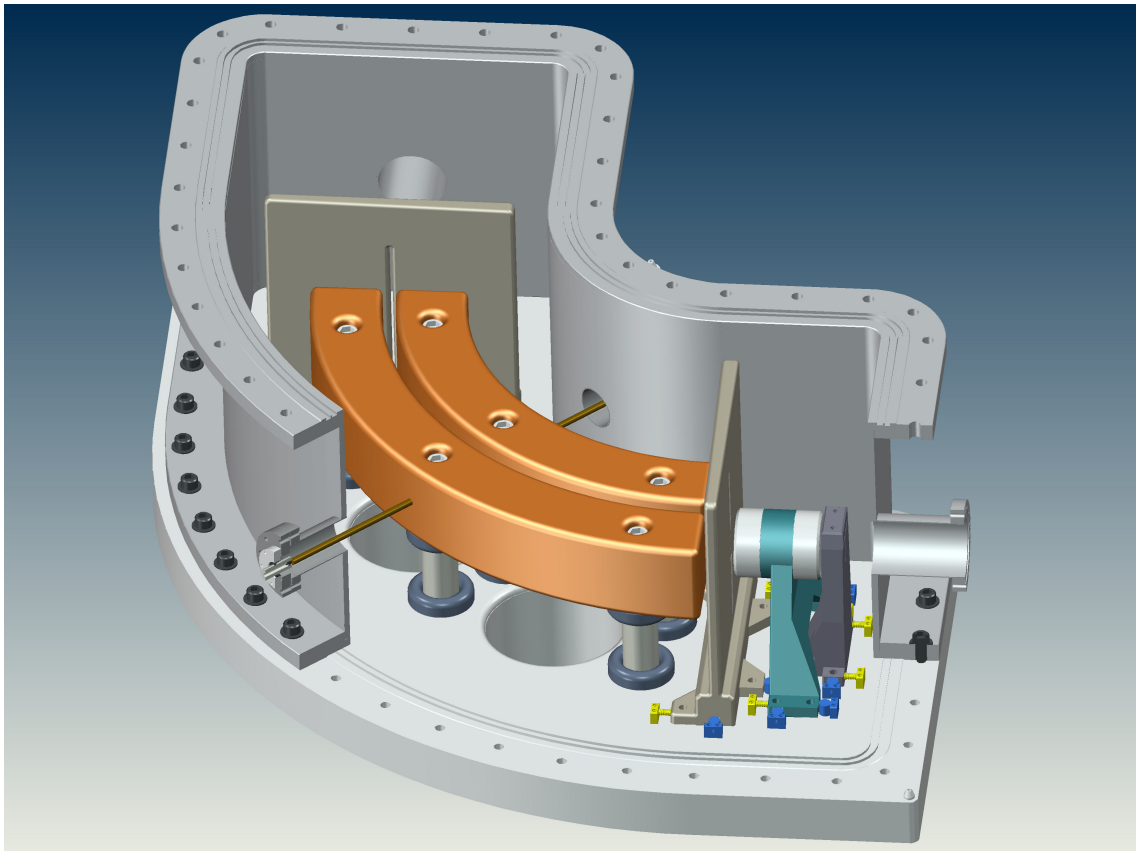


**Figure III-5**: Preliminary CAD drawing of a new energy analyzer under design.

For the 1 MeV HCX beam, initial tests led to high voltage breakdowns at the electrodes and excessive X-ray radiation, both of which could have prevented further use of the EA. However, minor modifications at the analyzer high-voltage

feedthroughs and a few days of conditioning of the electrodes were sufficient to eliminate both issues and applied voltages higher than the ones needed to measure the HCX beam energy were achieved routinely (i.e. ±55 kV or higher).

Another characteristic of any electrostatic energy analyzers is that the calibration of the analyzer relies heavily on its geometry and on the absolute calibration of the power supplies that provide the high voltage to the electrodes. In order to avoid such issues an independent calibration technique was developed, reducing the errors associated with the beam energy measurements. The beam was passed through a 28%-transparent hole-plate, and the gas cloud created at the hole-plate stripped singly charged $K^+$ beam ions into doubly charged $K^{2+}$ beam ions. The absolute calibration was then determined by varying the electric potential at the plate by a known amount, thus the energy of the $K^{2+}$ ions entering the EA (see Section - XI.2.3.1 -). Once calibrated, beam energy measurements simply require varying the potential difference of the EA electrodes and acquiring the resulting current distribution at the exit of the analyzer.

A more detailed discussion of the energy analyzer optics, its calibration and its functionality can be found in Section - XI.2 - which describes the entire beam energy measurements campaign.

### III.2.2 - *Time-of-flight (TOF) techniques*

Time-of-flight measurement techniques are widely used for mass spectrometry. Particles (often isotopes) of the same energy but different masses are separated by their different velocities. In our application, the philosophy is

somewhat different. We want to measure the absolute beam energy based on the time required for the particles to traverse the transport channel.

III.2.2.1 - Basics

The kinetic energy of a non-relativistic particle of mass $m$, moving with the velocity $v$, is

$$E = \frac{1}{2} m v^2$$
(Eq. III-6)

and since for constant $v$, the 'time-of-flight' is

$$\Delta t = \frac{d}{v}$$
(Eq. III-7)

with $d$ being the distance between two known locations. The energy of the particle follows from

$$E = \frac{1}{2} m \left( \frac{d}{\Delta t} \right)^2$$
(Eq. III-8)

III.2.2.2 - Improved TOF measurements using a fast High Voltage pulser

*III.2.2.2.1 -  Approximate measurements*

Initial time-of-flight measurements were performed by measuring the time delay of the leading edge of the beam current waveform at two different diagnostics location along the transport channel. The HCX beam line is relatively short for this kind of measurement. With a maximum distance of 5 m between two beam current monitors, at 1MeV, the expected time delay in between the two waveforms is 2.4 µs. In order to determine the beam energy to the 1 % accuracy,

this time needs to be measured to within 24 ns. At this level of precision, it is difficult to accurately define the start time of the beam pulse (by itself a few hundreds of nanoseconds long). Beam erosion (discussed in Section - II.2.4.3 -) alters the pulse waveforms as the beam propagates, making the determination of the start time more uncertain.

### III.2.2.2.2 -    Principle of the method using space-charge waves as time stamps

Space-charge effects inherent in the HCX can be exploited by perturbing longitudinally an interior portion of the beam with a small voltage pulse and measuring the arrival times downstream of the two space-charge wave current perturbations that result (see Section - II.2.4 - for details of the wave propagation). Comparing the measured and expected delay time of the perturbation determines the absolute energy of the beam [94] with an accuracy close to 2 %.

### III.2.2.2.3 -    Fast high voltage pulser design point and description

Calculations from Section - II.2.4.2 - show that a 1 kV voltage perturbation on the beam (induced as a step function) leads to a 1.6 mA current variation wave.

In this experiment, the first electrostatic quadrupole of the matching section (Section - VII.1 -) was used to introduce this energy offset (instead of a more complicated and dedicated system in the injector high voltage circuitry). Figure III-6 shows a quadrupole and the two 'accelerating gaps', g, across which the perturbation E is applied. The design is such that the electric field $E_z$ that

70

exists at both ends of the quadrupole has minimal effect on the transverse dynamics of the beam.
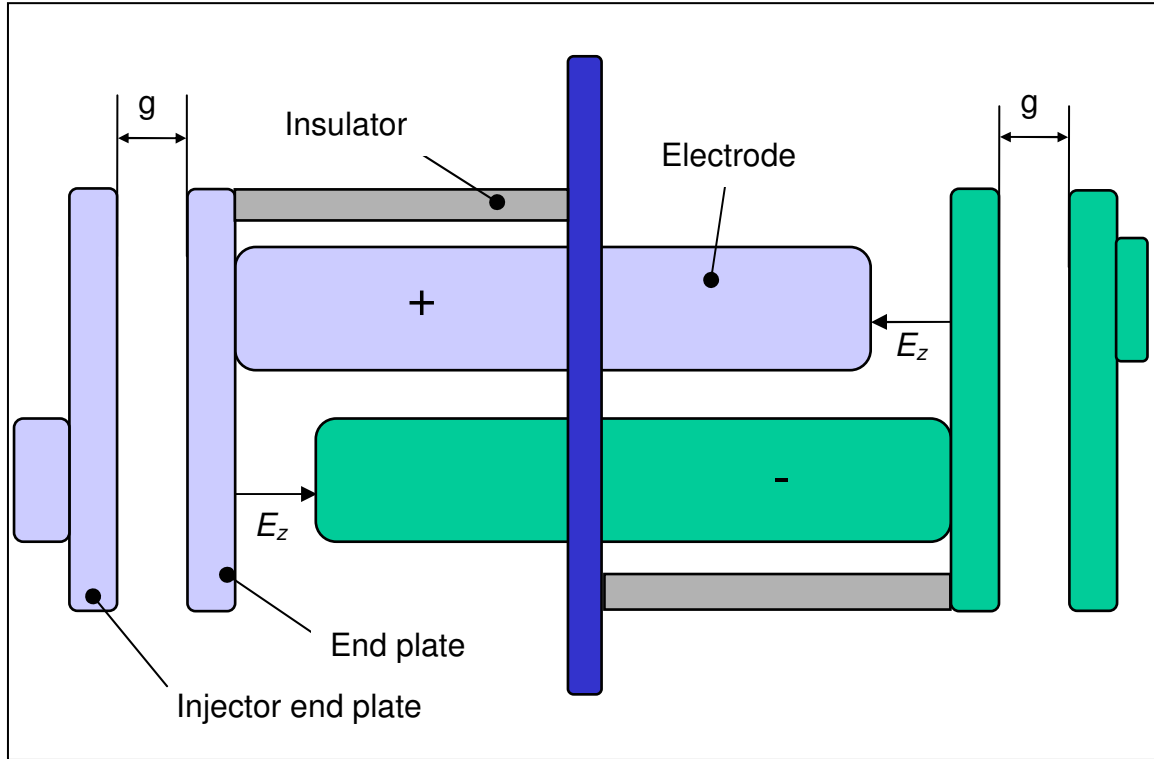


**Figure III-6**: QM1 electrostatic quadrupole design (side view schematic)

For normal operation, the quadrupole electrodes and end plates are energized at a constant DC level of ≈40 kV. Since the quadrupole voltage is always on, the energy of a beam passing through a quadrupole remains constant even though particles are accelerated and decelerated near the end plates. Then, to introduce an energy offset, the high voltage pulse occurs while particles are in the gaps, which leads to the fast rise time requirement of the pulser. At 1 MeV, the velocity of the $K^+$ beam is 222.5 cm.$\mu$s$^{-1}$ and the effective gap is ≈9 cm for the first matching section quadrupole. The transit time $t_r$ of the beam in

one gap is therefore ~40 ns. Along with the maximum voltage output of a few kilovolts, this maximum rise time is the main requirement of the high voltage pulser. The voltage perturbation is applied to all electrodes with the same polarity in order to preserve pure quadrupole focusing forces on the beam. If only one end plate (two electrodes) were pulsed, the transverse focusing forces would become asymmetric ($k_x \neq -k_y$). Also, because the gap appears at both end of the quadrupole, two closely spaced perturbations occur, leading to somewhat more complicated waves on the beam.

A simplified schematic of the circuit is shown on Figure III-7. The TOF pulser is a charged capacitor (C1) which is discharged through a thyratron (switch). There is a resistive load (R2) which defines the RC discharge pulse, which becomes capacitively coupled to the positive and negative electrodes of one of the matching section quads. The rise time of the high voltage pulse is then limited by the switching time of the thyratron. The geometrical configuration of the components are arranged to limit inductance in the circuit that would slow the rise time.
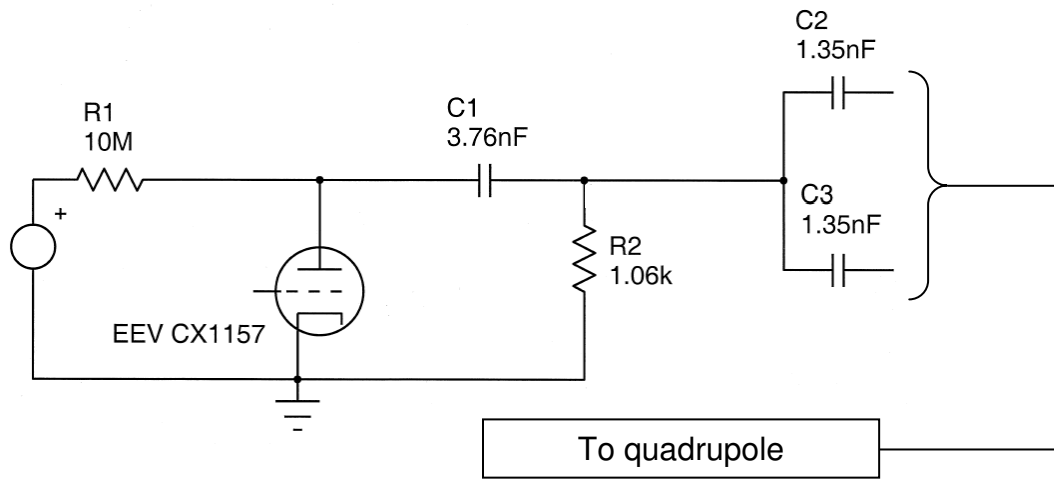
**Figure III-7**: Time-of-flight pulser simplified electric schematic.

For a peak voltage of about 9 kV, a rise time of ~10 ns and a fall time of ~400 ns are achieved. Figure III-8 shows the actual waveform (red) and an empirical fit (blue) used as an input for the space-charge wave model.
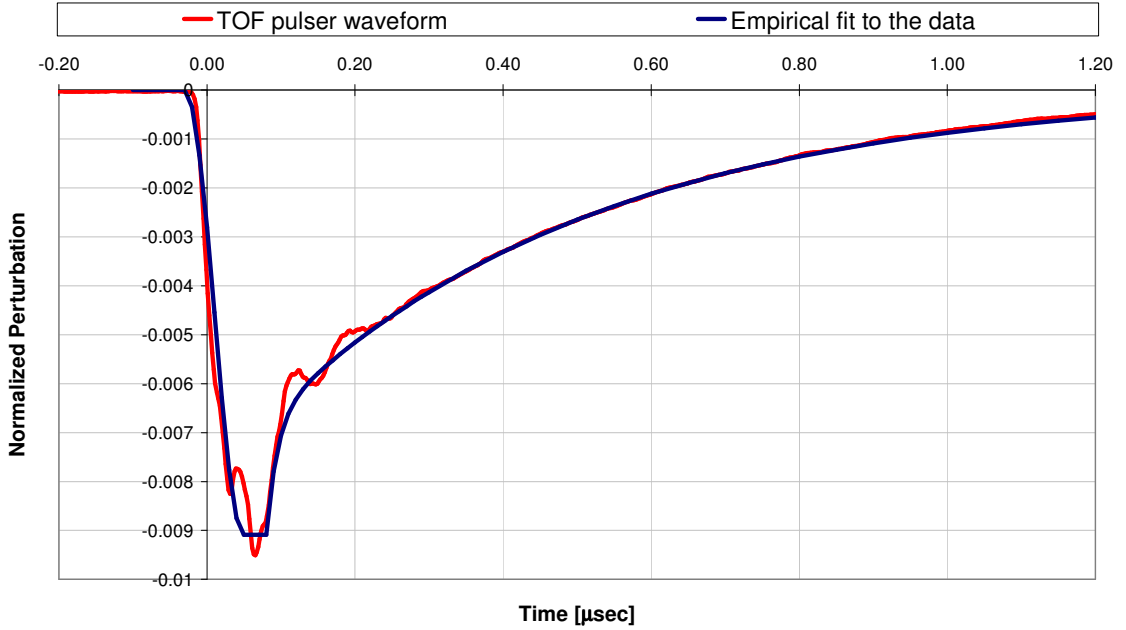
**Figure III-8**: TOF pulser waveform (filtered for high frequency electrical noise) and its empirical fit used as an input in the space-charge wave model. The perturbation amplitude is normalized to the beam energy.

The oscillations that can be seen on the measured TOF pulser waveform are small and fast enough such that they cannot be coupled to the beam significantly.

## III.3 - Beam envelope parameters and transverse distribution

### III.3.1 - Mechanical scanner description

The horizontal and vertical projections of the beam distribution are measured with transverse mechanical slit scanners. These devices consist of pairs of paddles (horizontally and/or vertically driven) holding stainless steel slits and "slit-cups" (i.e. a compact assembly composed of a shallow (~1 cm deep)

Faraday cup or simple collector plate located behind a masking slit). Each paddle is independently driven by a computer-controlled step motor, with a positioning accuracy of ≈10 μm. The step motors reside outside the vacuum system and drive the diagnostic slit (or slit-cup) via a ferrofluidic seal and lead screw assembly. On the slit-cups, an isolated mesh is located between the slit and the collector, as shown schematically in Figure III-9 and on a CAD drawing in Figure III-10.
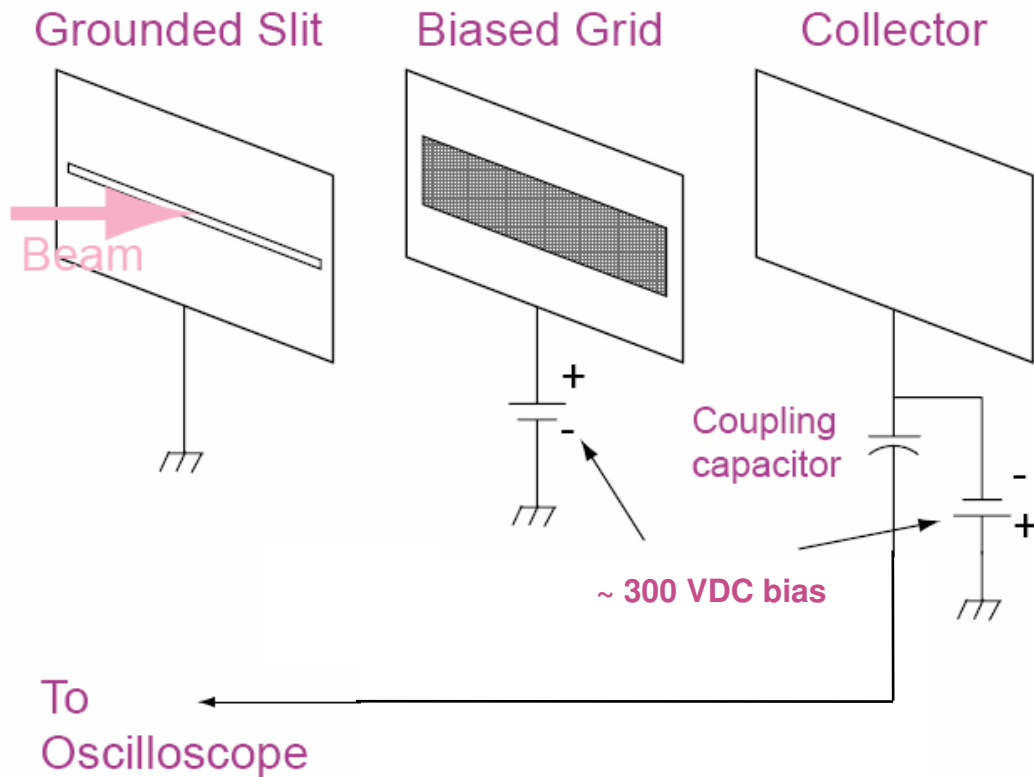


**Figure III-9**: Simplified schematic of the slit-cup circuitry [96].
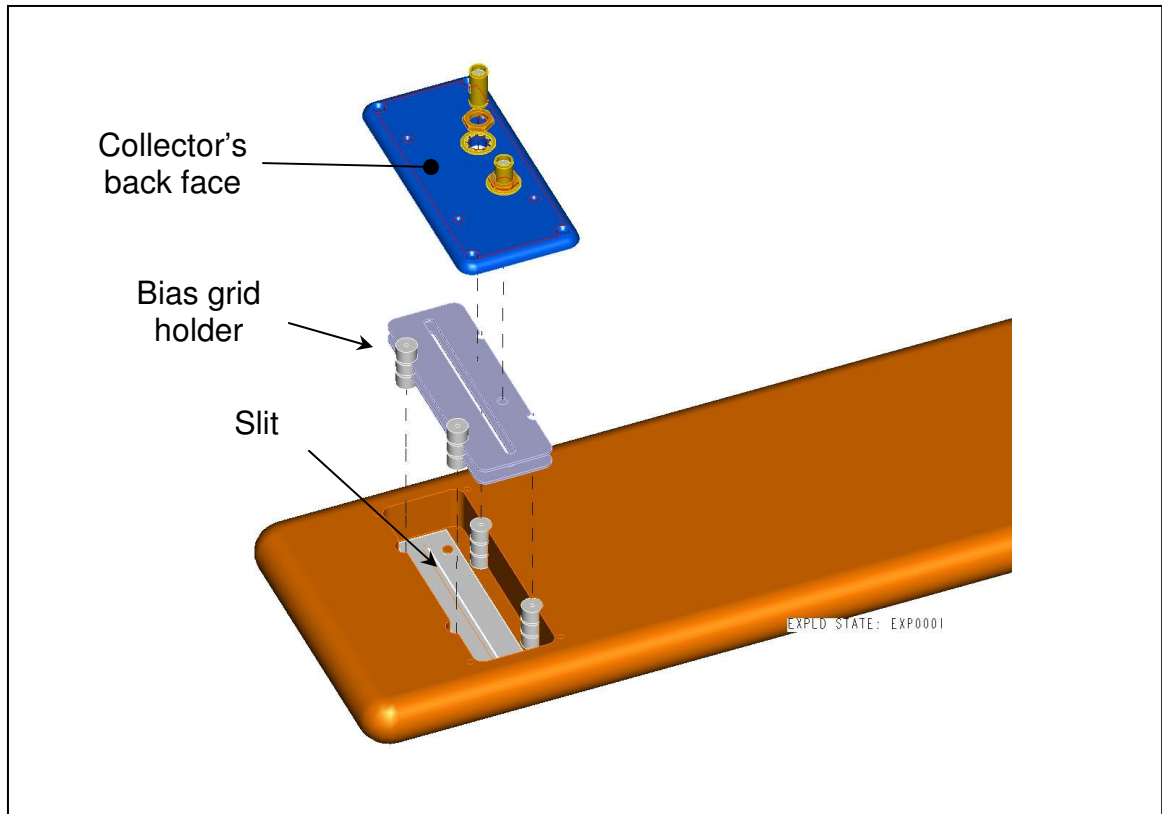
**Figure III-10**: CAD drawing of the slit-cup assembly (exploded view).

The grid is biased positive, and the collector negative, such that secondary electrons amplify the collected incident ion signal by a factor of ≈40, limiting the need for an amplifier. Note that this amplification factor depends on the field and geometry configurations and that, if operated in a similar regime, the Faraday cup signal would only be amplified by a factor of ≈2.5 (see Figure III-3) with respect to the normal operation bias. The resulting signal is sampled through a coupling capacitor before being digitized by the oscilloscope. The uncertainty of the signal amplitude due to digitization of the waveforms is less than 0.5%. This arrangement of shallow collector cup and grid with the ion impact angle controlled by the slit has no perceptible variation in response over the duration of

the measurement [95,96]. Depending on the diagnostic station, slits are 25 or 50 µm wide and 7 to 20 cm long. All the measurements made with the mechanical slit scanners are time-resolved with a resolution of 40 to 120 ns. The minimum time resolution is of the order of 10 ns, limited by the transit time of the ions through the slit-cup detector and the capacitance of the circuit (including the collector). Measurements made with the mechanical-slit scanner rely on the beam properties being both reproducible shot-to-shot and over long periods of time, since, with our current diagnostic setups, 100-300 pulses are required for transverse phase-space measurements and more for the full current-density distribution measurements. The stability of the injector is adequate and will be addressed in Section - VII.3.2 -. The power supplies that energize the quadrupoles of the matching and transport sections are stable to ±0.1%. Shot-to-shot variations in $I_B$ and $E_B$ contribute to overall uncertainties, which are folded into the evaluation of the uncertainties of the envelope parameters and emittance (discussed in later chapters). The signal-to-noise ratio ranges varies depending on the type of measurement (current-density map,15:1, phase-space scan,10:1-300:1, or single-slit profile, 15:1-500:1), the diagnostic station and the current density at the collector.

### III.3.2 -   Beam profile

Stepping through the beam with a slit-cup gives a transverse current-density profile. This measurement integrates over the current density in the plane perpendicular to the motion of the slit-cup. For instance, for a horizontal profile

77

($x$-direction) with the slit oriented vertically ($y$-direction), the measured signal is then simply proportional to

$$\rho(x,t) = \int J(x,y,t)\,dy \qquad \text{(Eq. III-9)}$$

and similarly in the other ($y$) direction, where $J(x,y,t)$ is the beam current density as a function of time. These measurements determine the beam centroid and radius in one of the transverse planes. They also indicate large-scale asymmetries or distortions of the ideal uniform-density elliptical cross section which, projected in this manner, produces a cosine-shaped distribution.

For the data reported here, step sizes varied from 0.25 mm to 2 mm, with beam profiles containing between 50 and 150 data points.

### III.3.3 -   Beam phase-space distribution and emittance

III.3.3.1 - Double-slit scanner

The projected phase-space distributions of the beam [$f(x,x',t)$ or $f(y,y',t)$], are measured with a slit and a parallel slit-cup. Depending on the diagnostic station, the slit is located 10 to 15 cm upstream of the slit-cup and determines the position coordinate, $x$ or $y$, of the beam being sampled. The slit-cup is then scanned through the transmitted slice to measure the transverse velocity distribution ($x'$ or $y'$) at that position (Figure III-11). This procedure is repeated over the entire beam distribution to map the phase-space density [96,31].
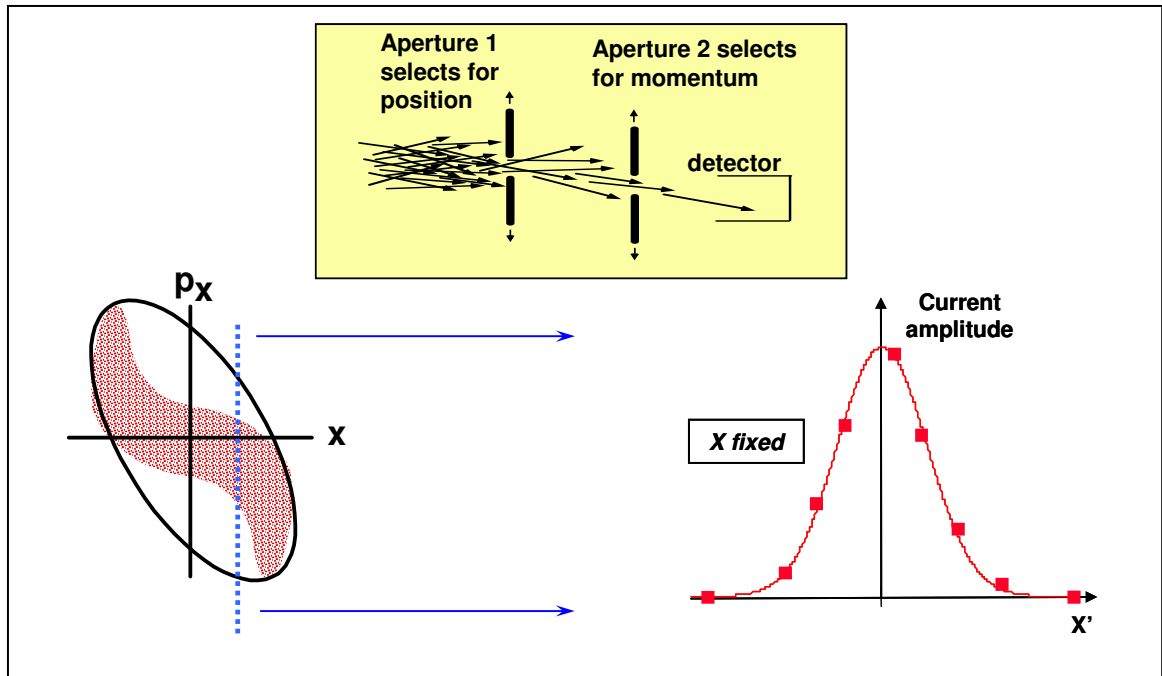
**Figure III-11**: Illustration of a phase-space distribution measurement.

The sampling intervals (spatial and angular) at which these phase-space distributions were acquired varied according to the beam size and beam transverse temperature at the location of the measurement. To minimize the uncertainties due to drifts in the system, the number shots per phase-space measurement was limited to 225-275 (an acquisition time of about an hour at a maximum repetition rate of 0.1 Hz).

From the signal amplitude as a function of position, angle and time, the beam can be described in terms of its first and second moments (including the beam emittance) where the integrals from Section - II.1.4 - (in the calculation of the averages) are replaced by discrete summations and the distribution function is replaced by the signal amplitude. Because the beam distribution may not be on

center, the centroid offsets ($< x >, < x' >$ or $< y >, < y'>$) need to be included in the calculation of RMS values. Therefore (Eq. II-28), (Eq. II-29) and (Eq. II-32) become

$$a = 2\sqrt{\langle (x - < x >)^2 \rangle} \, , \tag{Eq. III-10}$$

$$a' = \frac{4 \langle (x - < x >)(x' - < x' >) \rangle}{a} \, , \tag{Eq. III-11}$$

$$\varepsilon_{x,edge} = 4\sqrt{\langle (x - < x >)^2 \rangle \langle (x' - < x' >)^2 \rangle - \langle (x - < x >)(x' - < x' >) \rangle^2} \, , \tag{Eq. III-12}$$

and similarly for the $y$-direction.

III.3.3.2 - Additional considerations

The natural expansion of the 'sheet beam' that emerges from the first slit is due to two reasons. First, the self-fields of the beam push the particles outward, hence increasing the size of the beam. Second, the random transverse motion of the particles (temperature) causes divergence of the sheet beam. The slit width and the drift distance are chosen such that the latter effect is dominant since it is directly related to the parent distribution of the whole beam. From an envelope based analysis of a sheet beam propagating in free space [54], the contribution of each of these terms can be estimated. If a beam of radius $r_{beam}$ passes through a slit of width $s$ and drifts over the length $d$ (the distance between the slit and the slit-cup), then the thermal contribution to the envelope expansion (at the center of the incident beam where $a' = 0$) is given by

$$a(d)_{thermal} = \sqrt{\frac{s^2}{4} + \frac{\varepsilon_{beam}^2 d^2}{r_{beam}^2}} \, , \qquad\qquad \text{(Eq. III-13)}$$

where $\varepsilon_{beam}$ is the full-beam edge emittance. The self-fields contribution to the sheet beam envelope expansion is given by

$$a(d)_{sc} = K \frac{s \, d^2}{2 \, r_{beam}^2} \, . \qquad\qquad \text{(Eq. III-14)}$$

The ratio of (Eq. III-13) and (Eq. III-14) gives the relative importance of both terms and is typically about a hundred or more at all our diagnostics stations.

The accuracy of the emittance depends on the relative alignment of the slits. For most of the mechanical slit scanners used on the HCX beam line, this alignment is done on the bench since the slit and slit-cup are mounted on a common flange. The whole assembly is then installed on the beam line. However, due to geometry constraints, it is sometimes necessary to install the slit and slit-cup first and align them in situ.

Depending on the diagnostic location and the beam distribution, the finite width of the slits accounts for a ≤ 1% increase in the emittance [97,96]. Systematic effects due to the detector geometry (uncertainty of the drift distance between the slit and the slit-cup) and the sampling of the distribution account for ≈ ±4% uncertainty on the emittance.

## III.4 -    Beam current-density map

The beam current-density 'map' is a measurement of the 2-D current-density distribution $J(x, y)$. Three different diagnostics were used to perform this

measurement: a Kapton film, the mechanical slit scanner and a 32-channel Faraday cup array (in the diode region).

### III.4.1.1 - Kapton image

Kapton is an organic polymer that degrades when exposed to ionizing radiation. Darkening of the film (originally yellowish in color) indicates the time-integrated beam current distribution. A more detailed discussion of this diagnostic and its application to intense beams used in heavy-ion fusion research can be found in Ref. [98]. Advantages to using Kapton for imaging the beam are its linear dose response over the range of interest (1-2 MeV), its excellent spatial resolution and dynamic range in 50-100 beam pulses. It also discriminates against stray low energy and low mass particles (e.g.: electrons).

However, the beam images obtained with the Kapton film are time-integrated over the duration of the beam pulse, which sometimes makes interpretation of the image difficult. In particular, the dynamics of the bunch head and tail may be very different from the flattop. It is then necessary to examine the time dependence of the current-density distribution, which can be done with the mechanical slit scanner. Moreover, in order to analyze the Kapton image, the witness film needs to be taken out of the system, which requires the beam line to be opened up to air.

### III.4.1.2 - Crossed-slit measurements

In addition to imaging the beam with Kapton films, mechanical slit scanners can be used to measure the beam's time resolved current-density

distribution in the plane perpendicular to the beam motion, $J(x,y,t)$. Since all diagnostics stations are equipped with a horizontally and vertically driven slit and slit-cup assembly, a pair oriented perpendicular to each other describes the beam's spatial distribution. A typical scanning procedure is to set the front slit at one location, for instance $x_1$, step the slit-cup through the transmitted slice to measure the current-density distribution at this location, $J(x_1,y,t)$, and move the front slit to another location. The difference from the phase-space measurements described in Section - III.3.3.1 - is that the downstream slit is scanning through the long dimension of the transmitted sheet beam. This is illustrated in Figure III-12.
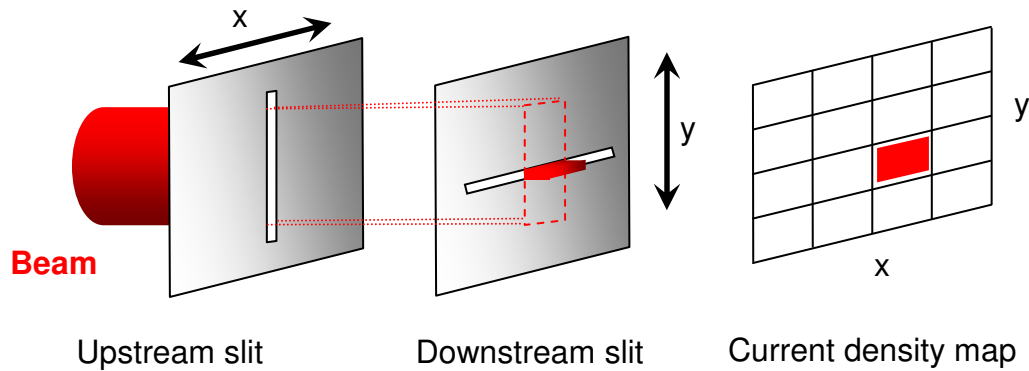


**Figure III-12**: Schematic illustrating the current-density mapping procedure.

Following this procedure requires about 10 hours to obtain a current-density map with typical scanning intervals of 1 mm x 1 mm, a resolution rather coarse with respect to that of the Kapton image. On the other hand, the data is time-resolved and does not require opening the vacuum system to retrieve the data. It is also

quite easily possible to cut down the data acquisition time by using multiple slits and slit-cups setups or other imaging techniques as described in the next section.

The image obtained in this manner is slightly distorted because the transmitted beam sheet expands before it is collected by the slit-cup. A true picture of the beam comparable to the one obtained with a Kapton film requires folding this effect into the data analysis.

III.4.1.3 - 32-channel Faraday cup array (FCA)

In early measurements of the current-density distribution at the exit of the injector diode, a 32-channel Faraday cup array was used [124]. As schematically depicted in Figure III-13, this device consists of two orthogonal rows of small Faraday cups mounted on a single movable assembly inside a grounded shield. The collectors in each row are staggered in radius with center-to-center separation of 3.8 mm [99,100].
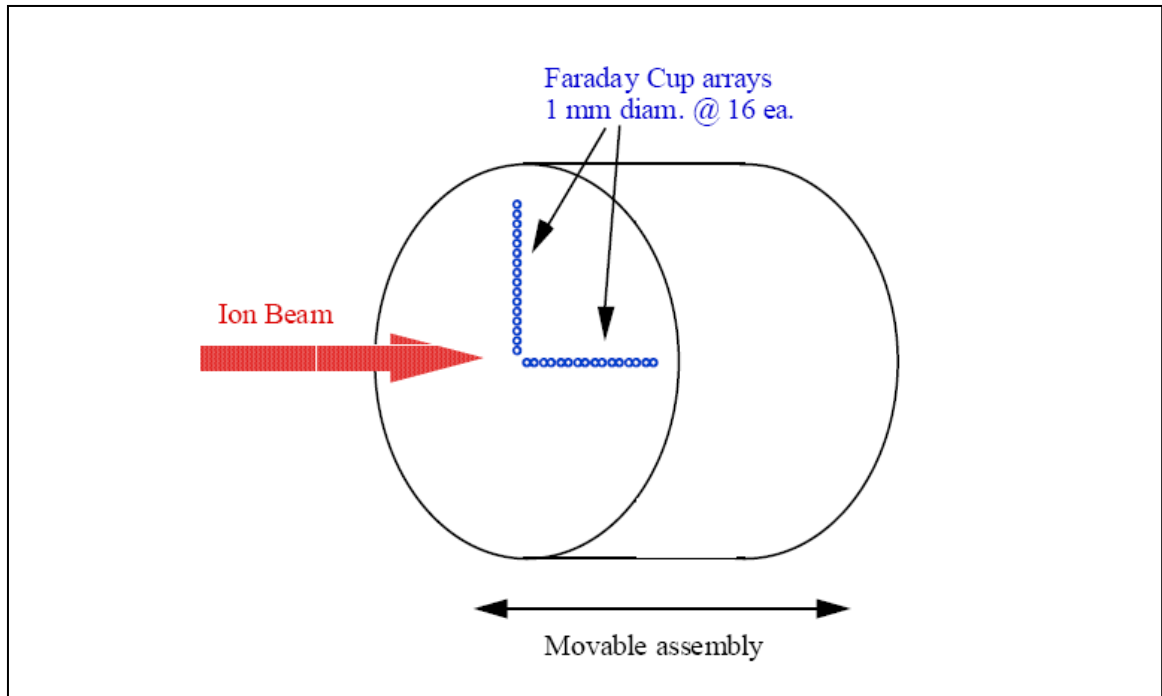
**Figure III-13**: Schematic diagram of the 32-channel Faraday cup array (FCA) [100].

The collectors inside the shield are preceded by an electron trap. A screen sits in front of the beam stop (bottom of the shield) creating a field-free region like the honeycomb structure in the Faraday cup. This limits the expansion of the gas/plasma that forms on the surface of the plate by interaction of the beam with the wall (Figure III-14).
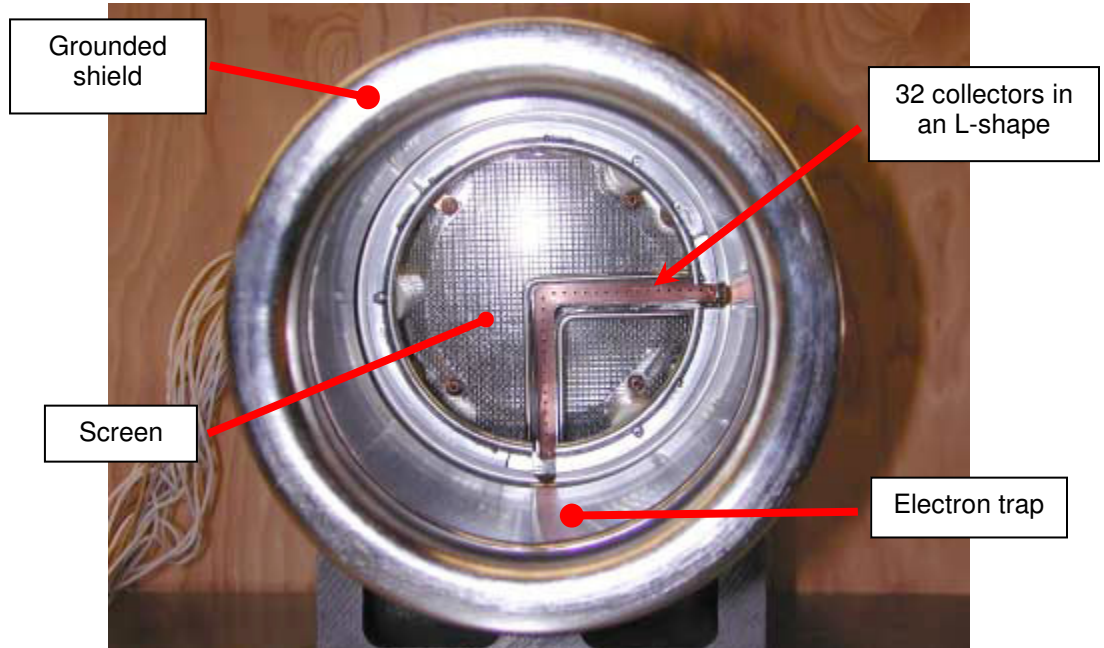
**Figure III-14**: Front view of the FCA on the bench. In front of the collector array are the electron trap and outer ground shield [100].

Additionally, holes were drilled in the front face of the collector pins to reduce secondary electron emission. The assembly can be rotated and moved along the beam axis.

## III.5 - Improved beam diagnostics

### III.5.1 - Multi-cup slit scanner

The principle of the multi-cup slit scanner is to replace the slit-cup assembly of the mechanical slit scanner described above with an array of cups. This removes the need for scanning through the transmitted slice, thus allowing acquisition of the data with a reduced number of pulses. Figure III-15 shows a

preliminary design of the collectors' arrangement, where each collector is only 250 µm across.
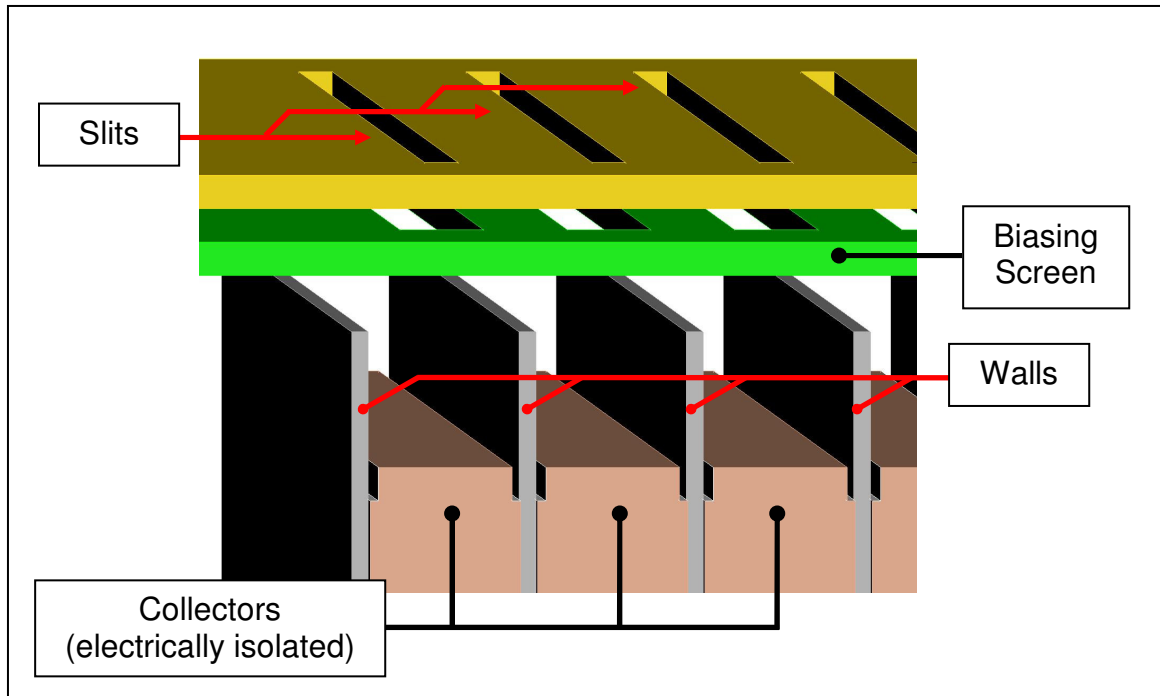


**Figure III-15**: CAD drawing (preliminary design) showing the arrangement of the collectors for the multi-cup slit scanner.

The challenges of such a device are twofold. First, each individual collector needs to be electrically isolated from its neighbors. Second, scattered ions need to be confined within a single collector (i.e. micro-cup). A rough prototype collector array (no screen or slits), consisting in a gold plated-on-glass printed circuit, has been built but has yet to be tested.

***III.5.2 -   Optical diagnostics***

III.5.2.1 - Motivation

We have developed an optical diagnostic using a scintilllator and a fast, image-intensified CCD camera that complement and may eventually replace the more traditional Kapton film image and mechanical-slit scanner techniques [101]. Its purpose is equivalent to the slit scanner described in Section - III.3.1 - with the additional advantage of providing correlated information about the full 4-D beam distribution rather than integrated slit projection, because intensity along the slit is also measured. It also allows for a much faster data acquisition time for equivalent spatial and angular resolution.

The optical diagnostic is related to the gated beam imager (GBI) [102], which uses a pepper-pot to create beamlets that are imaged directly onto a gated microchannel plate (MCP) and CCD camera. The scintillator-based technique replaces the MCP imager with a thin sheet of scintillator material. It is simple, compact, and more flexible, because only the scintillator material is placed in the path of the beam.

III.5.2.2 - Experimental setups

We have installed two optical diagnostic setups on the HCX beam line. For phase-space measurements, both can use the slits from the conventional mechanical slit scanners at these locations. A thin (~0.1 mm) alumina ceramic wafer replaces the slit-cup assembly and images the beam. Charge buildup is prevented by secondary electron emission from a high-transparency (80-90%

transmission) metallic wire grid placed on or near the scintilllator. The grid can be biased negatively to prevent contribution to the image from stray external electrons. Time-resolved beam-induced images are captured with a Princeton Instruments gated intensified CCD camera located outside the vacuum tank and viewing the scintillator through a glass window. In one setup (Figure III-16(a)), the image on the scintillator is viewed from the rear. In a more compact setup (Figure III-16(b)), the image is viewed from the front, adding some complexity to the optical system design and unfolding of the image.
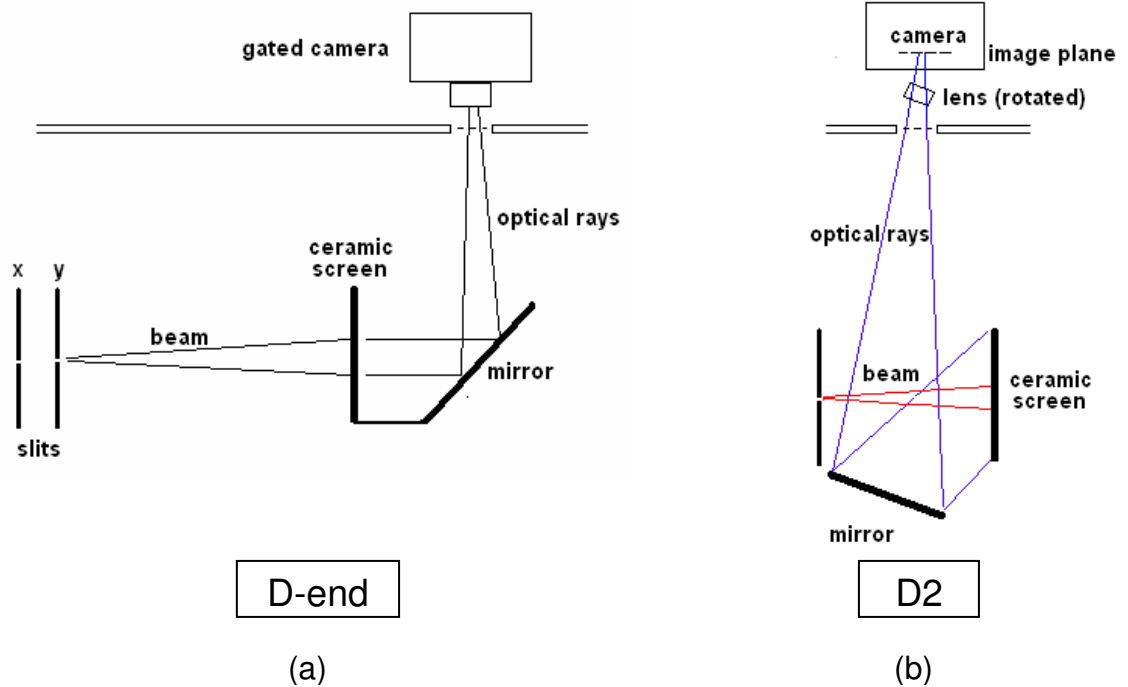


**Figure III-16**: Schematics of the two optical diagnostic setups. (a) The image is viewed from the rear of the scintillator; (b) the image is viewed from the front of the scintillator.

The rise time of the alumina wafer was measured to be less than 50 ns and is shorter than the rise and fall time of the beam current pulse. Its decay time has one very fast component (probably of the same order of magnitude as the rise time) and light output was observed with smaller-amplitude with e-folding time constants of ~2-4 μs and ~500 ms. The slower components of the measured light output may be due to intrinsic properties of light emission from the scintillator or beam plasma effects near the scintillator surface. Images are typically acquired over 0.25-1 μs intervals within the beam pulse in order to maintain a large signal to noise ratio.

III.5.2.3 - Current-density map

This measurement can be done in two ways. First, the scintillator directly intercepts the beam. This provides the full $J(x, y)$ distribution of the beam for the chosen time interval with a single pulse and high spatial resolution (< 250 μm). A representative color coded image (8 bit, fire palette) is shown on Figure III-17.
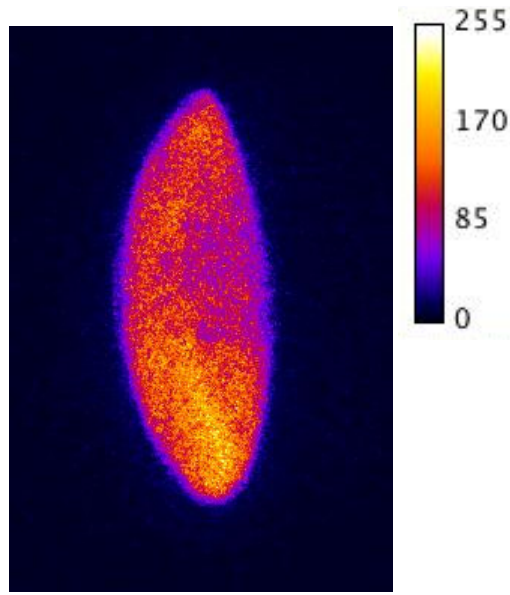
**Figure III-17**: Single pulse image (false color) of an apertured beam. The time window (1 μs) was chosen such that the image represents the mid-pulse of the beam.

However, because of the high intensity of the HCX beam, the lifetime of the scintillator for this kind of measurement is limited (optical emission e-folding rate decay of ~ 170 pulses). Thus, this rapid measurement of the beam current-density distribution is only used for fast tuning of the focusing gradients in the lattice or rough checking of the overall beam size. The preferred method is to place a slit upstream of the scintillator and step through the beam distribution. The $J(x, y)$ distribution is then reconstructed by the juxtaposition of several images (Figure III-18).
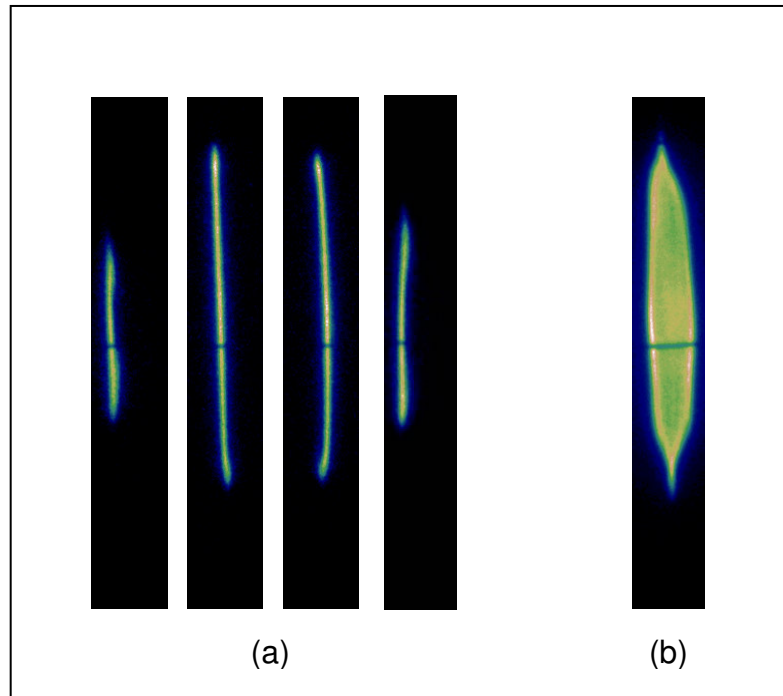
**Figure III-18**: (a) Series of representative images of the beam (false color) passing through a vertical slit at various horizontal locations across the beam. (b) Sum of the vertical slit images.

Note that the image then suffers the same distortion as the mechanical slit scanner data and requires the same type of transformation to correct it. Also, the resolution in the direction of the slit motion is determined by the step size chosen, usually 1-2 mm compared to the high resolution that remains in the slit direction. It is however a much faster measurement than the traditional crossed-slit, which has similar or lower spatial resolution.

III.5.2.4 - Phase-space distributions

The data acquisition procedure to obtain the transverse phase-space distributions $f(x, x')$ and $f(y, y')$ with the optical diagnostic is identical to the one described in the preceding section (using a slit upstream of the scintillator). Only the analysis of the set of slit images (Figure III-18(a)) is different. Instead of a simple juxtaposition of the images, one integrates them along the direction perpendicular to the slit. This provides plots of a simulated slit scan and a reconstructed phase-space distribution.

The images from Figure III-18(a) provide phase-space distributions such as $x'(x, y)$ and $y'(x, y)$ that the mechanical slit-scanner cannot measure. The unfolding and interpretation of these additional correlations is still under development.

Ultimately, slits will be replaced by a pepper-pot hole arrangement, which provides fully correlated four-dimensional transverse phase space data, in only a few beam pulses. However, the details of such a diagnostic remain to be determined.

III.5.2.5 - Optical technique validation

In order to reliably use the optical scanner, this technique has to be validated by comparison with conventional diagnostics. Comparison of the optical RMS beam parameters with the mechanical slit scan data is shown in Table IV.

**Table IV**: RMS beam parameters comparison of an 80% fill factor beam measured at D2a with the optical and mechanical slit scanner. The optical data were acquired for a 1-μs gate at mid-pulse. The mechanical slit scanner data were summed over the same time interval.

|  | Mechanical slit scanner | Optical slit scanner |
|---|---|---|
| $a$, mm | 12.3 | 12.1 |
| $b$, mm | 20.9 | 20.4 |
| $a'$, mm mrad | -37.9 | -35.8 |
| $b'$, mm mrad | 43.3 | 41.6 |
| $\varepsilon_x$, π mm mrad | 67 | 76 |
| $\varepsilon_y$, π mm mrad | 64 | 71 |

The agreement is within the experimental uncertainties for the beam size and angle. In addition, the details of the current-density distribution (shown in Ref. [101]) agree well between the two measurement techniques. However, increased noise or scatter in the optical image signal compared to the double-slit scanner is reflected in a consistently higher emittance value for a set background rejection criterion (defined as a fraction of the peak measured amplitude). Although more comparisons are needed, the optical diagnostic is now part of the set of available diagnostics for the heavy-ion fusion community.

## III.6 - Additional diagnostics

### III.6.1 - *Electrode capacitive monitors*

All electrostatic quadrupoles are biased through coupling circuits (Figure III-19) allowing them to act as capacitive pickups and beam loss monitors when the beam passes.
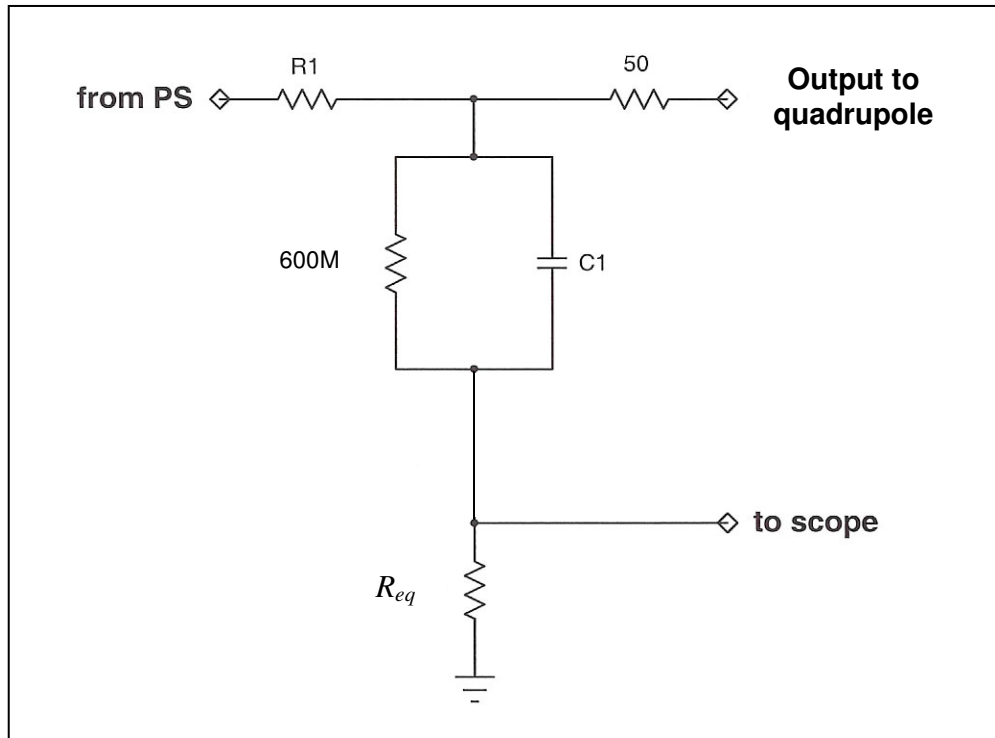


**Figure III-19**: Simplified schematic of the HCX quadrupole charge circuit

In a quadrupole, the beam induces image charges on the electrodes. As the charge subtended by the quadrupole electrodes builds up (or decreases), a current flows through the coupling circuit and a voltage drop appears across the resistor $R_{eq}$:

$$V(t) = R_{eq} \frac{dQ(t)}{dt} \qquad \text{(Eq. III-15)}$$

where $Q(t)$, the total charge in the quadrupole at time $t$, is proportional to the beam current, $I_{Beam}(t)$. For a trapezoidal current pulse (square pulse with finite rise and fall times), the resulting capacitive pickup signal consists of a positive and negative peak separated by the beam duration. A theoretical capacitive signal waveform of the beam passing through the first electrostatic quadrupole of the matching section is plotted on Figure III-20.
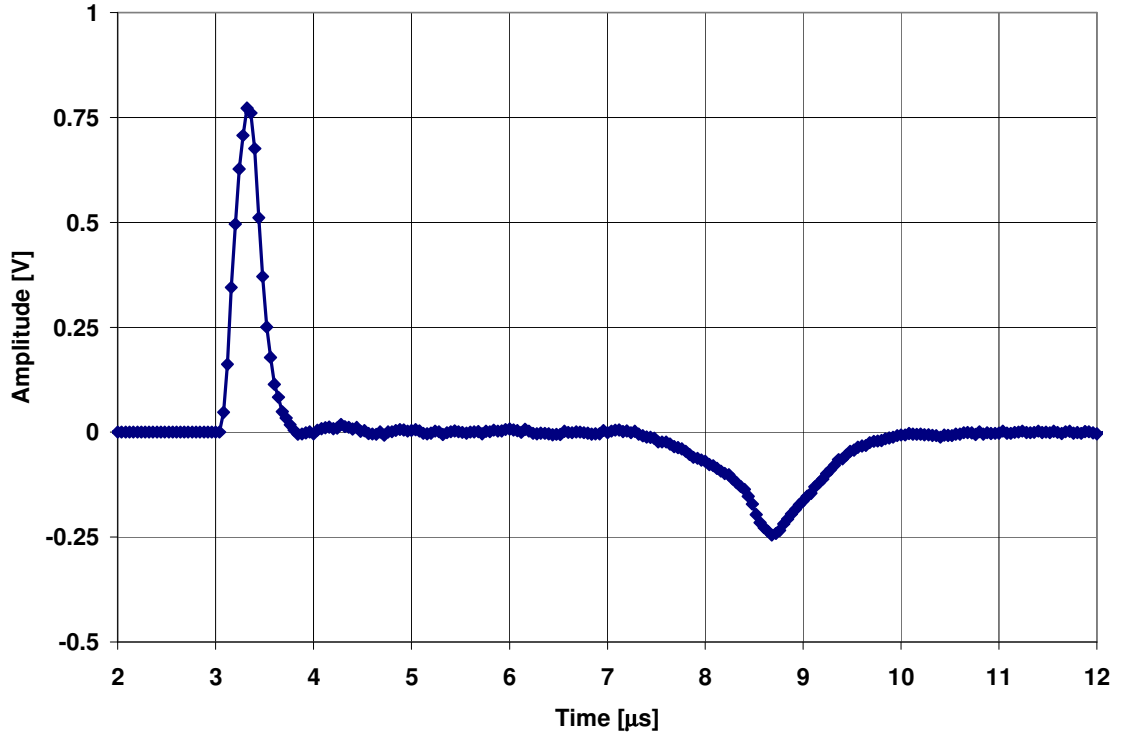


**Figure III-20**: Theoretical capacitive electrode monitor waveform derived from a measured beam current pulse. This calculation assumes a quadrupole length of 47 cm (the length of the first quadrupole of the matching section in the HCX beam line) and that the signal is fed to an oscilloscope through a 10 Ω resistor.

Here we see the two characteristic peaks (positive and negative) of the head and tail of the beam pulse. The amplitudes of the peaks differ because the rise time of the beam current pulse is different (faster) than the fall time. The integrals of each peak are a measure of the total charge of the beam subtended by the electrodes. These are equal if there is no beam loss or partial neutralization.

Secondary particles (ions and electrons) resulting from direct interaction with the electrodes travel from one electrode to another (of the opposite polarity). Since electrodes are biased in pairs and monitored through the same coupling circuit, this displacement of charges induces a current that is measured in addition to the capacitive effect. In particular, the collection of lost ions and emission of secondary electrons during the 'flattop' of the beam pulse generates a current offset (negative for positively biased electrode pairs and positive for negatively biased electrode pairs) directly proportional to the beam losses. The pickup signal due to lost ions is amplified by the large secondary electron coefficient (a parametric fit from data taken from $80°$ to $88°$ gives $\gamma_e \cong 7\cos^{-1}\theta$, where $\theta = 0°$ indicate normal incidence to the surface [49]; typical angles of lost ions are expected to be near grazing where $\gamma_e$ is largest), making this diagnostic more sensitive to beam loss than comparisons of the total beam current data at different locations along the beam line. Additionally, the former indicates regions of the lattice where envelope excursions and centroid offsets cause particle loss from scraping. However, since the collected signal is directly proportional to $\gamma_e$, which depends on the angle of incidence of the ions on the electrodes, the

97

uncertainty on the absolute value of the current loss is large. For interpretation of the pickup signals, we will assume an effective secondary electron yield $50 < \tilde{\gamma}_e < 100$. Then, viewed through $R_{Monitor}$ = 10 Ω a pickup signal amplitude of 1 V corresponds to 1 mA < $I_{B\,loss}$ < 2 mA.

At a pressure of $10^{-7}$ Torr, beam loss due to beam-background gas interactions over the length of the electrostatic transport section (2.2 m) is expected to be approximately 0.025% (e.g.: $I_{B\,loss}$ = 0.04 mA for $I_B$ = 175 mA), dominated by stripping ($K^+ \rightarrow K^{2+}$, $\sigma_{K^+ \rightarrow K^{2+}}$ = $3.5 \times 10^{-16}$ cm$^2$ [103]), assuming that the background gas mostly consists of $N_2$ and/or $O_2$. To reduce the beam-background gas interaction losses in a driver with a much larger path length, the pressure should be ≤ 1 x $10^{-8}$ Torr.

# Chapter IV - Numerical simulation tools

## IV.1 - Envelope codes

### IV.1.1 - Generalities

Portions of the experiment can be modeled with simple codes that follow the beam envelope parameters as a function of axial position. These codes numerically integrate the envelope equations [(Eq. II-23) and (Eq. II-24)] for a focusing lattice and input beam parameters. They also include routines that calculate the focusing strengths of four quadrupoles that match a beam to a given set of final beam parameters. Initial lattice designs are often the result of runs using this simple tool. Once the experiment is built, codes are used to quickly tune the focusing strength of the quadrupoles. Measured beam parameters at one location serve as input parameters, and comparisons to measurements are made at another location downstream. Based on the difference between the measured and calculated envelopes, the quadrupole voltages to be implemented in the experiment are re-evaluated. This procedure usually requires a couple of iterations to attain target envelope parameters.

Various envelope codes were used to model the HCX experiment. The codes describe the focusing field by use of a hard-edge model of the quadrupoles (except for the WARP envelope solver module discuss in Section - IV.2.1 -). For an electrostatic quadrupole lattice, the focusing fields are then given by

$$k_{x,y} = \pm \frac{V_q}{E_B} \frac{1}{r_{bore}^2},$$                    (Eq. IV-1)

where $V_q$ is the quadrupole unipolar voltage, and is applied over the effective length of the quadrupole. In the following sections, we highlight the specifics of each code.

### IV.1.2 -   *Java based*

The main advantage of the Java envelope code [104] is its graphical user interface (GUI) which allows the user to modify the initial beam parameters and the focusing strengths of the quadrupoles with the GUI giving immediate visual feedback of the calculated horizontal and vertical beam radius as a function of the longitudinal distance z. Also, the input files that describe the lattice are simple text files that contain the quadrupoles and drift lengths, aperture radius, quadrupole voltages and initial beam parameters as well as neutralization points where the charge of the beam is changed by some specified fraction (due to electrons). The focusing fields are derived for electrostatic quadrupoles where the quadrupole voltage is the input parameter; using this code with magnetic quadrupoles requires the user to scale the gradients appropriately to obtain the equivalent quadrupole voltage.

### IV.1.3 -   **FORTRAN based**

The FORTRAN code currently runs on UNIX operating systems. Basically equivalent to the Java envelope code in many respects, notably in the way the lattice geometry is described in a separated input file, it however lacks the

flexibility of the graphical user interface of the latter. On the other hand, it includes the calculation of the centroid trajectories, which are absent from the Java code. For this calculation, quadrupole displacements can be prescribed. Additionally, this envelope code includes acceleration gaps and an option to specify magnetic or electrostatic quadrupoles.

### IV.1.4 - *Excel spreadsheet*

The Excel [105] spreadsheet envelope code was specifically written for the HCX with the intent to take advantage of the solving routines included in Excel and the possibilities of writing simple macros to automate some of the fitting tasks. In particular, this code was used to model the matching section and for matching the beam to the transport lattice (see Sec. VII.2.3.2 -). It is not as flexible as the other codes (Java, Fortran) because the lattice geometry description is unique to the spreadsheet and is not simply defined in an input deck. On the other hand, all other parameters (e.g.: beam energy, beam current, quadrupole effective length, quadrupole voltages…) can be varied and fitted easily and the results displayed graphically. Additionally, a Monte-Carlo macro was developed to investigate the sensitivity of the beam dynamics to various transport lattice and initial beam parameters and assess errors in the envelope simulations based on the experimental uncertainties.

### IV.2 - WARP envelope model and particle-in-cell code

The simple hard-edge description of the quadrupoles is adequate for quick tuning of the quadrupole voltages and for converging on targeted envelope

parameters. However, better understanding of the beam envelope evolution between two measuring stations requires reliable prediction of the envelope parameters based on the experimental beam and lattice parameters. To do so, a better model of the lattice focusing forces is needed. The WARP envelope solver, described below, provides the necessary tools. WARP [106] is a suite of simulation codes written to analyze beam physics problems for heavy-ion inertial fusion, in particular taking into account the nonlinear self-fields of space-charge dominated beams [107,108]. WARP will be discussed in more detail in Section - IV.2.2 -.

### IV.2.1 -   WARP envelope solver and implementation for this experiment

The envelope solver is usually used prior to running full particle simulations as a check on the lattice specifications and initial parameters or for matching purposes. The WARP envelope solver is a more complete tool than other codes as it can handle accelerating gaps, electrostatic and magnetic lattices, and off-axis beams. It can also handle user-specified $z$-dependent current and emittance. More importantly, it is possible to describe the focusing forces more accurately by using Python scripts [109] that load multipole moments of the fields derived from 3D solutions of the Poisson equation, including fringe fields described in Section - II.1.9.1 -.

Because the WARP envelope solver is part of the WARP code, its use is rather complicated and requires familiarity with the WARP and Python programming languages. In order to add more flexibility and a rapid turnaround in the laboratory, a simpler, user-oriented script was developed for use on the HCX

beam line. In addition to a more realistic description of the fields, the beam energy variations due to the beam entering and exiting the quadrupoles and the resulting radial focusing forces are included. This code also includes the effect due to the electric self-field of the beam shorting out to the slit paddle when striking the emittance scanner. An analytical study of this effect showed that to leading order it is equivalent to the drop of the perveance term of the beam to zero as it approaches the metal boundary [152], and it is thus modeled in the envelope code.

Because of the high-level description of the lattice and the physics, this code is the primary tool to accurately predict the evolution of the envelope in the experiment and serves as the principal means of comparison of RMS beam parameters obtain from data and simulation (see Section -VIII.4 -).

## IV.2.2 - *Particle-in-cell (PIC) code*

The envelope model only describes the statistical edge evolution of the beam and does not include higher order multipoles (n>2) of the focusing fields or the effect of the image forces that become more important when the beam approaches the walls. Moreover, other effects like the behavior of halo particles (i.e. particles whose trajectories reside outside the core of the beam), space-charge waves and nonlinear self fields are not addressed in an envelope description of the beam. In order to consider the high-intensity beams needed for heavy-ion inertial fusion, all these effects need to be taken into consideration. Thus, the dynamics of the beam can be studied by calculating the trajectories of many macro-particles, each representing a large number of actual beam

particles. Particle-in-cell (PIC) codes such as WARP, described below, follow this principle.

IV.2.2.1 - Overview

The WARP code uses plasma simulation techniques to model self-consistently the behavior of high space-charge particle beams. It allows flexible and detailed multi-dimensional modeling of high current beams in a wide range of systems, and is designed and optimized for heavy ion fusion accelerator physics studies. The core model is the Particle-In-Cell (PIC) algorithm, which is combined with a general description of the accelerator lattice. At present it incorporates a 3-D field description, an axisymmetric $(r, z)$ description, a transverse-slice $(x, y)$ description, and a simple transverse envelope model (the envelope solver briefly discussed above) used for comparison to the RMS moments of the particle distribution obtained from the PIC simulations.

The 3-D description is fully three-dimensional and time-dependent; includes the entire geometry of the accelerator as well as any time dependencies of the applied fields. The axisymmetric and transverse-slice codes are two-dimensional models. The transverse-slice version models the behavior of a slice of the beam incrementally along the axis of the accelerator, ignoring any axial dependence of the self fields (axial dependence of the applied fields, such as acceleration, may be included, but time dependence is ignored).

WARP calculates the particle trajectories using the leap-frog algorithm [110], in which the positions and velocities of the particles are advanced alternately. The self-field is calculated in the beam frame using the PIC method,

104

in which the charge of the beam particles is deposited onto a rectangular grid, followed by solving Poisson's equation. Image forces (assuming perfect conductors) are calculated at each time step using the capacitive matrix technique [111,57,112]. The focusing fields can be modeled from the multipole moments derived from a 3-D solution of Poisson's equation or by directly using the Poisson's solution tabulated on a 3-D grid. The advantage of using the multipole decomposition of the fields is that the various components can be turned on and off in order to check their influence on the beam dynamics. Typically, 100-400 thousands macro-particles and a grid size of 0.2 mm are used in the calculations. At the end of a run, files that contain all the information needed for analysis or continue the simulation at a later time are generated as well as particle distributions constructed with the Python Gist package [113]. Initial particle distributions are typically either K-V or semi-Gaussian (i.e. uniform density, Maxwellian velocity with uniform temperature given by the beam emittance) but arbitrary particle distributions can be read via the Python interpreter.

IV.2.2.2 - Simulations in support of the experiment

*IV.2.2.2.1 - Planning the experimental agenda*

Once the main lattice parameters are set (by means of analytical studies and envelope calculations), detailed simulations using the PIC code WARPxy (i.e. transverse slice description) better predict the machine performance and identify potential phenomena of importance. For instance, early calculations [114], conducted with both a semi-Gaussian and a self-consistent distribution (i.e.

calculated by simulating the emitter, using space-charge-limited injection, through the injector and matching section), indicated that the dynamic aperture limit in the HCX was particle loss, rather than emittance growth, emphasizing the importance of beam current measurements in the experiment. These runs were carried out to represent as closely as possible the sequence of measurements in the experiment, namely, decreasing $\sigma_0$ to increase the beam radius and fill more of the bore clear aperture. Figure IV-1 shows two phase-space particle distributions that illustrate the type of distortions expected when filling a large fraction of the channel aperture (Figure IV-1(b)), with respect to the nominal case (Figure IV-1(a)).



(a)                                           (b)
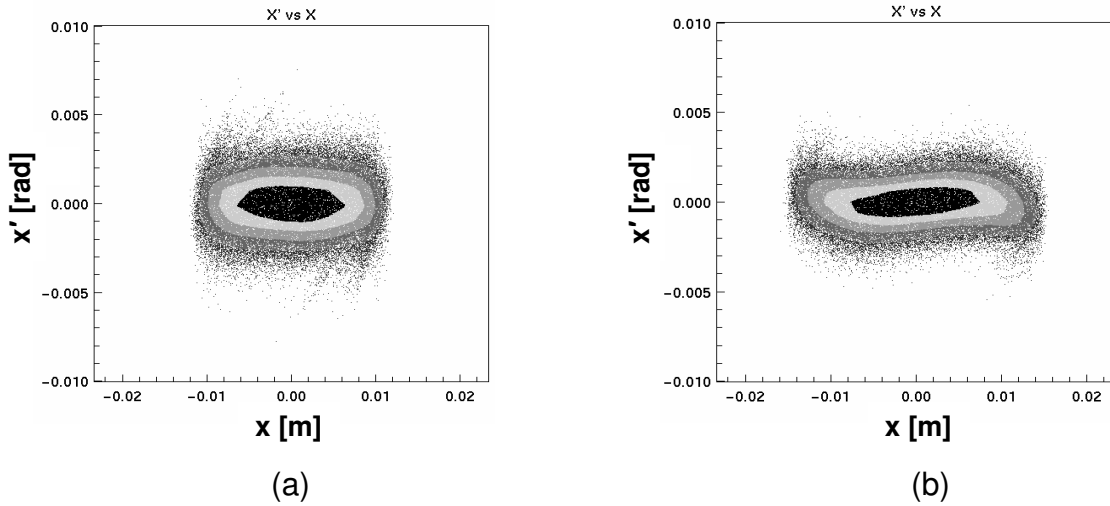
**Figure IV-1**: Phase-space plots (simulations) after passing through the HCX tank (10 quadrupoles) at the maximum beam excursion, where the beam fills (a) 60%; (b) 80% of the clear bore aperture. The physical aperture is at ±23 mm.

The results from these runs and other theoretical studies lead to the experimental agenda described in Section - V.1 -.

*IV.2.2.2.2 -    Beam distribution reconstruction for direct comparisons*

If simulations are to successfully design an experiment, they are likely not to grasp the entire complexity of the real system. It is therefore necessary to refine the calculations as more data become available from the experiment. Real operating conditions often differ from what was assumed in the early calculations.

The HCX is primarily an experimental study of intense beam dynamics and as such the measurements carry intrinsically valuable information. However, it is also important to understand the results from a theoretical point of view. The data is therefore compared to calculations in which the degree of complexity and physics input. Although the experiment and simulations agree reasonably well when second moments of the beam distribution and some gross features of the distributions are compared, the details of the beam distribution's 2-D projections are poorly predicted; most simulations start with idealized distribution functions not representative of the real beam distribution. Since even the self-consistent distribution derived from the source does not reproduce the measured 2-D projections, an algorithm that generates 4-D distributions from the available projections is being developed [115]. This algorithm uses maximum-entropy Monte-Carlo techniques to tomographically synthesize an approximation to the distribution function; the measured distributions in the $(x, x')$, $(y, y')$ and $(x, y)$ planes are not sufficient to uniquely specified the 4-D distribution. Some early results of simulations initialized with a distribution reconstructed from the data are

shown in Section - IX.2 - and a more detailed discussion can be found in Ref.

[154].

# Chapter V -    Experimental agenda and methods

## V.1 -    The HCX agenda

The transport experiment in HCX is designed assuming that a high-intensity and uniform beam with low emittance is delivered to the entrance of the channel. The design also relyies on planned modifications to the '2-MV Injector', which was originally designed for the earlier HTE [116,117], MBE-16 [118], ILSE [119,120,121] and ELISE [122] proposals. Construction was started at LANL and LBNL contributed to significant improvements and upgrades. The Injector was made 'HCX-ready' in 1999-2001 and the beam exiting the Injector was characterized (Section - VI.4 -) before installing the matching and transport sections. The initial configuration of the HCX beam line, which did not include the four magnetic quadrupoles, was completed in December 2001 and first beam was transported in January 2002.

The lattice was designed such that, for nominal operating conditions, the beam would fill 60% of the clear aperture and no beam loss or emittance growth was expected. This 60% fill factor case sets the reference for the larger fill factors to be investigated. The main beam characteristics to be probed along the beam line are:

- The beam current-density distribution, $J(x, y)$

- The emittance growth and phase-space distributions, $f(x, x')$, $f(y, y')$

- The beam centroid trajectory and sensitivity to alignment

These measurements are performed at the entrance and exit of the transport channel, with the set of diagnostics described in - Chapter III - , and compared to one another. They are also compared to PIC simulations, which support the experimental plan. The dynamic aperture is then parametrically explored by varying the fill factor. Methods to vary the fill factor include varying the focusing gradients, intentionally launching envelope mismatches, steering the beam close to the walls. A sample measurement sequence is shown on Figure V-1.
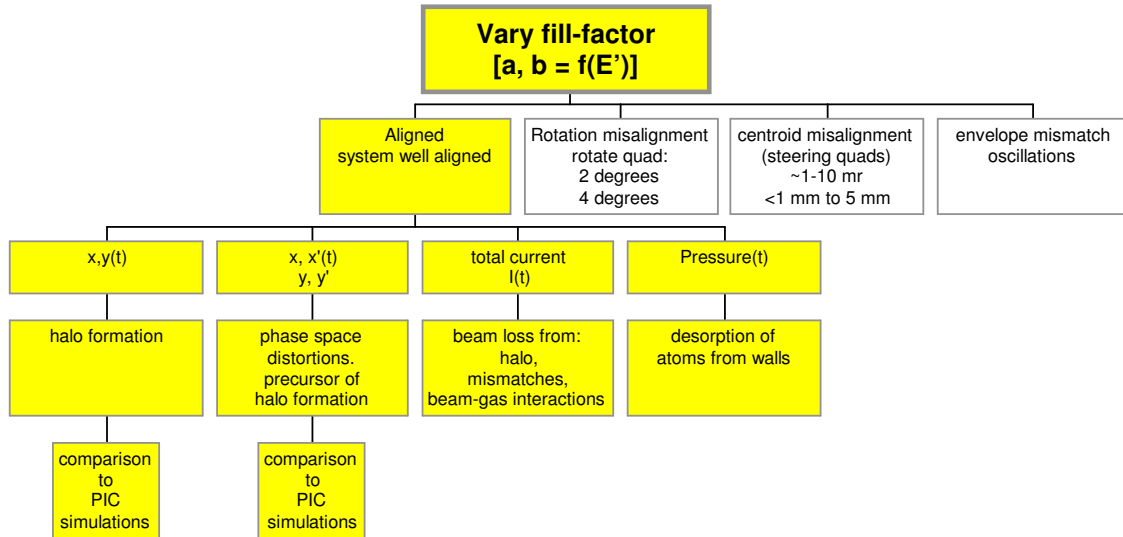


**Figure V-1**: Experimental plan – Sample measurement sequence. In the upper box, $a$ and $b$ are the envelope RMS sizes and E′ is the focusing field gradient.

To date, two fill factors have been measured (60% and 80%) with results presented in Chapter VII - and Chapter VIII - . However, beam control issues in the matching section (discussed in Section - VII.2 -) have so far limited the use and efficiency of the other methods (notably envelope-mismatch oscillations) for

moving the beam closer to the aperture bore radius. Quadrupole voltages in the electrostatic transport section are ±24.4 kV and ±17.5 kV, which correspond to 60% and 80% fill factor for matched and centered beams. The actual beam edge excursion (2× RMS) in the experiment is always slightly larger than 60% or 80% because of residual mismatch and misalignment. The nominal beam and lattice parameters for the data presented in this thesis are summarized in Table V.

**Table V**: Main beam and lattice parameters in the electrostatic transport section.

|  | 60% fill factor | 80% fill factor |
|---|---|---|
| Ion Energy, MeV | 1.0 | 1.0 |
| Pulse duration, μs | 4.5 | 4.5 |
| Ion speed/light speed ($\beta$) | 0.007 | 0.007 |
| Pulse length, m | 10.0 | 10.0 |
| Beam current, A | 0.18 | 0.18 |
| Brightness, A/mm$^2$ | 0.7 | 0.7 |
| Bore radius, mm | 23.3 | 23.3 |
| Averaged beam radius (2 x RMS), mm | 10.3 | 14.7 |
| Field gradient, kV/cm$^2$ | 9.0 | 6.4 |
| Undepressed phase advance ($\sigma_0$), ° | 69 | 48 |
| Tune depression ($\sigma/\sigma_0$) | 0.19 | 0.16 |
| Quadrupole longitudinal occupancy, % | 0.71 | 0.71 |
| Lattice period, cm | 43.3 | 43.3 |
| Number of quadrupoles | 10 | 10 |
| Electrostatic transport section length, m | 2.2 | 2.2 |

In March 2003, four room-temperature pulsed magnetic quadrupoles were installed to start the investigation of the specifics of the transport with magnets, in particular, electron effects which are not as critical in the electrostatic transport

section. A lengthy commissioning and preliminary experiments are not reported in this thesis.

## V.2 - Data acquisition system for the mechanical slit-scanners

Most of the data are collected with the mechanical slit scanner described in Section - III.3.1 -. The acquisition process for this diagnostic involves positioning the slit and/or slit-cup, triggering the Marx generator and extraction voltage to produce the beam and collecting the signal induced by the beam in the slit-cup collector. The pulse from the collector, first recorded on an oscilloscope, is immediately downloaded to a computer. This sequence is repeated up to a few thousand times (for a current-density map of the beam) and is completely automated. The data acquisition and control software package is written in Labview™ [126] and its functionality is described in Ref. [96]. Several modifications were implemented for the HCX experimental setup. First, instead of an analog output from a multifunction I/O card, a Stanford Instruments DG535 digital pulse generator, driven by the software, was used to produce the initial trigger pulse that fires the Marx generator and the extraction voltage. Then, to ensure that the beam parameters remain as constant as possible and misfires (i.e. no extraction pulse) are rejected, several characteristics of the Marx and extraction pulses (amplitude, width, relative timing) are monitored and compared to values specified by the experimenter and consistent with good shot-to-shot reproducibility. When these Marx and extraction gate voltage measurements are outside specifications, the slit-scanner data are automatically discarded and another shot is taken. Finally, to reduce the data acquisition time, the algorithm

used to acquire the phase-space distribution of the beam was modified. Originally, the user would define a parallelepiped region of the phase-space that the program would scan according to the number of steps specified by the user, following the procedure described in Section - III.3.3.1 -. But, when the beam phase-space is distorted, many of the data points lay outside the meaningful region of the phase-space being scanned, as illustrated on Figure V-2.
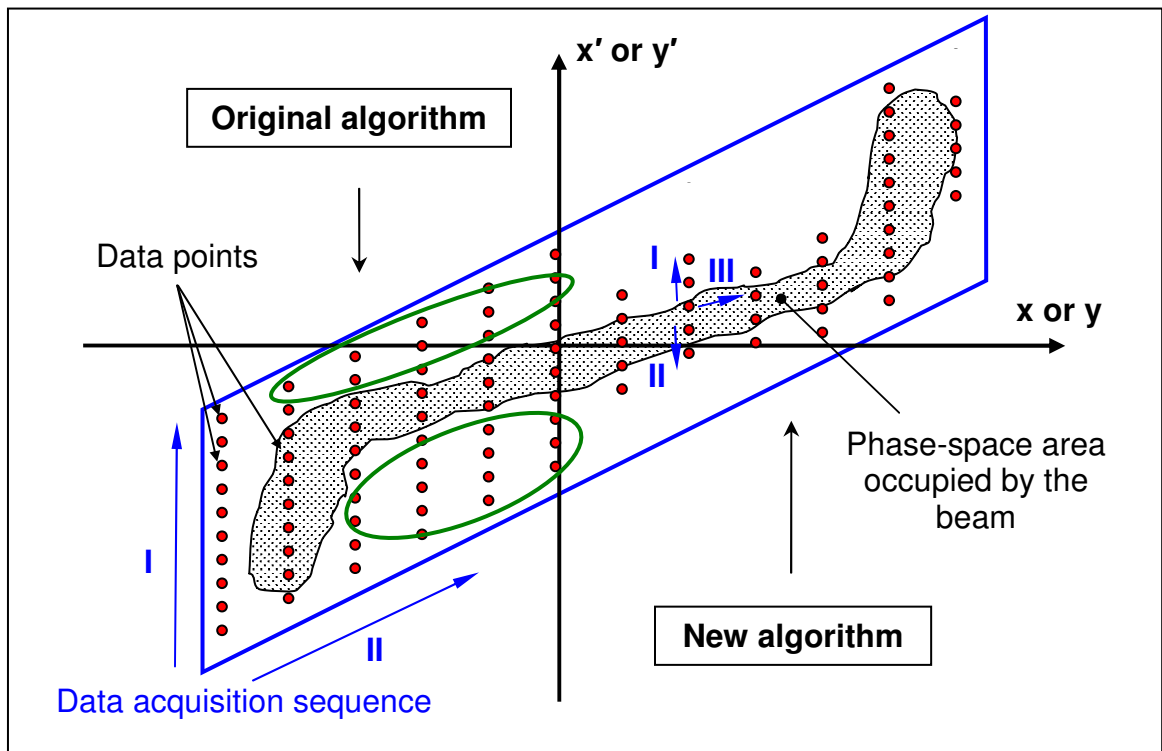


**Figure V-2**: Sketch of a phase space diagram illustrating how a distorted phase-space renders the original acquisition procedure (left) inefficient by taking several data points outside the region of interest (inside the green ellipses). The new algorithm (right) reduces the number of pulses needed.

The new algorithm follows the beam's phase-space footprint more closely by calculating the velocity ($x'$ or $y'$) distribution centroid at each position coordinate scanned and extrapolating the location of this centroid to the next position ($x$ or $y$) coordinate. Scanning the velocity distribution is done in two steps: First, from the extrapolated centroid location, the program displaces the slit-cup in the direction of positive angles and acquires data until the integral of the collected waveform falls below a limit set by the user. Then, the slit-cup is displaced in the other direction, starting again from the extrapolated centroid location and stops again when the data fall below the set limit. Finally the program calculates the centroid of the velocity distribution just acquired and proceeds accordingly to the next position and velocity coordinates. Note that to avoid 'missing' part of the beam distribution, the threshold limit is activated only after this limit has been exceeded for at least one pulse and reset for each new position coordinate before scanning the velocity space. For a determined phase-space area, following this procedure decreases the number of pulses by up to 40% with respect to the original procedure, significantly speeding the acquisition time. A further factor of >2 improvement in acquisition speed would be possible via modification of the slit-cup hardware to accommodate two or more slits and independent Faraday cup detectors as described in Section - III.5.1 -. In a series of measurements where both algorithms were successively employed, the more efficient algorithm gave the same the emittance within uncertainties.

Since the data acquisition and control software package includes several modules that can be used independently (e.g.: the 'Move' module that allows the

114

user to move the slit paddles to the locations of his choice), it was also used to move the slit and/or slit-cup when needed for other measurements. In particular, no new software has been written for the optical slit-scanner, which uses the same slits as the mechanical slit-scanners, and fully-automated acquisition software for this diagnostic is still needed.

## V.3 -      Presentation of the data

The data collected with the mechanical scanner is further analyzed using routines written in Matlab™ from Mathworks Corporation, one for each type of measurement (single-slit profile, phase-space scan and crossed-slit map) described in Sections III.3.2 -, III.3.3 - and III.4.1.2 -.

All data acquired with the mechanical scanner are time-resolved. The routines allow the user to step through the data one time slice at a time or select a time window over which the data is integrated before being displayed and the moments of the distribution calculated. The moments of the beam can also be plotted as a function of time.

Single-slit profiles are displayed as histograms, where the height of the bars corresponds to the collected signal amplitude (Figure V-3). This representation quickly shows major nonuniformities in the beam current-density distribution. In addition, the equivalent profile for a uniform-density beam with the same RMS beam size as the data can be plotted.

**Integrated profile**
(100 < t slice < 150)

mean = -1.133 mm
a = 6.485 mm

sum = 2.543e+002 V

mlpsout⌀9021507    Station DV2

V Marx = 43.7-43.9 V / V Gate = 12.49 kV [4.16 V] / I RogInj = 183.0 mA / Aperture IN - No Bias
Matching Sol. 171 Log #2 / QD1 to Q6 @ 23.43 kV / QI7 to QI10: Sol. p301 Log #3 / HCX globals /
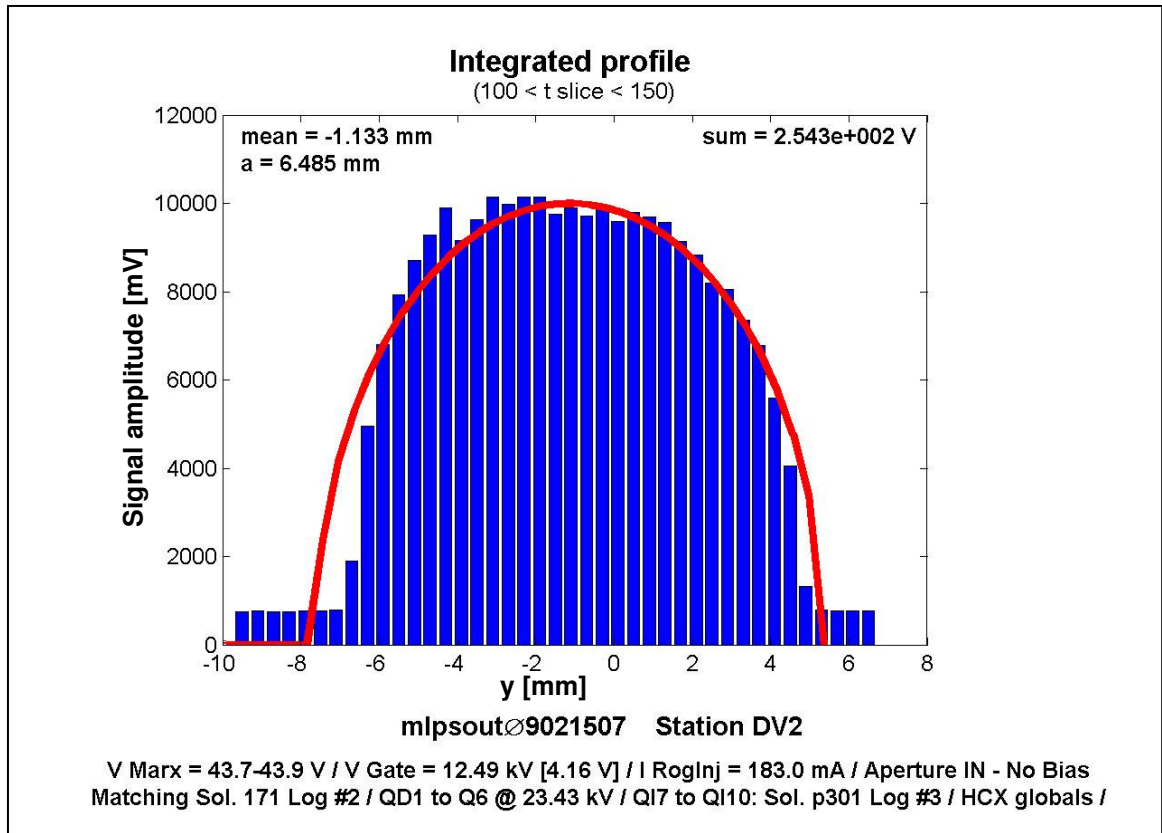
**Figure V-3**: Example of a single-slit current-density profile (vertical direction) displayed as a bar plot. The red line indicates the equivalent uniform beam profile. The first and second moments of the distribution are calculated and displayed on the top-left of the plotting area. The header indicates the time window chosen by the user.

The phase-space scan, where the beam amplitude is measured as a function of both position and transverse momentum along $x$ or $y$, is the most common measurement. First and second moments are extracted from these data, yielding the centroid position and angle of the beam as well as the extent of the beam edge in transverse position and velocity. Additionally, the moments are

116

used in the calculation of the beam emittance as described in Section -III.3.3.1 -.

An important factor in the calculation of the emittance is the minimum signal amplitude to be included in the calculation of the moments. For all the diagnostics, the signal-to-noise ratio is highest at positions in phase-space where little or no beam signal is present. In phase-space regions far from the centroid of the data, this noise level can weigh heavily in the calculation of the second moments, and therefore the calculation of the emittance. Data whose amplitude lies below a given threshold must be excluded from the calculation. To do so the calculated emittance versus percent of the signal included in the calculation is plotted as shown on Figure V-4.

Without background noise, one would expect $\varepsilon(p)$ to smoothly increase as $p \rightarrow 100\%$. The sharp break in the slope of the data seen in Figure V-4 is due to the addition of the noise and indicates where the emittance should be evaluated. Depending on the diagnostics station, 'amplitude cuts' range from 92% to 98% of the peak amplitude. This cut depends somewhat on the threshold level of the more efficient algorithm.
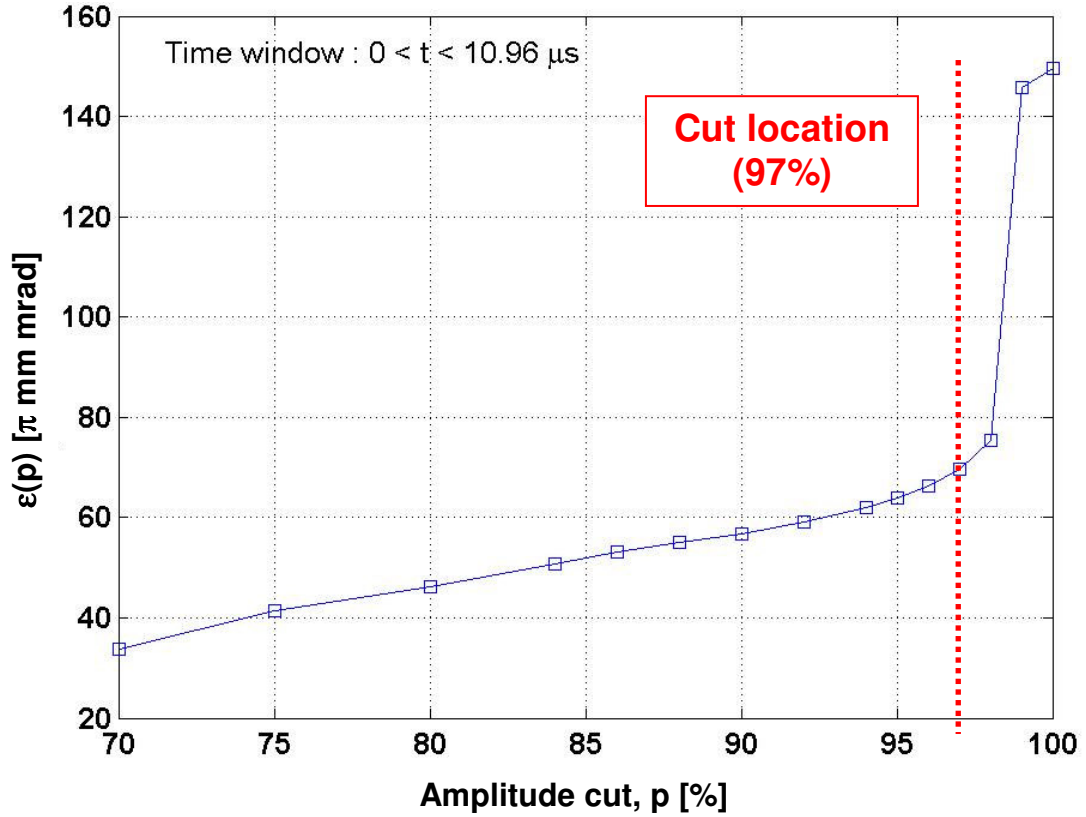
**Figure V-4**: Example of a plot of the calculated emittance versus percent of total signal included in the calculation. The red line indicates where the emittance is evaluated. The calculated emittance above 97% is dominated by noise.

Once the 'amplitude cut' chosen, the data is displayed in contour-plot form, with 10 contour levels ranging from 0% to 100% of the signal amplitude. By default, the phase-space plot includes the coherent-envelope expansion of the beam, usually with divergence/convergence angles of ±40 mrad. This is large compared to distortions at several mrad level and makes difficult to see the details of the phase-space distribution (Figure V-5(a)). For that reason, we

implement a coordinate transformation that zeroes the cross moments, and obtain the so-called 'sheared' phase-space plot shown in Figure V-5(b).
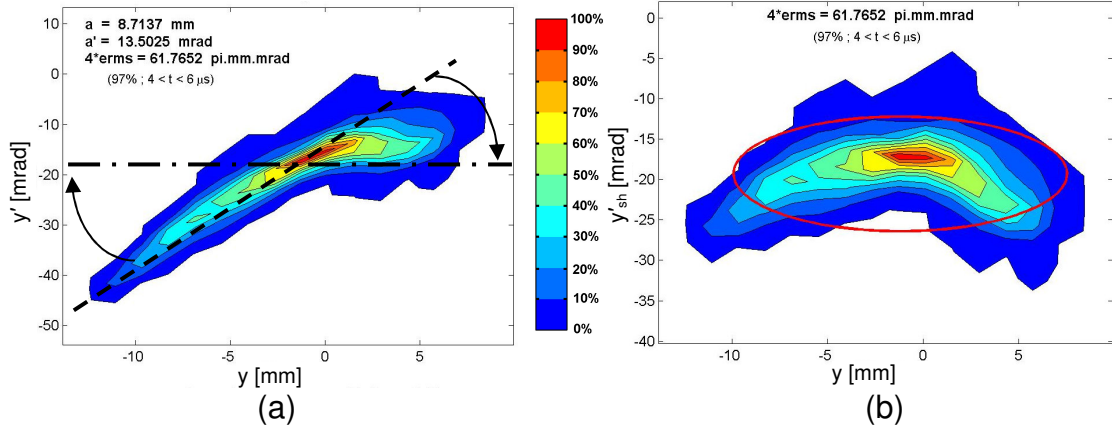


**Figure V-5**: Example of phase-space contour plots (vertical direction). In (a), the coherent envelope expansion has not been removed. In (b), the associated 'sheared' phase-space distribution is shown (the coherent-envelope expansion has been removed). The red ellipse shows the area of a uniform, RMS equivalent beam with the same emittance.

Mathematically, this transformation is expressed as:

$$x'_{sh} = x' - \left[ (x - <x>) \frac{a'}{a} \right], \qquad \text{(Eq. V-1)}$$

and similarly for the vertical ($y$) direction. This transformation preserves the local phase-space area so that distortions are clearly exposed. In addition, a red ellipse indicating the area of an RMS equivalent beam with the same emittance is plotted.

119

Finally, the crossed-slits scans that produce a transverse current-density map of the beam are either displayed as density plots (like an actual image of the beam) where the color of the individual 'pixels' (defined by the step size of the scan) is determined by the signal amplitude according to the associated color map, or as surface plots where the height of the surface corresponds to the signal produced by the incident beam current at the corresponding transverse position. In addition, the routine can step through the time slices and generate a 'movie' that illustrates the time dependent behavior of the current density.

# Chapter VI -      Injector upgrade and beam characterization at its exit

## VI.1 -      The '2 MV Injector'

### VI.1.1 -   Description of the existing '2 MV Injector'

The injector consists of a hot-surface ionization source assembly followed by a 750 kV extraction diode and by four electrostatic quadrupole accelerator (ESQ) biased to focus the beam transversely while accelerating longitudinally (2 MV) [123,127]. Figure VI-1 shows the source assembly, the gate electrode that provides the extraction and the ESQ column.
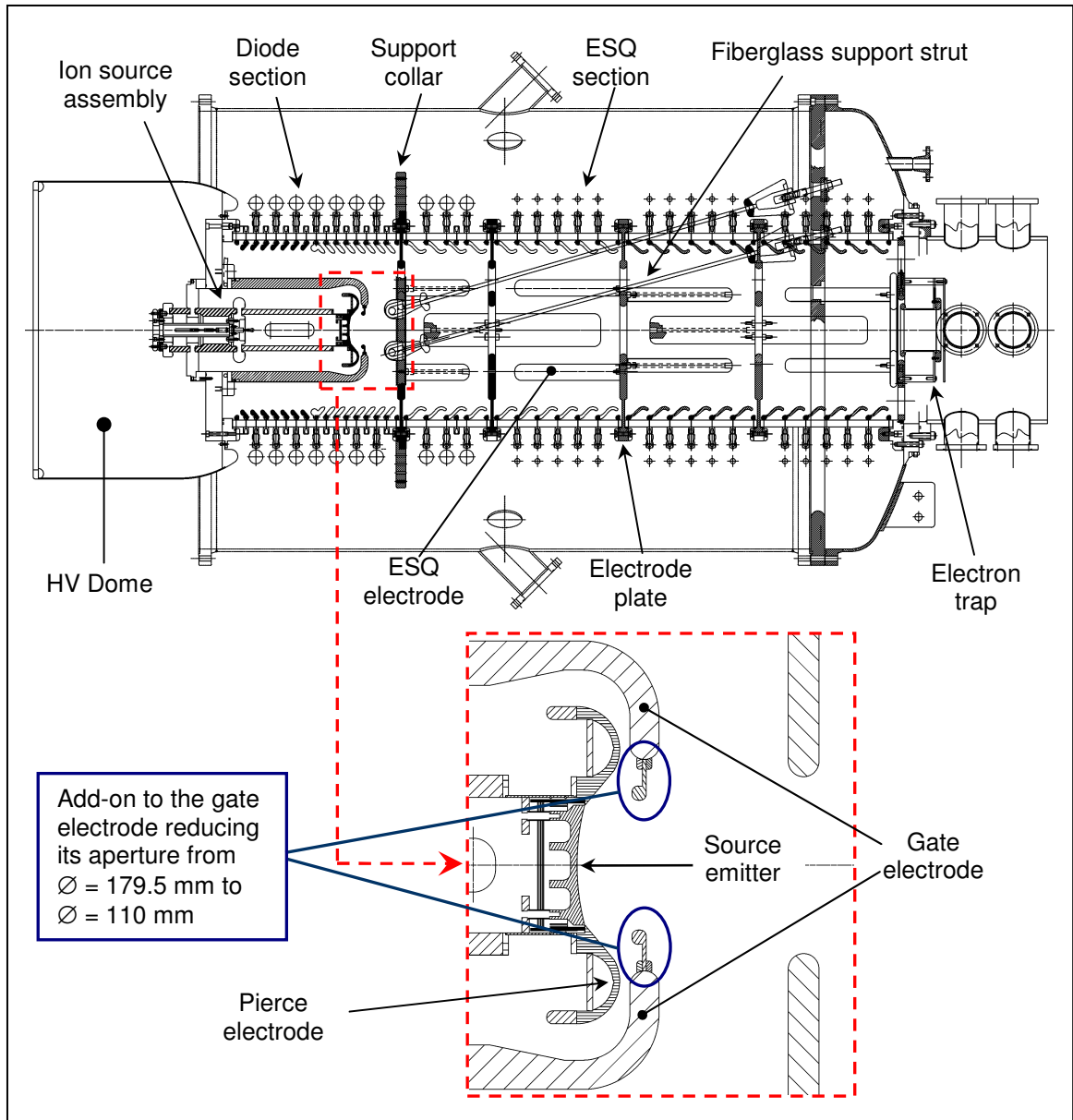
**Figure VI-1**: 2 MV Injector accelerator column showing fiberglass support struts. Column length is 2.4 meters.

It is contained inside a pressure vessel filled with a high-voltage insulating gas mixture (10% $SF_6$, 90% $N_2$). The vessel also houses 38 stages of a two-section network Marx generator, which produces a flat-top voltage pulse ($V_{Marx}$), and a

high voltage 'dome' containing the source and extraction pulse electronics (Figure VI-2).
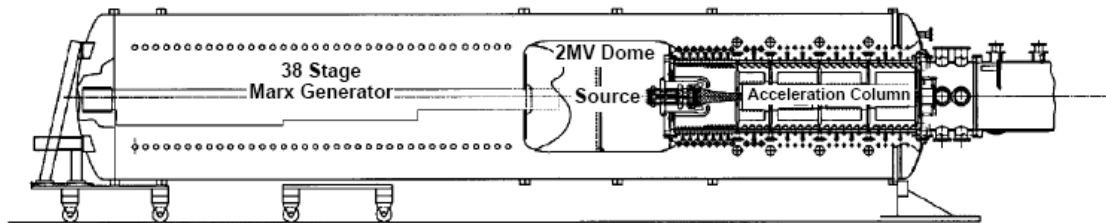


**Figure VI-2**: Overall cross-section of the '2 MV Injector' [123]. Attached to the injector (at the far right of the picture) is the D-end diagnostics tank.

The high voltage dome also houses a hydraulically driven 400 Hz, 10 kVA alternator which powers all the source electronics including the telemetry system. Voltages from the Marx circuit to the various electrodes of the diode and accelerating column are distributed via a water-based resistive divider (i.e. water resistor). The source is biased at a negative DC potential ($V_{Bias}$) and the gate electrode is at dome potential, thereby inhibiting ion emission from the hot surface. During ion extraction, the extraction circuit, which acts like a switch, delivers a pulse swing[3] ($V_{Gate}$) up to 140 kV, going from a bias voltage of -60 kV to an extraction voltage of +80 kV, applied to the source with respect to the gate electrode through a step-up transformer driven by a tunable pulse forming

---

[3] In its original configuration, the extraction circuit could deliver a pulse swing of up to 160 kV (-80 kV to +80 kV). The -80 kV power supply failed and was replaced with an available -60 kV power supply, which is sufficient for the current configuration.

network (PFN) [124,125]. The source filament transformer not only supplies the heater power (2500 Watts), but is also a high-voltage isolation transformer allowing the source to be biased at -80 kV. Trigger, timing and diagnostic information is transmitted to and from the high voltage dome by fiber optic links to provide electrical isolation. Finally, an ethernet-based instrument control system (FieldPoint™) programmed in Labview™ [126] remotely controls and monitors the power supplies' output voltages and currents. Note that the FieldPoint™ modules were not part of the original configuration described in Refs. [123,127].

To date, both contact-ionization and alumino-silicate ion sources have been used [128]. The injector beam characterization measurements and the first measurements through the transport section were made using the contact ionization source (i.e. doped source), before switching to the alumino-silicate source in April 2002. Earlier versions of alumino-silicate sources suffered from poor current density uniformity that was addressed in a source R&D effort during 2001-02 [129]. From improvements to the coating and firing procedure of the alumino-silicate paste onto the porous tungsten substrate, contact-ionization sources ultimately gave beam characteristics indistinguishable from alumino-silicate sources based on single-slit current-density profile and transverse phase-space measurements made further downstream (matching section exit), thus showed that beam nonuniformities are due to optics, rather than source emission irregularities. Present work is being carried out with long life alumino-silicate sources to avoid rapid depletion problems (~20 hours) associated with doped contact ionization sources that complicate data interpretation.
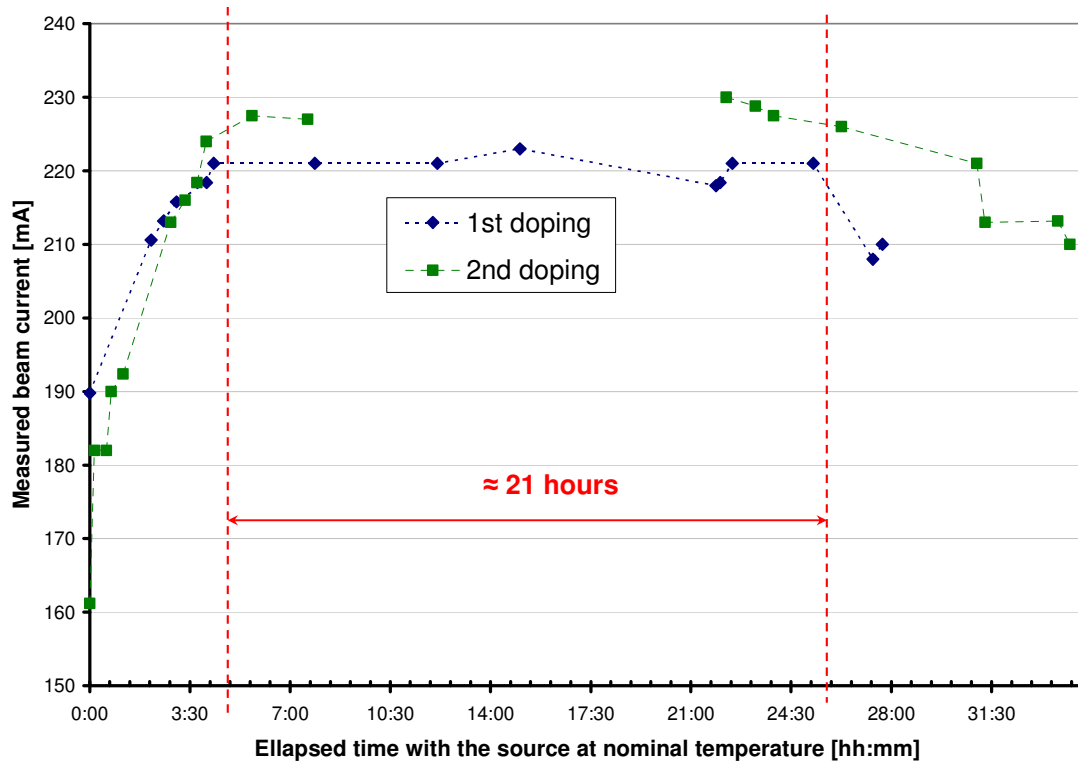
**Figure VI-3**: Doped contact ionization source lifetime. The beam current measured at the exit of the injector is plotted against the time when the source is hot. Two successive doping cycles are shown (blue: first doping; green: second doping).

The doped source lifetime (per doping) is illustrated on Figure VI-3. For about the first four hours of operation, the beam current increases as diffusion processes take place until the space-charge limited current is reached. After 18 to 21 hours, depending on the doping, the beam current starts decreasing from the space-charge limit which insures that the beam dynamics in the gun are reproducible.

The lifetime of the current aluminosilicate source is not known, but no signs of depletion have been observed so far (after 1 year of operation). A more detailed discussion of the doped and aluminosilicate sources can be found in Ref. [130].

## VI.1.2 -   *Motivations for the injector upgrades*

Previous experiments with the Injector have produced up to 0.8 A of $K^+$ ion beam at 2.0 MV by using a 17-cm diameter contact-ionization source [131]. However, the beam current-density distribution was hollow, inducing significant space-charge nonuniformities (i.e. nonlinear self fields). When injected into a linear transport channel, such distributions are far from an equilibrium condition (i.e. where particles are in local force balance) and consequently generate a broad spectrum of collective, space charge driven oscillations that can lead to emittance growth during the relaxation process and render the interpretation of the downstream transport experiments much more difficult [132,133,134,135]. The pulse length was also too short for the HCX specifications and needed to be extended significantly to study beam degradation over several microseconds due to the buildup of gas, secondary ions and electrons. This work (and an overall upgrade of the injector system) was performed in 1999-2001 and was successful at delivering a more uniform beam suitable for downstream experiments. A description of the main improvements follows.

## VI.2 -   Early injector upgrades required for HCX scientific goals

### VI.2.1 -  *Beam pulse extension*

In its original configuration, the '2 MV Injector' delivered a 1 µs square pulse and was soon after extended to 2 µs. However, growing interest in investigating long-pulse effects led to another, more significant, extension of the beam pulse. This took place in two steps. First, the Marx voltage pulse length was increased, then the extraction voltage pulse ($V_{Gate}$) was extended.

The Marx voltage pulse length increase was achieved by adding magnetic coupling between the two capacitive legs of the original electrical circuit on each tray [136]. As a result, the theoretical model predicts that the flat portion of the pulse to 99.7% of the peak voltage would increase from 2.1 µs to 4.4 µs and from 3.2 µs to 5.2 µs at the 99% level [137]. In practice, the final Marx voltage pulse is flat within 1% over 4.2 µs and within 2% over 5 µs. Due to this pulse extension, at a fixed charge voltage, the flattop output voltage was reduced by about 6%.

The extraction pulse extension required building a new PFN with additional capacitors and resistors. A new extraction transformer was also necessary to deliver the required volt-seconds. The resulting pulse length was 4.5 µs, up from ≈2.5 µs initially [137], corresponding to a beam pulse length of 4 µs, up from 2 µs. Note that tuning of the PFN (rise time and pulse flatness) is accomplished by sliding inductor sections on a common support tube to adjust their mutual inductance.

The resulting Marx and gate pulses are shown on Figure VI-4.
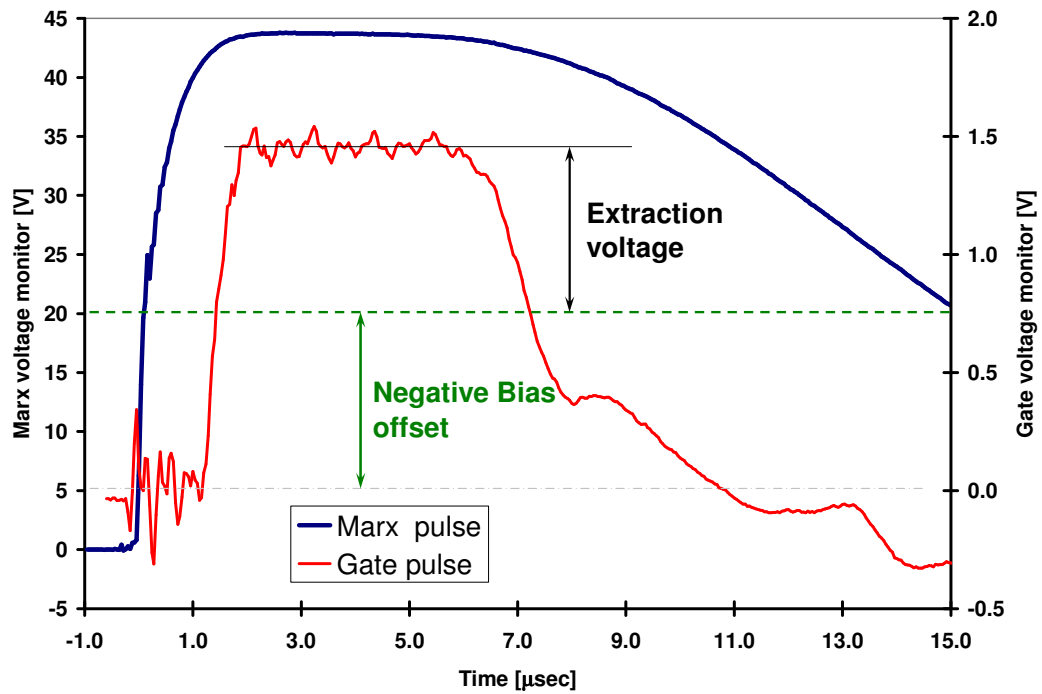
**Figure VI-4**: Typical Marx (blue) and gate (red) pulses. The Marx voltage is viewed through a capacitive monitor, with gain 21.4 kV/V. The gate voltage is viewed through a resistive divider and an optical link. In green, we show the negative DC bias that is applied to the source. The ripples seen on the gate voltage early and during the flattop are due to electrical noise picked up on the cables when the trigger chassis of the Marx generator fires.

The relative timing between the two pulses is initially set such that ion extraction occurs during the flat portion of the Marx voltage pulse. However, as much as 2 µs time jitter was observed due to spark gaps in both the Marx and extraction triggering circuits. The time delay between the Marx voltage pulse and the extraction voltage pulse is monitored as described in Section - V.2 -. A ≤ 0.5 µs

jitter is allowed. The contribution to the relative jitter from the Marx pulse is removed by triggering the extraction pulse from a pickup of the Marx HV pulse. Fortuitously, the Marx column generates noise with the appropriate delay to reliably trigger the extraction voltage. At other times, this noise is not sufficient to trigger the extractor reliably. A delay circuit in the dome triggered via an antenna to pick up the Marx pulse is recommended as a permanent solution.

### VI.2.2 - *Improved reliability*

Over the two-year upgrade, various actions were carried out to improve the overall reliability of the operation of the '2 MV Injector' [138]. The main improvements came from reducing the number of high voltage breakdowns in the Marx generator (pressurized tank) and in the extraction region (vacuum tank) that eventually cause electrical and mechanical failures.

In order to hold voltage at the megavolt level, the Marx generator was originally pressurized with pure $SF_6$ gas. For economic reasons, $SF_6$ was replaced with $CO_2$, which is less efficient and generates some sort of dust micro-particles when breaking down [139,140]. A mixture of $N_2$ gas and $SF_6$ ($\approx 10\%$) was finally adopted. This combination is a good electrical insulator and helps keep the Marx trays clean, even when breakdowns occur.

In the early design of the source assembly, the Pierce electrode [141] was fabricated of graphite due to ease of machining. Because of the confined geometry in the diode (making pumping inefficient) and the relatively high outgasing rate of graphite, the vacuum deteriorates when the source was hot, resulting in frequent high voltage breakdowns. During operation, the predominant

residual gas species were $CO/N_2$, $CO_2$, $H_2O$ and $H_2$ [138]. Switching to a copper electrode improved the vacuum level by almost an order of magnitude, significantly reducing the number of high voltage break downs in the diode and eliminating residual $CO_2$. Moreover, breakdowns of the graphite electrode generated carbon dust in the vacuum system that deposited on the various electrodes and required frequent cleaning. The copper electrode eliminated the need for cleaning.

Finally, many of the electronics components were replaced or refurbished and rearranged.

## VI.3 -   Beam measurements and consequences

### VI.3.1 -   Current-density measurements

Since spherical aberration occurs near the edge of the emitter, is more pronounced when the source radius is large and because of a high current-density spike in the center of the beam, a first iteration for improving the beam optics in the injector was to reduce the source diameter from 17.0 cm to 10.0 cm. Once installed, two-dimensional time-dependent profiles of the current density (i.e. current-density maps) 23.2 cm from the emitter surface were measured [142] (Figure VI-5(a)) using the 32-channel Faraday cup [99] described in Section - III.4.1.3 -.
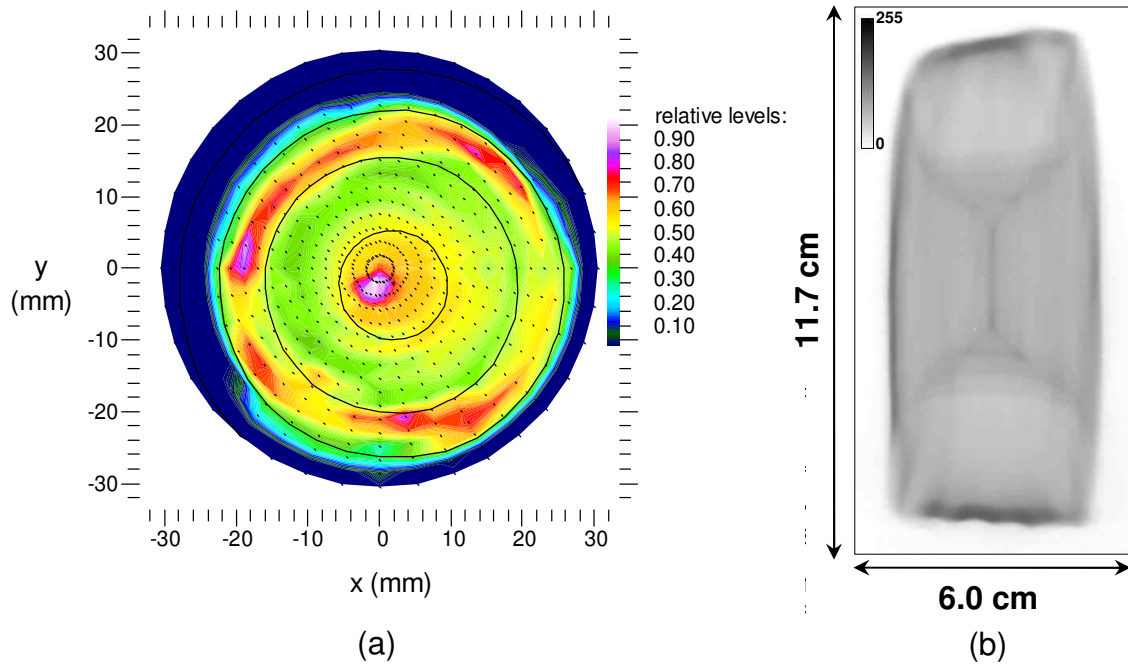
**Figure VI-5**: (a) Contour map of the beam current-density profile 2.54 cm downstream of the gate electrode for the 10.0 cm diameter contact-ionization source. Intensities are the mean of a 1.2 μs window taken in the middle of the 4.5 μs pulse [142]. (b) Kapton film image taken at the exit of the injector (time integrated).

The two main features are the central density peak and the high density rim near the beam edge. By integrating the measured signals in Figure VI-5(a), the remaining central peak represents ≤ 1% of the total beam current. The outer rim leads to a hollow beam that persists to the exit of the injector system. This is evident in Figure VI-5(b) or in single-slit current-density profiles (Figure VI-6). In

Figure VI-5(b), dark regions, resulting from degradation of the Kapton film by the incident ions, represent high current density [101].
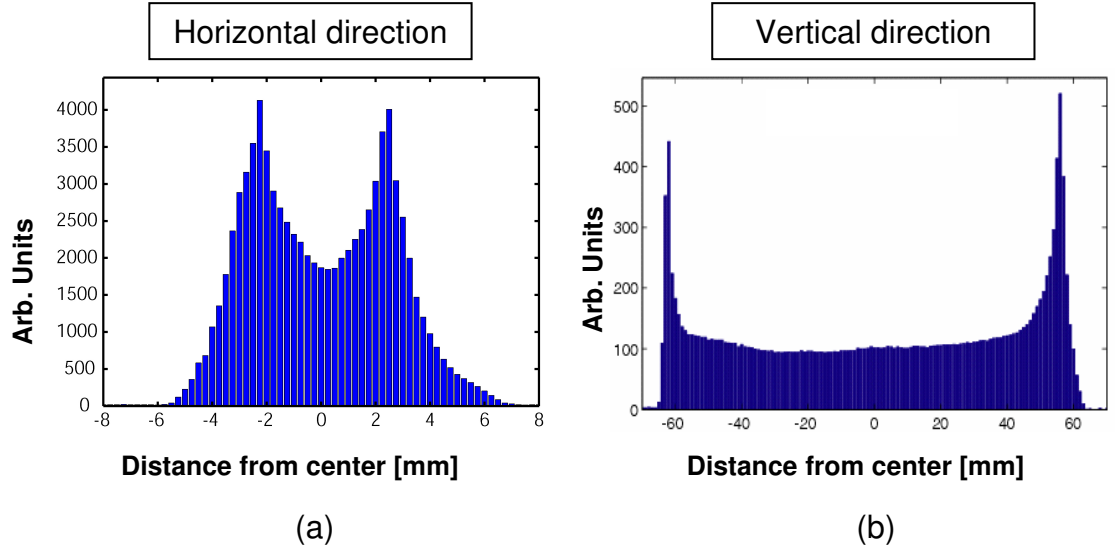


**Figure VI-6**: Single-slit current-density profiles: (a) horizontal direction; (b) vertical direction. The single slit profiles are time-resolved and a single time slice ($\Delta t = 0.16 \, \mu s$) taken in the flattest portion of the beam pulse (4.96 $\mu s$ after turn on) is shown here. The step-size is 0.25 mm for the horizontal profile and 1 mm for the vertical profile. Horizontal and vertical profiles are measured 20.5 cm and 22.6 cm downstream of the Kapton film location, respectively.

Since the Kapton film image is time-integrated, additional time-resolved measurements, such as the single-slit current-density profiles of Figure VI-6, are needed to identify the time of the features in the Kapton image. Stepping through time slices of the transverse current-density profiles shows that some of the structures in the center of the beam (Figure VI-5(b)) occur only at the head (i.e. beginning) and the tail (i.e. end) of the beam pulse. The single time slice shown

in Figure VI-6(b) indicates that in the middle of the pulse the current density of the beam remains nearly constant except at the edges. Due to having different current and energy from the main part of the pulse, the head and tail of the beam have very different dynamics than the middle of the beam pulse (See Section - X.3 -)

### VI.3.2 - *Phase space measurements*

In addition to current-density measurements at the diode and at the exit of the injector, the phase space distribution of the beam was measured and is shown on Figure VI-7.



(a)   (b)
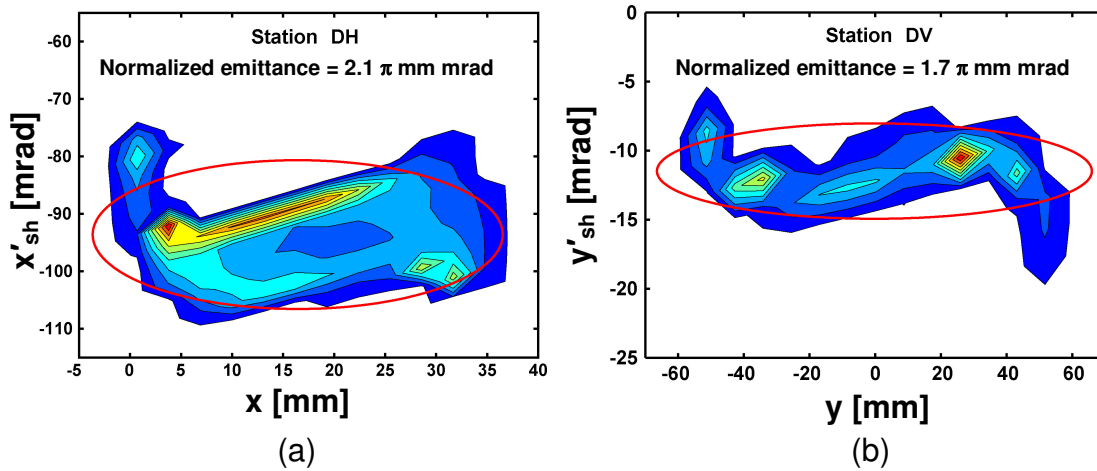
**Figure VI-7**: Emittance diagram (sheared) taken at the exit of the injector; (a) $x - x'$ (horizontal direction), (b) $y - y'$ (vertical direction). Note that on (a), the large apparent centroid offsets is due to an uncertainty in determining the center line of the channel. Data have been summed over two time slices ($\Delta t = 0.32 \, \mu s$) for the horizontal direction and over three time slices ($\Delta t = 0.36 \, \mu s$) for the vertical direction, both 3.36 µs after the turn on of the beam pulse. The sampling

intervals are: 3.1 mm and 3.3 mrad for the horizontal scan, and 8.6 mm and 2.3 mrad for the vertical scan.

The normalized emittance is large in both planes (>1 $\pi$ mm mrad), in particular due to the large phase-space distortions ('hooks' at large values of $x$ or $y$). In the horizontal direction, the width of the distribution ($\approx$ 20 mrad) is consistent with the fact that the beam is compressed and therefore hotter than in the vertical direction. Note that the red ellipses indicate the area of an RMS equivalent beam with the same emittance.

### VI.3.3 - Consequences

Simulations, in which the beam edge clearance to the electrodes is increased, have shown that the square shape observed at the exit of the injector system (Figure VI-5(b)) is indicative of the chromatic aberrations [143] due to the so-called 'energy effect' [144]. The cause of the energy effect is that, in a strong quadrupole field, ions at the beam edge will have energies very different from those on the axis, which in turn lead to a spread in betatron motion and it results in kinematic aberrations. These kinematic aberrations also lead to the large phase-space distortions shown in Figure VI-7 [145]. Because particles located in the hooked region of the phase-space can lead to emittance growth or large collective particle oscillations that can drive beam halo and thereby cause particles to be lost to the walls, more modifications were required.

## VI.4 - Diode modification and beam characterization

To further improve the gun optics, the extraction electrode aperture diameter was decreased from 179.5 to 110.0 mm (its current diameter) by adding a steel annulus to the inner diameter original electrode (Figure VI-8) and the accelerating gap was shortened by 2.7 cm.
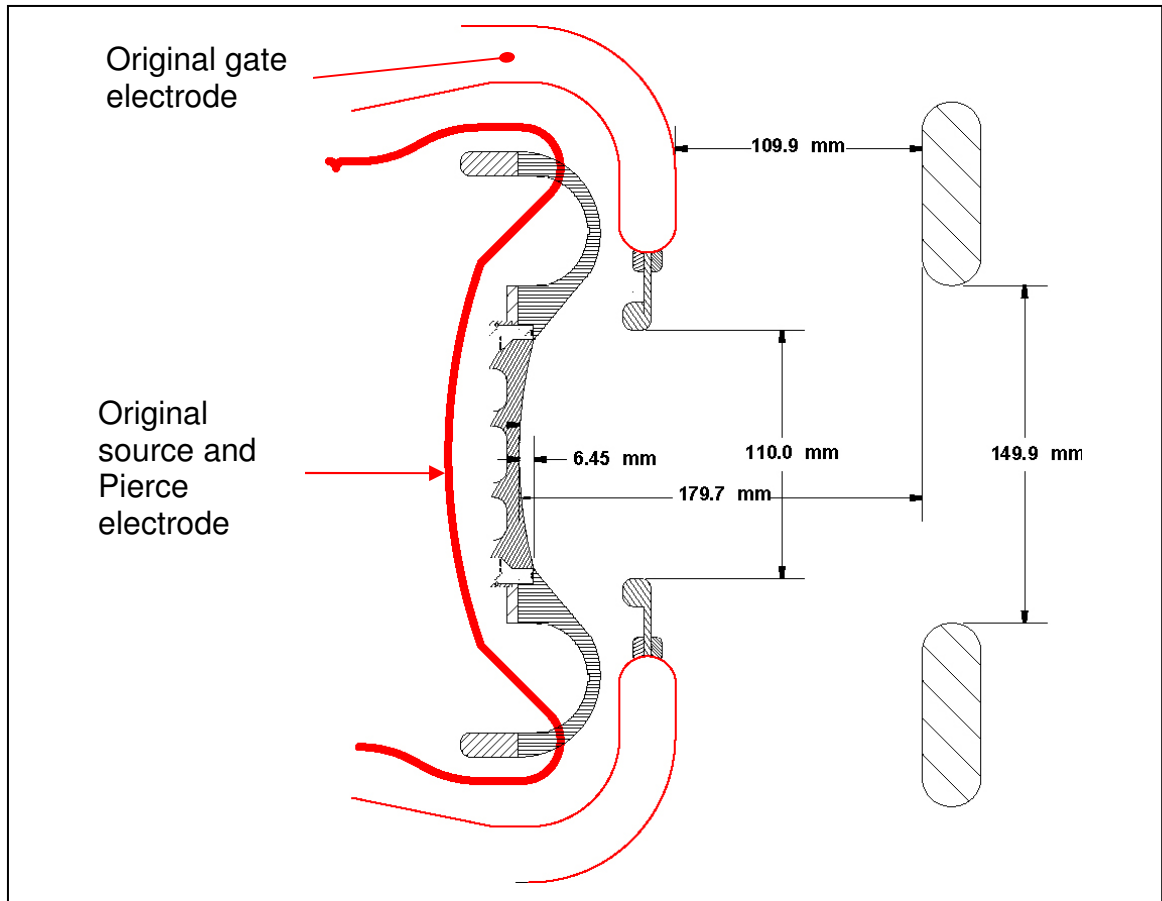


**Figure VI-8**: Mechanical drawing of the new injector gun design (smaller source, new Pierce electrode and modification to the gate electrode) superimposed with the old injector gun design (red) showing the different geometries.

These modifications were intended to reduce the chromatic aberrations (driven by space-charge) [125] and increase the clearance between the edge of the beam and the electrodes in the accelerating column. The latter reduces the influence of beam image multipoles that can lead to phase-space distortions and emittance growth [125].

### VI.4.1 -   *Beam characterization for HCX*

After the diode was modified, the transverse phase-space of the beam exiting the injector was characterized including measurements with the Kapton film, single-slit profiles and phase-space scans. Figure VI-9(a) shows the Kapton image of the beam after the final optimization and reveals a more uniform beam current distribution than in Figure VI-5(b). The 1.5-1.8x enhancement in current density previously observed (Figure VI-5) near the horizontal beam edge is absent, and the ≈3x enhancement previously observed in the vertical beam edge has been reduced to 1.6x. Additionally, the overall size of the beam is more suitable for further manipulation downstream.
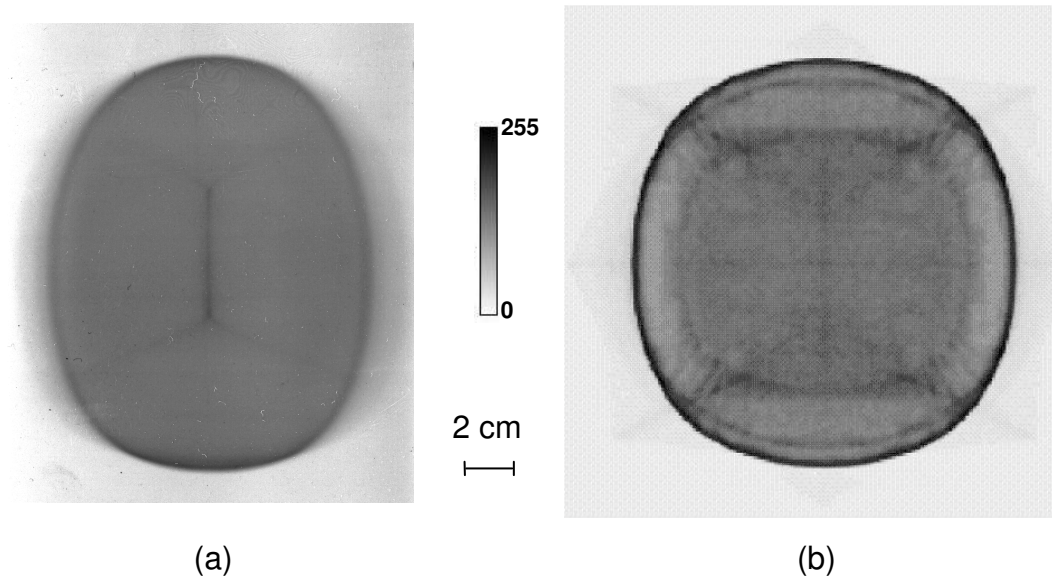
**Figure VI-9**: Images of the beam at the exit of the injector, (a) Kapton film image taken after the diode final optimization, (b) Corresponding image obtained from time-dependent WARP PIC simulation (shown on the same scale) [147]. The simulation integrates the signal collected over a full pulse to create a comparable image. The internal structures observable in (b) are found to derive mostly from the far tail of the pulse since the tail is not gated and is long.

The good beam uniformity is more apparent when looking at single-slit current-density profiles, excluding the head and tail of the pulse which are expected to be not as uniform as the middle time slices (Figure VI-10). In particular, the large rims observed in the vertical profile in Figure VI-6(b) have totally disappeared.
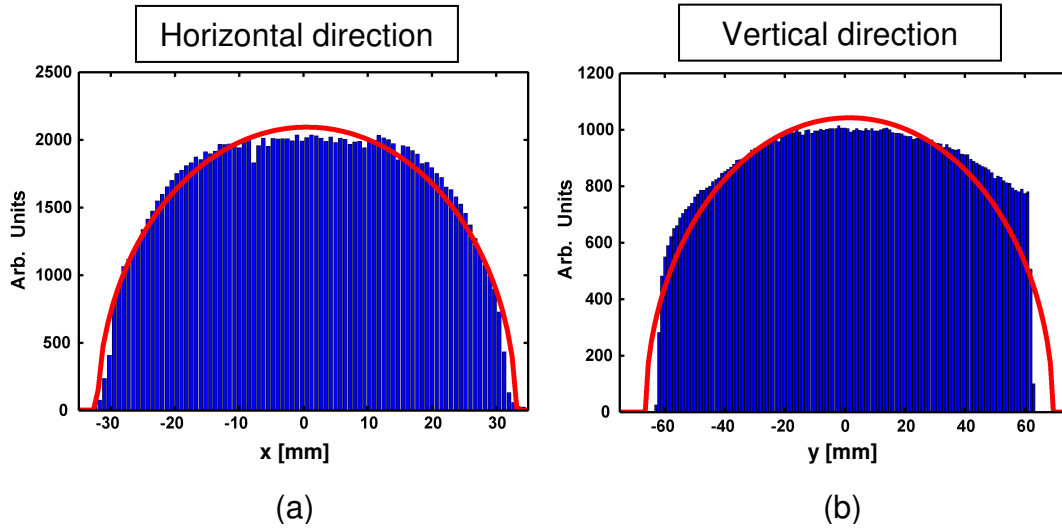
**Figure VI-10**: Single-slit current-density profiles taken at the exit of the injector after final optimization of the diode: (a) Horizontal profile, (b) Vertical profile. The red curve is the profile of a uniform density beam with the same RMS beam size as the data. Data shown here have been summed over 12 time slices ($\Delta t = 1.44~\mu s$), corresponding to a portion of the beam pulse flattop, 2.4 $\mu s$ after the start. The step-size is 0.75 mm for the horizontal profile and 2 mm for the vertical profile.

On Figure VI-10 are also plotted (in red) the profiles that one would obtain if the beam was uniform. The agreement with the data is excellent in the horizontal direction and somewhat less in the vertical direction, where the rate of fall off at the edge is faster for the data than for the calculated profile, because of the remaining enhancement of the edge that can be seen on the Kapton image but also partly because the beam is not exactly elliptical.

Figure VI-11(b) shows the corresponding phase-space measurement in the vertical direction, where the hooking is significantly reduced compared to Figure VI-7(b). The injector diode retrofits decreased $\varepsilon_n$ from 1.7 to 0.9 $\pi$ mm mrad in the vertical direction and from 2.1 to 0.5 $\pi$ mm mrad. The theoretical minimum based on the emitter size (radius = $R$) and temperature ($T \approx 1100\,°C$) is

$$\varepsilon_n = 2R\sqrt{\frac{kT}{m}} = 0.18 \ \pi \text{ mm mrad.} \qquad \text{(Eq. VI-1)}$$



(a)

(b)
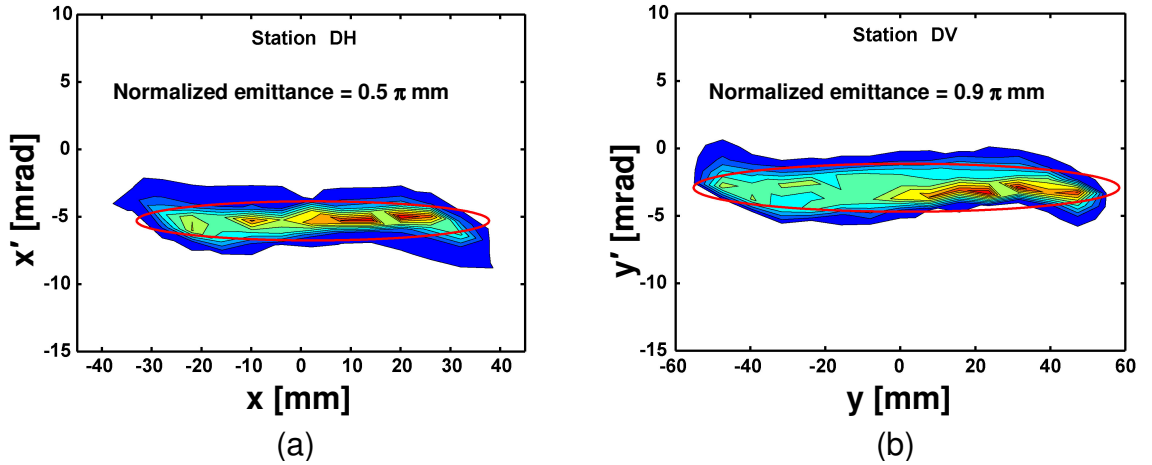
**Figure VI-11**: Emittance diagram (sheared) taken at the exit of the injector system after optimization of the injector diode; (a) $x - x'$ (horizontal direction), (b) $y - y'$ (vertical direction). Data shown here have been summed over eight time slices ($\Delta t = 0.96$ μs) corresponding to the flattest part of the beam pulse (3.12 μs after start). The sampling intervals are: 6.2 mm and 0.9 mrad for the horizontal scan, and 7.6 mm and 1.1 mrad for the vertical scan.

So far, most measurements have been made at 1.0 MeV. Future measurements will establish operating experience at higher injection energy (i.e. 1.5 to 1.8 MeV). Reliably running the experiment at beam energies higher than ~1.5 MeV is not practical until the water resistor utilized for resistive grading of the voltage divider of the high-voltage accelerating column is modified. It was found that, at the high pressures required to hold voltage at the 1.5 to 2 MV level (about 80 psi in the injector pressure vessel), the water resistor tube, typically having an inlet pressure of about 80 psi and a pressure drop of about 40 psi, would partially deform under the pressure load, affecting the voltage division along the accelerating column and modifying the injector optics [146]. Beam measurements are then not reproducible. Nevertheless, the Marx column has operated at 1.8 MV during checks of the injector optics modifications.

### VI.4.2 - *Comparisons to simulations and discussion*

VI.4.2.1 - Beam distribution and envelope parameters

For each case, self-consistent time-dependent PIC simulations were performed [147] and comparisons with the data (Figure VI-9 and Figure VI-12) show qualitative agreement in the shapes of the distributions.

In particular, Figure VI-9(b) was generated from a 3-D time-dependent WARP PIC calculation that followed the head and the tail of the beam for direct comparison with the Kapton film data and show similar patterns within the core of the beam.
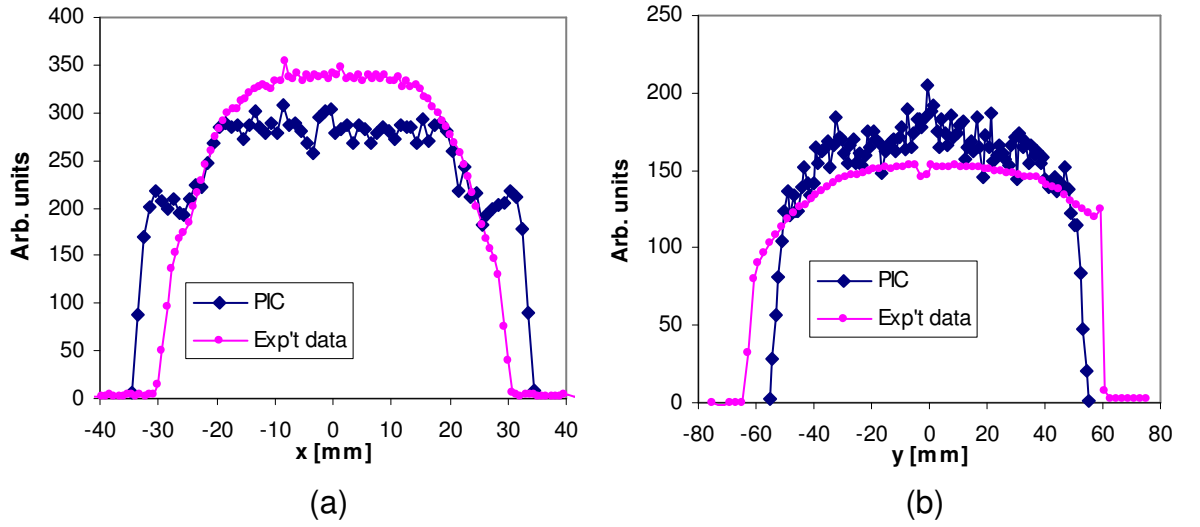
**Figure VI-12**: Single-slit beam profiles (a) in the horizontal direction (b) in the vertical direction at the injector exit. In blue is the simulation (PIC) and in pink is the experimental data (single time slice ($\Delta t = 0.12$ µs) taken 3.84 µs after turn on of the beam current pulse). Vertical scale is normalized such that the integration is identical for both the PIC run and the experimental data.

The envelope parameters measured in the experiment cannot be entirely reproduced in the simulations. They differ by as much as 30% (for the horizontal convergence angle) from experiment. However, qualitative trends and scalings are found to be consistent. Theoretical sensitivity studies made for the original design of the injector gun showed that geometric deformations of the anode (i.e. the emitting surface), extraction voltage errors, or imperfect emission can all lead to very different beam current-density distributions and therefore very different beam dynamics in the ESQ section, which could explain the differences we observe.

### VI.4.2.2 - Beam current and subsequent gate voltage calibration

During the checks of the injector optics modifications, extracted beam current, $I_B$, of up to 380 mA at a beam energy $E_B$ = 1.5 MeV and $I_B \approx$ 600 mA at $E_B$ = 1.8 MeV were measured. Earlier reports [125] indicated as much as 20% more beam current calculated with WARP compared to the beam current measured in those experiments. Since $I_B$ is sensitive to the applied extraction voltage the calibration procedure for the gate electrode was improved [148] and is described in Appendix A. The effective extraction voltage uncertainty from this procedure is ±5%. With the gate electrode voltage thus calibrated, the experimental current falls within 10% of the expected value based on WARP 3-D PIC simulations. For future experiments at 1.8 MeV, to maintain similar beam dynamics (i.e. same ion trajectories) as our 1 MeV measurements, we expect to extract 442 mA (scaled from $I_B$ = 183 mA at $E_B$ = 1 MeV). At higher extraction voltages and $E_B$ = 1.8 MeV, the Injector could deliver at least 600 mA without scraping in the ESQ section.

### VI.4.2.3 - Conclusion

The envelope parameters' inconsistencies observed at the exit of the Injector will be explored with further measurements and simulations on HCX and other dedicated test stands [149], where detailed diagnostics near the source can be more easily carried out. However, the beam emittance is low and the distribution is adequate for the experimental agenda.

# Chapter VII - Beam preparation for periodic transport in the electrostatic lattice

## VII.1 - The matching section and diagnostics

### VII.1.1 - Introduction

The matching section is designed to compress the beam area transversely by a factor ≈25 and produce the matched beam parameters for periodic transport in the electrostatic lattice, while limiting the emittance growth and phase-space distortions.

### VII.1.2 - Description of the matching section

The matching section was installed after the beam transverse distributions at the exit of the injector were characterized in detail since, once the matching section in place, the beam can not be diagnosed before it exits it and enters the electrostatic transport section where the first electrostatic quadrupole (QD1) can be taken out of the way and diagnostics inserted.

The matching section consists in six electrostatic quadrupoles which bores' radii go from $r_{ap}$ = 100 mm (QM1) to $r_{ap}$ = 31 mm (QM6) (Figure VII-1 and Figure VII-3).
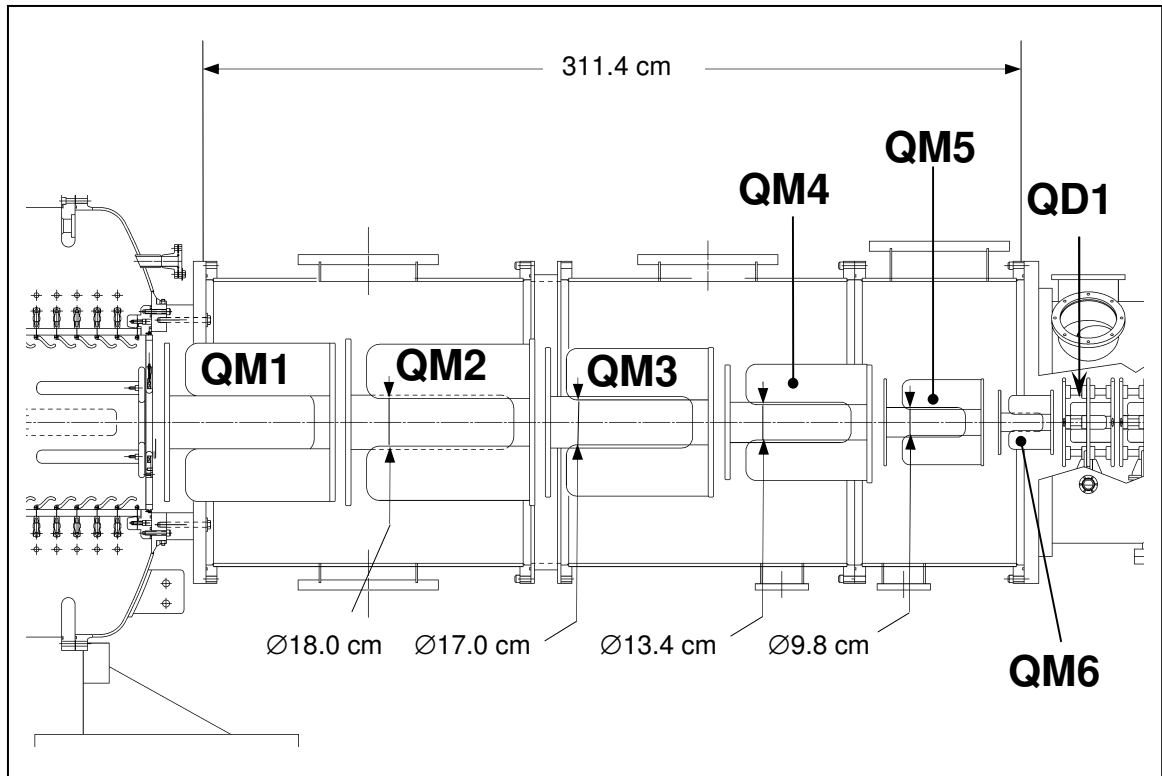
**Figure VII-1**: Mechanical drawing (elevation view) of the matching section. On the left is the injector. On the right is the first quadrupole of the transport section (QD1) which is movable to allow room for diagnostics.

Each quadrupole is independently energized and the power supplies remotely controlled and monitored via an ethernet interface. Matching quadrupole voltages range up to ±43 kV for $E_B$ = 1.0 MeV, and focusing gradients up to 9 kV/cm². (Experiments at higher injection energy will require proportional increase in the quadrupole potentials for an identical envelope solution.) Note that the individual HV feedthroughs are rated to 150 kV. One HV feedthrough (Figure VII-2) supplies voltage to two quadrupoles via coaxial conductors added to the structure.
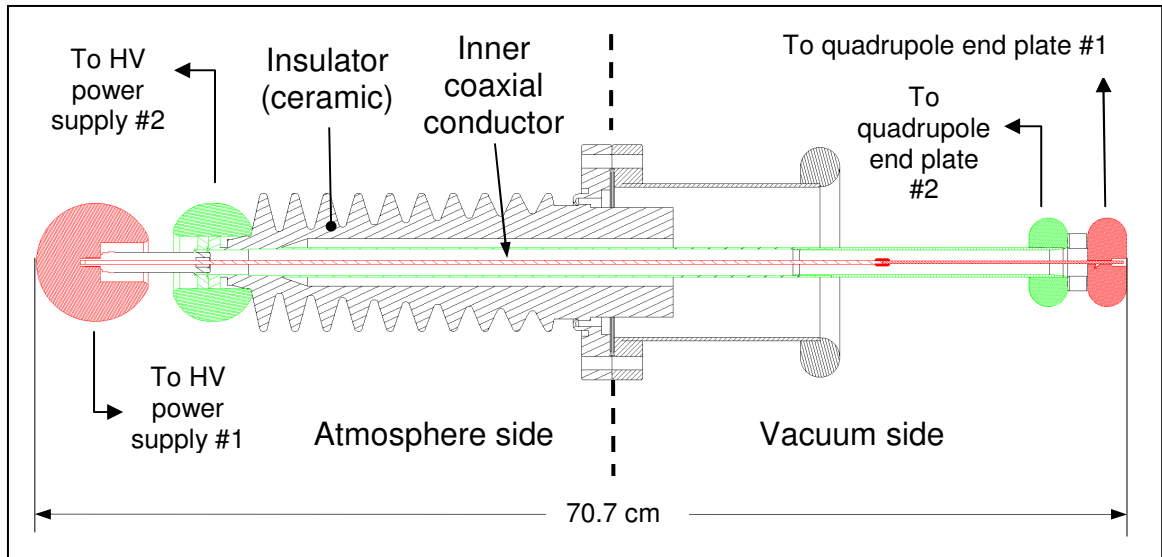
**Figure VII-2**: Feedthrough assembly mechanical drawing. The parts in red and green represent parts electrically connected, forming two independent circuits. For the green circuit, there is a coaxial conductor running along the insulator wall (not shown in the drawing).

Thus each feedthrough assembly feeds adjacent quadrupoles in the vacuum tank and to prevent breakdowns the voltage difference between the quadrupoles is limited to 20 kV. This provides ample flexibility for various matching envelope solutions.

Due to residual misalignment of the source in the diode region, non-uniformities in the source's current-density distribution and alignment of the focusing elements of the injector and matching section, the centroid undergoes betatron oscillations through the quadrupoles of the matching section. QM4-6 may each be moved in the horizontal and vertical directions by ±15 mm to correct the beam centroid offset.

145
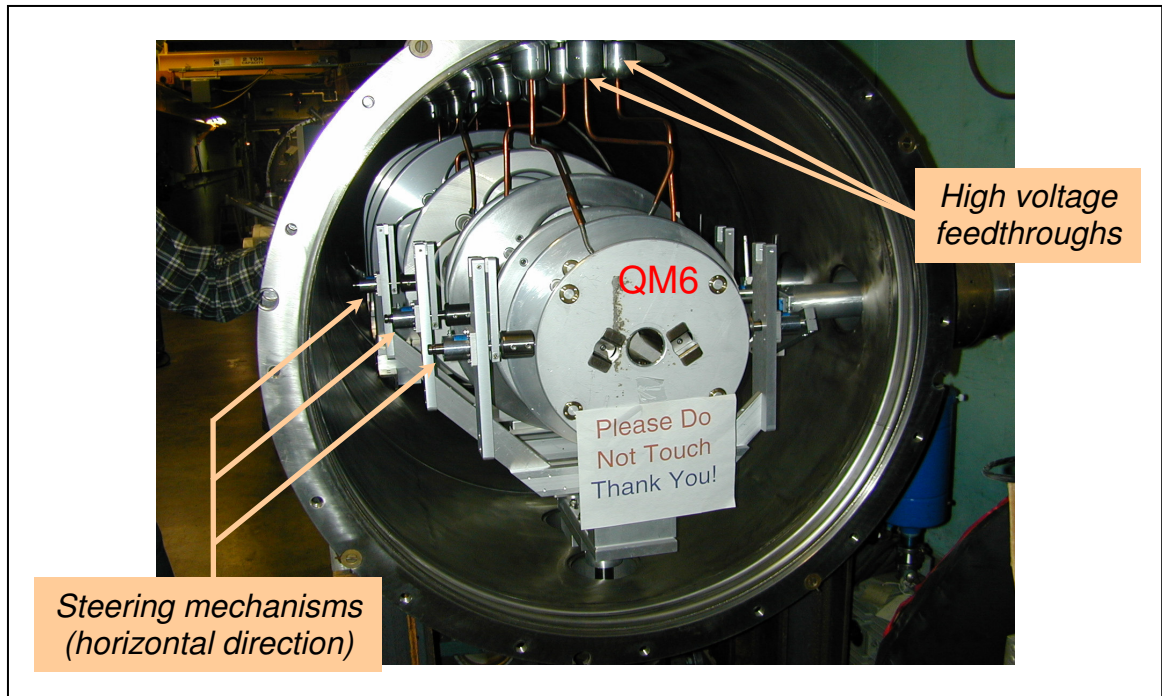
**Figure VII-3**: Photograph of the matching section quadrupoles.

### VII.1.3 - The QD1 diagnostics station

Diagnostics at QD1 comprise a deep Faraday cup, a Pearson current monitor and two mechanical slit scanners (one in the horizontal direction, one in the vertical direction). The arrangement of the different diagnostics is pictured on Figure VII-4.

**Whole beam Faraday cup**

**Pearson current monitor**

**Vertically driven slit # 1**

**Vertical slit # 2 (& collector)**

**Horizontally driven slit # 1**

**Horizontal slit # 2 (& collector)**

SIMPLFD REP: NO_TANK_WALL
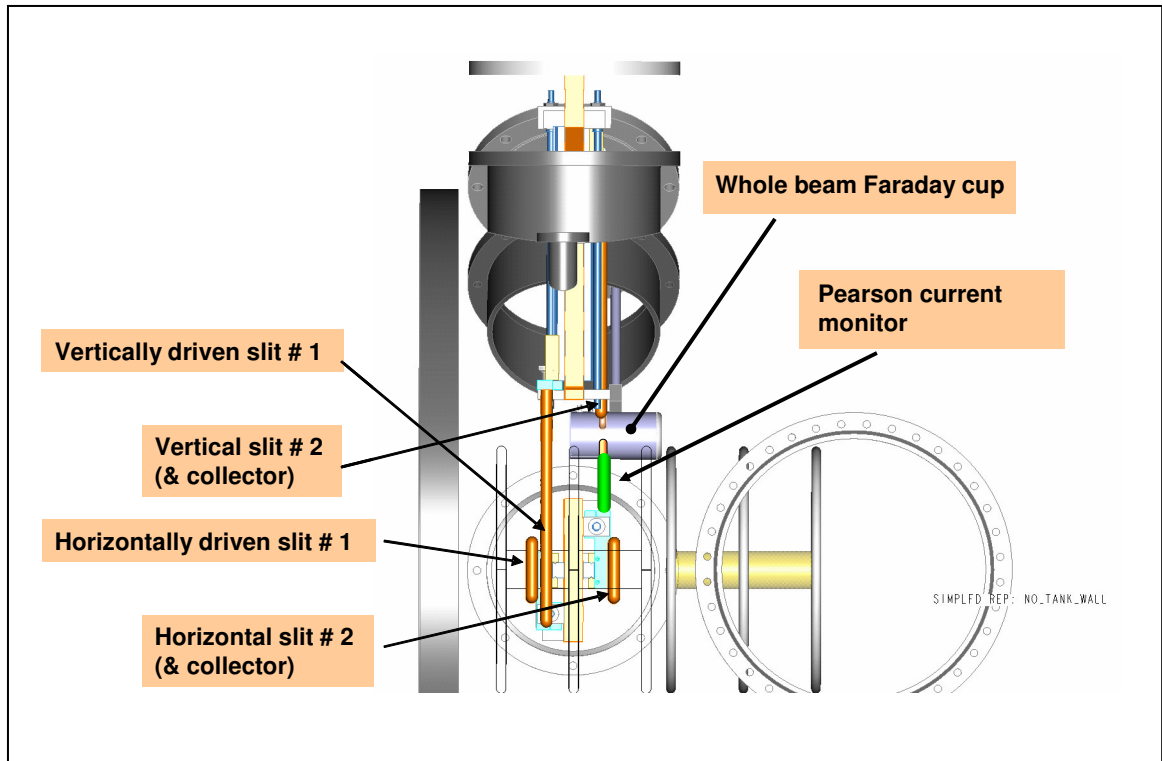
**Figure VII-4**: CAD drawing of the diagnostics at QD1.

Figure VII-5 displays some photographs of the QD1 diagnostics station. The current monitor is mounted on the same mechanical drive as the Faraday cup.
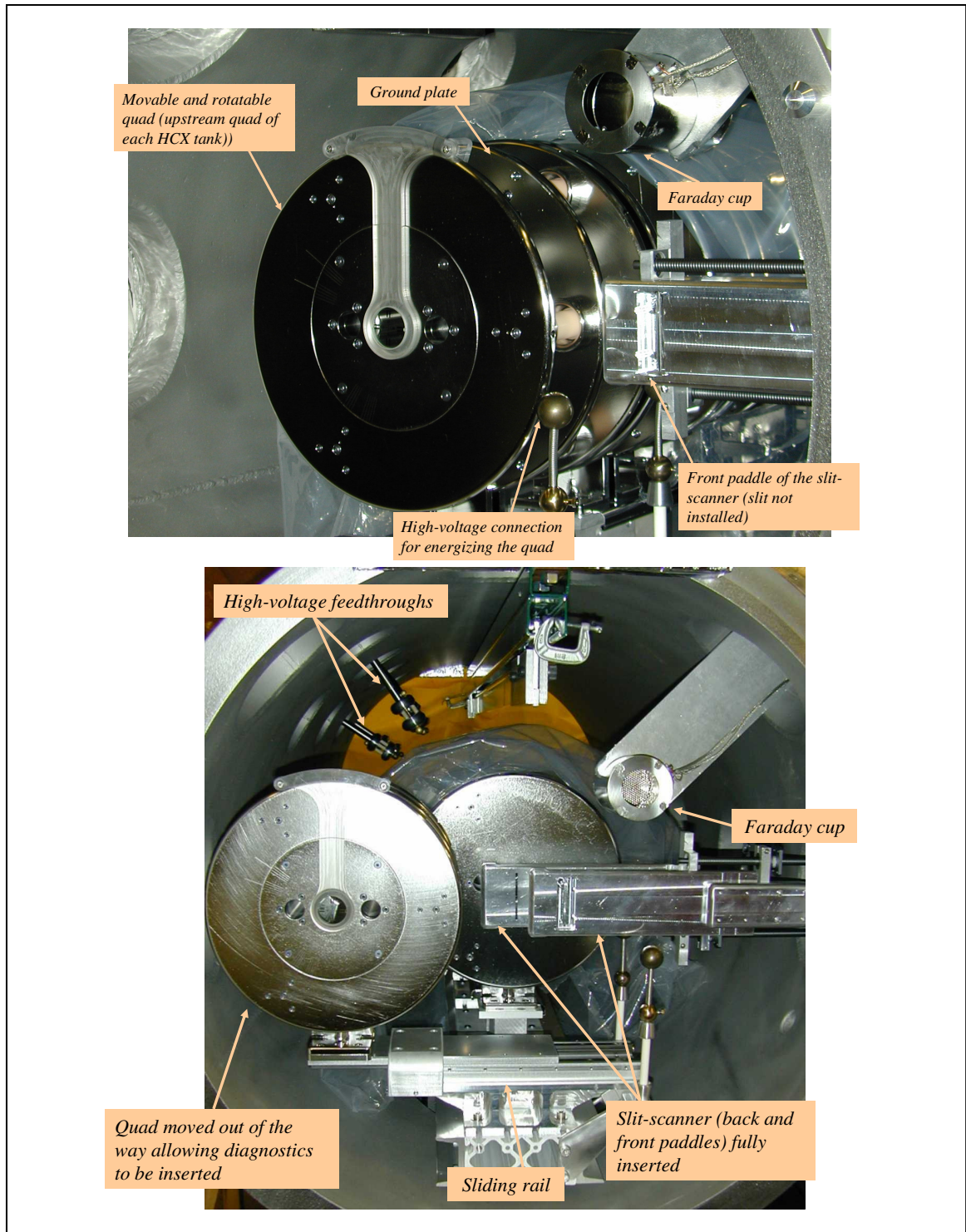
**Figure VII-5**: Photographs of the QD1 diagnostics station when the diagnostics are parked (top) and when they are inserted in the beam path (bottom). (Photos taken before installation of the current monitor)

148

This set of diagnostics allows us to measure the beam before it enters the transport lattice. We use these measurements to ensure that the beam parameters are matched for transport downstream, and as a reference to which downstream measurements will be compared.

## VII.2 -    Beam control

As a starting point, envelope calculations (with hard edge focusing elements) initialized with the measurements made at the exit of the injector determined the quadrupole voltages to be applied in the experiment in order to reach the required beam parameters at the entrance of the transport channel. Unfortunately, with the prescribed voltages, we were unable to transport the beam through the matching section without severe beam loss. Empirical adjustments of the voltages and quadrupole offsets improved the transmission to 85%-90% but the envelope parameters measured at QD1 remained far from the predictions.

### VII.2.1 -  Verification of the quadrupoles' focusing strengths

Once most of the beam was successfully transported through the matching section, we were able to determine whether the focusing strengths of the quadrupoles were in agreement with our expectations. As mentioned in Section - II.1.9.2 -, the beam centroid motion is governed by the equations of motion of a single particle undergoing periodic forces that only depend on the

quadrupole focusing strength (neglecting image forces). In the thin lens approximation, the focusing strength of a quadrupole lens is given by:

$$\theta = \sqrt{\kappa} l_{eff} \, ,$$ (Eq. VII-1)

where $l_{eff}$ is the lens effective length and, for an electrostatic quadrupole, $\kappa$ can be expressed as

$$\kappa = \frac{V_q}{E_B \, r_{ap}^2} \, ,$$ (Eq. VII-2)

in which $V_q$ is the applied quadrupole voltage in Volts and $E_B$ is the beam energy in electron-Volts. Therefore, by changing the applied voltage on QM3 to QM6 one at a time and measuring the beam centroid displacement that results, one can infer the focusing strength of the quadrupole and compare it to $\theta$ calculated from the applied voltage and our knowledge of the quadrupole geometry, where the main parameter in question is the effective length to be used in envelope calculations. Within uncertainties, the measurements agreed with the calculated effective lengths of the quadrupoles obtained from 3-D field calculations.

### VII.2.2 -  *Centroid control*

Once the focusing strengths of the quadrupoles were confirmed, good centroid control was possible since the procedure rely on our ability to calculate single particle trajectories for a given quadrupole voltage. Typically, the beam centroid exiting the injector is offset from the beam line axis by 1-2 millimeters and 3-5 milliradians, followed by betatron oscillations through the quadrupoles of the matching section. The centroid at QD1 is then centered by mechanical

translation (≈±1-4 mm) of the three steering quadrupole QM4-6 in the matching section. The required displacements are determined by calculating the single particle motion through these quadrupoles, and then solving for the quadrupoles displacements needed to center the beam. Three steering quadrupoles (QM4-6) are used to align the beam centroid at QD1 (instead of the minimum of two displacements) subject to the additional constraint of minimizing the sum of displacements of the lenses. To leading order, a displaced quadrupole acts as a quadrupole with the same gradient plus a dipole proportional to the displacement, and the manipulation does not significantly alter the beam envelope. By this procedure, the beam centroid positions ($<x>$, $<y>$ ) and angles ($<x'>$, $<y'>$) are centered to within 0.5 mm and 2 mrad respectively. The $<x>$ and $<y>$ equations of motion are decoupled.

### VII.2.3 - *Envelope control*

Figure VII-6 shows the result from an envelope calculation using hard-edge quadrupoles for the focusing fields. Because of the lack of a self consistent model that would successfully predict the beam parameters at the exit of the matching section initialized with the beam parameters measured at the exit of the injector and the applied quadrupole voltages, several procedures to match the beam to the transport section were tested and assessed.
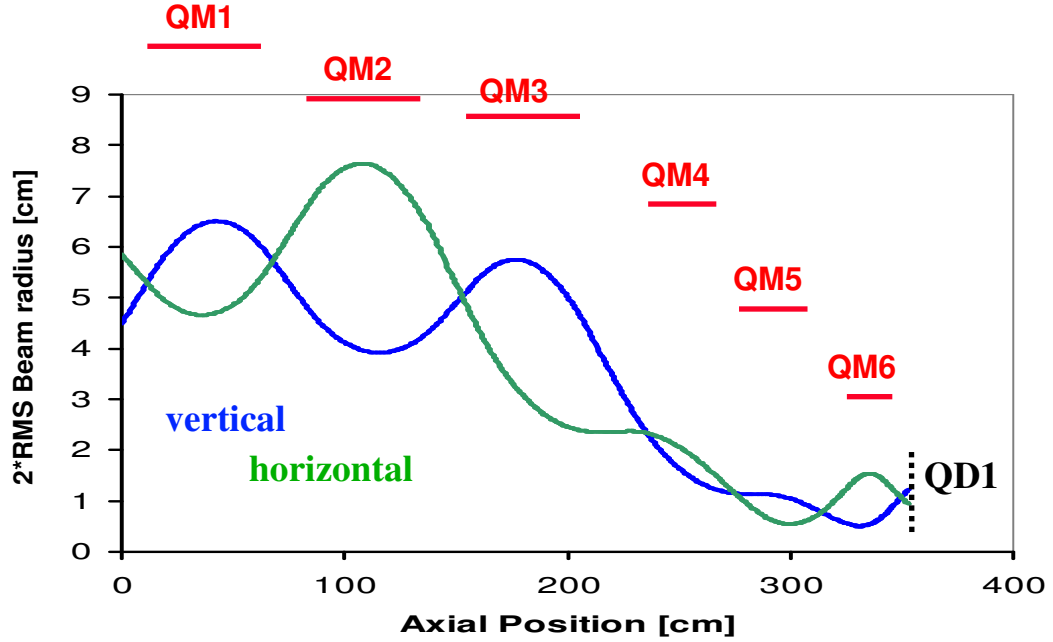
**Figure VII-6**: Representative envelope calculation through the matching section (for the 60% fill factor case in the downstream lattice). The calculation was constrained by phase-space data at QD1. The red lines represent the quadrupoles' bore radii. The quadrupole voltages are (QM1 to QM6): 42.8, 32.8, 37.5, 31.5, 44.4 and 45.2 kV, respectively ( $E_B$ = 1026 keV and $I_B$ = 170 mA are fitted parameters).

VII.2.3.1 -    Empirical matching

We treated the last four quadrupoles of the matching section as a first order linear transport system such that at the exit of the matching section we can write:

$$\delta a = \frac{\partial a}{\partial V_{QM3}} \Delta V_{QM3} + \frac{\partial a}{\partial V_{QM4}} \Delta V_{QM4} + \frac{\partial a}{\partial V_{QM5}} \Delta V_{QM5} + \frac{\partial a}{\partial V_{QM6}} \Delta V_{QM6} \, , \qquad \text{(Eq. VII-3)}$$

and similarly for the other beam parameters ($a'$, $b$ and $b'$). It can be represented as a 4×4 matrix, where the matrix elements are the partial derivatives of (Eq. VII-3). To determine the matrix elements, we measure the variations of all four beam parameters with respect to a reference solution for a known $\Delta V_i$, varying one quadrupole voltage at a time. Thus determined, the matrix can be inverted and used to find the voltage changes required to establish the desired beam parameters. With this procedure, we were able to transport 95% to 99% of the beam through the matching section and the measured beam parameters were within 2 mm and 7 mrad of the targeted ones.

VII.2.3.2 -    Matching iterations based on envelope calculations

Tough the linearized approach to the matching problem improved our control of the envelope parameters, better accuracy was needed for the experiments downstream. The adopted procedure for controlling the beam envelope in the matching section rely on an envelope model similar to the one used to produced Figure VII-6 but, instead of doing a forward calculation, small empirical adjustments are made to some of the parameters (e.g.: $I_B$, $E_B$) to make the simulation agree with the data. Then, a new set of gradients are calculated and implemented in the laboratory. These adjustments compensate for effects not included in the simple hard-edge envelope model (i.e., fringe fields, the $E_z$ component of the focusing fields, and to a lesser extent, image

153

forces and the evolution of the emittance). Achieving the desired envelope parameters at the exit of the matching section requires several iterations to reach reasonable agreement between the measured envelope parameters and the targeted ones. We chose to evaluate the deviation of the measured envelope parameters from the desired ones via a unique expression defined as follows:

$$A_1 = \sqrt{(a_m - a_t)^2 + (b_m - b_t)^2 + \left(\frac{a'_m - a'_t}{\delta}\right)^2 + \left(\frac{b'_m - b'_t}{\delta}\right)^2}, \qquad \text{(Eq. VII-4)}$$

where the subscript $m$ refer to the measured beam parameters and the subscript $t$ to the targeted ones. $\delta$ is a scale parameter that is semi-empirically determined from on a study of envelope mismatch modes [68]. In Ref. [68], mismatches are induced by letting initial envelope parameters deviate from the ideal matched conditions and the resulting mismatch amplitudes in an AG lattice are calculated for various configurations. From these calculations, it can be seen that a deviation of 1 mm from the ideal matched beam size results in the same mismatch amplitude than a deviation of ≈6 mrad from the ideal matched beam angle. Thus, we set $\delta \cong 6$ mrad/mm to normalize the relative importance of the angles to the sizes, and acceptable convergence was then defined as $A_1 \leq 1$ mm. This was typically achieved with 3-4 iterations.

The matching procedure just described eventually determines the required quadrupole voltages such that the envelope parameters at the exit of the matching section are usually within 0.4 mm and 2.1 mrad (±1σ) of the ideal matched parameters. In order to reduce the number of iterations and have a better theoretical understanding of the beam dynamics in the matching section,

an improved model of the matching section that includes fringe fields and the $E_z$ component of the focusing fields is being developed.

VII.2.3.3 -    Additional comments on beam control

Though, to date, the envelope codes do not accurately predict the evolution of the beam in the matching section, the model clearly shows that the beam envelope is very sensitive to certain beam and lattice parameters. For instance, sub-percent quadrupole voltage variations on QM1 and QM2 lead to as much as several millimeters and milliradians variations of the envelope at the exit of the matching section. Between 1% and 2% beam energy or beam current variations have a similar effect. The consequences are twofold. First, in order to have the envelope calculations accurately agree with the data, the beam and lattice parameters need to be well determined. Then, in order to successfully conduct measurement campaigns downstream over several days or weeks, a lot of care must be taken to keep all the parameters of the system as constant as possible.

**VII.3 -    Measurements and conclusions**

*VII.3.1 -  Beam loss*

Figure VII-6 indicate that the beam fills up to 80% of the aperture in the first (QM1) and second (QM2) quadrupoles. Pickup signals capacitively connected to the quadrupole electrodes indicate that beam loss is minimal through the middle, or flattop of the beam pulse.
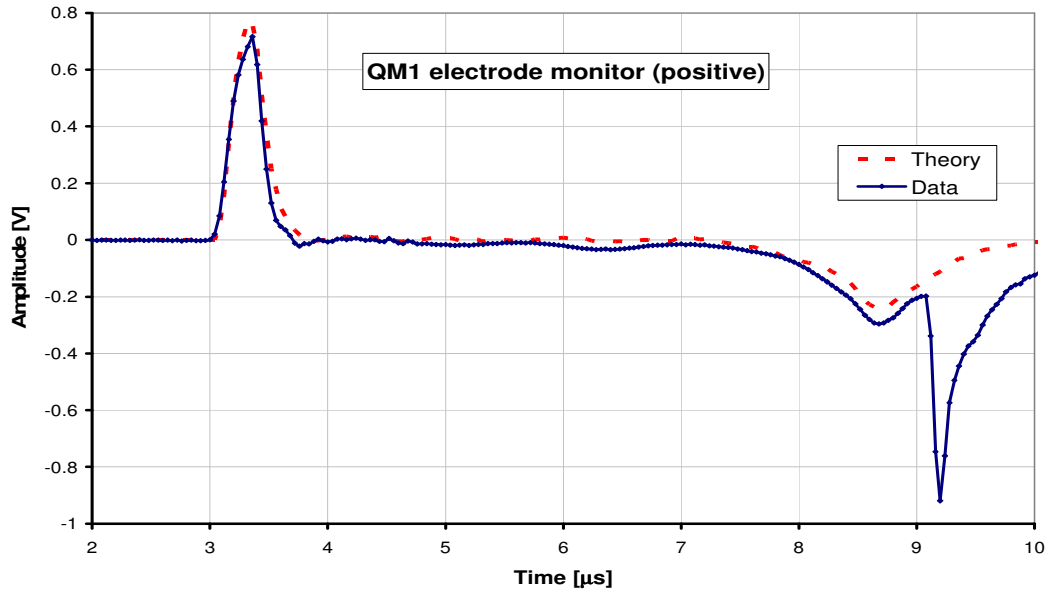
(a)
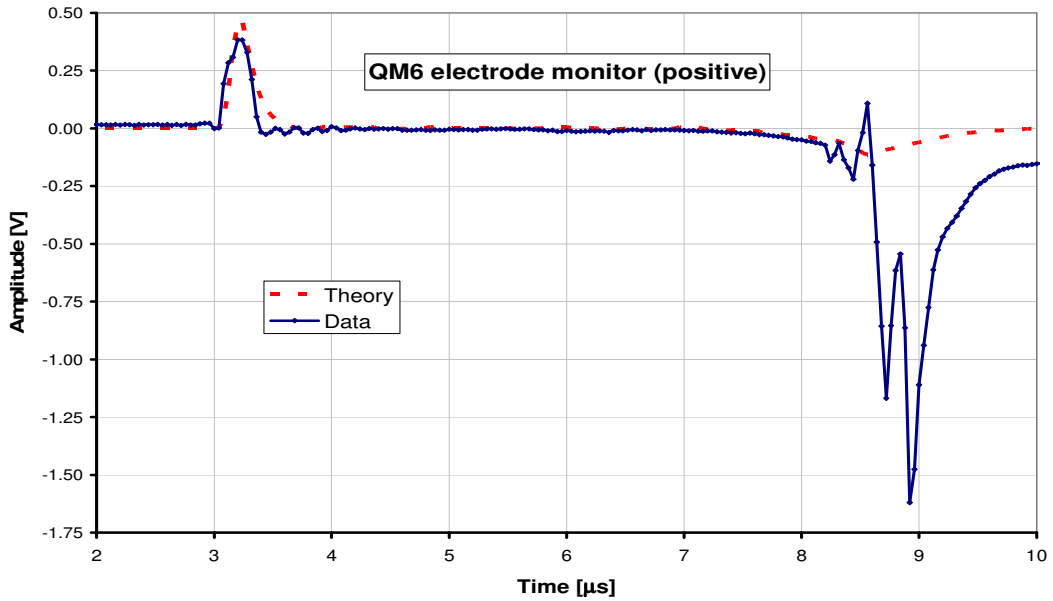


(b)

**Figure VII-7**: Electrode monitors for the first (a) and last (b) electrostatic quadrupoles of the matching section. The blue curve is the raw signal across 10 Ω. The dashed red curve is the expected signal derived from a current

transformer waveform at the injector exit using (Eq. III-15). Note that the difference in peak amplitude for the head of the beam in between QM1 and QM6 is due to the fact that QM6 is 30% shorter than QM1 and therefore the total charge subtended by the electrodes is proportionally lower in QM6.

This is illustrated in Figure VII-7 where the capacitive monitor waveforms or QM1 (Figure VII-7(a)) and QM6 (Figure VII-7(b)) positive electrodes are plotted along with the expected capacitive signals derived from the upstream total beam current diagnostic (Section - III.6.1 -). The excellent agreement of the calculation with the electrode monitors for the head of the beam (see Figure VII-7) shows that the monitor signals in the matching section are from the capacitive pickup of the passage of the beam through the quadrupole, except for the very end of the beam pulse.

In Figure VII-7, the signal amplitude in the flattop region of the pulse (between the peaks) is very small. Following the discussion from Section - III.6.1 -, based on the sum of all six matching section quadrupole pickup signals (not shown on Figure VII-7), we conclude that the beam loss is < 0.5% of the total beam current. Because of the slow fall time of the beam pulse, the tail is mismatched and the beam loss is greater there, as indicated by the large negative spike on the QM6 (Figure VII-7) and other capacitive monitor waveforms. The higher frequency peaks at the tail are a consequence of the incident ions striking the quadrupoles and the monitor response is difficult to model and interpret in detail.

## VII.3.2 - *Phase-space distribution and emittance evolution*

The horizontal and vertical phase-space (sheared) of the beam at QD1 are shown in Figure VII-8 for the two fill factor measurements (60% and 80%).
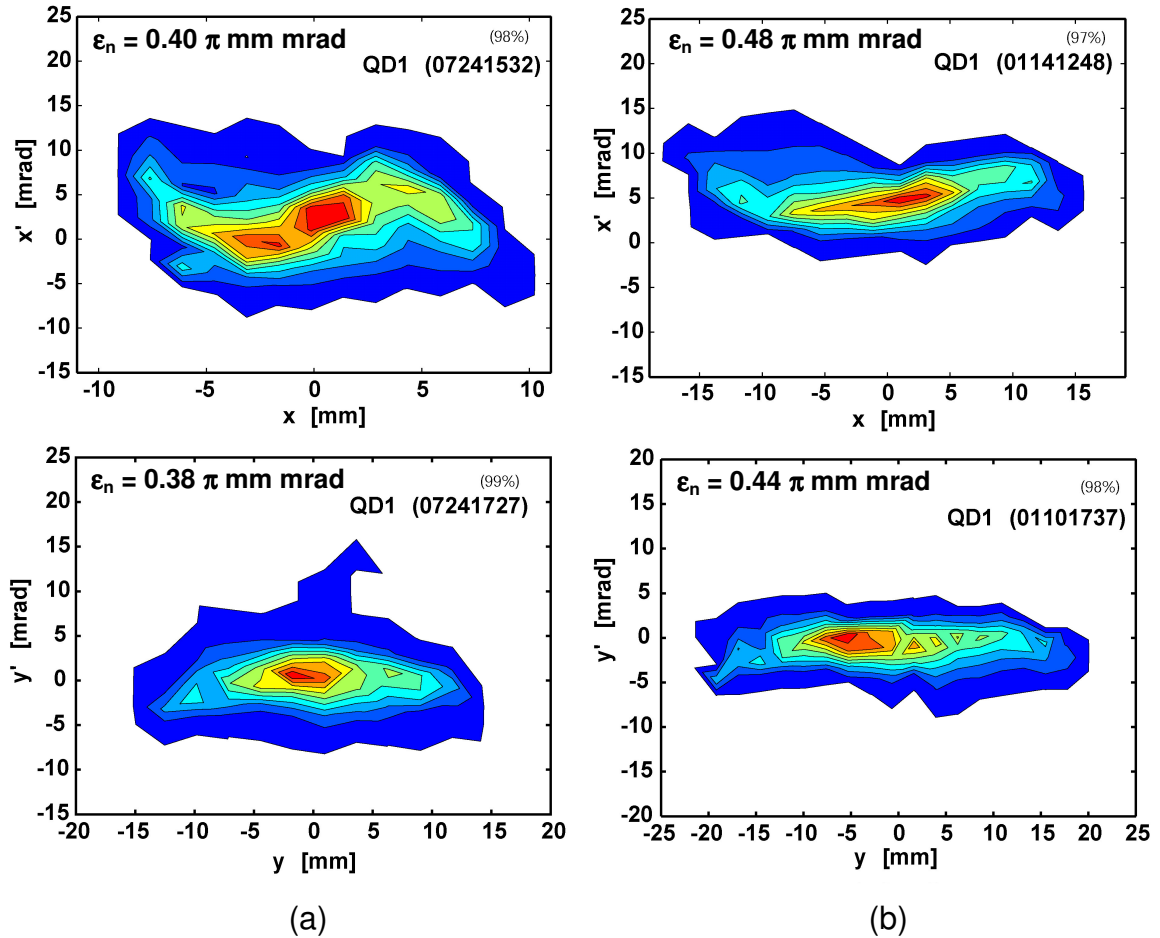


**Figure VII-8**: Phase-space diagrams (sheared) in the horizontal (top) and vertical (bottom) directions for (a) 60% fill factor; (b) 80% fill factor, for a time slice ($\Delta t = 0.12$ µs) near mid pulse (1.96 µs after turn on), at QD1. For the 60% fill factor, the sampling intervals are: 1.5 mm and 2.3 mrad for the horizontal scan and 2.7 mm and 2.1 mrad for the vertical scan. For the 80% fill factor, the

sampling intervals are: 2.1 mm and 1.9 mrad for the horizontal scan and 2.3 mm and 1.7 mrad for the vertical scan.

From more than 10 independent data sets at the diagnostics stations at the entrance and exit of the transport section and slightly different lattice gradients (i.e. various quadrupole voltage solutions in the matching and transport sections that resulted in the beam filling 60% or 80% of the clear aperture), the estimated emittance measurement uncertainty is 10% ($1\sigma$). Though the phase-space distribution appears more distorted for the 60% fill factor case than fro the 80% fill factor case, the normalized emittance is nearly independent of the matching solution within experimental uncertainties. However, the beam emittance measured at the exit of the matching section appears to be lower than the one measured at the exit of the injector system (by 2.0-2.4 times in the vertical plane and, 1.0-1.2 times in the horizontal plane, for the 60% and 80% fill factor cases, respectively, Figure VI-11). Since a sub-percent beam loss can not account for such a large discrepancy, these differences point to a large overestimation of the emittance measurements made at the exit of the injector due to systematic instrumental effects: the finite width of the slits, the misalignment of the slits with respect to one another (i.e. slit and slit-cup not exactly parallel to one another), and the rotation of the beam principal axis with respect to the main axis of the transport channel (and to which the slits are aligned). The errors due to finite slit width may account for a systematic ≤1% increase in the perceived emittance. Both alignment effects increase the apparent beam emittance, and are

159

pronounced when the beam is large ($a \approx 40$ mm and $b \approx 60$ mm at the injector exit) and are negligible when the beam has been transversely compressed by the matching section ($a \approx 10$ mm, $b \approx 15$ mm). A Monte-Carlo simulation of particles followed through the emittance scanner shows that the larger emittance at the injector exit may be explained by a transverse beam rotational misalignment of $\approx 1.5°$ plus the slit and slit-cup misaligned by 0.25 mrad. Additionally, 3-D PIC simulations of the HCX experiment indicate that the emittance should (initialized with a semi-Gaussian distribution at the matching section entrance) remain constant in the matching process or increase by 1.3 times (particle distribution initialized at the ion emitter surface) [154].

The uncertainties for the beam envelope parameters were characterized by calculating the standard deviation ($\pm 1\sigma$) of five repeated measurements, where the data was 'averaged' over a 1.5 µs window near the flattop region of the beam current pulse. Thus, the stability and reproducibility of the envelope coordinate ($a$, $b$) and angle ($a'$, $b'$) measurements are $\approx 0.3$ mm and $\approx 1$ mrad, respectively. The reproducibility and the precision of the envelope measurements include the effect of the beam current drift over the course of the measurement (~1 hour) of up to $\approx 2$ mA.

# Chapter VIII - Fill factor study

## VIII.1 - Description of the electrostatic transport section

The electrostatic transport section consists of 10 quadrupoles on a common supporting rail (Figure VIII-1 and Figure VIII-2). The quadrupoles are aligned to within ±100 μm on the bench before installation inside the vacuum tank.
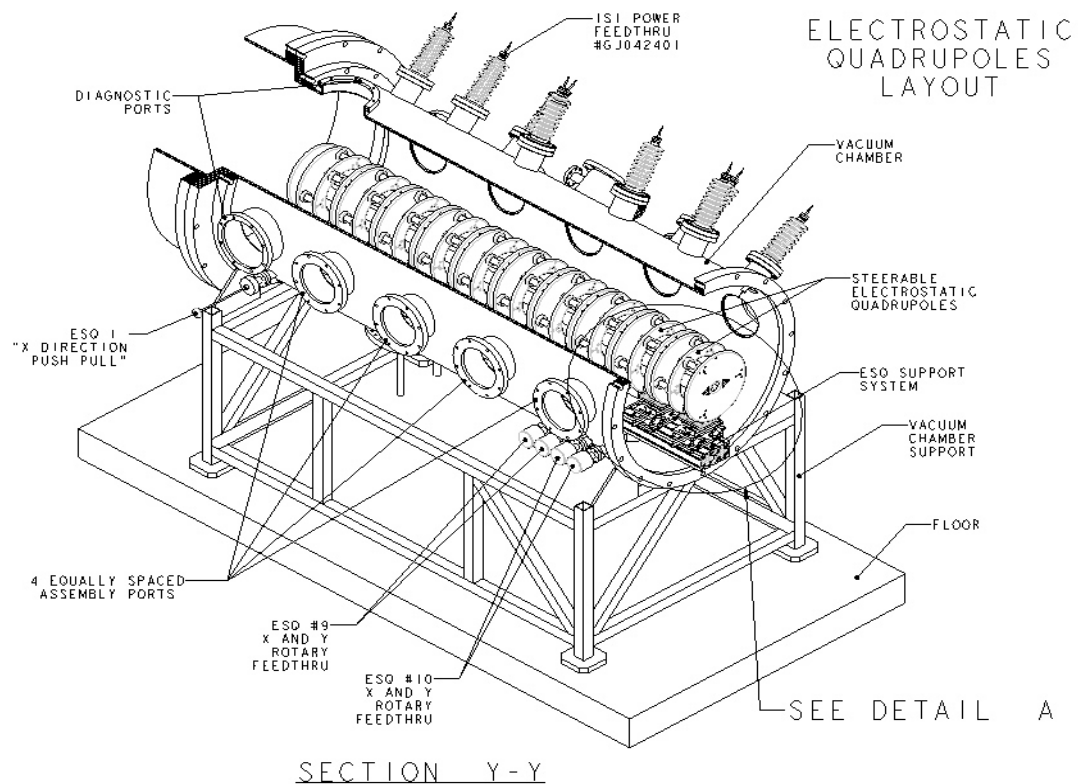


**Figure VIII-1**: Cutaway view of the electrostatic transport section.

161

The rail is mounted on a six-strut/kinematic system with alignment fiducials outside the vacuum chamber decoupling it from the vacuum tank. It is then aligned independently with the rest of the beam line.
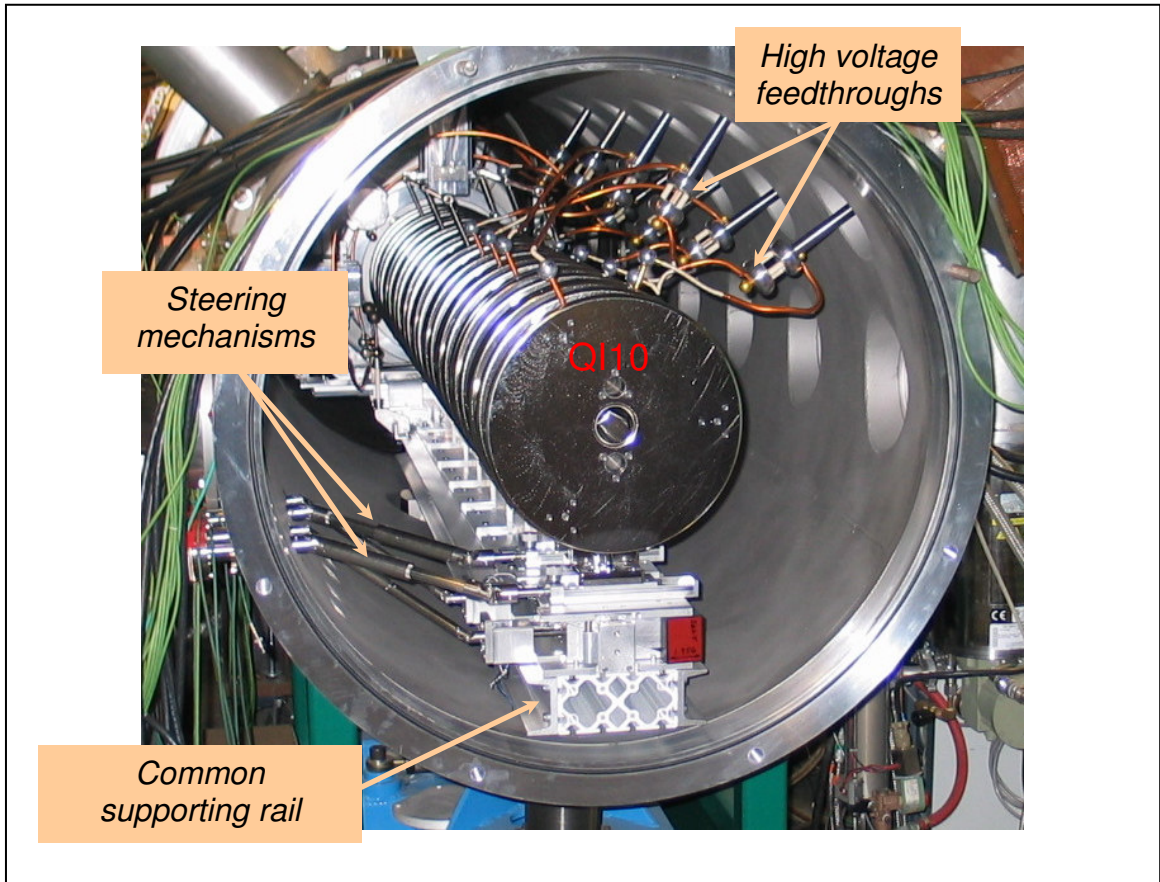


**Figure VIII-2**: Photograph of the electrostatic transport quadrupoles inside the vacuum tank on their support rail (view from downstream).

The first quadrupole (QD1) is movable, allowing insertion of various diagnostics to measure the beam properties before transport (see Section - VII.1.3 -). The last two quadrupoles (QI9 and QI10) may be displaced (horizontal and vertical directions) to correct betatron oscillations. Additionally, QD1 can be rotated by two or four degrees for studying the effect of rotated quadrupoles on the beam.

QD1 and QI7 to QI10 are independently biased. The second to sixth quadrupoles (Q2 to Q6) are energized in parallel. Some feedthroughs supply different voltages to pairs of quadrupoles, preventing a voltage differential larger than 20 kV between QI7 and QI8, and QI9 and QI10. All power supplies are remotely controlled and monitored via and ethernet links. Figure VIII-3 shows the adopted quadrupole design. They are operated bipolar and prototypes have held voltages up to ±120 kV (in absence of beam), twice the maximum operating voltage.
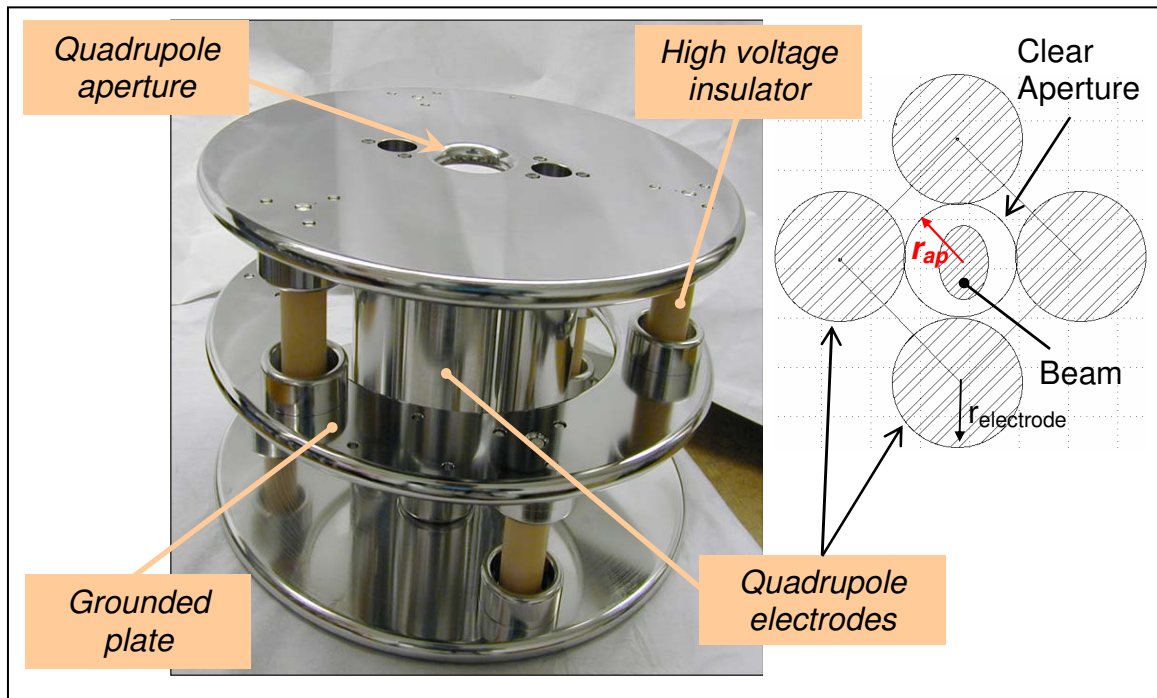


**Figure VIII-3**: Photograph of a quadrupole and cut view schematic.

The bore radius of the quadrupoles defined by the inner edge of the electrode is $r_{ap}$ = 2.3 cm. The electrodes are cylindrical (as in a multi-beam

array) and follow $r_{electrode} = (8/7)\ r_{ap}$ to minimize the unwanted high order multipoles. A drawing with the quadrupole dimensions is shown on Figure VIII-4.
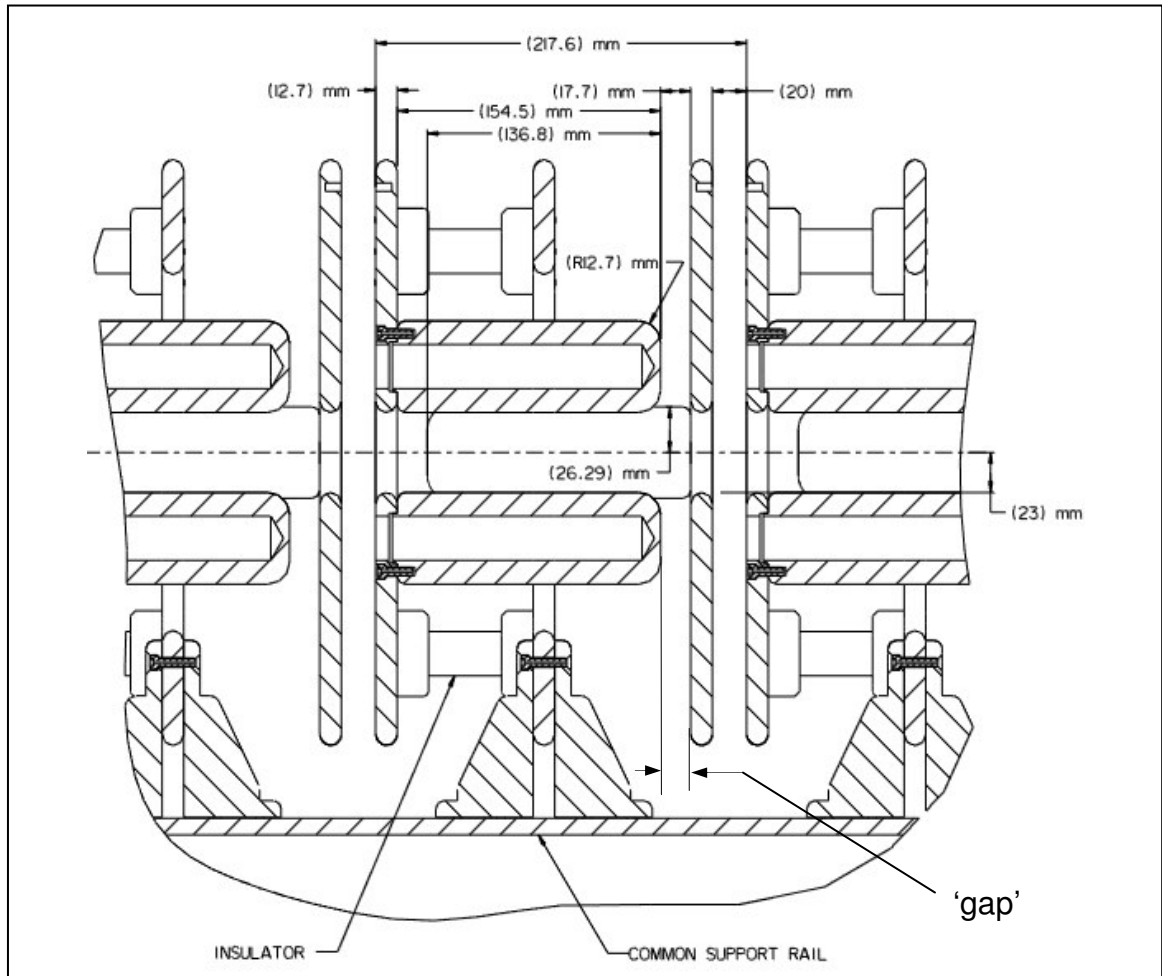


**Figure VIII-4**: Mechanical drawing (side view) of a quadrupole installed on the beam line.

The drift between two quadrupole end-plates is 2 cm and the half lattice period, $L$ = 43.3 cm. The lattice occupancy is $\eta$ = 0.70. A calculation of the electrostatic

field based on the mechanical design showed very good field quality. A multipole decomposition of the calculated electric field is plotted on Figure VIII-5.
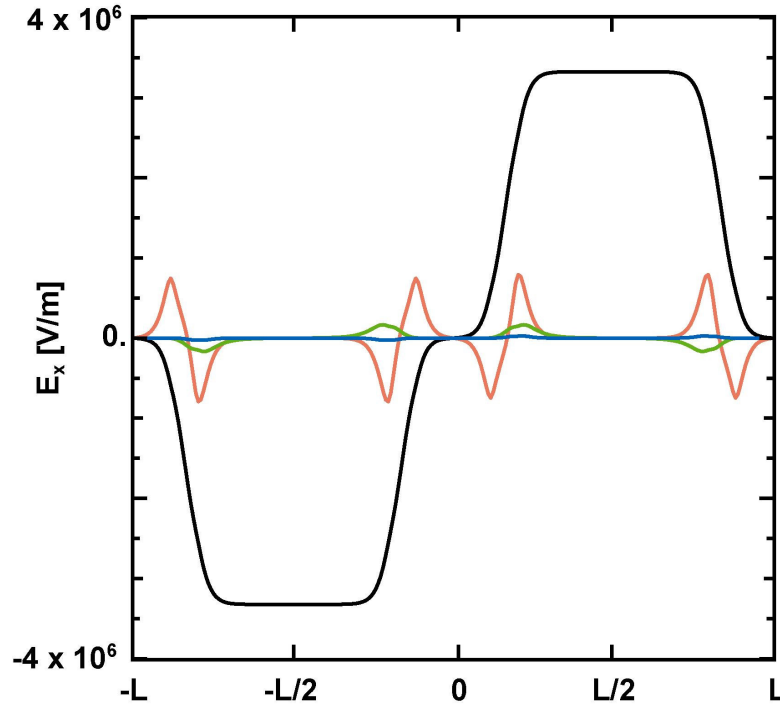


**Figure VIII-5**: Calculated longitudinal dependence of the electric field at radial distance $r$ = 1.5 cm from the center of the quadrupole for a unipolar applied voltage of 60 kV (the results for two quadrupoles with opposite polarities are plotted (i.e. one lattice period, $2L$)). Various moments of the field are shown: Quadrupole (black), 'pseudo-octupole' (red), octupole (green) and dodecapole (blue). The 'pseudo-octupole' moment is proportional to $(r/r_{ap})^3 \cos 2\theta$ (i.e. radial dependence of an octupole moment and angular dependence of a quadrupole moment) and arise from the end geometry of the quadrupole.

In Figure VIII-5, higher order multipoles integrated over half a lattice period (one quadrupole) represent 0.73% of the integrated quadrupole component at a radius $r$ = 2 cm from the center of the quadrupole, down to 0.24% at $r$ = 1.5 cm and 0.06% at $r$ = 1 cm. Also based on Figure VIII-5, the calculated effective length of the quadrupole field, $l_{eff}$, is equal to the region where the electrodes overlap plus 0.83 times the length of the gap between the end of the electrodes and the end-plate of the quadrupole (shown on Figure VIII-4).

## VIII.2 -    Preliminary remarks

Ideally, the fill factor experiment would be done using constant density beams of various sizes, for which $I_B \propto a^2$ and the interior trajectories are self-similar. The immediate thought is to use apertures to obtain such beams, but previous experience proved to be difficult. The beam aperturing process can induce significant undesirable complications (e.g.: desorbed gas and secondary electrons production) that may distort the beam in the transport section. The next solution, making several guns of different sizes, was too expensive. Consequently, we chose to vary the tune and matching to achieve various fill factors, but at varying current densities. PIC simulations of the experiment in which various fill factors were achieved either at fixed current density or by varying the quadrupole tune gave similar results [151], giving confidence that the experimental approach (i.e. exploring the fill factor by decreasing the lattice focusing strength) will give information relevant to the driver case.

We have made two fill-factor measurements, for the envelope filling ≈60% and ≈80% of the available bore diameter in the transport channel of 10

electrostatic quadrupoles arranged in a periodic lattice. For each fill factor measurement, the transverse phase-space of the beam was characterized in detail at the exit of the matching section as discussed in Section - VII.3.2 -. Each case required a different matching solution (i.e. different quadrupole voltages) in the matching section. Because the fill factor was changed by tuning the upstream beam to the matched beam conditions in the transport section for a lower focusing gradient, the undepressed betatron phase advances per lattice period ($\sigma_0$) for the two fill factors are 69° and 48° for the 60% and 80% fill factor cases, respectively. The space-charge depressed phase advance per lattice period ($\sigma$) are 13° and 8° for the 60% and 80% fill factor cases, respectively.

## VIII.3 -    Beam measurements

### VIII.3.1 - Current transmitted through the periodic electrostatic lattice

Figure VIII-6 shows electrode pick-up signals for both fill factor cases.



(a) 60% filling factor                    (b) 80% filling factor
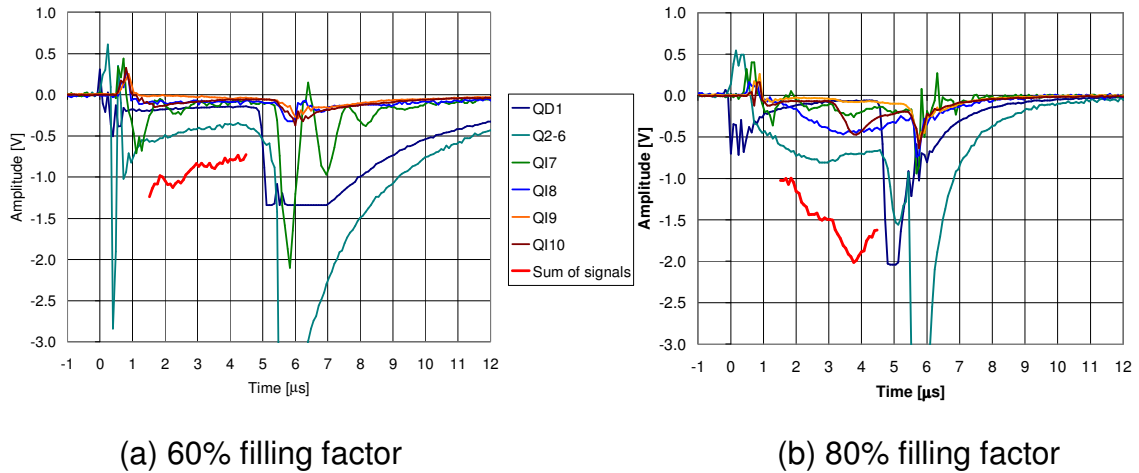
**Figure VIII-6**: Quadrupole electrode pick-up signals in transport section (a) for a 60% filling factor case; (b) for a 80 % filling factor case. In red is the sum of all 10

quadrupole pickup signals in the middle of the pulse, representative of the total

beam loss through scraping and beam/background gas interactions.

Based on the discussion from Section - III.6.1 -, a signal amplitude of 1 V in

Figure VIII-6 corresponds to ≈1-2 mA of beam loss. Therefore, the measured

beam loss with these pickups is 1-2% in the flattop of the beam. However, this

diagnostic is very sensitive to the details of the beam envelope evolution in the

lattice. For instance, for a 80% fill factor case, a better matched and centered

beam than the one corresponding to the capacitive pickup signals shown in

Figure VIII-6(b) lead to a much improved transmission (Figure VIII-7).
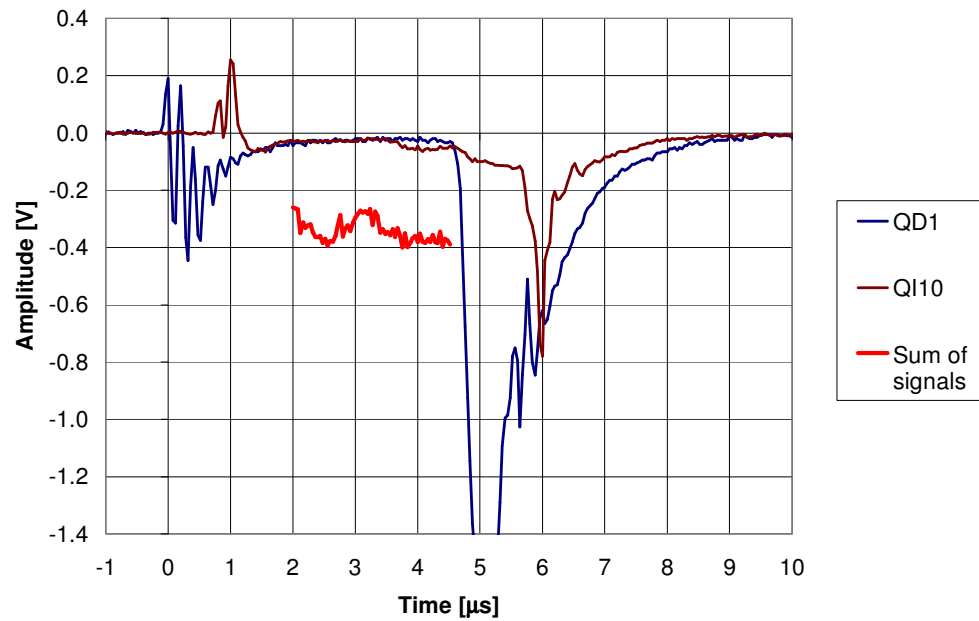


**Figure VIII-7**: Electrode monitors for the first (blue) and last (brown) electrostatic

quadrupoles of the transport section for an 80% fill factor case. In red is the sum

of all 10 quadrupole pick-up signals in the middle of the beam pulse and is

representative of the beam loss through scraping and beam/background gas interactions.

In comparison to Figure VIII-6(b), the beam loss has been decreased by as much as a factor of five. Also note that the sum of all 10 quadrupole signals is flatter than in Figure VIII-6 thanks to the beam current pulse flattening discussed in Section -X.1 -. Thus, in the entire length of the transport section, considering the middle part of the beam pulse and both fill factor cases, the sum of the currents collected on all 10 quadrupole electrodes indicate maximum particle losses of <1%, while ratios of Faraday cup signals taken at the entrance and exit of the transport section indicate ≈1% losses. Because the pickup signals at the head and tail of the beam pulse are the result of a combination of both capacitive response and the collected currents, it is difficult to interpret. Qualitatively, because of the intrinsic mismatch of the head and tail of the beam, the individual electrode monitor signals amplitude is smaller or in some instances negative at the beginning of the pulse and is more negative at the end of the pulse, indicating more beam loss at the extremities of the pulse.

### VIII.3.2 - Beam phase-space measurements

On Figure VIII-8, the horizontal (converging plane) and vertical (diverging plane) phase-space diagrams are shown for both fill factors.
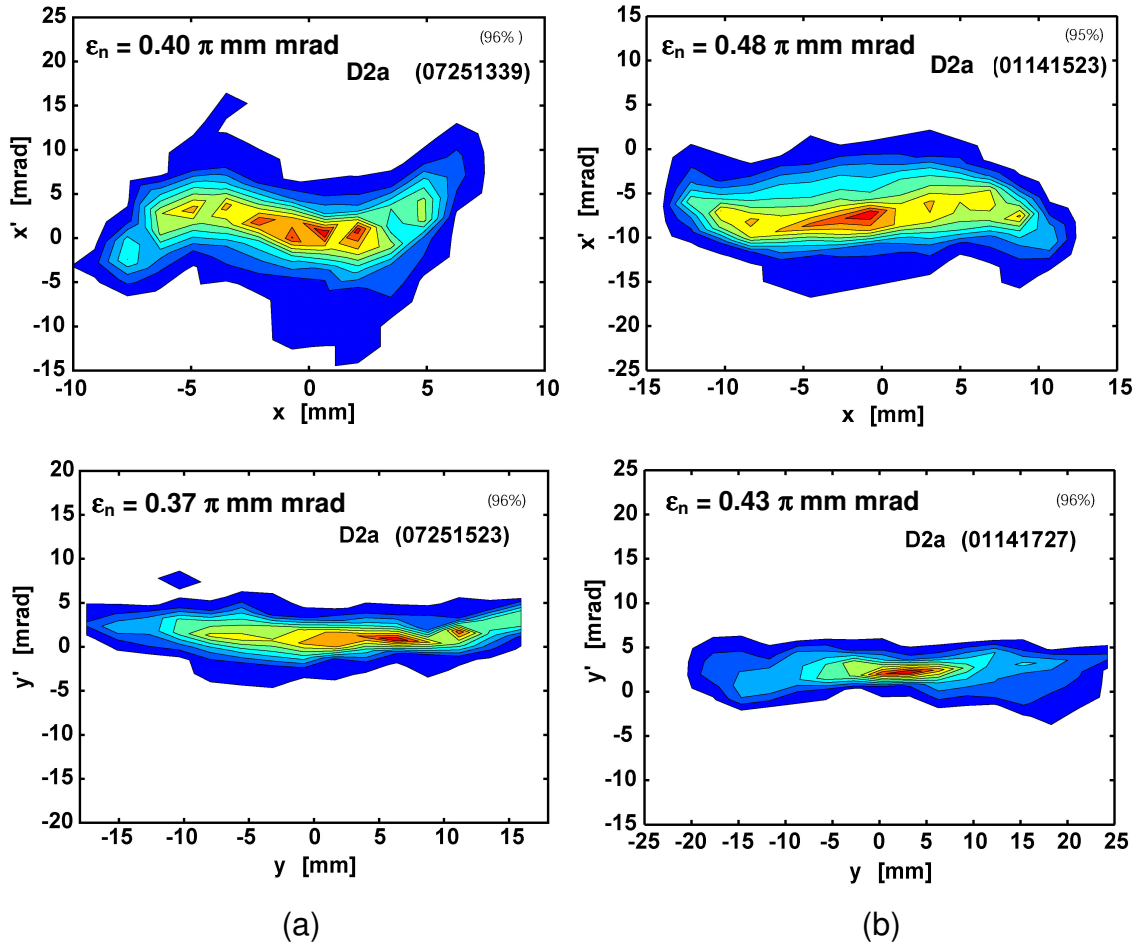
**Figure VIII-8**: Phase-space diagrams (sheared) in the horizontal (top) and vertical (bottom) directions for (a) 60% fill factor; (b) 80% fill factor, for a time slice ($\Delta t = 0.12$ μs) near mid pulse (1.96 μs after turn on), at the exit of the electrostatic transport section. For the 60% fill factor, the sampling intervals are: 1.4 mm and 2.2 mrad for the horizontal scan and 2.4 mm and 1.5 mrad for the vertical scan. For the 80% fill factor, the sampling intervals are: 1.9 mm and 1.8 mrad for the horizontal scan and 3.0 mm and 1.5 mrad for the vertical scan.

Comparing Figure VIII-8 with Figure VII-8, it can be seen that within the experimental sensitivity, there is no evidence of emittance growth at the end of the electrostatic lattice for both the 60% and 80% fill factors. Note also that the details of the beam phase-space distribution remain practically unchanged except for the small 'hooking' regions that mirror one another in between QD1 and D2a in the horizontal direction for the 60% fill factor case. PIC simulations initialized with semi-Gaussian distributions [150,151] have also predicted that matched beam excursions filling 80% of the quadrupole bore would result in negligible emittance growth, assuming perfect alignment and envelope control. However, these simulations do not include nonideal effects resulting from particle losses.

**VIII.4 -   Mismatch evaluation and envelope control**

Integrating the envelope equation from QD1 to D2 (initialized with QD1 measurements of envelope radii, convergence angles, current, and measurements of beam energy) gives a calculated envelope in agreement with the experiment at the D2 location to within 0.4 mm and 3 mrad, (<10%). This level of agreement allows us to confidently rely on envelope model predictions (such as Figure VIII-9) to tune the lattice and control the beam envelope excursions in the experiment. Early calculations of the envelope showed discrepancies as large as 25%. After including additional effects to the theoretical model, as well as a more accurate determination of the beam current, the beam energy and the variation of the beam parameters over the pulse, the agreement was good. The model improvements were: (1) Realistic quadrupole fringe fields

based on 3-D field calculations; (2) quadrupole $E_z$ from the 3-D lattice structure and corresponding radial focusing force; (3) corrections due to the grounded slit plates of the intercepting diagnostics that short out the self-field of the beam near the diagnostic [152]. In Figure VIII-9, examples of calculated beam envelopes with these improvements are plotted.



(a)                                        (b)
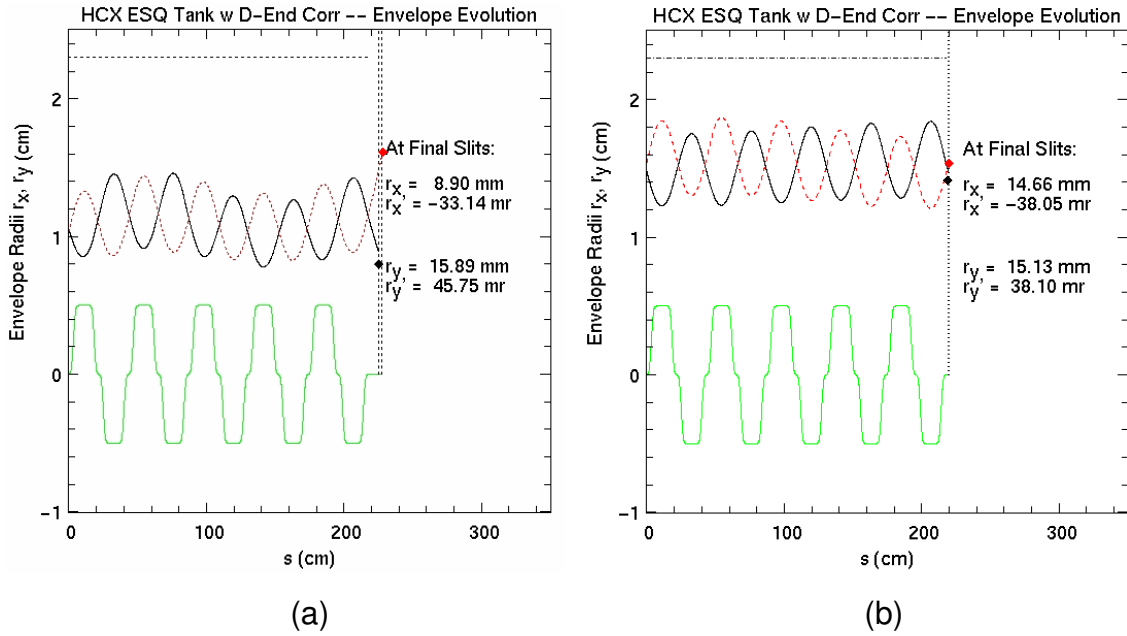
**Figure VIII-9**: Calculated envelope from QD1 (a) to D2a for a 60% fill factor case; (b) to D2b for a 80% fill factor case. Runs are initialized with data taken at QD1. Black: horizontal direction; Red: vertical direction; Green: focusing forces quadrupole gradients. Diamonds are the corresponding data points.

In Table VI, envelope measurements at the exit of the electrostatic lattice for two 80% fill factor data sets are compared to predictions of the envelope model. Data set A is for a more mismatched beam than data set B (Figure

172

VIII-9(b)). Envelope simulation uncertainties are taken from the standard deviation of a Monte Carlo distribution of envelope predictions through the transport section, where several thousands envelopes are calculated with initial conditions randomly distributed about the measured values. The initial distributions for the parameters that are varied are Gaussian with standard deviations representing the measurements uncertainties or the equipment accuracies (e.g.: stability of the quadrupole voltages).

The uncertainties for the data at D2 are estimated as for the QD1 uncertainties described in Section -VII.3.2 -. Thus, the RMS envelope model is accurate to within the measurement uncertainty.

**Table VI**: Experimental envelope parameters compared to envelope model predictions at the exit of the electrostatic section for two 80% fill factor cases. Note that in this table, data sets A and B were taken at different $z$ locations in the lattice, as described in Section - I.5.2 -. The data are from a 120 ns interval of the flattop region of the beam pulse, 2.64 µs after the start of the beam pulse.

| | | a [mm] | a′ [mrad] | b [mm] | b′ [mrad] |
|---|---|---|---|---|---|
| Data set A | *Data* | **12.24** | **-38.52** | **21.10** | **43.04** |
| | *Env. Model.* | **12.07** | **-35.46** | **20.95** | **46.10** |
| Data set B | *Data* | **14.07** | **-38.50** | **15.54** | **39.84** |
| | *Env. Model* | **14.66** | **-38.05** | **15.13** | **38.10** |
| Uncertainty (±1σ) | *Data* | **0.3** | **1.0** | **0.3** | **1.0** |
| | *Env. Model* | **0.5** | **2.1** | **1.2** | **3.0** |

Further data analysis shows that RMS beam parameters are more sensitive to beam current variations for a 60% fill factor case than for an 80% fill factor case. This is understood in terms of envelope mismatch oscillations, which arise when one or more of the terms in the envelope equation is perturbed (i.e. small variations around the 'matched beam' parameters that satisfy the equation) [153]. In an AG lattice, envelope oscillations can be decomposed into the combination of two fundamental modes equivalent to the breathing and quadrupole modes derived from a continuous focusing analysis, but at slightly different characteristic frequencies (as shown in Section - II.1.7 -). Using an envelope model in which the beam current is varied for otherwise fixed matched parameters, Fourier transforms of the calculated envelope suggests that the current perturbations excite the breathing mode more strongly compared to the quadrupole mode. For the 80% fill factor case, where the undepressed phase advance per lattice period, $\sigma_0$, is 48°, the total phase advance of the breathing mode envelope oscillation through 10 quadrupoles (i.e. 5 lattice periods) is ≈360°. Thus, the envelope parameters should show a reduced sensitivity to small beam current variations, in line with the observations.

Defining the envelope mismatch as $\delta_M = Max(a_{Max}, b_{Max}) - R_{0,Max}$, where $Max(a_{Max}, b_{Max})$ is the maximum of the envelope excursions in both planes of the calculated envelope initialized with QD1 measurements, and $R_{0,Max}$ is the maximum excursion for the theoretical matched beam, for both fill factor cases shown on Figure VIII-9, we were able to match the beam to within

174

$\delta_M$ = 1 ±0.5 mm. The uncertainty in $\delta_M$ is based on the Monte Carlo analysis discussed above.

If the envelope model fails to agree with the data, another method to determine the degree to which the beam is mismatched would be needed. Comparing the beam envelope measurements at homologous points in the lattice gives a qualitative, parameter independent (i.e. no knowledge of the beam energy, emittance or current is necessary) measure of the matched beam. In the ideal case where the beam is perfectly matched, $a$, $a'$, $b$ and $b'$ will have the same values at homologous points in the lattice. Deviations from this situation indicate a mismatched beam. Taking the sum of the squared differences between two measurements,

$$A_{1H}^2 = \left(a(z_1) - a(z_2)\right)^2 + \left(\frac{a'(z_1) - a'(z_2)}{\delta}\right)^2 \\ + \left(b(z_1) - b(z_2)\right)^2 + \left(\frac{b'(z_1) - b'(z_2)}{\delta}\right)^2$$

(Eq. VIII-1)

similar to the $A_1$ parameter from Section - VII.2.3.2 -, made at homologous locations $z_1$ and $z_2$ in the lattice will help determine the better matched beam. However, this procedure cannot lead a quantitative determination of the degree of mismatch $\delta_M$ since the envelope evolution between the two measurement locations is not known *a priori*.

Envelope simulations for which the quadrupole voltages were allowed to vary randomly by the expected tolerance on voltage control (0.1 kV or ≈0.5%) about their nominal value, including the experimental constraint that five of the 10

quadrupoles are energized with common power supplies, indicate that the average envelope mismatch excursion grows by 0.2-0.3 mm over the first five lattice periods. This rate decreases to less than 0.1 mm per five lattice periods after transport through 50 lattice periods.

### VIII.5 -   Beam centroid control

The quadrupoles were aligned with respect to their common support rail to within ±100 μm before installation into the beam line. With the beam centered to within 0.5 mm and 2 mrad upstream (QD1), we observe 1-2 millimeters and 1-5 milliradians centroid offsets after 10 quadrupoles, and the beam centroid varies by ≤ 0.5 mm and ≤ 1 mrad during the flat top of the beam pulse. However, the predicted centroid values from simulations do not agree with the downstream beam measurements. Furthermore, there is no hypothetical misalignment of the quadrupoles support rail that satisfies multiple data sets, or is consistent with uncertainties of the beam line survey. Dipole fields from image charges in the 10 transport quadrupoles or induced by the image charge of the beam on the support slit scanner paddles in the relatively open diagnostic regions may be responsible for the discrepancy. However, it was observed that upstream (QD1) beam centroid offsets as large as 2 mm and 5 mrad would not lead to any noticeable beam loss or emittance growth in the electrostatic transport section. Moreover, in the same way as for the matching section steering, we can successfully steer the beam back on axis by displacing appropriately QI9 and QI10 once the beam has been diagnosed at D2.

# Chapter IX - Beam charge distribution

## IX.1 - Beam current-density measurements and interpretation

From crossed slit measurements (i.e. perpendicular slits upstream of a Faraday cup, each sampling the beam distribution in $\Delta x = \Delta y = 1$ mm intervals) at QD1 and D2, the time-resolved current-density distribution $J(x, y, t)$ (Figure IX-1) of the beams was measured. Depending on the applied focusing strength in the matching and transport section, $J$ may be peaked or hollow in radial profile. The initial nonuniformities in the current-density distribution arise from the diode spherical aberration [125]. Also, the shape of the transverse beam profile exhibit diamond like distortions to ideal elliptical symmetry at both diagnostics stations. Transverse oscillation frequencies (e.g. plasma, space charge wave and envelope oscillations frequencies) are influenced by the change in $\sigma_0$ associated with the two fill-factor measurements. As a result, different current-density distributions were observed.
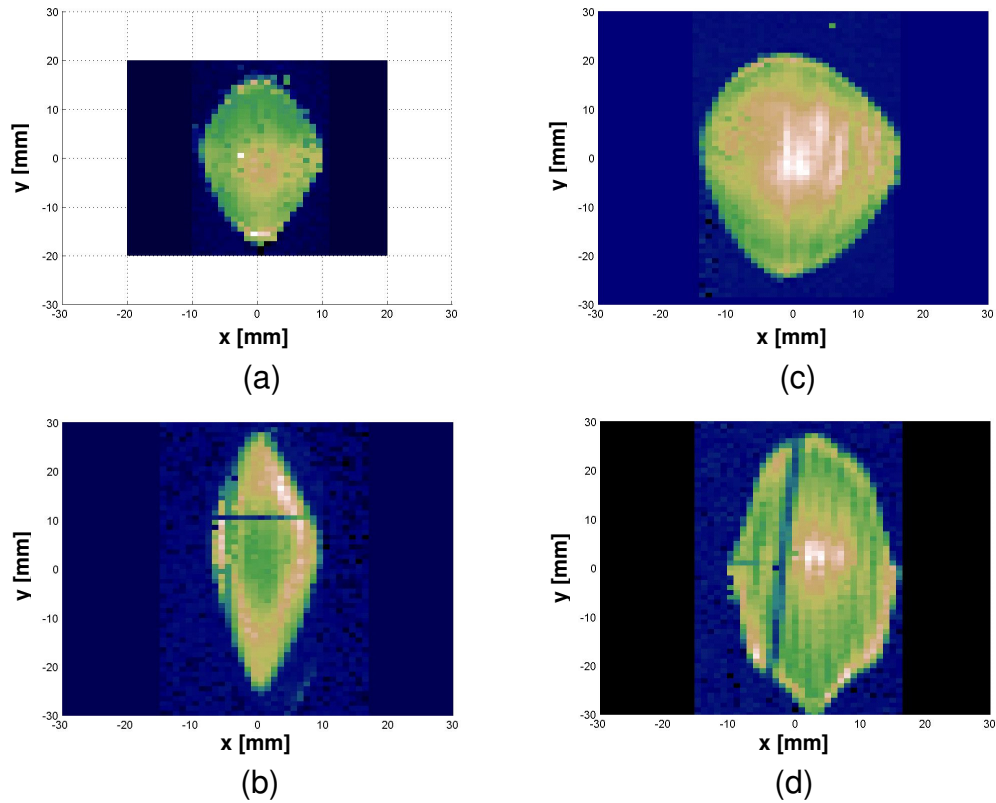
**Figure IX-1**: Beam current-density profiles $J(x, y)$ measured with crossed slits. (a) - (b) 60% fill factor case at QD1 and D2a respectively, single time slice ($\Delta t = 0.12$ μs) taken 2.64 μs after turn on of the beam, (c) - (d) 80% fill factor case at QD1 and D2a respectively, single time slice ($\Delta t = 0.12$ μs) taken 3.12 μs after turn on of the beam. In (b) and (d) the dark crossed (or line) pattern that is seen comes from bridges across the slits that are there to strengthen the slit structure and avoid deformations. Upstream (QD1) slits are shorter and do not require the bridges.

The diamond-shaped pattern is attributed to nonlinear fields arising from the space charge component of the distribution and the collective evolution of the

178

distribution in the ESQ injector and in the matching and transport sections. The fact that the 60% fill-factor beam is more diamond-shaped than the 80% fill-factor beam indicates that nonlinearities from the image forces and the applied fields in the transport section do not play a significant role. Most of the distortion is initiated upstream, in the injector and matching section. Recent PIC simulations (using a semi-Gaussian beam distribution) showed some indications that the diamond-shape pattern could result from large aspect ratios of the beam in one or more quadrupoles.

Simulations indicate that the peaked and hollow patterns are due to space-charge waves that move rapidly in and out of the body of the beam (from Ref. [70,164] $\omega_{space\,ch\arg e\,wave} > \omega_p$ for all modes). Therefore, the details of the beam current-density distribution vary with the longitudinal position in the lattice. Note that in Figure XI-10 the distributions at D2 are significantly different (peaked for the 80% fill factor case and hollow for the 60% fill factor case). These differences are understood qualitatively with a warm-fluid description of intense beam equilibrium [73] discussed in Section - II.1.8 - and also consistent with a full kinetic treatment for an AG lattice of Hoffman $et$ $al.$ [164]. Although the theory is developed for small amplitude perturbations in axisymetric geometry, it appears to have predictive power in our non-ideal context. In this context, the normalized frequency $\left|\dfrac{\omega}{\nu_0}\right|$ of axisymmetric flute perturbations as a function of the tune depression $\dfrac{\nu}{\nu_0}$ for a K-V beam equilibrium in the electrostatic approximation is given by (Eq. II-53). Since for both fill factor cases the beam distribution at QD1

is peaked (Figure IX-1(a, c)), we define these measurements to represent the initial perturbation of the density profile (mainly to a radial $n = 2$ mode; a fuller description of the perturbation is composed of additional higher order eigenmodes). Then, the difference in the density profiles at the exit of the transport section (D2) is interpreted as the difference in the phase of the perturbation. At respective tune depressions $\dfrac{\nu}{\nu_0}$ = 0.19 and 0.16 for the 60% and 80% fill-factor cases, the phase difference expected at D2 (five lattice periods downstream) is $\Delta\phi$ = 167 degrees. Since the beam distribution started peaked at QD1 for both cases, we expect the distribution to be almost completely out of phase at D2, as observed in the experiment (Figure IX-1(b, d)).

## IX.2 -   Comparison to PIC simulation distributions

Figure IX-2 shows the first simulations of the beam starting with a distribution reconstructed from measurements of the 60% fill-factor case at QD1 [154]. The simulation uses 2 x $10^5$ particles on a 0.2 mm grid and the focusing fields were obtained from a multipole decomposition of the calculated electrostatic field based on the mechanical design of the HCX quadrupoles.
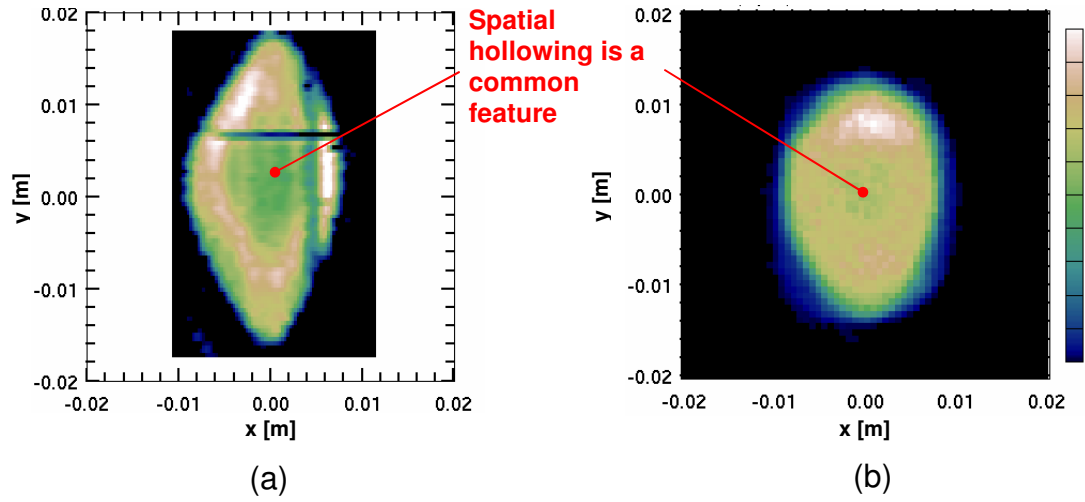
**Figure IX-2**: : Beam current-density profiles $J(x, y)$ at mid-pulse (2.64 μs after turn on) (a) data at D2a, (b) WARP simulation at D2a initialized with data at QD1, projected to a common plane in the lattice. Spatial hollowing in the center of the beam is a common feature to both the data and simulation.

Both the simulated and measured beam configuration space distributions are hollow (center to edge: ≈1:2) but the distributions are also different. However, second order parameters such as the RMS beam size and convergence/divergence angles differ significantly between the experiment and the simulation. Several items contribute to the disagreement: First, the reconstruction algorithm (still under development) does not exactly reproduce the measured second moments of the beam at QD1. In particular, $a'$ and $b'$ differed from the experiment by 1 mrad. Then, the beam energy for this data set is not known to better than 5 to 10%. Combined, these two errors could account for as much as 10 mrad and 2 mm differences in the beam envelope parameters

expected at D2. Another effect which is, at this point, not taken into account in PIC calculations, is the beam self-electric field shorting out by the measuring slit [152]. Envelope calculations including this effect show that it contributes to another ≈0.5 milliradian difference to the final beam envelope angles expected at D2. Finally, the measurement of the 4-D phase space with the standard slit/cup diagnostics is incomplete, since only the $x - x'$, $y - y'$ and $x - y$ projections are measured. In order to realistically describe the detailed evolution of the beam distribution, the full 4-D phase-space needs to be known since cross correlations exist between the vertical and horizontal projections [$f(x, y', t)$, $f(x', y, t)$ and $f(x', y', t)$]. A new optical diagnostic (discussed in Section - III.5.2 -) measures the missing projections of the 4-D phase-space distribution and will improve our ability to simulate accurately the beam throughout its transport in the electrostatic section and beyond.

Note that on Figure IX-2(a), interpolation of the data (spline fit) was necessary for consistency with the grid resolution in the PIC simulation.

## IX.3 - Beam edge and halo

### IX.3.1 - Beam edge fall-off

IX.3.1.1 - Debye length for a beam in thermal equilibrium

To later describe the thermal equilibrium properties of an expanding beam in an alternating gradient lattice (and in particular its edge at the point of measurement) and compare it to the data, it is convenient to first express the

Debye length in terms of the measured emittance. We will work in the horizontal direction ($x$) for the purpose of the following derivation.

For a nearly uniform density (low temperature) thermal beam, we can take a K-V like model of the coherent component of the beam expansion resulting from an alternating gradient quadrupole focusing:

$$x'_{th} = x' - a'\frac{x}{a}. \tag{Eq. IX-1}$$

Then, the spatial average $x$-temperature is:

$$T_x \equiv m\gamma\beta^2c^2\left\langle x'^2_{th}\right\rangle. \tag{Eq. IX-2}$$

By use of (Eq. II-28), (Eq. II-29) and (Eq. II-32) along with (Eq. IX-2), we can write

$$\left(\frac{T_x}{m\gamma\beta^2c^2}\right) = \frac{\varepsilon_x^2}{4a^2}, \tag{Eq. IX-3}$$

and similarly in the $y$-direction. Note that the temperature is measured in energy units. Next, we assume that the beam core is at low temperature in each direction, corresponding to a uniform density out to near the beam edge, and that the beam profile is elliptical in shape. The line charge density can then be approximated by

$$\lambda \approx qn_0\pi ab, \tag{Eq. IX-4}$$

where $n_0$ is the density of the central "core". Finally, using (Eq. IX-3) and (Eq. IX-4) with the definition of the Debye length

$$\lambda_{Dx,y} = \sqrt{\frac{\varepsilon_0 T_{x,y}}{q^2 n_0}} \, , \qquad \text{(Eq. IX-5)}$$

we find

$$\lambda_{Dx} = \frac{\varepsilon_x}{2} \sqrt{\frac{b}{2K\gamma_b^2 a}} \, , \qquad \text{(Eq. IX-6)}$$

$$\lambda_{Dy} = \frac{\varepsilon_y}{2} \sqrt{\frac{a}{2K\gamma_b^2 b}} \, . \qquad \text{(Eq. IX-7)}$$

IX.3.1.2 - Continuously focused thermal distribution model and comparison to the

data

Crossed-slit current-density profile data prompted a comparison to an idealized thermal equilibrium distribution using the Vlasov equation [84]. In that model the equivalent thermal distribution profile falls rapidly in 5 Debye lengths (95 to 5%), $\lambda_{Dx,y}$, outside a near-constant density core (Figure IX-3).
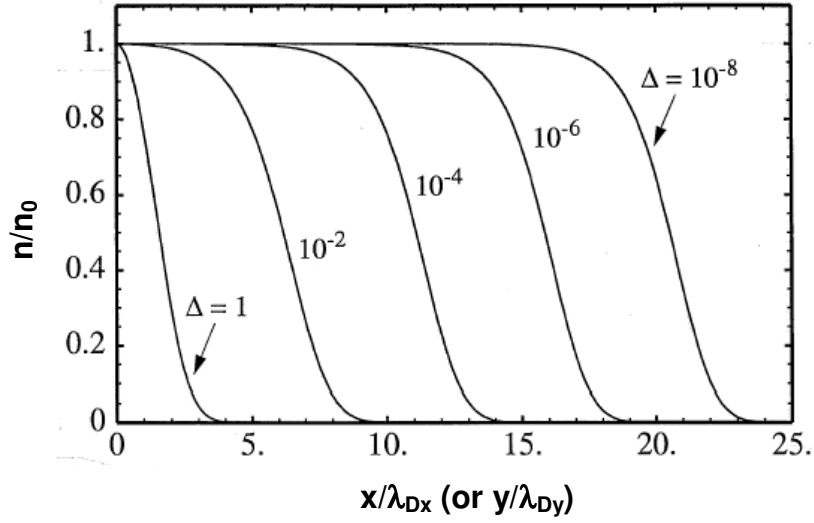
**Figure IX-3**: Density profiles along the principal axes of the beam, modeled by a continuously focused thermal distribution [84].

In Figure IX-3, $\Delta$ is a pure number that is related to the space-charge tune depression of the beam in thermal equilibrium. It is defined as:

$$1 + \Delta \equiv \frac{2\gamma^3 \beta^2 c^2 k_{\beta_0}^2}{\omega_p^2},$$

(Eq. IX-8)

where $k_{\beta_0}$ is defined in (Eq. II-47) and $\omega_p$ is the plasma frequency formed from the on-axis beam density

$$\omega_p \equiv \sqrt{\frac{q^2 n_0}{\varepsilon_0 m}}.$$

(Eq. IX-9)

Note that on Figure IX-3, the rate of fall-off is quasi-independent of $\Delta$, except for values approaching unity. For the HCX beam parameters, $\Delta \approx 10^{-6}$.

185

Based on our measurements, using (Eq. IX-6) and (Eq. IX-7), we find $\lambda_{Dx} \approx$ 0.8-0.9 mm (80%-60% fill factor) and $\lambda_{Dy} \approx$ 0.4-0.7 mm (60%-80% fill factor). Thus, the rate of fall-off calculated is in reasonable agreement with the data (~2-5 mm) and measured beam emittance, though the actual beam is not in thermal equilibrium (Figure IX-4).
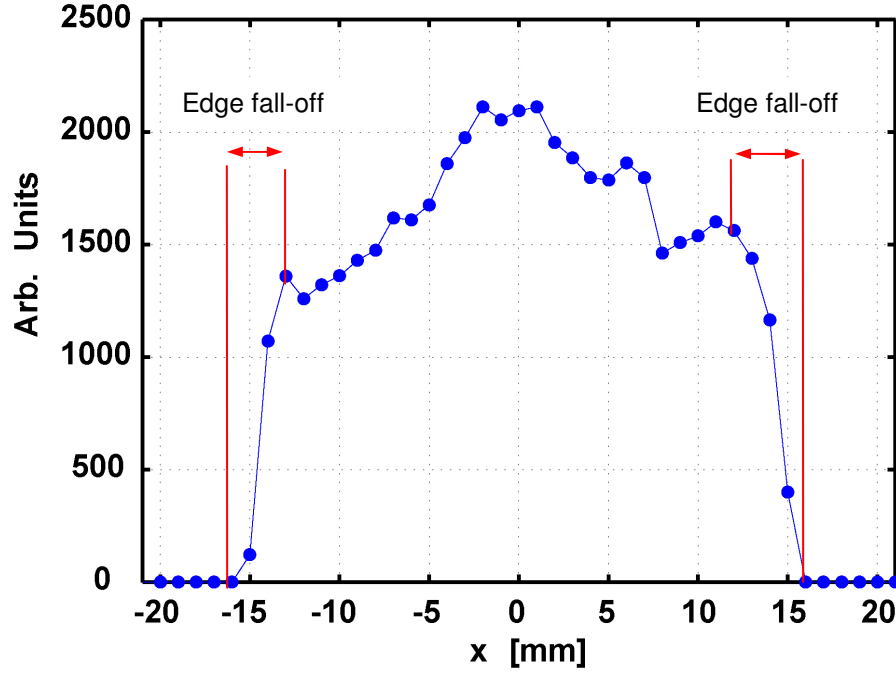


**Figure IX-4**: Line density profile $J(x, y = -2 \text{ mm})$ extracted from the 80% fill factor case current-density map at QD1. The data is summed over 10 time slices ($\Delta t = 1.2$ μs), 2.88 μs after turn on of the beam.

The beam temperature is not the same in both projection planes due to the different beam sizes, so the model predicts that the rate of the beam edge fall-off should be steeper in the vertical (y) direction (diverging, colder at all measurement planes) than in the horizontal (x) direction (converging, warmer at

all measurement planes). However, because of the 1-mm spatial resolution of our current-density maps, the relatively small difference that may exist was not resolved. Moreover, the quantitative interpretation of the data is made more difficult by the presence of dynamics induced halo and space charge waves.

### IX.3.2 -   *Preliminary halo characterization*

Halo measurements using single-slit profiles upstream and downstream of the transport section and for both directions ($x$ and $y$) indicate that the beam profile intensity ≈5 mm from the steep-edge of the beam distribution falls to the order of $10^{-3}$ of the peak density in the core of the beam, the sensitivity limit with present slit-cup diagnostics. This is illustrated in Figure IX-5, which shows single-slit intensity profile measurements of the beam at the exit of the matching section for a 60% fill factor case.
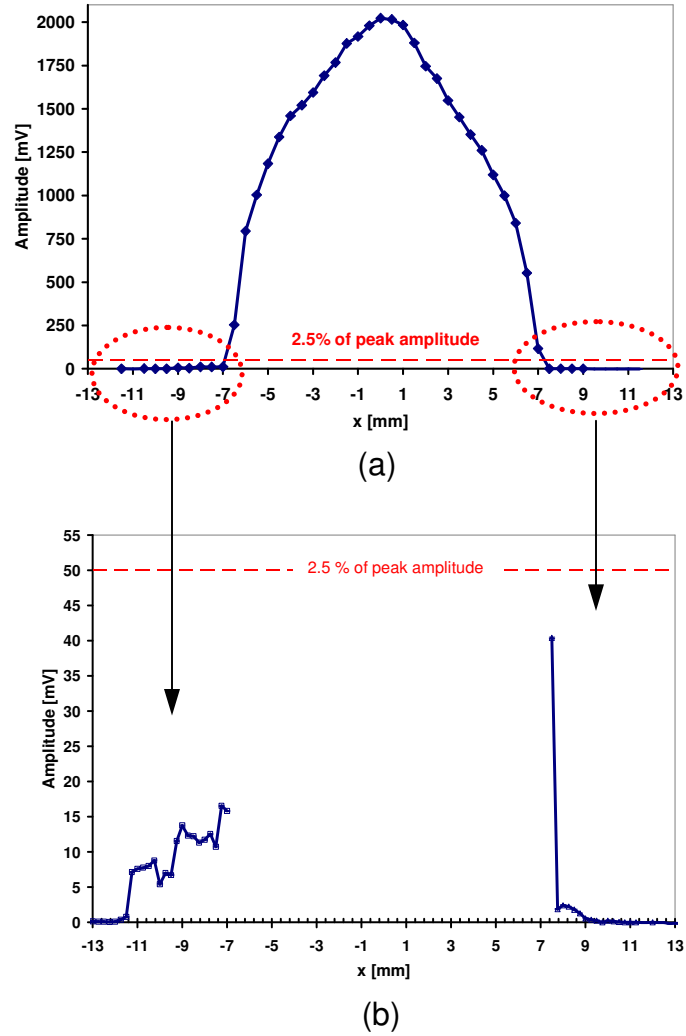
**Figure IX-5**: Single slit profile measurements showing the extent of the halo and our present diagnostics' sensitivity for a 60% fill factor case at QD1 (horizontal direction). (a) is a typical whole beam profile; (b) are partial profiles (acquired close to the beam edges only) with 100x greater gain on the oscilloscope. Error bars are smaller than the plot points.

# Chapter X - Envelope parameters dependence to beam current variations and consequences on their time evolution

## X.1 - Envelope parameters sensitivity to current variations

The head and the tail of the pulse, where the current varies from 0 to 95% of the maximum, have very large systematic variation in envelope parameters, inevitably leading to envelope mismatches. But, partly because of the lower beam current, we find that for the head, the envelope can remain confined with negligible beam loss. However, even between the head and the tail, as much as 50% variations in beam size and angle were observed at QD1 (for a 60% fill factor solution) when the beam current varied by ~15% in early measurements (Figure X-2). The time dependence of the envelope parameters emerging from the matching section are driven by variations in the gate voltage which controls most of the emission (and therefore the beam current) at the beginning of the injector. The trajectories in the injector differ greatly with current when the extraction voltage varies independently of the Marx voltage. This is in contrast to the situation where all injector voltages are scaled together and the trajectories are identical. In addition, as mentioned in Section - VIII.4 -, the sensitivity of the beam envelope parameters to beam current variations also depends on the focusing gradients used in the matching and transport sections since it leads to envelope mismatches with different frequencies. Thus, the location of the measurements and the measurement direction ($x$ or $y$) will exhibit different sensitivities to current variations. Table VII lists typical measured envelope

189

parameters variations at the injector exit and QD1 for a 10% beam current increase and for the two fill factor cases.


**Table VII**: Typical 60% and 80% fill factor envelope parameters variations at the injector exit and QD1 diagnostics station induced by a ~10% beam current increase.

|            | Injector exit | QD1 (60%) | QD1 (80%) |
|------------|:-------------:|:---------:|:---------:|
| $\Delta a$ [%]  | -8   | +3  | +22 |
| $\Delta a'$ [%] | +11  | -27 | -70 |
| $\Delta b$ [%]  | -1.5 | -35 | -38 |
| $\Delta b'$ [%] | -1   | -38 | -58 |


An interesting feature is the asymmetry in the sensitivity to the current variations that exists in between the horizontal and vertical beam size at the exit of the injector and at QD1. In the injector, because the convergence angle of the axisymetric beam exiting from the extraction electrode decreases with the beam current and since the ESQ quadrupole have a fixed transverse focusing gradient for a given Marx voltage, the beam trajectories vary as a function of the beam current extracted. At the exit of the injector, the phase of these 'oscillations' is such that the vertical beam size is insensitive to the beam current variations, in contrast the horizontal beam size exhibits marked sensitivity. Such sensitivities were predicted by 3-D PIC simulations of the injector followed by envelope simulations through the matching section, but a quantitative agreement was not reached.

## X.2 - Time dependence and beam pulse flattening

The strong correlation between beam current and envelope parameters is illustrated in Figure X-1 and Figure X-2, which show measured current waveforms and the corresponding envelope parameters, $b$ and $b'$, before and after extractor waveform tuning, for which the time dependence is significantly different. A time slice, $t_A$, at which the beam current waveforms at the different times intersect (Figure X-1) is identified. The corresponding time slice at QD1 (Figure X-2) is also identified. Note that the measured envelope parameters at this time slice intersect to within the measurement uncertainties.
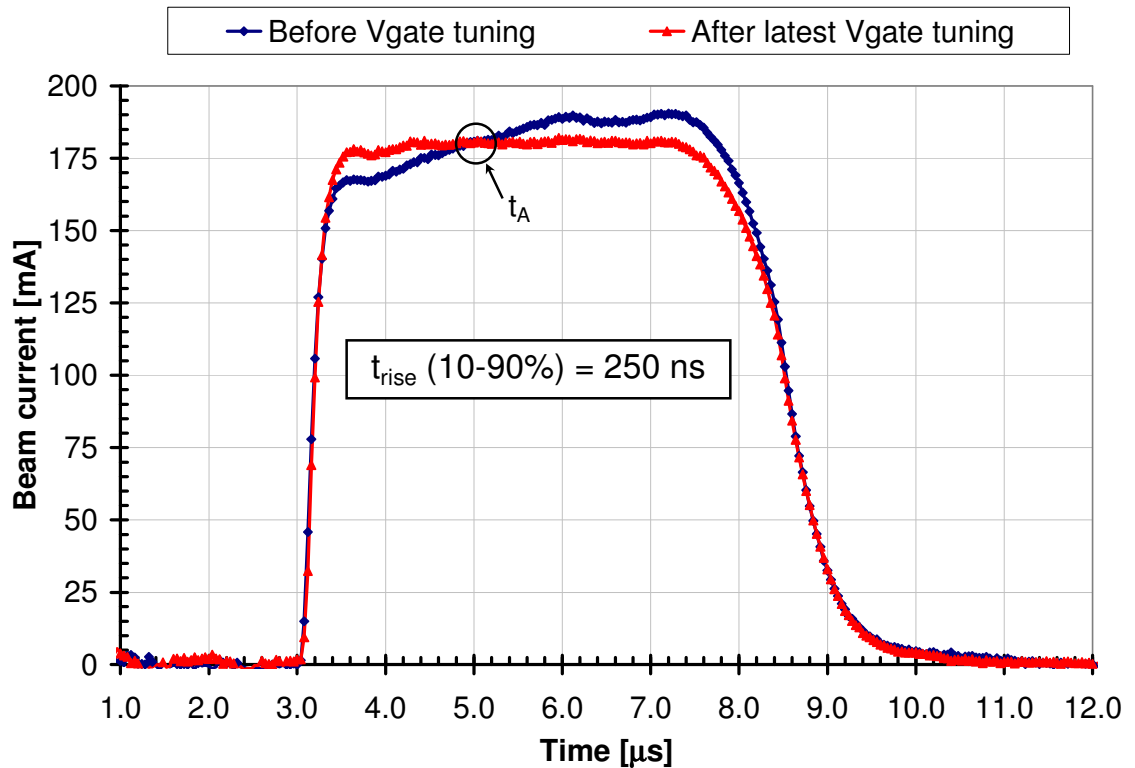


**Figure X-1**: Beam current comparison (before (blue) and after (red) extractor voltage adjustments) measured at the exit of the injector with a current monitor.

We flattened the beam current pulse by tuning the gate voltage pulse. After the corrections, the beam current is flat to within 1.5% over 3.1 µs (Figure X-1). As a result, the beam envelope parameters vary by less than 15% over that same time window.
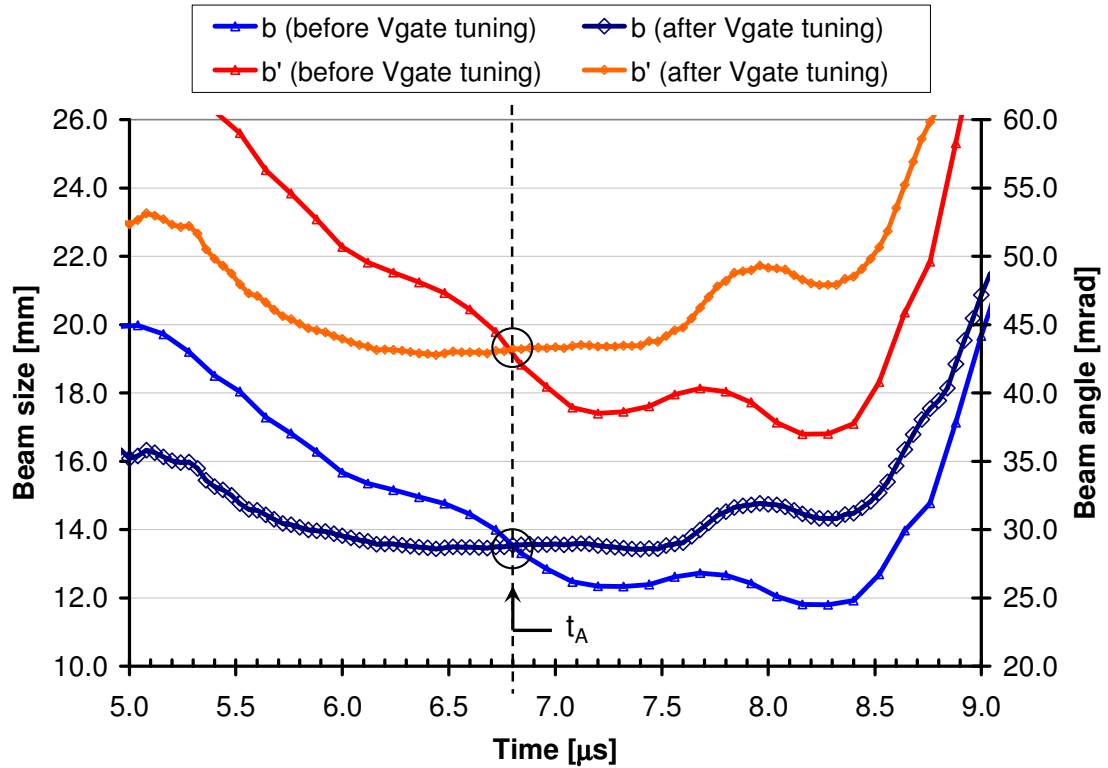


**Figure X-2**: Vertical envelope parameters ($b$ (dark and light blue curves) and $b'$ (red and orange curves)) at QD1 diagnostics station as a function of time before and after the extractor voltage adjustments.

The envelope radii and angles sensitivity to beam current (as well as energy) is important in determining the maximum fill factor since variations in these parameters drive the beam envelope evolution along the bunch length. For instance, if for a given time slice the beam parameters are such that it would

undergo large envelope mismatch oscillations leading to beam scraping somewhere in the lattice, the transport of the rest of the beam bunch would be affected or even prevented. Moreover, the average beam current also drifts by several percents if left uncorrected during an ~8 hour period. This drift is attributed to electronics and possibly material effects in the source. Therefore, beam parameters are also kept constant by empirically adjusting the charge voltage of the gate electrode pulser to maintain a constant averaged beam current.

## X.3 -    Head and tail behavior

### X.3.1 -   *Beam current-density distribution measurements*

The time-resolved crossed-slit data show that at QD1 the profile of the beam during the rise and fall of the beam current pulse is larger than during the flattop (Figure X-3).
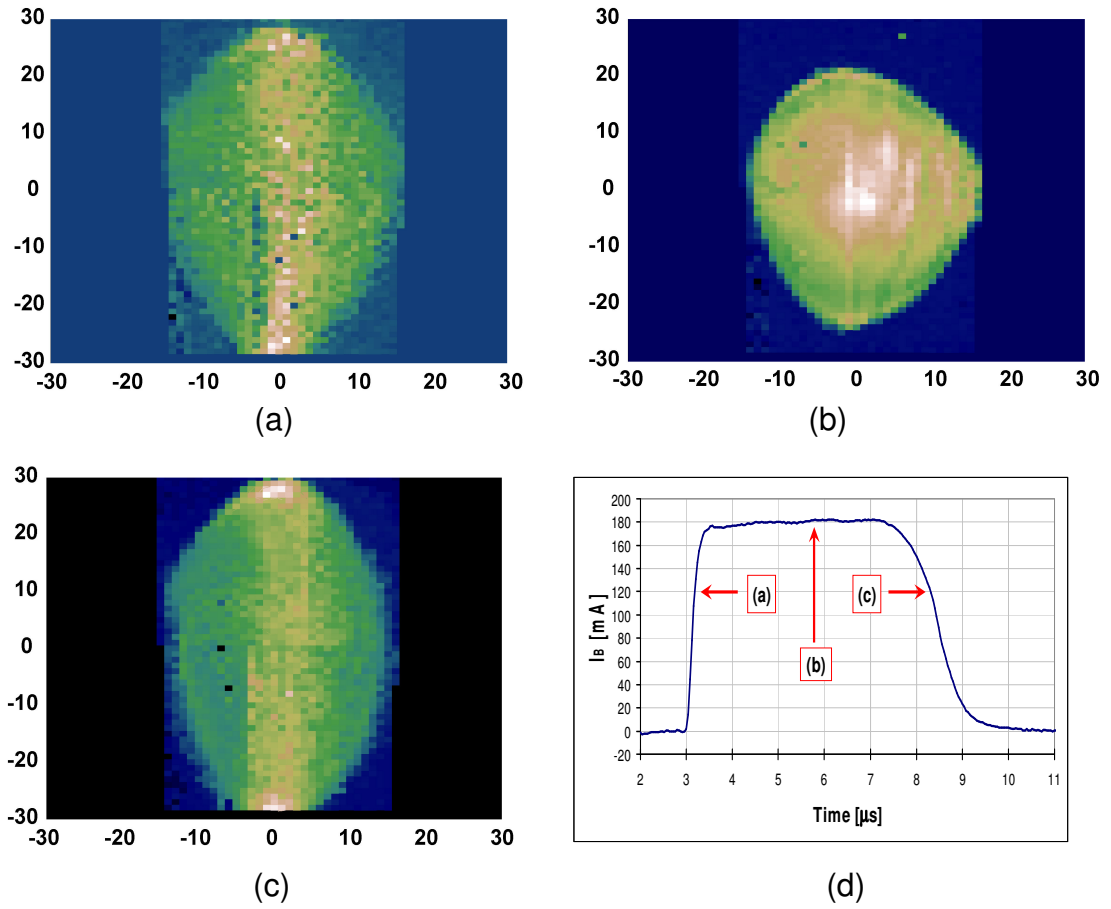
**Figure X-3**: Beam current-density profiles $J(x, y)$ at QD1 for the 80% fill factor case. (a) Head of the beam (0.36 μs after turn on); (b) mid-pulse (3.12 μs after turn on); (c) tail of the beam (5.04 μs after turn on); (d) injector beam current waveform showing the total beam current and locations in the pulse for the density profiles in (a-c). Time jitter is responsible for the noisier pictures in (a) and (c), which were taken over 4000 pulses.

Ballooning of the beam head is predicted for the beam exiting the injector from time dependent 3-D particle-in-cell simulations and is attributed to an extraction voltage rise time in the diode presently too slow to match the space-charge field

194

of the beam head [155,156]. The calculations also suggest that a 50% decrease of the rise time would greatly reduce such ballooning and avoid early scraping in the injector (Figure X-4).



(a)                                        (b)
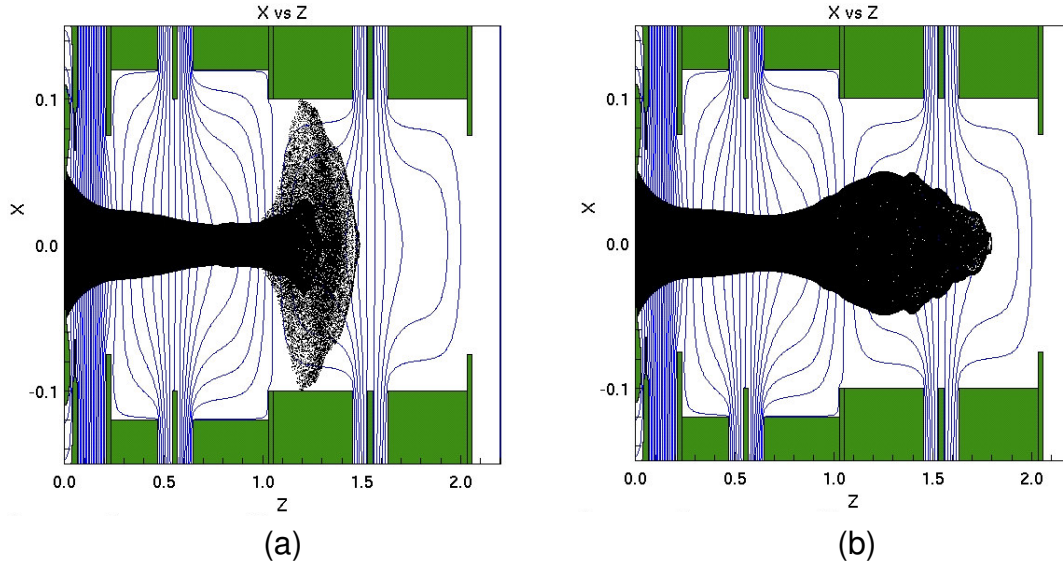
**Figure X-4**: $x-z$ particle projections from two time dependent 3D Particle In Cell (PIC) simulations showing the behavior of the head of the beam pulse according to the extraction voltage rise time for (a) 800 ns extractor pulse rise time (0-100%, close to the experimental rise time) and (b) 400 ns rise time showing a more confined beam head. Actual particle emission only occurs when the field on the emitting surface extracts particles consistent with the applied pulse structure and the geometry [147,156].

The simulations shown on Figure X-4 were carried out using the WARP code, including the 3-D conductor structure of the electrostatic quadrupole injector and self-consistent Child-Langmuir emission [157,158] from the curved

emitter using the voltage profile measured in the experiment (Figure VI-4). These are computationally intensive ($\approx 2 \times 10^5$ particles, grid size $50 \times 50 \times 550$, 0.5 ns time step) first principles simulations of the full beam pulse.

### X.3.2 - *Extraction voltage modifications for a faster rise time*

In an attempt to reduce the beam head size, the rise time of the extraction voltage pulse was decreased by 30% as suggested by the simulations shown above. This was accomplished by reducing the leakage inductance of the isolation transformer (smaller gap between the primary and the secondary coils and smaller number of turns per coil). Beam current measurements made at the exit of the injector with the large beam current monitor showed that the rise time was decreased from 250 ns to 200 ns (10-90%). However, beam current measurements made further downstream (D2) with a Faraday cup were inconclusive. These observations (upstream versus downstream) may not be contradictory, since that the beam pulse erodes (i.e. a longitudinal expansion of the bunch that results in a slower rise time of the pulse, as shown in Section -II.2.4.3 -) as it propagates down the beam line due to its own space-charge. The erosion has been observed in the experiment in upstream vs downstream current waveform comparisons.

In addition to the beam current measurements made downstream, single-slit current-density profiles taken at the exit of the electrostatic transport section did not clearly show that the beam head size evolution was significantly modified (Figure X-5). Note that at this location and this direction (horizontal), the beam head is actually smaller than the middle part of the pulse.
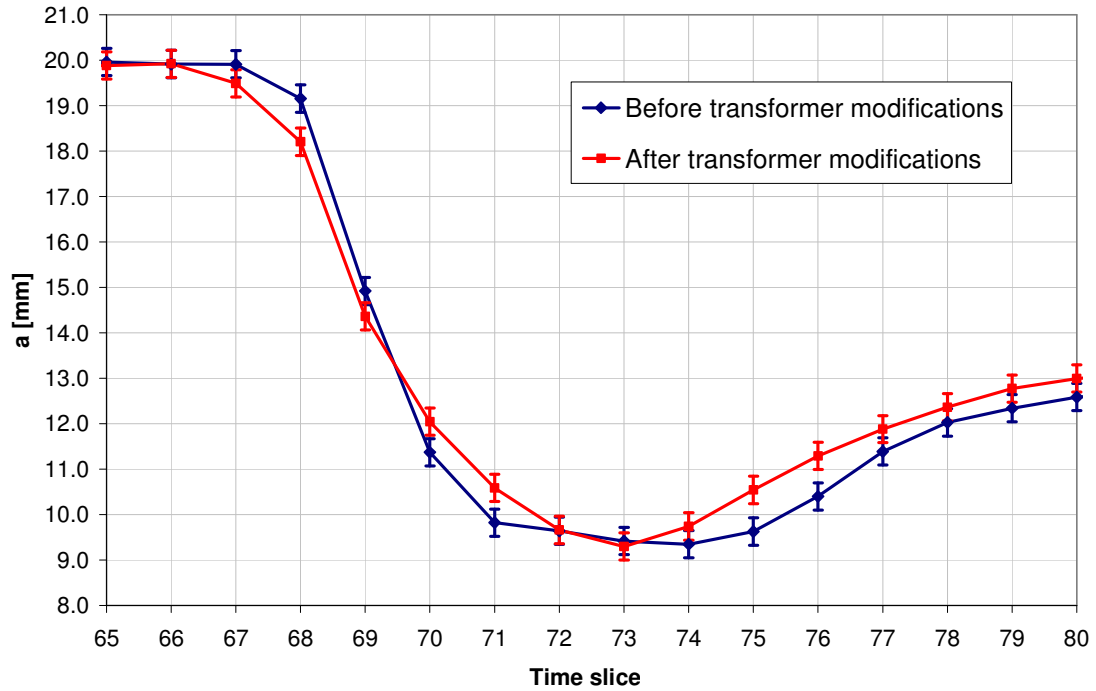
**Figure X-5**: Horizontal envelope beam size as a function of time near the beginning (i.e. head) of the beam current pulse, before (blue) and after (red) modifications were made to the step up transformer to decrease the rise time of the pulse. One time slice represents $\Delta t = 40$ ns. The systematic offset between the two data sets after time slice 74 could be attributed to slight differences in the extraction voltage waveforms since it had to be retuned after the transformer modifications. At early time slices, the value of $a$ is simply determined by the random noise and the size of the scanned region (if the signal was identically zero, only then the calculation of $a$ would give zero).

Note that further reduction of the rise time of the beam current pulse would require major modifications to the source assembly. However, it is possible that the effect of the faster rise time on the beam envelope is obscured by the large

197

compression and mismatch of the head through the matching section, for instance if the head scrapes early in the lattice. It would be interesting to be able to measure the beam at the exit of the injector to verify that the predictions from the simulations hold. Calculations of the head-tail dynamics through the rest of the HCX are underway.

# Chapter XI -       Beam energy study

## XI.1 -       Motivation

Along with the beam current, knowing the beam energy distribution is essential for understanding and controlling the dynamics of the beam throughout the transport channel. For instance, envelope and particle in cell codes both showed that the beam parameters exiting the matching section were very sensitive to the input beam energy. Moreover, small uncertainties in the beam energy can lead to relatively large envelope mismatch in the transport section (Figure XI-1).
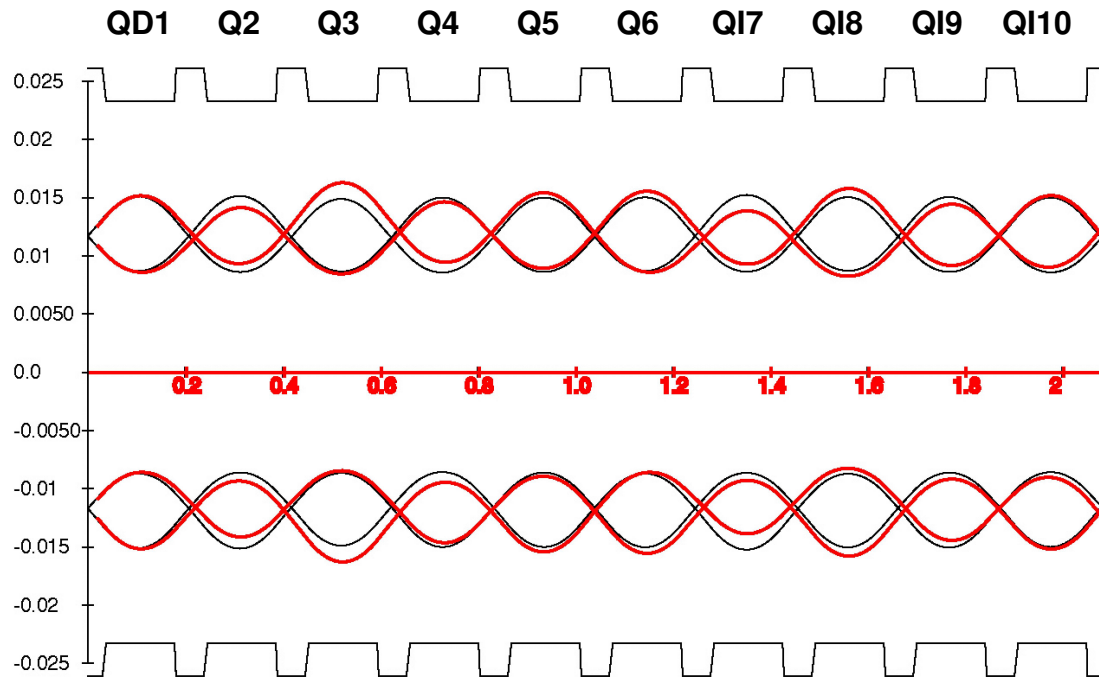


**Figure XI-1**: Simple envelope calculation of the electrostatic transport section illustrating the importance of energy measurement to minimize envelope

mismatch oscillations. Black curves are for a perfectly matched beam. Red curves are for 5% higher beam energy.

Initially, the determination of the beam energy was based on the Marx column calibration. However, the difficulties encountered in the matching section to provide desired beam parameters at its exit and persistent discrepancies between experimental results and simulations revealed a need for a direct beam energy measurement.

The beam energy was measured with two different instruments: An Electrostatic Energy Analyzer (EA) and a specially designed time-of-flight (TOF) pulser (see Section - III.2.2.2.3 -). Both instruments could be used simultaneously and provided independent measurements of the beam energy distribution.

## XI.2 -    Energy Analyzer description and measurements

### XI.2.1 -   Electrostatic analyzer with cylindrical sector field

If we consider a sector-type analyzer [159] of mean radius $R$ and total angle $\Phi$, in the coordinate system described on Figure XI-2, the radial electric field is then given by

$$E = E_0 \frac{R}{r}$$  (Eq. XI-1)

with

$$E_0 = -\frac{2T_0}{eR} \qquad \text{(Eq. XI-2)}$$

where $T_0$ is the beam energy at the entrance of the analyzer.
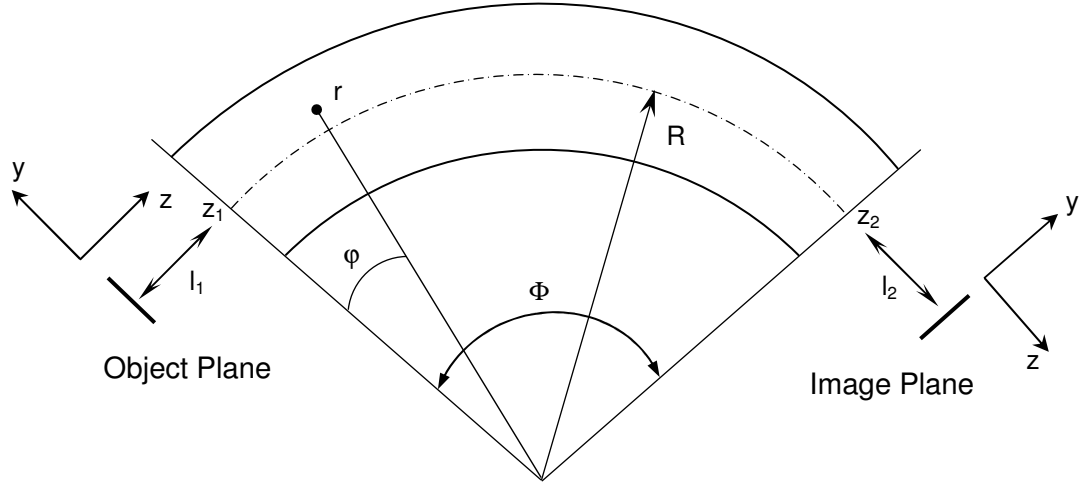


**Figure XI-2**: Sector-field geometry description with coordinate system

The potential is zero on the central path $R$ and outside the sector (neglecting fringe fields). It is also noted that

$$E = -\frac{2T_0}{er} \qquad \text{(Eq. XI-3)}$$

which shows that the energy is $T_0$ for all circular trajectories $r = const$ in the cylindrical field.

Starting from the equations of motion in polar coordinates $(r, \varphi)$:

$$\ddot{r} = r\dot{\varphi}^2 + \frac{eE}{m} \qquad \text{(Eq. XI-4)}$$

$$r^2\dot{\varphi} = const \qquad \text{(Eq. XI-5)}$$

the imaging matrix leading from $z_1$ to $z_2$ is:

$$\begin{bmatrix} y_2 \\ y_2' \end{bmatrix} = \begin{bmatrix} \cos\sqrt{2}\Phi & \dfrac{R}{\sqrt{2}}\sin\sqrt{2}\Phi \\ -\dfrac{\sqrt{2}}{R}\sin\sqrt{2}\Phi & \cos\sqrt{2}\Phi \end{bmatrix} \begin{bmatrix} y_1 \\ y_1' \end{bmatrix}$$  (Eq. XI-6)

along with the dispersion matrix

$$\begin{bmatrix} y_2 \\ y_2' \end{bmatrix} = \begin{bmatrix} \dfrac{R}{2}(1-\cos\sqrt{2}\Phi) \\ \dfrac{1}{\sqrt{2}}\sin\sqrt{2}\Phi \end{bmatrix} \gamma$$  (Eq. XI-7)

where $\gamma$ is the energy spread.

From these, 'standard' focal properties of the instrument are derived and relationships are established between the object $(y_o, z_o)$ and image $(y_i, z_i)$ planes [160]:

$$(l_1 - g)\,(l_2 - g) = f^2$$  (Eq. XI-8)

with

$$y_i = R\,\frac{\varepsilon}{2}\,(1+\frac{f}{l_1-g}) - y_o\,\frac{f}{l_1-g}$$  (Eq. XI-9)

with

$$g \equiv \frac{R}{\sqrt{2}}\cot\sqrt{2}\Phi$$  (Eq. XI-10)

$$f \equiv \frac{R}{\sqrt{2}}\csc\sqrt{2}\Phi$$  (Eq. XI-11)

$$\varepsilon \equiv \frac{E - E_0}{E_0}$$  (Eq. XI-12)

It is also convenient to introduce the magnification $M$ of the instrument define as

$$M = \frac{f}{g - l_1}$$ (Eq. XI-13)

Then, with the beam being limited by a slit of width $w_o$ in the object plane, the imaged slit will have the width $w_i$ such that

$$w_i = -M w_o$$ (Eq. XI-14)

Finally, we can define the analyzer 'intrinsic resolution' as the fractional energy change $\varepsilon$ for which the image is displaced a distance equal to its width and from (Eq. XI-9), we obtain

$$\text{Res} = -\frac{2M}{(1-M)} \frac{w_o}{R}$$ (Eq. XI-15)

### XI.2.2 - Description of the apparatus

XI.2.2.1 - Mechanical description

The spectrometer consists of a 90° sector of two coaxial cylinders (electrodes). The mean radius is $R$ = 45.72 cm and the gap in between the two electrodes is $d$ = 2.54 cm. Figure XI-3 shows the detailed drawing of the analyzer.
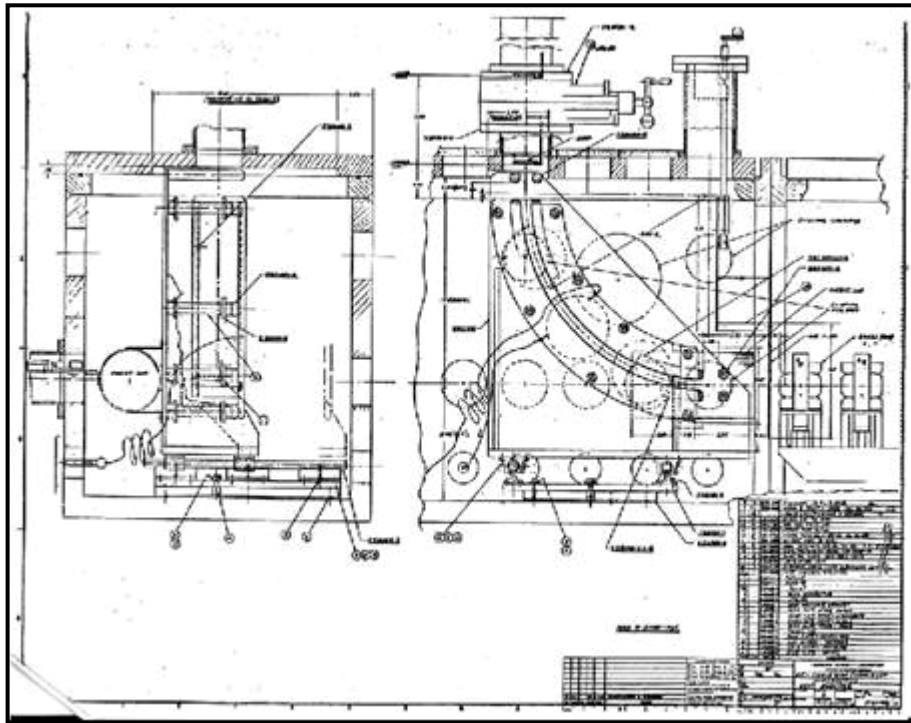
**Figure XI-3**: Mechanical drawing of the Energy Analyzer (LBNL drawing #21B0466).

The beam is apertured by a 500 μm wide slit ($w_o$) at the object plane located 16 cm upstream ($l_1$) of the sector entrance and is collected in a slit-cup 16 cm downstream ($l_2$) of the sector exit, such that the magnification $M$ of the analyzer is equal to -1. The intrinsic resolution (Res) is then 0.11 %. However, to achieve such precision, the alignment of the optical elements (electrodes, slits) is also required to be within 0.1 %.

## XI.2.2.2 - Electrical description

The potential difference to apply to the electrodes in order to bend the particle trajectories follows

$$\Delta V_q \approx \frac{2d}{R} T_0 \qquad \text{(Eq. XI-16)}$$

where $T_0$ is the kinetic energy of the ions traveling on the central path in electron volts and $d$ is the gap between the electrodes.

As mentioned previously, the analyzer was designed to measure beam energies up to 0.9 MeV and therefore requires power supplies capable of delivering up to ±50 kV to the plates accurately. The power supplies are connected to the electrodes through a coupling circuit described in Figure XI-4.
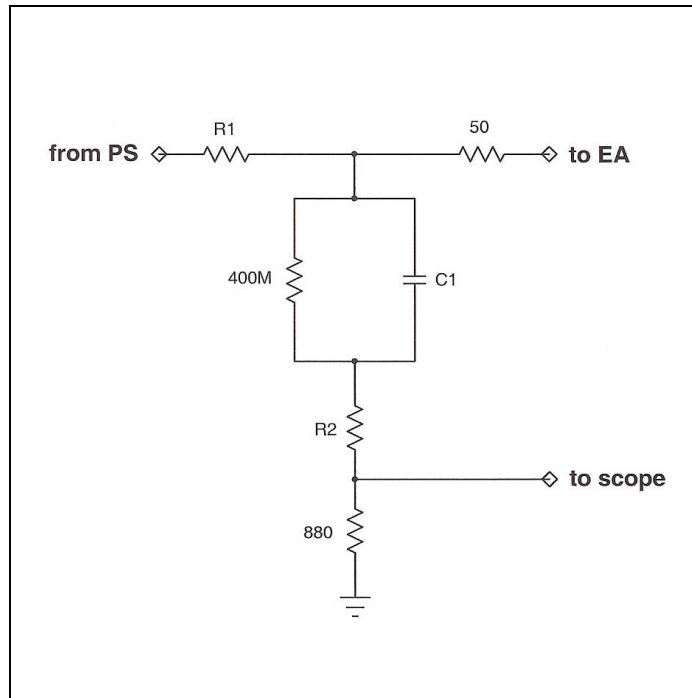


**Figure XI-4**: Schematic of the Energy Analyzer coupling circuit.

The main purpose of this circuit, which is basically just a capacitance in series with a voltage divider, is to protect the power supplies in case of breakdown at the electrodes and to ensure that the voltage remains constant at the electrodes during the beam pulse. It also permits the monitoring of the current drawn at the electrodes.

When particles are lost to the electrodes of the EA, a current is drawn and a time dependent voltage drop results (beam loading). Using again (Eq. XI-9) with $y_o = 0$ and $y_i = d = 2.54$ cm (the distance of the gap between the electrodes), we find that the maximum energy acceptance of our analyzer, $\varepsilon_{max}$, is about 5.5 % (or 55 keV for a 1 MeV beam). But it is expected that the energy variation during the beam pulse exceeds this window, leading to beam loading. Moreover, we used the EA in a slightly different way from the original design prescription [93], as we performed energy scans with a fixed single slit collector instead of setting the analyzer electrodes to a fix voltage and using a multi-wire harp to detect the beamlet current distribution at the focal plane. This procedure increases the amount of particles lost to the electrodes, especially while scanning extremities of the beam distribution since much of it is deflected to scrape the electrodes.

Figure XI-5 shows a typical mean beam energy distribution as it was measured early with the Energy Analyzer. The high-energy head and low-energy tail are understood to be from longitudinal space charge, which accelerates particles at the front end of the bunch and decelerates particles at the rear of the pulse. However, the slow rise in the main part of the pulse was not expected

based on the Marx voltage monitor that indicates that the beam pulse should be flat to within a few percent over 3.5 µs (Section - VI.2.1 -).
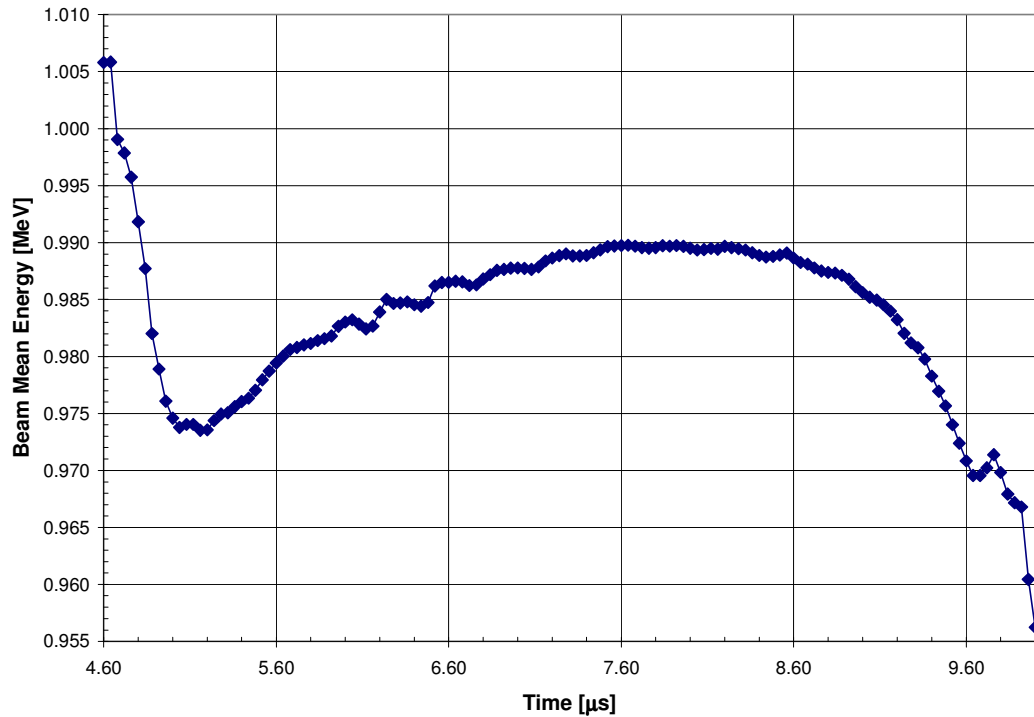


**Figure XI-5**: Preliminary mean beam energy distribution as a function of time.

As the energy scan progresses, ions near the tail of the pulse appear to have a higher energy than the ions belonging to the main part of the beam pulse. This behavior can be attributed to the fact that the effective electrode voltage difference drops as more beam is collected onto the electrodes, forcing to set the electrode potential to a higher level in order to keep these late ions on the central path of the analyzer. By looking at the current drawn on the EA electrodes through the coupling circuit of the charging power supplies, it was found that beam loading could explain this rising behavior.

207

The beam loading effect was first expected to be small since the beam is apertured before entering the EA and the current of the beamlet actually going through the analyzer is about 0.5 mA. But because of a long drift between the last focusing element and the entrance slit, the paddle on which the slit is mounted is not large enough to mask the fairly large beam we obtain at this location. Therefore, some ions strike the EA stands at the bottom of the tank, right beneath the positive electrode. The secondary electrons generated (100-500 mA) are readily collected and induce a large voltage drop on the electrode. This interpretation is confirmed by the asymmetric currents collected on the positive and the negative electrodes of the EA (a factor of 15 for the peak to peak amplitude).

The voltage drop was eventually reduced by lowering the resistance R2 (from 3 k$\Omega$ to 50 $\Omega$) and by increasing the capacitance C1 (from 1.25 nF to 40 nF) of the coupling circuit.
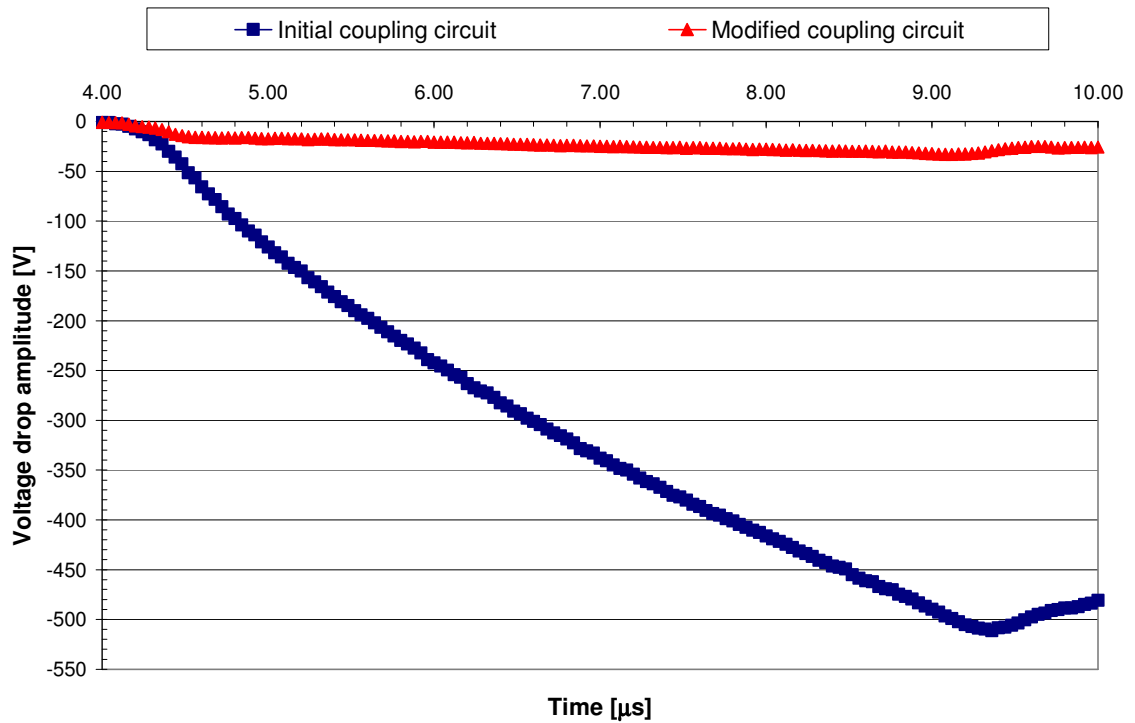
**Figure XI-6**: Voltage drop observed in the initial and modified coupling circuits.

Figure XI-6 shows the total voltage drop as a function of time on the electrodes for the initial and revised circuit configurations. At its maximum (late in the pulse), the improvement reaches a factor of 10 or more (from ~500 V to less than 50 V) for the voltage drop. This ultimately leads to a maximum error of about 0.1% for the electrode voltage. As a result of this improvement, the beam energy distribution appears flatter than initially measured (Figure XI-7), which is consistent with our expectations based on the Marx voltage monitor.
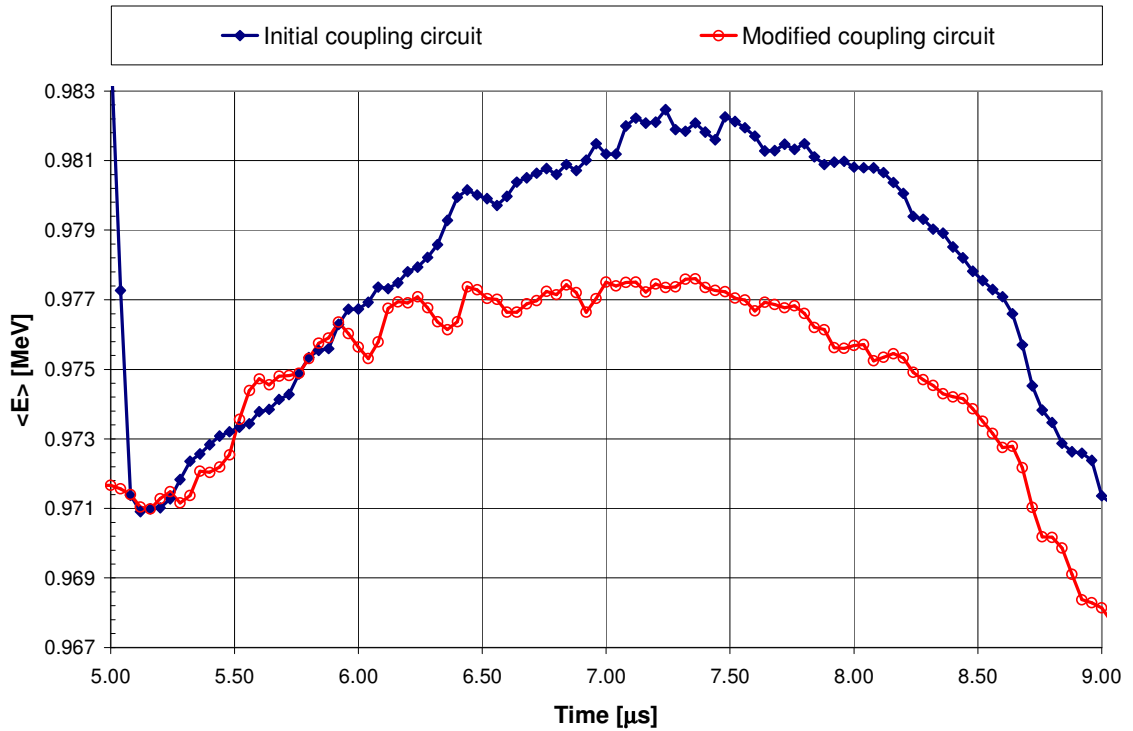
**Figure XI-7**: Beam mean energy distribution as a function of time (middle of the pulse) showing the effect of modifying the electrode coupling circuit.

Another, less significant, modification was made to the coupling circuit as difficulties arose while calibrating the high voltage power supplies. High voltage measurements with typical DC high voltage probes require that the probe impedance be much greater than the impedance of the measured device. For that reason, it was decided to lower R1 (in Figure XI-4) from 7.5 MΩ to 1 MΩ, thereof reducing the uncertainties on the electrode potential determination.

XI.2.2.3 - Additional considerations

*XI.2.2.3.1 -   Space-charge effect*

210

The optics calculations from Section - XI.2.1 - do not include the space charge of the beam. As the beam goes through the cylindrical electrodes, its charge density will alter the external field, which in turn will displace further the focal plane of the analyzer. Therefore, placing the collector at this theoretical focal distance would potentially lead to an increase in the measured energy spread. In SBTE, it was observed that the focal plane of the analyzer could be displaced by as much as 11.68 cm downstream from the expected single particle limit (low-current limit) , which was determined to be 16.26 cm downstream of the exit of the analyzer [161]. In our case, the slit-cup could be displaced by ±6 cm about the calculated focal plane and no scan indicated that the focal spot of the analyzer had been displaced. Simulations using the WARP code, which allows turning on and off the space charge of the beam in the calculations, also showed no effect on the predicted focal point location. Finally, comparing the dimensionless perveance of a ribbon beam going through the EA for the SBTE and HCX beam lines revealed that the space charge forces were stronger by a factor of 2.5 for the earlier case, making it more sensitive to a possible focal spot displacement.

*XI.2.2.3.2 -   Field quality*

Like for space-charge, the fact that field lines extend outside the electrodes in a real device was not taken into account in any of the calculations made in Section - XI.2.1 - and, if not accounted for or corrected for, would change the expected performance of the energy analyzer.

The first issue is to ensure good field quality in between the electrodes. The sector geometry used for the field calculation is obviously an ideal situation and the real field will deteriorate close to the edges (direction perpendicular to the page in Figure XI-2). One remedy is to have the 'corona rings' on the top and bottom electrodes slightly stick into the gap (Figure XI-8(a)). The ≈6.35 mm diameter rings sticking into the gap about 0.76 mm increase the good field region by about 20% over the case with no rings [93].



(a)                                                                 (b)
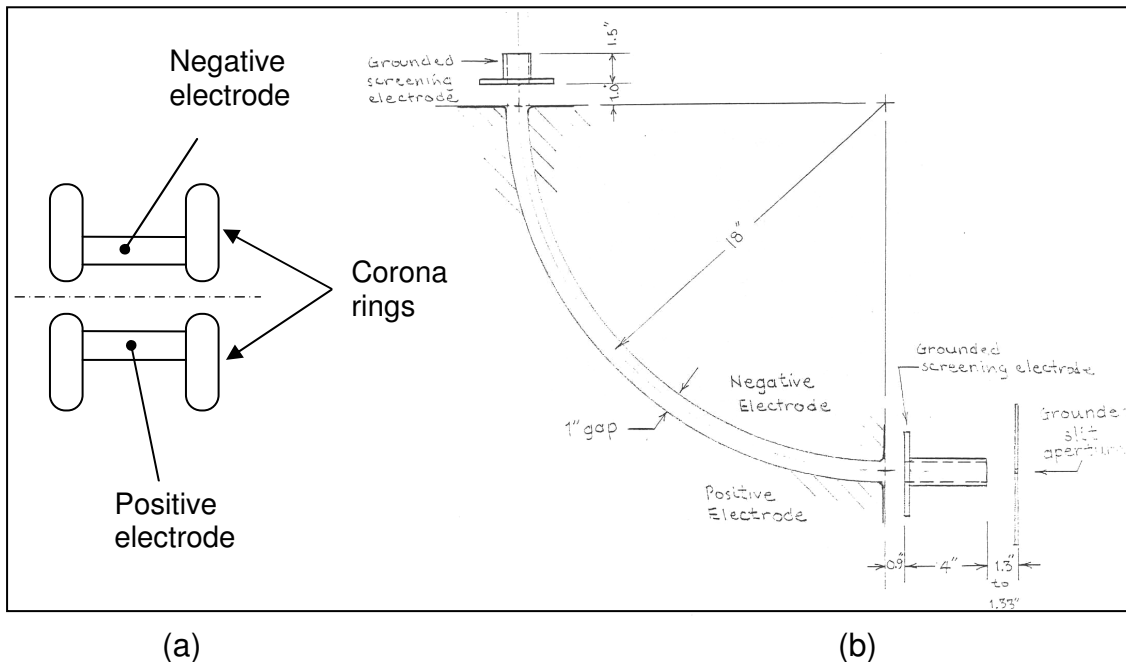
**Figure XI-8**: Sketches of the EA electrode configuration showing the 'corona rings' and screening electrodes. (a) Front view section; (b) side view section.

The second issue has to do with the termination of the fields at the extremities of the analyzer and is commonly addressed by grounded screening electrodes, thereby reducing the effect of these fringing fields on the beam

(Figure XI-8(b)). Considering that the radius $R$ of the analyzer is large with respect to the gap in between the electrodes, the entrance and exit of the sector electrodes can be viewed as half-planes with coinciding edges. Then the field in the gap between the electrodes is homogeneous and takes the character of a field in a $\pi$-sector outside. Therefore, at large distances $l = z_1 - z$, the field strength in the unscreened fringing field is proportional to $l^{-1}$. When a screening electrode is inserted, the effective sector boundary $z_{eff}$ is defined by

$$\int_{-\infty}^{z_0} E_y \, dz = \int_{z_{eff}}^{z_0} E_0 \, dz, \quad (x, y) = (0,0) \qquad \text{(Eq. XI-17)}$$

where $z_0$ is located in the interior ideal sector field (where $E = E_0$) [159].

In our energy analyzer, this effective boundary occurs approximately 0.9 cm out from the electrodes [161]. Interpreted as an effective increased path through the field region, the ideal image plane is then moved ~0.5 cm closer to the cylindrical electrodes' exit.

## XI.2.2.4 - Experimental setup and procedure

The Electrostatic Energy Analyzer was attached to the end of the diagnostic tank such that the entrance slit ended up 1.5 meters downstream of the last HCX quadrupole. A slit-cup detector is located at the image plane of the analyzer with the 100 µm slit being aligned on the center path in between the electrodes. Later on, a 28%-transparent hole-plate (with the capability of being driven in and out of the beam path) was installed 50 cm upstream of the analyzer entrance slit. Its purpose was to provide higher charge state ions for an absolute

calibration of the EA (see following section). A simplified schematic of the setup is shown on Figure XI-9.
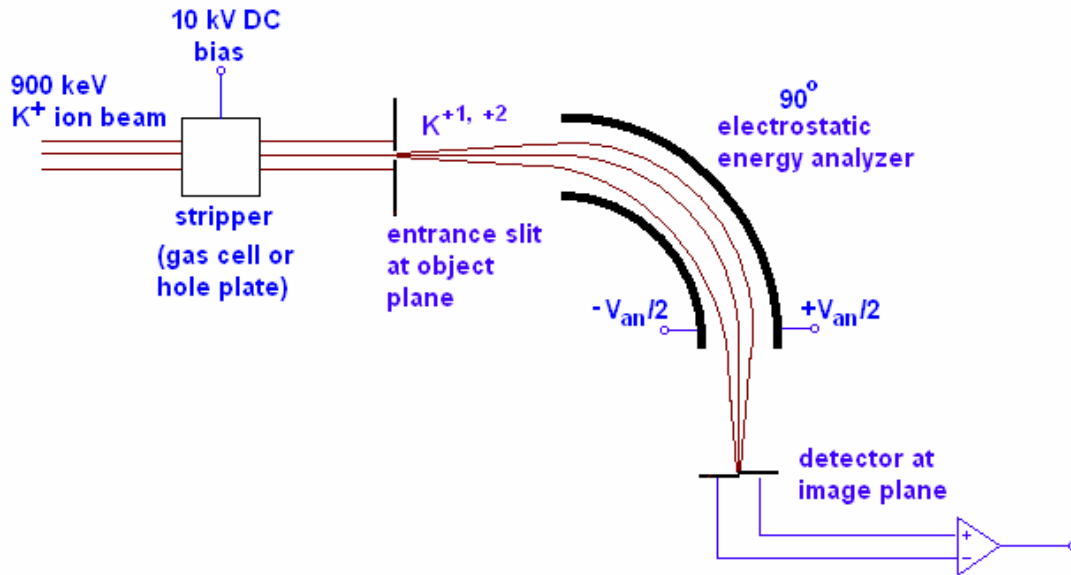


**Figure XI-9**: Schematic of the EA experimental setup.

For each electrode potential difference, there is only one corresponding kinetic energy that represents the energy of the ions traveling on the central path of the analyzer and therefore would be collected in the slit-cup. By varying the electrode potential difference, we then scan the different energy levels that constitute the beam. For each potential difference, the pulse waveform is recorded and saved for further analysis.

This procedure results in measuring the full time dependence of the energy throughout the beam pulse, along with the energy spread for each time slice. From these data the mean beam energy can easily be derived.

### XI.2.3 - *Beam mean energy measurements*

In regards of the HCX research agenda, we were mostly interested in measuring the beam absolute energy to a few percents (or ideally sub-percents) accuracy. However, many factors need to be considered when determining the EA calibration.

XI.2.3.1 - Absolute calibration of the energy analyzer

Typically, precise measurements of the beam energy with electrostatic energy analyzers can only be achieved if the mechanical geometry of the analyzers is known absolutely and the fringe fields understood. In particular, it is difficult to ensure that the gap in between the electrodes remain constant. An uneven gap would affect particle orbits and lead to errors in determining the measured beam energy.

Beam energy measurements also usually depend on the absolute calibration of the power supplies since there is a linear relation between the electrode potential difference and the kinetic energy of the ions traveling on the central path, in our case [integrating (Eq. XI-1) over the gap region]:

$$T\,[keV] = 8.998\,\Delta V\,[kV] \qquad\qquad \text{(Eq. XI-18)}$$

In order to alleviate the issues related to uncertainties in the analyzer geometry due to mechanical tolerances, EA voltage calibration and complex fringe fields, a novel and independent calibration procedure was implemented. It consists in partially stripping the beam into higher charge state ions to which known energy variations can be applied before entering the EA. Comparing the applied energy

with the measured energy offset (i.e. the applied potential difference at the electrodes) provide the independent calibration. This manipulation does not require knowing the exact geometry of the analyzer (or the exact configuration of the electric field) and neither requires knowing the absolute voltage applied to the analyzer electrodes. It 'merely' relies on a good measurement of the energy variation applied to the beam and reproducible output voltages from the electrode power supplies. Then, we can deduce a direct relation similar to (Eq. XI-18) between the beam energy change and the applied potential change.

The extra energy imparted to the beam is done through doubly (or higher) charged ions being accelerated as they are generated. The following sketch shows how, going through a biased hole-plate (stripper), doubly charged ions generated at the plate will end up having an extra kinetic energy equal to the plate voltage whereas singly charged ions kinetic energy will remain unchanged.
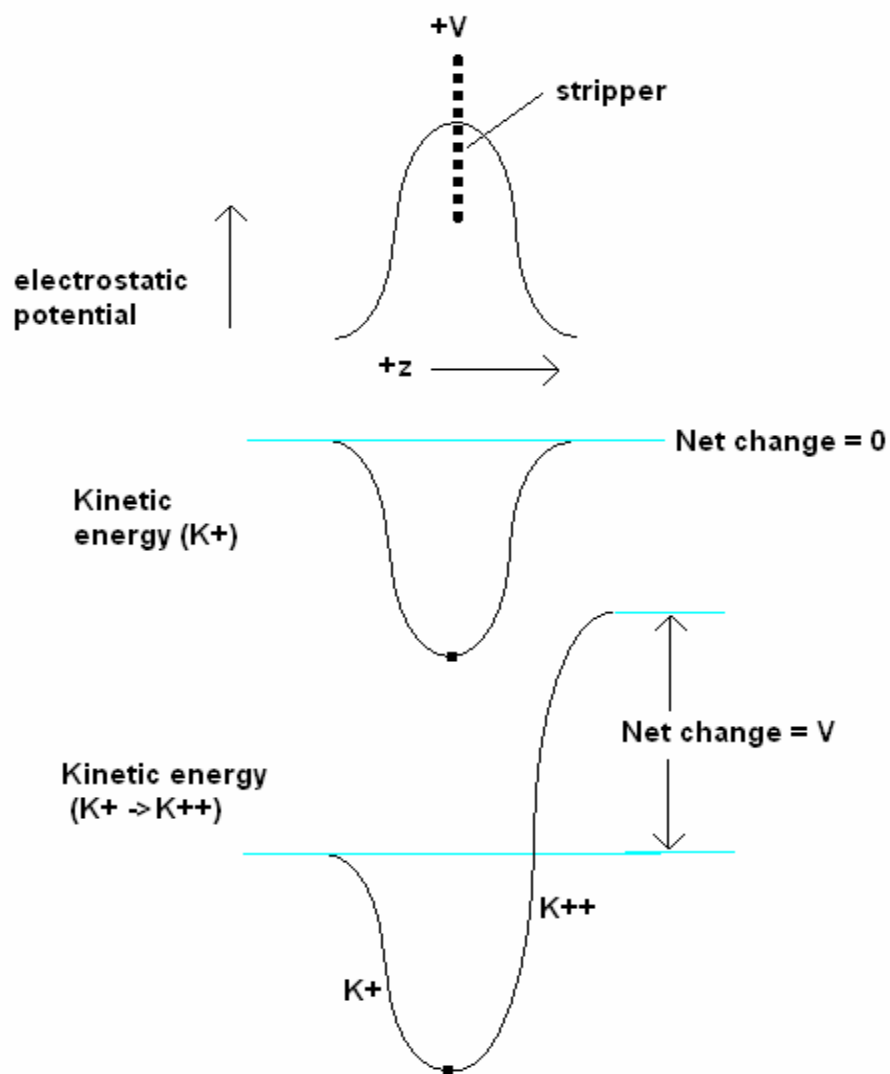
**Figure XI-10**: Schematic description of the way to impart a small energy variation to doubly charged ions generated at a stripper plate.

Preliminary trials indicated that the amount of doubly charged ions generated at the hole-plate would be sufficient to be detected and perform the calibration. It was also observed that higher charge states exist but in much lower abundance

and the signal amplitude at the collector plane would be barely larger than the background noise, therefore making the measurement unreliable.

Then, the calibration procedure consists in acquiring two energy scans of the doubly charged ion energy distribution: one with the hole-plate being grounded, the second with the hole-plate biased to a known voltage (9.20 kV in our case). These energy distributions are shown in Figure XI-11.
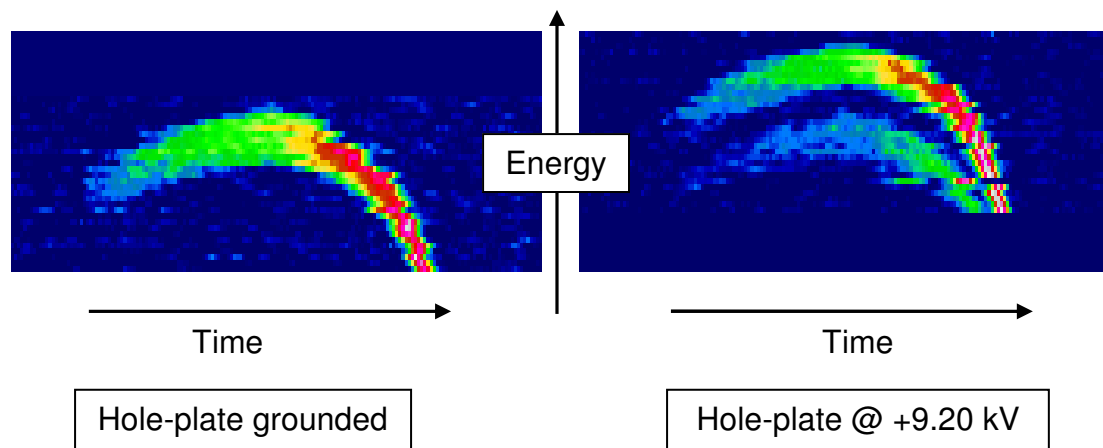


**Figure XI-11**: $K^{2+}$ Energy distribution density plots (blue: low amplitude; red: high amplitude).

The data is plotted such that the energy window is the same for both plots. It is then clear that the distribution acquired with the hole-plate biased is shifted up with respect to the distribution acquired with the hole-plate grounded. Two interesting features should be noted here.

First, when the hole-plate is biased, we observed two distinct distributions. The lower level one is the result of doubly charged ions generated off the entrance slit, which are not accelerated (since not created at the hole-plate).

Second, the signal amplitude gets larger as we approach closer to the tail of the beam pulse (and the high energy head of the beam is not present). This is better shown on the following figure where the energies are summed up and only remains the beam current time dependence for the doubly-charged ions distribution.
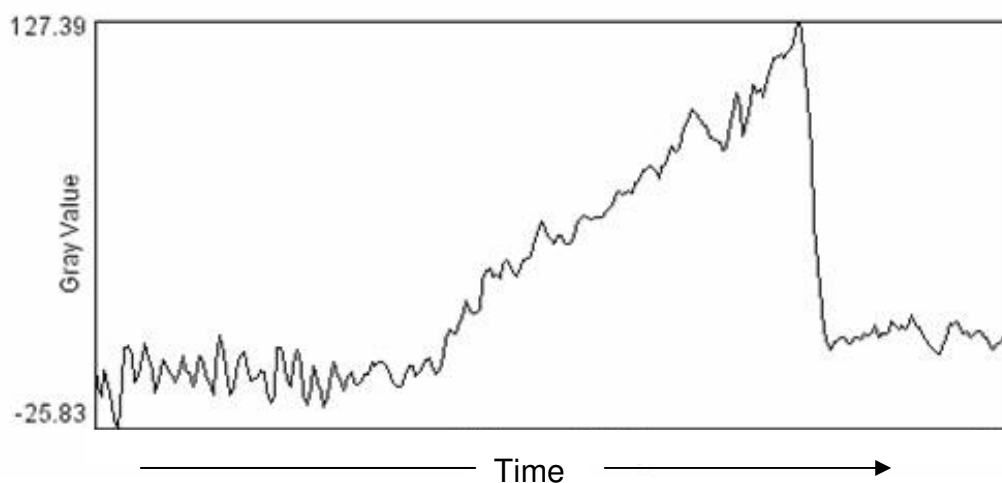


**Figure XI-12**: Reconstructed beam current pulse for doubly charged ions generated at the hole-plate (arbitrary units on vertical axis).

The time behavior shown on Figure XI-12 is consistent with the hypothesis that higher charged state ions are generated by beam-gas interaction. As the beam hits the plate, gas molecules are released and enter the beam path resulting in the linear ramp seen in Figure XI-12. At the beginning of the pulse, few molecules are present and no stripping occurs. As more gas is released, stripping of the singly charged ions takes place and doubly charged ions are created.

The next step in the calibration procedure is to determine the electrodes potential difference offset that resulted from biasing the hole-plate. To do so, a correlation between the two data sets (grounded, $f_1$, and 9.20 kV, $f_2$) was obtained:

$$C\,(\Delta V) = \sum_j \sum_i f_1(V_i, t_j) \cdot f_2(V_i + \Delta V, t_j) \qquad \text{(Eq. XI-19)}$$

where $V_i$ and $t_j$ are the vertical and horizontal data coordinates of Figure XI-11. The maximum of the cross correlation function $C\,(\Delta V)$ defines the voltage offset $\Delta V$ needed to compensate the energy gained by the doubly charged ions generated at the biased hole-plate with respect to the grounded case. The cross correlation results are shown in Figure XI-13.
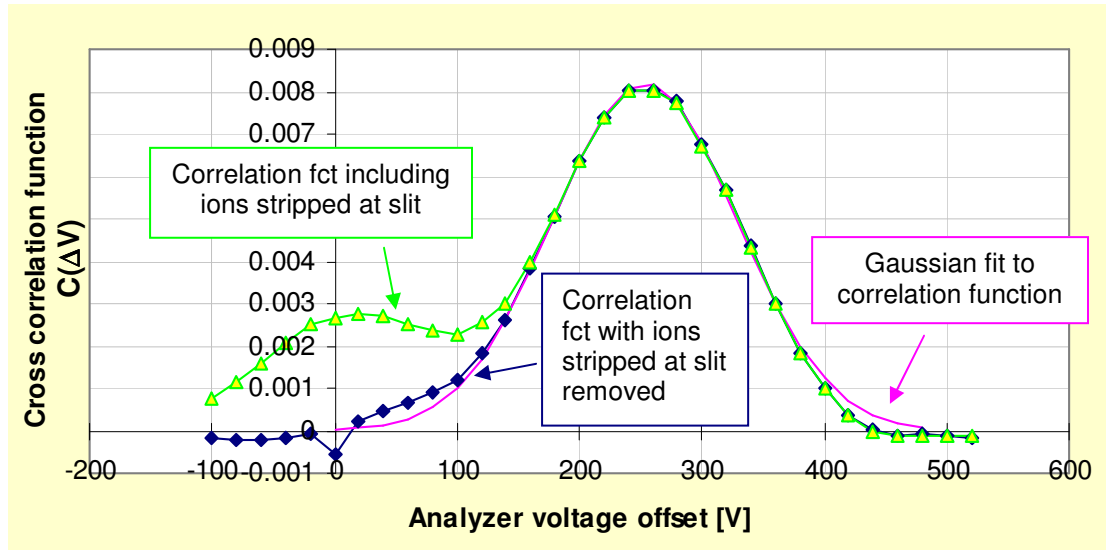


**Figure XI-13**: Cross correlation between grounded and 9.20 kV data sets.

The Gaussian fit (pink curve in Figure XI-13) leads to a well determined mean analyzer voltage offset of 253.8 V for the applied 9.20 kV bias. Allowing for a measured 20 V loading of the hole-plate potential by the beam (i.e. an actual bias voltage of 9.18 kV), the measured gain of the analyzer is then:

$$T\,[keV] = (9.0 \pm 0.1)\,\Delta V\,[kV] \qquad \text{(Eq. XI-20)}$$

The uncertainty quoted in (Eq. XI-20) comes from the accuracy to which the maximum of the correlation function can be determined and the measurement precision of the hole-plate bias, each of about 1%, added in quadrature. Note that the uncertainty of $T$ is then only affected by the linearity and the reproducibility of the applied potential difference $\Delta V$ but not by the absolute calibration of the power supplies. The linearity of the power supplies used with the EA was checked to be better than $10^{-4}$ (accuracy to which the R-squared value, as defined in Microsoft Excel, between the power supplies calibration curve and a linear fit is computed) with day-to-day variations of less than ±0.1 %, both effects being negligible compared to the measured gain uncertainty. Also note that the gain of the analyzer determined through this independent calibration agrees to within 1% of the calculated value based on its ideal geometrical design (Eq. XI-18).

XI.2.3.2 - Mean measurements results

*XI.2.3.2.1 -  Beam energy determination*

Figure XI-14 shows the beam mean energy distribution as measured after the EA was calibrated and errors associated with beam loading eliminated.
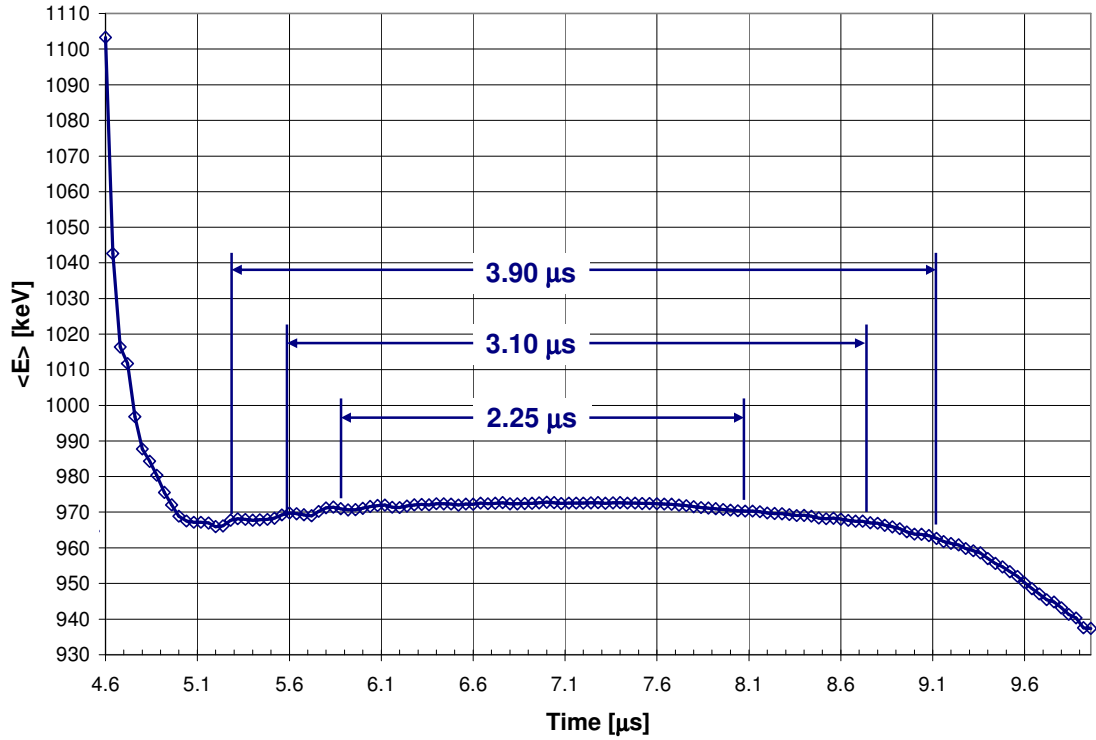
**Figure XI-14**: Beam mean energy distribution as a function of time showing that the energy remains constant for about 4 μs to within 1%. Not shown are the systematic normalization uncertainties based on the absolute calibration.

From this (and the uncertainties associated with the EA absolute calibration mentioned at the end of Section - XI.2.3.1 -), we can determine the beam energy to be 972 ± 13.6 keV (max of flattop). Previous indirect measurements and calibrations were leading towards slightly higher beam energy (more than 1 MeV).

The relative accuracy of the measurements (mostly driven by the digitization of the beam current waveforms) is ±0.2 %, allowing us to follow variations in the beam energy as a function of time during the beam pulse. Then,

along with the absolute beam energy, this measurement indicates that the energy of the beam throughout the pulse is fairly constant, which is a primordial requirement for transporting the entire beam pulse without losses, as energy mismatches will rapidly erode the beam pulse. More specifically, we can see from Figure XI-14 that the mean beam energy remains constant for 2.25 µs to within 0.25 %, 3.10 µs to within 0.5 % and 3.90 µs to within 1 %. For reference, the maximum pulse width achievable based on the Marx column upgrade was a 4.0 µs plateau to within 1% of the maximum [137].

The last feature to be noted for this measurement is the relative energy variations of the head and tail of the pulse. Both the high energy head and low energy tail are expected from the finite rise and fall times of the voltages applied to the extractor plates back at the diode region in the injector. However, 3-D PIC simulations (Figure XI-15) carried out through the injector and matching section only [162], were indicating a somewhat lower relative energy peak for the head with respect to the main part of the beam pulse. Agreement is fair when describing the tail behavior.
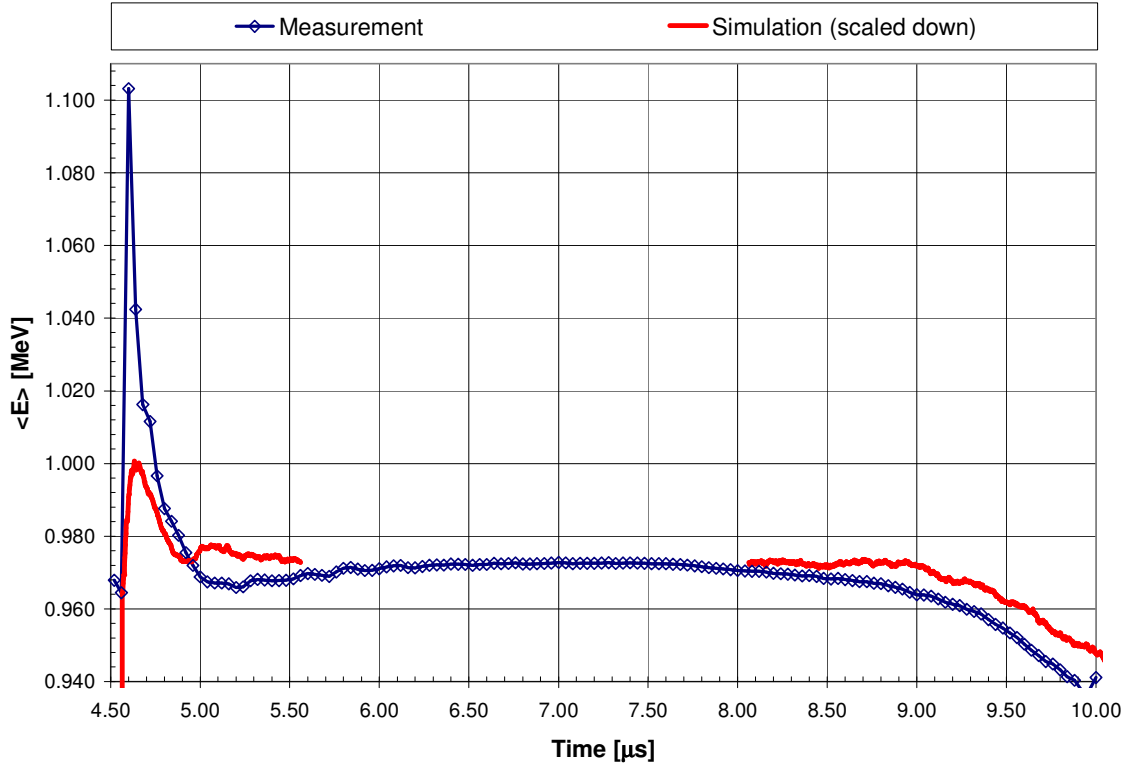
**Figure XI-15**: Beam mean energy comparison: Experimental data versus 3-D PIC simulation [162]. In the simulation, the middle part of the beam was truncated to reduce the computation complexity and not carried out all the way to the point were the data was actually taken.

Even though the simulation was launched using the measured rise and fall time observed in the experiment when switching on and off the extractor voltage, it appears that some efforts remain in modeling the detailed time dependent behavior of the injector system.

*XI.2.3.2.2 - Beam longitudinal emittance*

By design, the Energy Analyzer is a complete diagnostic of the beam energy. We were therefore able not only to determine the beam energy, but also, the energy spread or longitudinal emittance of our beam as a function of time. Each energy scan described in Section - XI.2.2.4 - gives a plot similar to the one shown in Section - XI.2.3.1 - or the one below.
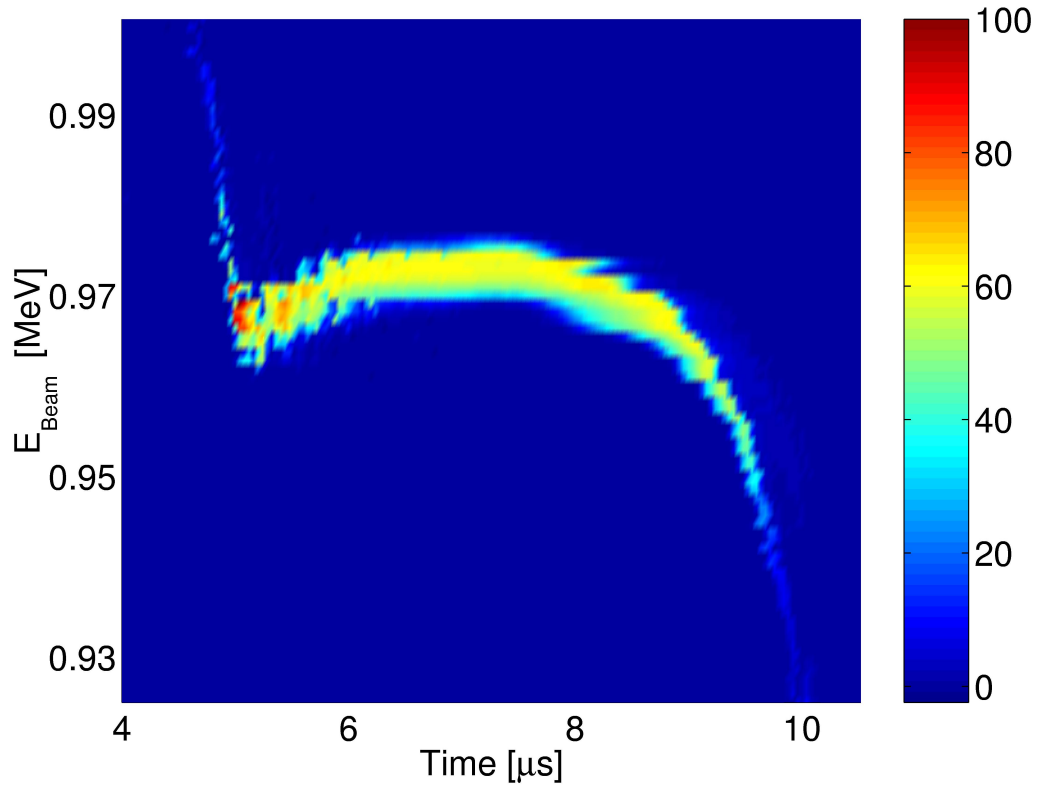


**Figure XI-16**: Longitudinal energy distribution (K$^+$ ions). Ions were detected at the beam head with 1.1 MeV (see Figure XI-15).

Figure XI-16 is the longitudinal 'phase-space' of the beam for the singly charged species (K$^+$) as opposed to the plots from Figure XI-11, which showed the longitudinal 'phase-space' for the doubly charged ions (K$^{2+}$). The differences to be noted here are, first, that the head of the beam is not truncated in the case of

the singly charged ions distribution and, second, that the signal amplitude remains quasi constant throughout the whole pulse. This is true with or without the hole-plate (used for calibration purposes) being in the beam path as $K^+$ ions are not influenced by the formation of the $K^{2+}$ ions at the hole-plate.

For each time slice, the width of the distribution is representative of the energy spread occurring within the beam, sometimes referred as the temperature of the beam. In our case, the width of the distribution in the main part of the pulse is about 9 keV or, expressed as a relative energy variation with respect to the beam mean energy $\frac{\Delta E}{E}$, $\approx 0.9\%$.

More quantitatively, the energy spread can be represented by the second moment of the beam distribution (standard deviation or variance) (Figure XI-17).
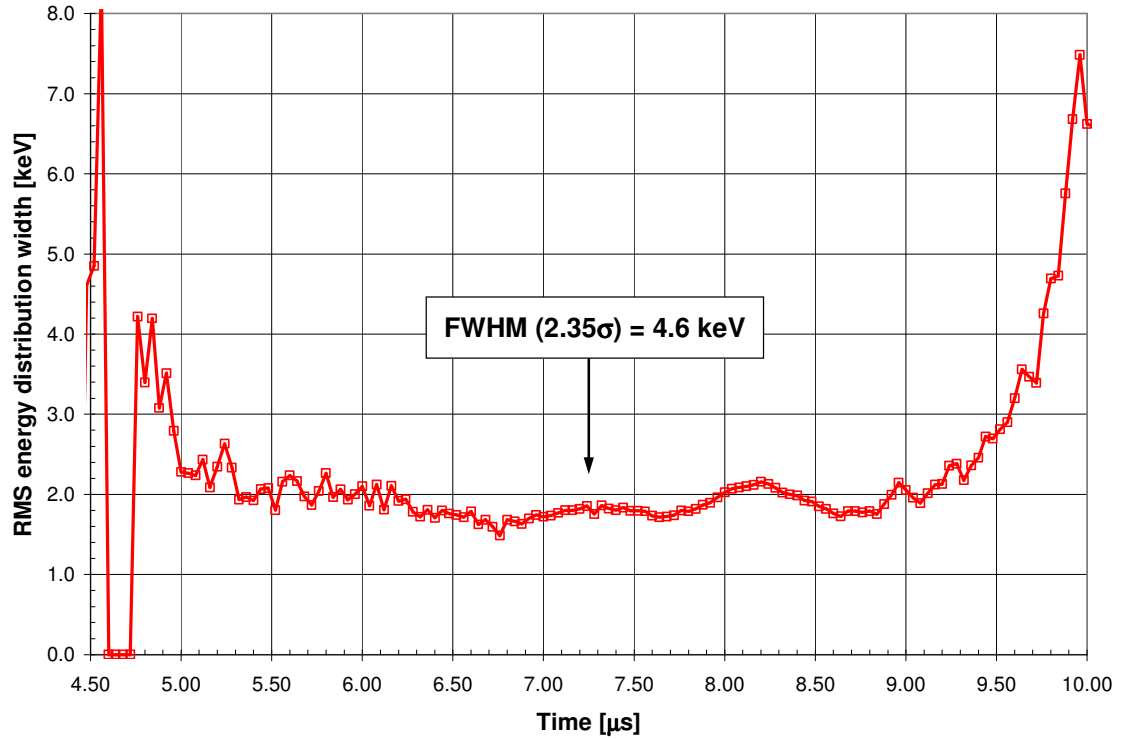
**Figure XI-17**: Beam energy spread as a function of time.

Once again, the large energy spread observed at the head and the tail of the beam pulse was expected. It may however be quite greatly enhanced by the time jitter of the extractor voltage with respect to the Marx voltage.

When designed, the energy spread resolution of the EA was estimated to be of about $\frac{\Delta E}{E} = 0.3\%$ [93]. However, here, partly because the width distribution remained unchanged as the collector was moved in front of or behind the theoretical image plane, it is thought that the energy spread resolution we achieved may be as high as 1%. For instance, the 20 mils entrance slit width alone (assumed to be perfectly aligned with the center path of the EA) accounts

for a 1 keV spread. Rough calculations based on intra beam scattering of the particles (known as the Boersch effect [163]) indicate an expected energy spread of a few electron volts. This is well beyond the capability of the energy analyzer (by at least a factor of 10) and therefore no attempts were made to improve its energy spread resolution.

## XI.3 -    TOF pulser energy measurements

### XI.3.1 -   *Experimental setup and procedure*

The TOF pulser (described in Section - III.2.2.2.3 -) was connected to the first matching section quadrupole such that the space-charge wave could develop for about 5 meters before being measured in the diagnostics tank with either a large Faraday cup or slit-cups, both being used to check the results against one another. Also, all the cables used for data acquisition were timed in order to later compensate for the delays resulting from the signals traveling relatively long distances in between the end of the transport channel and the instruments located in the control room. We also used a delay generator that controlled the time at which the perturbation pulse would be applied to the beam. This allowed us to scan the beam energy as a function of time.

Precisely knowing when the perturbation was applied first thought to be a source of error. It turned out that we were able to use the noise generated by the fast pulser thyratron and picked up on the current monitor waveform (upstream of the first matching section quad) as a time stamp of when the high voltage pulse would occur.

A typical sequence of measurements would simply involve taking a few shots with different time delays for the TOF pulser and record the beam current waveform each time at the end of the machine. A reference pulse (no perturbation applied) would complete the data set. The determination of the time-of-flight, therefore of the beam energy, would happen off line as a few manipulations described next are required.

### XI.3.2 - *Measurements interpretation*

As mentioned previously, the purpose of the imposed perturbation on the beam is merely to help determining the time-of-flight in between two points in the system. To do so, the measured waveforms were compared to the simple space-charge wave model described in Section - II.2.4.2 -.
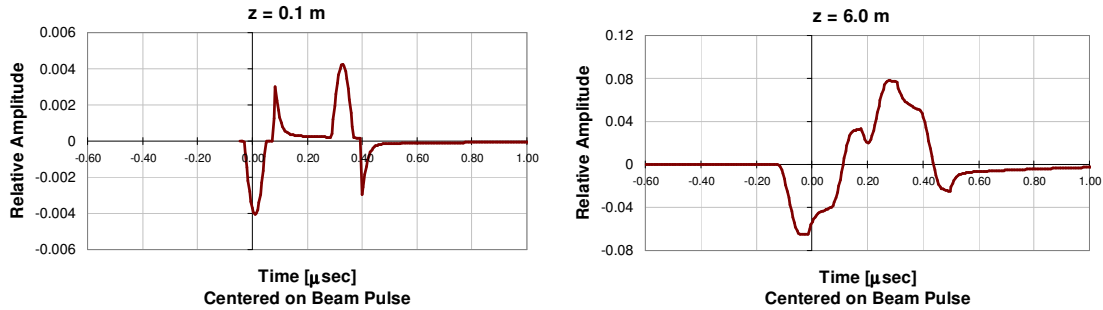


**Figure XI-18**: Space-charge wave in a K[39] beam 10 cm away from the location where the voltage perturbation is applied and at the end of the transport channel. The time ($x$-axis) is taken in the beam frame.

A fit to the actual TOF waveform was used to initialize the calculation. Then, the induced waves are propagated throughout the channel up to the location where

the data are acquired. Figure XI-18 illustrates the output of the calculation by showing the space-charge wave expected 10 cm after the perturbation was applied and six meters downstream. As mentioned when discussing the implementation of the TOF experimental setup in Section - III.2.2.2.3 -, it can be seen that the wave that we obtain by applying the voltage perturbation at the two gaps shown in Figure III-6 is somewhat more complicated than the initial picture only involving one fast and one slow wave. Here, each gap produces such waves that add up and interact as they progress throughout the transport channel leading to the convoluted picture observed at $z = 6.0$ meter downstream of the perturbation location.

The principle of the analysis is to make coincide the measured waveform and the calculated waveform. This is done by varying the beam energy for the calculated waveform as demonstrated in Figure XI-19.
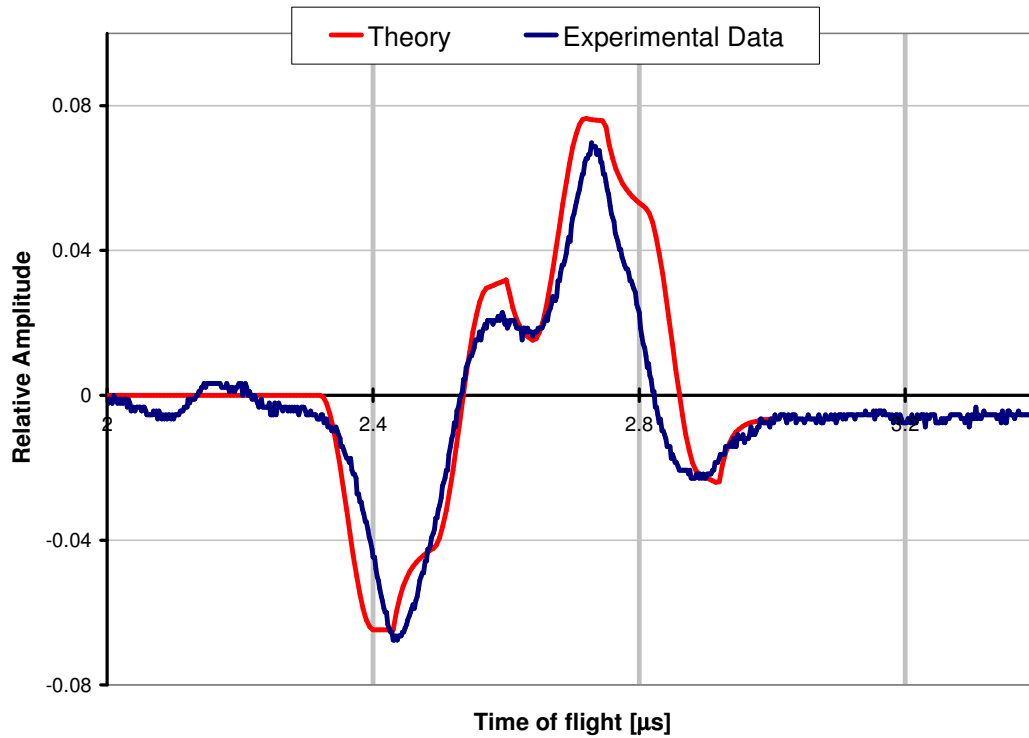
**Figure XI-19**: Comparison between the calculated space charge waveform and the data. The beam energy to reach such good agreement was set to 980 keV. Here, the $x$-axis is the actual time-of-flight (time elapsed after the voltage perturbation was implemented). The upstream voltage pulse waveform and pulsed quadrupole length was input to the model calculation.

When both waveforms closely overlap one another, the beam energy is set. Note that in line with the discussion from Section - II.2.2 -, the 'g-factor' used in the calculation of the predicted waveform was chosen such that the amplitude of the calculated waves and the measured waves match. However, the choice of the 'g-factor' has a minimal effect on determining the beam energy, especially for such a short propagation distance. It merely results in a poorer or better fit of the

theory to the data with respect to the detailed shape of the waveforms, but the main timing features (peaks and valleys) remain unaffected.

### XI.3.3 - *Mean beam energy results*

Several measurements were performed using both the large Faraday cup and the slit-cup available at the end of the transport channel. Results are shown on Figure XI-20.
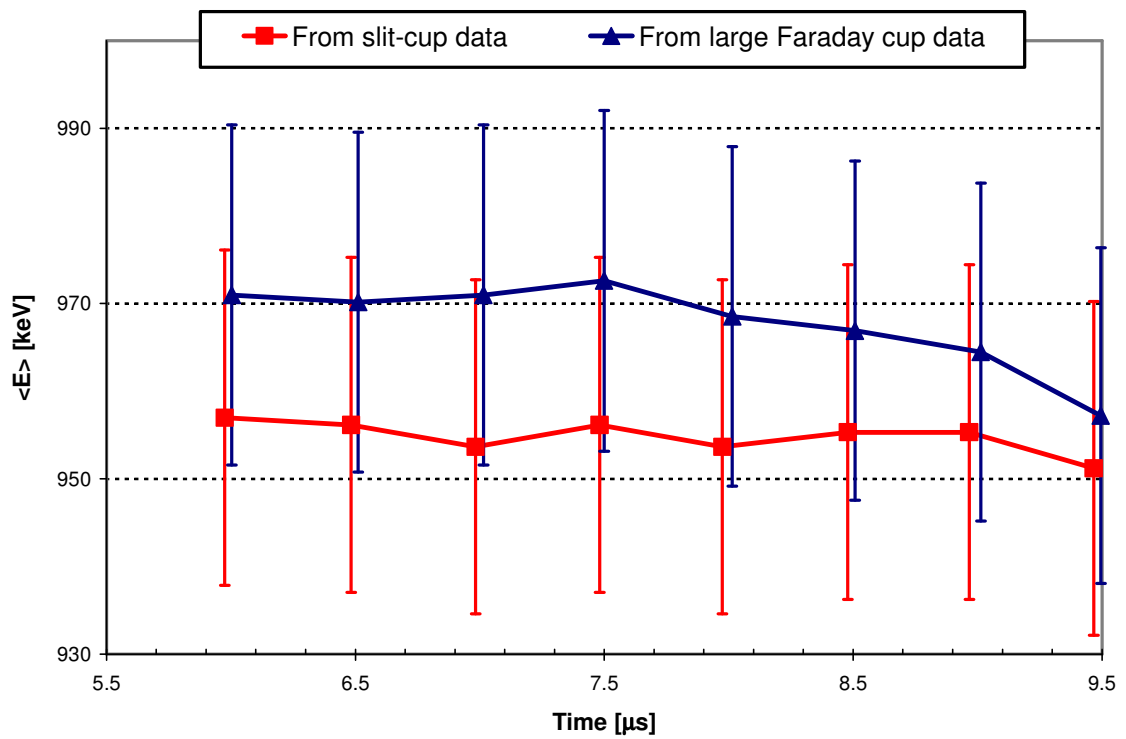


**Figure XI-20**: Mean beam energy as a function of time obtained from time-of-flight measurements.

These measurements indicate that the beam energy is comprised between 950 and 980 keV. The error bars shown above result from various uncertainties on determining the time-of-flight accurately.

First, the procedure described in the preceding section leads to a timing accuracy of 5 to 10 ns (careful timing of the cables included) equivalent to a 4 to 8 keV uncertainty on the beam energy. Then, the axial position survey of the instruments (slit-cups, large Faraday cup) is probably accurate to within 1 cm, corresponding to a 4 keV uncertainty. Finally, when using the large Faraday cup, there is an additional timing uncertainty due to the way deep Faraday cups respond to the presence of beam in their vicinity. Even before actually collecting particles on the collector bottom plate, a capacitive signal is induced when particles are close to the cup structure. Calculations of the field configuration of our Faraday cup showed that the collector plane is 'virtually' located about 1 cm before the entrance of the collector. This must be taken into account when assessing the time-of-flight.

Overall, we estimate that all these uncertainties add up to a ±2% error in the determination of the mean beam energy. However, this estimate is probably an upper limit as, unlike the measurements performed with the EA, each 'time slice' is actually an independent measurement of the beam energy. The very small variations observed on Figure XI-20 from successive time slices indicate the possibility of much smaller errors.

## XI.4 -   Method comparison and conclusions

The goal of the beam measurement campaign was to determine the absolute beam energy as accurately as possible. For that purpose, two independent way of measuring the beam energy were considered and implemented. As shown in Figure XI-21, the agreement between the two methods is very good, well within the error bars of one another.
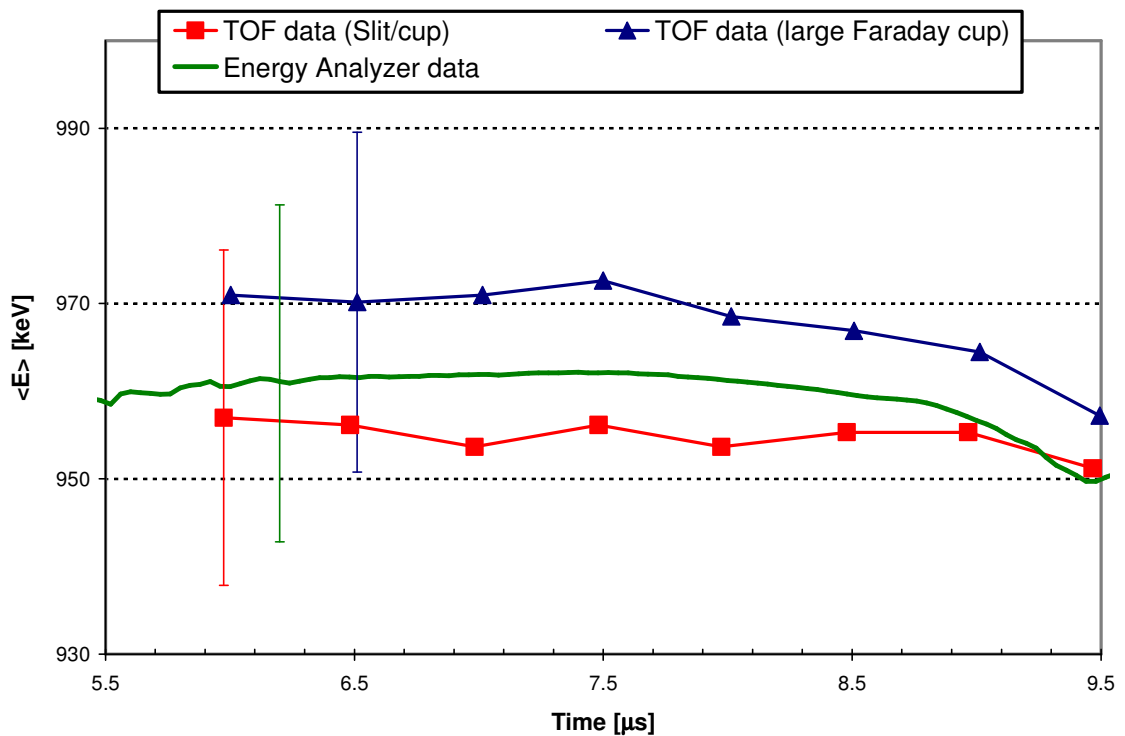


**Figure XI-21**: Comparison between the Time-of-flight and the Energy Analyzer measurements of the beam mean energy.

All three measurements show the same time dependence for the main part of the beam. The head and tail of the pulse could not be characterized with the TOF measurements.

More than simply giving us the absolute beam energy for specific injector settings, these measurements were used to recalibrate the Marx voltage monitor, which is routinely used to measure the beam energy ensuring that we have a good handle of what the beam energy is at any time. It should however be noted that these measurements revealed that the initial calibration was over estimating the beam energy by about 5-7%. This discrepancy remains somewhat inexplicable.

Once the beam energy (and associated calibration) was established, the Energy Analyzer was removed from the system. The Time-of-flight pulser remained and could be used at any time for checking that the calibration of the Marx voltage monitor does not drift with time.

# Chapter XII -     Conclusions

## XII.1 -     Experimental achievements

We successfully improved the optics of the 2-MV injector to deliver a beam compatible with the experiments downstream, with reduced emittance and reduced phase-space distortions. While the current-density distribution remains non-ideal, the final beam normalized emittance is low ($<$ 0.5 $\pi$ mm mrad at the exit of the matching section). The fact that the beam phase space is slightly more distorted in the 60% fill factor case than in the 80% fill factor case might be due to a larger envelope excursion in one or more of the matching quadrupoles (non-linear fields) or dynamical effects related to the beam envelope having a more extreme compression (and larger aspect ratio) in QM5. A detailed understanding of the phase space distribution awaits a better model of the matching section fields and PIC simulations.

The achievable beam envelope and centroid control in the matching section are key ingredients in determining the allowable fill factor in the downstream transport channel. We find that the large transverse compression factors of the matching section result in greater sensitivity to the fringe field of the optics. This renders achieving the target envelope parameters for high fill factor transport in the downstream HCX quadrupoles challenging. Though it often required several iterations, the needed beam control was successfully achieved.

In the electrostatic transport section, the data agree well with envelope calculations that include realistic fringe fields and the effects of the intercepting

diagnostics, which are significant at the level of agreement pursued (<10%, see Table VI). This improved envelope model will improve our ability to manipulate the beam envelope for further experiments, such as launching almost pure envelope mismatch modes (quadrupole or breathing) and to predict the proximity of the 2× RMS beam edge to the bore aperture. The agreement between model and experiment supports the assumption that electrons are promptly swept out of the path of the beam by the focusing electric fields (and measured on the electrode pickups).

The predictions of the beam centroid trajectory over the length of the electrostatic transport section, which requires absolute measurements of any misalignments of the focusing elements and diagnostics with respect to the system center line, are not as accurate (≈3 mm, ≈6 mrad) as the predictions of the envelope parameters (< 0.5 mm, ≤ 3 mrad). Image charges and stray dipole due to asymmetric boundary conditions at the diagnostics while acquiring the data may explain this discrepancy. However, beam steering using 2-3 movable quadrupoles, which requires a good knowledge of the focusing fields and relative displacements of the quadrupoles, is successful at centering. Transport lattice for HIF will have centroid corrections periodically. Understanding the accumulation of centroid errors will be important to determine the frequency of correction elements.

The time dependence of beam parameters is also important when defining the limit of the transportable current. The envelope variations throughout the beam pulse inherently lead to a mismatch that can be severe. Beam stability

throughout the pulse was significantly improved by flattening the beam current waveform. The time-dependence of the beam parameters near the head of the beam pulse shows that good injector waveform rise time is critical for beam matching, since this manipulation of the beam involves rapid envelope transitions and could easily deteriorate the beam bunch uniformity (as a function of time) at the beginning of the accelerator. Time dependent focusing gradients might be possible depending on specifications and cost. At the head of the beam bunch, size and angle mismatch may disrupt the propagation of the rest of the bunch, especially in magnetic focusing transport channels where secondary electrons from halo scrape-off may be trapped in the rising beam potential. Aperturing the beam in order to scrape off the beam head must be done at a few lattice locations where the envelope excursion of the beam head is relatively large and may be implemented in future experiments. An elegant but not trivial solution to minimize the 'ballooning' of the head is to tailor the extraction pulse waveform such that its rise time matches the space-charge field buildup at the emitter.

The velocity tilt for bunch compression at the beginning of a fusion driver in an electrostatic quadrupole transport channel results in a beam whose transverse size increases throughout the bunch (smaller head, bigger tail) while keeping its length constant. Although WARP simulations show that during this manipulation the beam remains nearly matched for all time slices, one must take into account these variations in envelope excursion throughout the beam pulse when assessing the acceptable fill factor, and allow for a range of envelope sizes.

The injected beam is non-uniform and remains so for the length of the present beam line as shown by current-density measurements at D2 (Section - IX.1 -). The non-uniform distribution induces space-charge waves that oscillate as the beam propagates. The current-density distribution differences seen at the exit of the electrostatic transport section between the two fill factor measurements was explained qualitatively using a warm-fluid description of intense beam equilibrium [73], also consistent with a full kinetic treatment for an AG lattice of Hofmann *et al.* [164]. An additional 20-30 quadrupoles would increase the transport length to 4.5-6 times ($2\pi v/\omega_p$) plasma periods and theoretical models predict that this would be just enough for the space-charge waves to phase mix, eliminating most of the phase space and distribution inhomogeneities [150,154,132].

In order to develop the capability to simulate intense beams for accelerator design, details of the measured phase space distribution are being used to initialize particle-in-cell simulations for comparison of data with theoretical models. Prototype diagnostics with scintillator imaging show that the higher data acquisition rates and measurement of all the correlations in the four-dimensional transverse phase-space available with this diagnostic will enhance the theory/experiment comparison.

To study the possible improvements that can be made to the beam longitudinal uniformity, an induction core module will added to the beam line in early summer 2004. It is designed to correct ±20 kV waveform imperfections and also provides 100-200 kV longitudinal focusing voltages to counteract the longitudinal space-charge field at the head and tail of the beam.

Higher fill factors will also be studied. For an induction linac driver comprised of many (~100) parallel beams that should be nearly identical, there will be additional system complexity, alignment and matching issues which have not been addressed explicitly in this experiment. In the context of multiple beam arrays for heavy-ion fusion, electrostatic quadrupoles composed of cylindrical electrodes make a compact unit cell. For the 1-MeV beam measurements, the current-density averaged over a unit cell is $<J> \approx 40$ A m$^{-2}$ (denominator includes the area occupied by the beam focusing electrodes between adjacent channels of an array), and future measurements at 1.8 MeV will increase this by a factor of 2.4, to nearly 100 A m$^{-2}$.

## XII.2 -   Consequences for future designs

The High Current Experiment studies the question of how much clearance is needed to transport high-line-charge-density, high-perveance beams with acceptable beam degradation, and from this also refine the value of the channel size for the transport of the maximum charge averaged over an array of beams. This is important input for the future design of a heavy-ion fusion driver.

The results of transport through the first ten electrostatic quadrupoles indicate that transport with a high beam fill factor ($\approx 80\%$) at the front end of a heavy-ion induction linear accelerator might be possible with acceptable emittance growth and beam loss. This was achieved in a single beam line that includes most of the uncertainties that surround the construction of a full-scale driver (e.g.: manufacturing of components, system alignment, high voltage stability) and the production of a high current beam (current-density non-

uniformities, velocity tilt, halo particles, partial neutralization) except for the uncertainties related to an array configuration. Accurately modeling some of these effects like the behavior of halo and secondary particles that result from interactions with the wall or the background gas, or the actual beam current distribution is where present theoretical and computational efforts are focused. While 10 or 20 quadrupoles are too few for settling questions of emittance evolution in a long transport system, they are of the correct length for the rapid initial evolution of the emittance and beam profile, which is expected in the front end of an accelerator. Whereas filling 80% of the bore radius is not required for a fusion driver, system studies show that the cost dependence of a fusion power plant with respect to the fill factor makes high fill factors very desirable [165]. PIC simulations initialized with a semi-Gaussian distribution indicate that 80% might be a limit of what is achievable [150] as it is near the threshold for particle loss from halo formation.

Designing a future linear accelerator for heavy ion fusion on the basis of the 60-80% fill factor would constitute a significant departure from other linear accelerators, which rarely exceed 50% (at 2σ) in order to accommodate the tail of the Gaussian beam distributions. For example the SNS linac [38,166] or Rare Isotope Accelerator (RIA) [167,168,169] have design fill factors in the range of 30-55%, where the maximum fill factor only occurs over short regions in the lattice. This is illustrated on Figure XII-1, combined with the fact that typically such beams carry ≤ 0.1× the line charge density than beams for heavy-ion fusion.
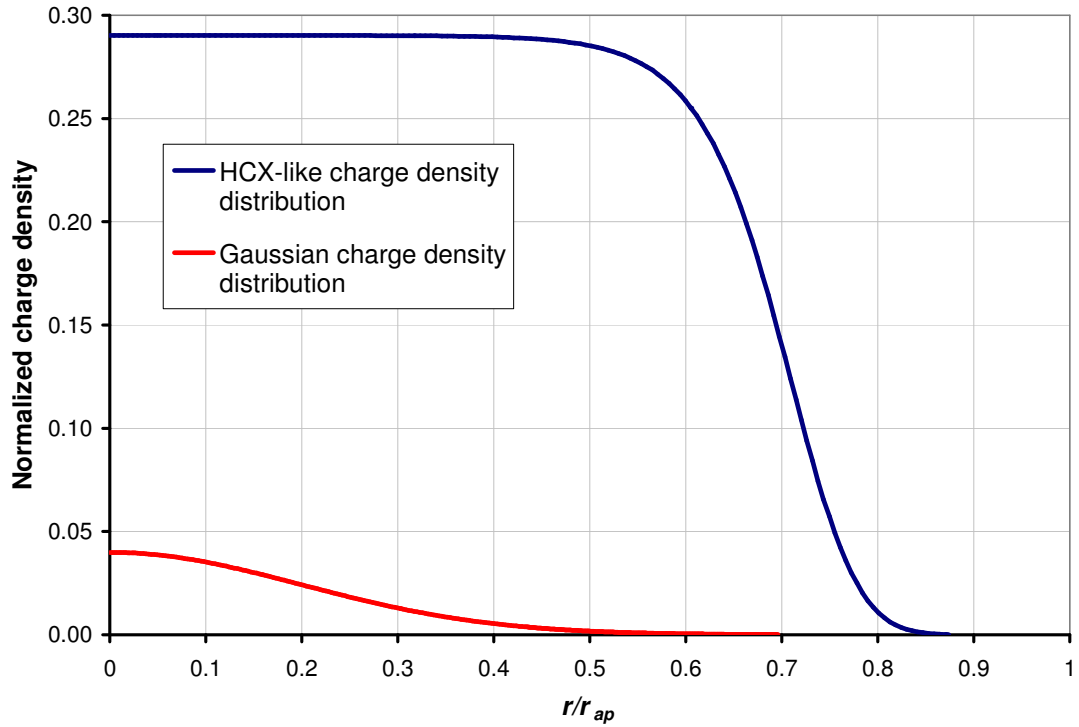
**Figure XII-1**: Typical theoretical current-density profiles for a space-charge dominated beam like HCX ($\sigma/\sigma_0 = 0.2$) (blue) and for a Gaussian current-density profile (red) plotted as a function of the normalized radial coordinate $r/r_{ap}$. The amplitude normalization is such that the integral of the Gaussian distribution is 10 times smaller than the integral of the 'HCX-like' distribution, which is representative of the RIA or SNS beam lines.

Most of a fusion driver will use magnetic quadrupole focusing, due to their increased strength at higher ion velocity. Though the field quality of magnetic [170] and electrostatic lattices may be similar in an integrated sense, field nonlinearities are different in spatial distribution at the lead and return ends. The

useful fill factor in the magnetic lattice will also be influenced by trapped secondary electrons [171], and gas desorption. The influence of gas desorption is mitigated by shorter pulse length at higher ion kinetic energy.

There is a design trade-off between: (a) the frequency of diagnostics, steering and matching adjustments, (b) manufacturing and alignment tolerances, and (c) fill-factor. A higher fill factor will generally require more frequent beam adjustments. In particular, the difficulties we encountered in controlling the beam centroid motion emphasize the importance of measuring and correcting for beam centroid displacements. However, the 80% fill factor results together with additional observations made for misaligned beams at the entrance of the electrostatic transport section (Section - VIII.5 -) suggest that beam steerers may only be needed every ten lattice periods (20 quads, 4.4 m). Note that the beam centroid oscillations are driven by the applied strength of the focusing element, which in our experiment produced $\sigma_0$ < 70°. A fusion driver would probably operate at $\sigma_0$ ≈ 80°, making it more sensitive to misalignment errors and centroid offsets. For comparison, in the SNS linac, the MEBT-CCL section and MEBT-Front-End will have the capability to measure the beam centroid and correct for misalignments every 4-6 quadrupoles (at a fill factor of ≈ 20% at $2\sigma$) [40,172], but in the DTL section, the number of steering dipoles locations is reduced to every 24-25 quadrupoles. At RIA, the design approach was to relax the alignment tolerances to ±2 mm and allow the beam centroid to have a maximum excursion of ±5 mm, with corrections [169] which occur as often as every two focusing solenoids (and eight accelerating cavities).

The calculated maximum envelope excursion is only expected to grow by about 0.1 mm per five lattice periods (Section - VIII.4 -). This result implies that, for RMS envelope control, beam re-matching is not critical for the transport of high fill factor beams over long (50 lattice periods) distances. However, these extrapolations do not address the associated magnitude of emittance growth and halo formation over long distances.

Future plans include a integrated transport experiment with ≈100 quadrupoles such as described in Ref. [173,174,175], designed to explore transverse phase-space dynamics as well as longitudinal phase-space dynamics during compression and final focusing, integrating for the first time several beam physics manipulations required in a fusion driver. It is a necessary step to develop and demonstrate integrated modeling capabilities of all significant beam manipulations from source to target.

# REFERENCES[4]

[1] J. P. Holdren *et al.*, *Exploring the Competitive Potential of Magnetic Fusion Energy: The Interaction of Economics with Safety and Environmental Characteristics*, Fusion Technology **13**, 7 (1988)

[2] A. D. Rossin and T. K. Fowler, eds. *Conversations about Electricity and the Future* (1991). Available through American Nuclear Society, La Grange, Ill

[3] T. K. Fowler, *The Fusion Quest*, John Hopkins University Press, Maryland (1997)

[4] J. L. Bromberg, *Fusion*, MIT Press, Cambridge (1982)

[5] Rainer Feldbacher., *The AEP barnbook DATLIB. Nuclear reaction cross sections and reactivity parameter library and files*, Technical Report INDC(AUS)-12/G Vers. 1, International Atomic Energy Agency, International Nuclear Data Committee, IAEA Nuclear Data Section, Wagramerstrasse 5, A-1400 Vienna, Austria (1987)

[6] J. D. Lawson, *Some Criteria for a Power Producing Thermonuclear Reactor*, in Proceedings of the Physical Society of London, Sect. B **70**, 6 (1957)

[7] J. Sheffield, The Physics of Magnetic Fusion Reactors, Rev. of Modern Physics **66**, 1015 (1994)

[8] R. P. White, *Theory of Tokamak Plasmas*, Amsterdam, North-Holland (1989)

[4] HIFAR notes are HIF internal reports that are not published. HIFAN notes are HIF internal reports that have been turned into LBNL reports with public access through the LBNL Library website.

[9] ITER official website: http://www.iter.org/

[10] J. Lindl, *Development of the Indirect-Drive Approach to Inertial Confinement Fusion and the Target Physics Basis for Ignition and Gain*, Physics of Plasmas **2**, 3933 (1995)

[11] W. J. Hogan, ed. *Energy from Inertial Fusion*, International Atomic Energy Agency, Vienna (1995)

[12] NIF official website: http://www.llnl.gov/nif/

[13] T. J. Dolan, Fusion *Research - Volume 1 - Principles*, Pergamon Press, New York (1982)

[14] M. D. Rosen, *The physics issues that determine inertial confinement fusion target gain and driver requirements: A tutorial*, Physics of Plasmas **6**(5), 1690 (1999)

[15] M. D. Rosen, *Lecture notes for Nuclear Engineering 280: Fusion technology*, University of California, Berkeley (2000)

[16] Lawrence Livermore National Laboratory Lasers Program, *Inertial fusion energy: Opportunity for fusion innovation*, Technical Report UCRL-MI-125743, Lawrence Livermore National Laboratory, 7000 East Avenue, Livermore, CA 94550-9234, (1997)

[17] N. C. Christofilos, *A design for a high-power density ASTRON reactor*, J. Fusion Energy **8**, 97 (1989)

[18] D. Keefe, *Inertial confinement fusion*, Annual Review of Nuclear and Particle Science **32**, 391 (1982)

[19] R. O. Bangerter and R. M. Bock, *Heavy Ion Drivers*, Energy from Inertial Fusion, edited by W. J. Hogan (International Atomic Energy Agency, Vienna, 1995) p. 111

[20] J. Hovingh, V. O. Brady, A. Faltens and D. Keefe, *Heavy-Ion Linear Induction Accelerators as Drivers for Inertial Fusion Power Plants*, Fusion Technology **13**, 255 (1988)

[21] S.S. Yu *et al.*, *An Updated Point Design for Heavy Ion Fusion*, Fusion Science and Technology **44** (2), 266-273 (2003)

[22] Fusion Power Associates, *HIBALL-II — An improved conceptual heavy ion beam driven fusion reactor study*, Technical Report KfK 3840; FPA-84-4; UWFDM-625, Kernforschungszentrum Karlsruhe, Institut für Neutronenphysik und Reaktortechnik, Karlsruhe, Germany (1985)

[23] R. W. Moir et al., *The HYLIFE-II progress report*, Technical Report UCID-21816, Lawrence Livermore National Laboratory, 7000 East Avenue, Livermore, CA 94550-9234 (1991)

[24] D. A. Callahan-Miller and M. Tabak, *A distributed radiator, heavy ion target driven by Gaussian beams in a multibeam illumination geometry*, Nuclear Fusion **39**(7), 883 (1999)

[25] M. Tabak and D. A. Callahan-Miller, *Design of a distributed radiator target for inertial fusion driven from two sides with heavy ion beams*, Phys. Plasmas **5**, 1895 (1998)

[26] G. B. Zimmerman and W. L. Kruer, Comments Plasma Phys. Control. Fusion **2**, 51 (1975)

[27] D. A. Callahan-Miller and M. Tabak, *Progress in target physics and design for heavy ion fusion*, Physics of Plasmas **7**(5), 2083 (2000)

[28] C. Debonnel, D. R. Welch, D. V. Rose, S. S. Yu and P. F. Peterson, *Gas Transport and Density Control in the HYLIFE Heavy-Ion beamlines*, Fusion Science and Technology **43**(3), 408 (2003)

[29] P. A. Seidl *et al.*, *Experiments at the Virtual National Laboratory for Heavy Ion Fusion*, Nucl. Instrum. Methods in Phys. Res. A **464**, 369 (2001)

[30] L. Ahle *et al.*, *Results from the Recirculator Project at LLNL*, Nucl. Instr. Methods in Phys. Res. A **464**, 557 (2001)

[31] P. A. Seidl, C. M. Celata, A. Faltens, E. Henestroza and S. A. McLaren, *Scaled beam merging experiment for heavy ion inertial fusion*, Physical Review ST Accel. Beams 6, 090101-1 (2003), http://prst-ab.aps.org/abstract/PRSTAB/v6/i9/e090101

[32] J. J. Barnard *et al.*, *Induction accelerator architectures for heavy-ion fusion*, Nucl. Intr. Methods in Phys. Res. A **415**, 218 (1998)

[33] S. A. MacLaren, M. de Hoon, A. Faltens, W. Ghiorso and P. Seidl, *Results from the scaled final focus experiment*, Nucl. Instr. Methods in Phys. Res. A **464**, 126 (2001)

[34] W. M. Fawley *et al.*, *Beam dynamics studies with the heavy-ion induction accelerator MBE-4*, Phys. Plasmas **4**, 880 (1997)

[35] M. G. Tiefenback and D. Keefe, *Measurements of stability limits for a space-charge-dominated ion beam in a long A.G. transport channel*, IEEE Trans. Nuc. Sci. **32**, 2483 (1985)

[36] P. A. Seidl and S. M. Lund, *The High Current Experiment: Motivation and Overview*, Private communication (presented during LBNL's AFRD Division review, July 2000)

[37] P. A. Seidl *et al.*, *Overview and Scientific Objectives of the High Current Experiment for Heavy-Ion Fusion*, in Proceedings of the 2001 Particle Accelerator Conference, Piscataway, 2001, edited by Peter Lucas and Sara Weber, (IEEE Piscataway, NJ, 2001), p.2932, http://accelconf.web.cern.ch/accelconf/p01/PAPERS/RPAH037.PDF

[38] M. White, *The Spallation Neutron Source*, in Proceedings of the XXIst International Linac Conference, Gyeongju, Korea, 2002, (Pohang Accelerator Laboratory, Gyeongju, Korea, 2002), p. 1, http://accelconf.web.cern.ch/accelconf/l02/PAPERS/MO101.PDF

[39] A. Ratti *et al.*, *Results of the SNS Front-end Commissioning at Berkeley Lab*, in Proceedings of the XXIst International Linac Conference, Gyeongju, Korea, 2002, (Pohang Accelerator Laboratory, Gyeongju, Korea, 2002), p. 509, http://accelconf.web.cern.ch/accelconf/l02/PAPERS/TU483.PDF

[40] *SNS parameters list*, Report prepared for the US Department of Energy, Office of Science, November 2003, SNS-100000000-PL0001-R10, http://www.sns.gov/documentation/100000000-PL0001-R09.pdf

[41] C. Johnstone *et al.*, *A Proposed 100-400 MeV Beam Facility at Fermilab*, in Proceedings of the 1995 Particle Accelerator Conference, Dallas, 1995, (IEEE, Piscataway, NJ, 1995), p 86

[42] D. Errede *et al.*, *The MUCOOL Test Area Linac Experimental Facility at Fermilab*, in Proceedings of the 2003 Particle Accelerator Conference, Portland, 2003, edited by Joe Chew, Peter Lucas, and Sara Webber, (IEEE, Piscataway, NJ, 2003), p. 983, http://accelconf.web.cern.ch/accelconf/p03/PAPERS/MPPB078.PDF

[43] D.E. Young, V. Dudnikov, M. Popovic, C. W. Schmidt and D. Sun, *Low Energy Improvements to the Fermilab 400-MeV Linear Accelerator*, in Proceedings of the 2001 Particle Accelerator Conference, Piscataway, 2001, edited by Peter Lucas and Sara Weber, (IEEE Piscataway, NJ, 2001), p. 3915, http://accelconf.web.cern.ch/accelconf/p01/PAPERS/FPAH102.PDF

[44] http://www.ipr.umd.edu/ebte/ring/

[45] P. G. O'Shea *et al.*, *The University of Maryland Electron Ring (UMER)*, in Proceedings of the 2001 Particle Accelerator Conference, Piscataway, 2001, edited by Peter Lucas and Sara Weber, (IEEE Piscataway, NJ, 2001), p. 159, http://accelconf.web.cern.ch/accelconf/p01/PAPERS/TOAA008.PDF

[46] S. Bernal *et al.*, *Beam Transport Experiments Over Half-turn at the University of Maryland Electron Ring (UMER)*, in Proceedings of the 2003 Particle Accelerator Conference, Portland, 2003, edited by Joe Chew, Peter

Lucas, and Sara Webber, (IEEE, Piscataway, NJ, 2003), p. 426, http://accelconf.web.cern.ch/accelconf/p03/PAPERS/WOAC006.PDF

[47] W. Meier, R. Bangerter and A. Faltens, *An integrated systems model for heavy ion drivers*, Nucl. Instrum. Methods in Phys. Res. A **415**, 249 (1998)

[48] W. Meier, R. Bangerter and J. Barnard, *A 3.3 MJ Rb$^{+1}$ driver design based on an integrated systems analysis*, Nucl. Instrum. Methods in Phys. Res. A **464**, 433 (2001)

[49] A. W. Molvik *et al.*, *Gas desorption and electron emission from 1 MeV potassium ion irradiation of stainless steel*, Physical Review ST – AB, (to be published)

[50] A. P. Banford, *The Transport of Charged Particle Beams*, Spon, London, 1966

[51] H. Bruck, *Accélérateurs Circulaires de Particules*, Presses Universitaires de France, Paris, 1966; (translated by R. McElroy, Los Alamos Report No. LA-TR-72-10, 1972)

[52] Martin Reiser, *Theory and Design of Charged Particle Beams*, John Wiley and Sons Inc., New York (1994)

[53] H. Wiedemann, *Particle Accelerator Physics I and II*, Second Edition, Springer, Verlag Berlin Heidelberg New York (1999)

[54] S. Humphries, *Charged Particle Beams*, John Wiley and Sons Inc., New York (1990)

[55] D. A. Edwards, M. J. Syphers, *An Introduction to the Physics of High Energy Accelerators*, John Wiley and Sons Inc., New York (1992)

[56] Edward P. Lee, *Kinetic theory of a relativistic beam*, Phys. Fluids, **19**(1) 60 (1976)

[57] David P. Grote. *WARP Manual*, Lawrence Livermore National Laboratory, Livermore, CA 94550-9234, July 1998

[58] I. M. Kapchinsky and V. V. Vladimirsky, *Limitations of proton beam current in a strong focusing linear accelerator associated with the beam space charge*, in Proceedings of the 1959 International Conference on High Energy Accelerators, Geneva, 1959, (CERN, Geneva, Switzerland, 1959), p. 274

[59] L. Jackson Laslett, *Selected works of L. Jackson Laslett*, Technical Report PUB-616, Lawrence Berkeley National Laboratory, September 1987, Volume II, pp. 3-113 – 3-123

[60] P. M. Lapostolle, IEEE Trans. Nucl. Sci. **NS-18**, 1101 (1971)

[61] F. J. Sacherer, IEEE Trans. Nucl. Sci. **NS-18**, 1105 (1971)

[62] Martin Reiser, *Theory and Design of Charged Particle Beams*, John Wiley and Sons Inc., New York, p. 358 (1994)

[63] Edward Lee, *Envelope Relations*, HIFAR 425, January 9, 1994

[64] M. Reiser, *Physics of intense charged-particle beams for heavy-ion inertial fusion*, Fusion Engineering and Design **32–33**, 133 (1996)

[65] Edward P. Lee, *The beam envelope equation — systematic solution for a periodic quadrupole lattice with space charge*, Particle Accelerators, **52**, 115 (1996)

[66] J. Struckmeier and M. Reiser, Part. Accel. **14**, 227 (1984)

[67] Martin Reiser, *Theory and Design of Charged Particle Beams*, John Wiley and Sons Inc., New York, pp. 243-251 (1994)

[68] S. M. Lund and B. Bukh, *Stability properties of the transverse envelope equations describing intense ion beam transport*, Physical Review ST Accel. Beams **7**, 024801 (2004)

http://link.aps.org/abstract/PRSTAB/v7/e024801

[69] J. D. Lawson, *The Physics of Charged-Particle Beams*, Oxford Science, New York (1988)

[70] R. L. Gluckstern, in Proceedings of the 1970 Proton Linear Accelerator Conference, Batavia, 1971, edited by R.M. Tracy (National Accelerator Laboratory, Batavia, IL, 1971), p. 811

[71] R. C. Davidson and N. A. Krall, Phys. Fluids **13**, 1543 (1970)

[72] Martin Reiser, *Theory and Design of Charged Particle Beams*, John Wiley and Sons Inc., New York, pp. 491-492 (1994

[73] S. M. Lund, R.C. Davidson, *Warm-fluid description of intense beam equilibrium and electrostatic stability properties*, Phys. Plasmas **5** (8), 3028 (1998)

[74] Martin Reiser, *Theory and Design of Charged Particle Beams*, John Wiley and Sons Inc., New York, pp. 106-107 (1994)

[75] M. de Hoon, *Drift Compression and Final Focus Systems for Heavy Ion Inertial Fusion*, Ph.D. thesis, University of California, Berkeley, 2001

[76] Philip Francis Meads, Jr., *I. The Theory of Aberrations of Quadrupole Focusing Arrays. II. Ion Optical Design of High Quality Extracted Synchrotron Beams with Application to the Bevatron*, Ph.D. thesis, University of California, Berkeley, 1963

[77] Martin Reiser, *Theory and Design of Charged Particle Beams*, John Wiley and Sons Inc., New York, pp. 252-260 (1994)

[78] L. J. Laslett, *The image-field potential of a uniformly-charged ellipse situated between a set of conducting hyperbolic surfaces*, HIFAN Note 117 (1980). Also LBNL Report: LBID-244

[79] R. Cohen *et al.*, *Stray-electron Accumulation and Effects in HIF Accelerators*, in Proceedings of the 2003 Particle Accelerator Conference, Portland, 2003, edited by Joe Chew, Peter Lucas, and Sara Webber, (IEEE, Piscataway, NJ, 2003), p. 132, http://accelconf.web.cern.ch/accelconf/p03/PAPERS/TOAA010.PDF

[80] A. Cucchetti, M. Reiser and T. Wangler, *Simulations Studies of Emittance Growth RMS Mismatched Beams*, in Proceedings of the 1991 Particle Accelerator Conference, San Francisco, 1991, edited by L. Lizama and J. Chew,

(IEEE,                 Piscataway,                 NJ,                 1991)

http://accelconf.web.cern.ch/accelconf/p91/PDF/PAC1991_0251.PDF

[81] J. M. Lagniel, *On halo formation of space-charge dominated beams*, Nucl. Instrum. Methods in Phys. Res. A **345**, 46 (1994)

[82] R. Gluckstern, *Analytic Model for Halo Formation in High Current Ion Linacs*, Phys. Rev. Letters **73**(9), 1247 (1994)

[83] Martin Reiser, *Theory and Design of Charged Particle Beams*, John Wiley and Sons Inc., New York, pp. 414-428 (1994)

[84] John J. Barnard and Steven M. Lund, *Space Charge Effects in Beam Transport*, Course Notes of the United States Particle Accelerator School held June 4-8, 2001 at Boulder, Colorado

[85] J. Barnard, *Implications of Pulse Voltage Ripple*, HIF Note Number 96-112, September 24, 1996

[86] A. Faltens, E. P. Lee and S. S. Rosenblum, *Beam end erosion*, J. Appl. Phys. **61**(12), 5219 (1987)

[87] J. C. Maxwell, *A Treatise on Electricity and Magnetism*, 3rd edition Vol I, Clarendon, Oxford, 1891

[88] D. Kucerovsky and Z. Kucerovsky, *Analysis of the dynamic Faraday cup*, J. Phys. D: Appl. Phys. **36**, 2407 (2003)

[89] A. Faltens, private communication

[90] D. A. Ward and J. La T. Exon, *Using Rogowski coils for transient current measurements*, Engineering Science and Education Journal, June 1993

[91] D. G. Pellinen, M. S. Di Capua, S. E. Sampayan, H. Gerbracht and M. Wang, *Rogowski coil for measuring fast, high-level pulsed currents*, Rev. Sci. Instrum. **51**, 1535 (1980)

[92] http://www.pearsonelectronics.com

[93] Andris Faltens and Stephen Rosenblum, *Electrostatic Energy Analyzer (EEA) for HIFAR*, HIFAR 17, February 7, 1985

[94] A. Faltens, *Measuring Average Beam Velocity Through Space Charge Waves*, Private Communication, April 26, 2002

[95] M.G. Tiefenback, *Space-charge Limits on the Transport of Ion Beams in a Long Alternating Gradient System*, Ph.D. thesis, University of California, Berkeley, 1986

[96] S. McLaren, *A Scaled Final Focus Experiment for Heavy Ion Fusion*, Ph.D. thesis, University of California, Berkeley, 2000

[97] W. Namkung and Eric P. Chojnacki, *Emittance measurements of space-charge-dominated electron beams*, Rev. Sci. Instrum. **57**(3), 341 (1986)

[98] F. Bieniosek, J. Kwan, L. Prost, P. Seidl, *Imaging of heavy-ion beams on Kapton film*, Rev. Sci. Instrum., **73**, 2867 (2002).

[99] F. M. Bieniosek, E. Henestroza, J. W. Kwan, *Performance of the $K^+$ ion diode in the 2 MV injector for heavy-ion fusion*, Rev. Sci. Instrum., **73**, 1042 (2002).

[100] F. M. Bieniosek, E. Henestroza, J. W. Kwan, *Parametric study of the ion diode in the 2MV Injector*, HIFAR 528, July 12, 2001

[101] F. M. Bieniosek. L. Prost and W. Ghiorso, *Beam Imaging Diagnostics for Heavy-Ion Fusion Experiments*, in Proceedings of the 2003 Particle Accelerator Conference, Portland, 2003, edited by Joe Chew, Peter Lucas, and Sara Webber, (IEEE, Piscataway, NJ, 2003), p. 2524, http://accelconf.web.cern.ch/accelconf/p03/PAPERS/WPPB050.PDF

[102] L. Ahle and H.S. Hopkins, *Gated beam imager for heavy ion beams*, in Proceeding of the 1998 Beam Instrumentation Workshop, Stanford, 1998 (SLAC, Stanford, CA, 1998)

[103] Dehmel, Chau, Fleischmann, Atomic Data **5**, 231 (1973)

[104] M. J. L. De Hoon, W. Fawley, and J. Novotny, *Java Envelope: A code for beam envelope modeling*, Computer program written in the Java programming language, based on the Basic code "*Rematch*" written by K. Hahn, and converted to Fortran by C. M. Celata

[105] http://www.microsoft.com/Excel

[106] D. P. Grote, A. Friedman, I. Haber, W. Fawley and J.-L. Vay, *New Developments in WARP: Progress Toward End-to-End Simulation*, Nucl. Instr. Methods in Phys. Res. A **415**, 428 (1998)

[107] Alex Friedman, David P. Grote, and Irving Haber, *Three-dimensional particle simulation of heavy-ion fusion beams*, Phys. of Fluids B **4**(7), 2203 (1992)

[108] David P. Grote, *WARP Manual*, Lawrence Livermore National Laboratory, 7000 East Avenue, Livermore, CA 94550-9234 (1998)

[109] Guido van Rossum, *Python 1.5.2*, www.python.org, June 1999, Copyright 1991–1995 Stichting Mathematisch Centrum, Amsterdam

[110] K. Birdsall and A. Bruce Langdon, *Plasma Physics via Computer Simulation*, McGraw & Hill, New York, 1985

[111] D. P. Grote and A. Friedman, *3D simulations of axially confined heavy ion beams in round and square pipes*, Particle Accelerators **37–38**, 141 (1992)

[112] R. W. Hockney and J. W. Eastwood, *Computer Simulation using Particles*, McGraw & Hill, New York (1981)

[113] Zane Mottler, Lee Busby, and Fred N. Fritsch, *The Python Graphics Interface, Part IV: Python Gist Graphics Manua*l, Lawrence Livermore National Laboratory, 7000 East Avenue, Livermore, CA 94550-9234, (1998). UCRL-MA-128569, Manual 4.

[114] C. M. Celata, I. Haber and D. P. Grote, *PIC Simulations of the Beam Dynamics Experiments Planned for the High Current Experiment*, in Proceedings of the 2001 Particle Accelerator Conference, Piscataway, 2001, edited by Peter Lucas and Sara Weber, (IEEE Piscataway, NJ, 2001), p.2926, http://accelconf.web.cern.ch/accelconf/p01/PAPERS/RPAH033.PDF

[115] A. Friedman, D.P. Grote, C.M. Celata, and J.W. Staples, *Use of projectional phase space data to infer a 4D particle distribution,* Laser and Particle Beams **21**(1), p. 17 (2003)

[116] D. Keefe and S. S. Rosenblum, *Berkeley Research Program on Ion Induction linacs for Inertial Fusion*, in Proceedings of the Symposium on

Accelerator Aspects of Heavy Ion Fusion, Darmstadt, Germany, 1982, p. 161. (GSI-82-8)

[117] HIF Staff, *A Proposed Program to Develop Linear Induction Accelerator Technology in Support of the National Accelerator Inertial Fusion Plan*, February 1982, LBNL report PUB-5065. (HIFAN 184)

[118] HIF staff, *The Multiple Beam Experiment (MBE-16) Conceptual Design as of June 1984*, June 1984, LBNL report PUB-5123. (HIFAN-243)

[119] T. Fessenden *et al.*, *ILSE: The next step toward a heavy ion induction accelerator for inertial fusion energy*, in Proceedings of the 14th International Conference On Plasma Physics and Controlled Nuclear Fusion Research, 30 September – 7 October 1992, Wurzburg, Germany, (IAEA, Vienna, 1993), vol.3, p. 89

[120] C. M. Celata *et al.*, *The ILSE experimental program*, in Proceedings of the International Symposium on Heavy Ion Inertial Fusion, Frascati, Italy, 1993, edited by S. Atzeni and R. A. Ricci (ENEA, Frascati, Italy, 1993), p. 1631

[121] S. Eylon, E. Henestroza, W. W. Chupp and S. Yu, *Low-Emittance 0.8 A K^{+} Ion Source for the LBL Induction Linac System Experiment (ILSE)*, in Proceedings of the International Symposium on Heavy Ion Inertial Fusion, Frascati, Italy, 1993, edited by S. Atzeni and R.A. Ricci (ENEA, Frascati, Italy, 1993), p. 1509

[122] J. W. Kwan *et al.*, *Elise plans and progress*, in Proceedings of International Symposium on Heavy Ion Inertial Fusion, Princeton, 1996, edited by J. J. Barnard, T. J. Fessenden and E. P. Lee (PPPL, Princeton, NJ, 1996), p. 299

[123] W. Abraham *et al.*, *Design and Testing of the 2 MV Heavy Ion Injector for the Fusion Energy Research Program*, in Proceedings of the 1995 Particle Accelerator Conference, Dallas, 1995, (IEEE, Piscataway, NJ, 1995), p 902

[124] F. M. Bieniosek, E. Henestroza, J. W. Kwan, L. Prost, P. Seidl, *2-MV Injector for HCX*, in Proceedings of the 2001 Particle Accelerator Conference, Piscataway, 2001, edited by Peter Lucas and Sara Weber, (IEEE, Piscataway, NJ, 2001), p. 2099, http://accelconf.web.cern.ch/accelconf/p01/PAPERS/WPAH011.PDF

[125] J.W. Kwan, F. M. Bieniosek, E. Henestroza, L. Prost and P. Seidl, *A 1.8 MeV $K^+$ injector for the high current beam transport experiment*, Laser and Particle Beams **20** (3), p. 441 (2002)

[126] National Instruments Corporation, Austin, TX 78759 http://www.ni.com

[127] S. Yu *et al.*, *Heavy Ion Fusion Injector Program*, in Proceedings of the 1993 Particle Accelerator Conference, Washington, DC, 1993, edited by S. T. Corneliussen, (IEEE, Piscataway, NJ, 1993), p. 703, http://accelconf.web.cern.ch/accelconf/p93/PDF/PAC1993_0703.PDF

[128] J. W. Kwan, *Ion sources for heavy ion fusion induction linacs*, Nucl. Instrum. Methods in Phys. Res. A **415**, 268 (1998)

[129] D. Baca, J. W. Kwan, J. K. Wu and E. Chacon-Golcher, *Fabrication of large diameter alumino-silicate K+ sources*, in Proceedings of the 2003 Particle Accelerator Conference, Portland, 2003, edited by Joe Chew, Peter Lucas, and Sara Webber, (IEEE, Piscataway, NJ, 2003), p. 3294, http://accelconf.web.cern.ch/accelconf/p03/PAPERS/FPAB005.PDF

[130] E. Chacon-Golcher, *Studies in High Current Density Ion Sources for Heavy Ion Fusion Applications*, Ph.D. thesis, University of California, Berkeley, 2002

[131] S.S. Yu *et al.*, *2 MV injector as the Elise front-end and as an experimental facility*, in Proceedings of International Symposium on Heavy Ion Inertial Fusion, Princeton, 1996, edited by J. J. Barnard, T. J. Fessenden and E. P. Lee (PPPL, Princeton, NJ, 1996), p. 309

[132] S.M. Lund, J.J. Barnard, E.P. Lee, *Emittance Growth from the Thermalization of Space-Charge Nonuniformities*, in Proceedings of the XX International Linac Conference, Monterey, 2000, edited by A. W. Chao (SLAC, Stanford, CA, 2000), p290, http://accelconf.web.cern.ch/accelconf/l00/papers/MOE11.pdf

[133] Martin Reiser, *Theory and Design of Charged Particle Beams*, John Wiley & Sons Inc., New York, pp. 491-525 (1994)

[134] R. C. Davidson, *Physics of Nonneutral Plasmas*, Addison-Wesley, Reading, MA (1990) and references therein

[135] T. P. Wangler, K.R. Crandall, R.S. Mills and M. Reiser, IEEE Trans. Nucl. Sci. **32**, 2196 (1985)

[136] F. M. Bieniosek, *Design of electrical upgrades for pulse length extension in the 2-MV Injector*, HIFAR Note 512 (2001)

[137] F. M. Bieniosek, *Doubling the pulse length of the 2-MV Injector*, HIFAR 533 (2002)

[138] F. M. Bieniosek, J. W. Kwan, E. Henestroza and C. Kim, *Development of the 2-MV Injector for HIF*, Nucl. Instrum. Methods in Phys. Res. A **464**, 592 (2001)

[139] F. M. Bieniosek and D. Baca, *Dielectric strength of mixtures of $SF_6$ and $CO_2$*, HIFAR Note 511 (2001)

[140] L. G. Christophorou, *Insulating Gases*, Nucl. Instrum. Methods in Phys. Res. A **268**, 424 (1988)

[141] J. R. Pierce, *Theory and Design of Electron Beams*, Van Nostrand, Princeton, 1949

[142] F. M. Bieniosek *et al.*, *Diagnostics for Intense Heavy Ion Beams*, in Proceedings of the 15th International Symposium on Heavy Ion Inertial Fusion, Princeton, June 7-11, 2004

[143] Martin Reiser, *Theory and Design of Charged Particle Beams*, John Wiley and Sons, Inc., New York, p108 (1994)

[144] S. Yu *et al.*, *Heavy ion fusion 2 MV injector*, in Proceedings of the 1995 Particle Accelerator Conference, Dallas, 1995, (IEEE, Piscataway, NJ, 1995), p 1178 http://accelconf.web.cern.ch/accelconf/p95/ARTICLES/TAE/TAE01.PDF

[145] E. Henestroza, S. S. Yu, S. Eylon and D. P. Grote, *Beam Dynamics studies of the heavy ion fusion accelerator injector*, in Proceedings of the 1995 Particle Accelerator Conference, Dallas, 1995, (IEEE, Piscataway, NJ, 1995), p 926 http://accelconf.web.cern.ch/accelconf/p95/ARTICLES/WPA/WPA09.PDF

[146] F. M. Bieniosek, *Collapse of the water resistor in the 2-MV Injector due to overpressure*, HIFAR 532 (2002)

[147] 3-D time dependent WARP PIC calculations were carried out by David Grote (LLNL) and are reported here with his permission.

[148] The calibration procedure was developed and written by Frank Bieniosek (LBNL) and is reported in Appendix A

[149] J. W. Kwan *et al.*, in Proceedings of the 2003 Particle Accelerator Conference, Portland, 2003, edited by Joe Chew, Peter Lucas, and Sara Webber, (IEEE, Piscataway, NJ, 2003), p. 3297, http://accelconf.web.cern.ch/accelconf/p03/PAPERS/FPAB006.PDF

[150] C. M. Celata, D. P. Grote and I. Haber, *Particle-in-cell simulations of the dynamic aperture of the HCX*, Laser and Particle Beams **20** (4), 577 (2002)

[151] C.M. Celata *et al.*, *Particle-in-cell simulations of the High Current Experiment*, in Proceedings of the 2003 Particle Accelerator Conference, Portland, 2003, edited by Joe Chew, Peter Lucas, and Sara Webber, (IEEE, Piscataway, NJ, 2003), p. 1518, http://accelconf.web.cern.ch/accelconf/p03/PAPERS/TPAG039.PDF

[152] S. M. Lund, B. Bukh, Physical Review ST – AB, (to be published)

[153] S. M. Lund and B. Bukh, *Stability properties of the transverse envelope equations describing intense ion beam transport*, Physical Review ST Accel. Beams **7**, 024801 (2004), http://link.aps.org/abstract/PRSTAB/v7/e024801

[154] A. Friedman *et al.*, *Simulation using initial 4D beam particle distributions synthesized from experimental data*, in Proceedings of the 2003 Particle Accelerator Conference, Portland, 2003, edited by Joe Chew, Peter Lucas, and Sara Webber, (IEEE, Piscataway, NJ, 2003), p. 275, http://accelconf.web.cern.ch/accelconf/p03/PAPERS/TOPB006.PDF

[155] M. Lampel and M. Tiefenback, *An applied voltage to eliminate current transients in a one-dimensional diode*, Appl. Phys. Lett. **43**(1), 57 (1983)

[156] J.-L. Vay *et al.*, *Application of adaptive mesh refinement to particle-in-cell simulations of plasmas and beams*, Phys. Plasmas, to be published.

[157] C. D. Child, Phys. Rev. Ser. I **32**, 492 (1911)

[158] I. Langmuir, Phys. Rev. Ser. II **2**, 450 (1913)

[159] Poul Dahl, *Introduction to electron and ion optics*, Academic Press, New York and London, 1973

[160] R. E. Warren, J. L. Powell and R. G. Herb, *Electrostatic Analyzer for Selection of Homogeneous Ion Beam*, Rev. Sci. Instrum. **18**, 8 (1947)

[161] A. H. Sato, *An Electrostatic Energy Analyzer for Longitudinal Energy Measurements*, HIFAN Note 296. (LBNL Report: LBNL-55072)

[162] 3-D WARP PIC simulations carried out by J.-L. Vay (LBNL) and reported here with his permission

[163] Martin Reiser, *Theory and Design of Charged Particle Beams*, John Wiley and Sons, Inc., pp525-530 (1994)

[164] L. I. Hofmann, L. J. Laslett, L. Smith and I. Haber, *Stability of the Kapchinskij-Vladimirskij (K-V) distribution in long periodic transport systems*, Particle Accelerators **13**, 145 (1983)

[165] Wayne Meier (LLNL), Private communication

[166] D. Jeon, *Beam Dynamics in the Spallation Neutron Source Linac*, in Proceedings of the 2003 Particle Accelerator Conference, Portland, 2003, edited by Joe Chew, Peter Lucas, and Sara Webber, (IEEE, Piscataway, NJ, 2003), p. 107, http://accelconf.web.cern.ch/accelconf/p03/PAPERS/TOAA003.PDF

[167] R. C. York, *Overview of the Rare Isotope Accelerator (RIA)*, Radiochemistry at RIA Symposium in conjunction with the 225th ACS National Meeting, March 27th 2003, New Orleans, LA, http://www.cem.msu.edu/~mantica/radio-ria/york_radioria.pdf

[168] P. N. Ostroumov *et al.*, *Design of 57.5 MHz CW RFQ for medium energy heavy ion superconducting linac*, Phys. Rev. ST Accel. Beams **5**, 060101 (2002), http://link.aps.org/abstract/PRSTAB/v5/e060101

[169] X. Wu *et al.*, *The misalignment and RF error analyses for the RIA driver linac*, in Proceedings of the XXIst International Linac Conference, Gyeongju, Korea, 2002, (Pohang Accelerator Laboratory, Gyeongju, Korea, 2002), p. 133, http://accelconf.web.cern.ch/accelconf/l02/PAPERS/MO441.PDF

[170] G. L. Sabbi *et al.*, *Superconducting focusing quadrupoles for heavy ion fusion experiments*, in Proceedings of the 2003 Particle Accelerator Conference, Portland, 2003, edited by Joe Chew, Peter Lucas, and Sara Webber, (IEEE, Piscataway, NJ, 2003), p. 1990, http://accelconf.web.cern.ch/accelconf/p03/PAPERS/WPAE023.PDF

[171] R. Cohen *et al.*, *Stray-electron accumulation and effects in HIF accelerators*, in Proceedings of the 2003 Particle Accelerator Conference, Portland, 2003, edited by Joe Chew, Peter Lucas, and Sara Webber, (IEEE, Piscataway, NJ, 2003), p. 132, http://accelconf.web.cern.ch/accelconf/p03/PAPERS/TOAA010.PDF

[172] John Staples (LBNL), Private communication

[173] M. A. Leitner *et al.*, *Design choices for the Integrated Beam Experiment (IBX)*, in Proceedings of the 2003 Particle Accelerator Conference, Portland, 2003, edited by Joe Chew, Peter Lucas, and Sara Webber, (IEEE, Piscataway, NJ, 2003), p. 1521, http://accelconf.web.cern.ch/accelconf/p03/PAPERS/TPAG040.PDF

[174] J. J. Barnard *et al.*, *Integrated experiment for heavy ion fusion*, Laser and Particle Beams **21**(4), 553 (2003)

[175] C. M. Celata *et al.*, *The Integrated Beam Experiment-A Next Step Experiment for Heavy Ion Fusion*, in Proceedings of the Third International Conference on Inertial Fusion Sciences and Applications (IFSA 2003), Monterey, CA, Sept. 7-12, 2003. LBNL-52409

# APPENDIX A: Extraction voltage calibration procedure

(*Frank M. Bieniosek, LBNL*)

The extraction voltage applied to the ion source is the difference between a DC reverse bias voltage ($V_{Bias}$) and a pulsed extraction voltage ($V_{Gate}$), which is developed by the capacitively coupled secondary of a step-up transformer, which is in turn connected to the output of a pulse forming network (PFN). Since HCX operation is very sensitive to Injector conditions, such as the pulsed extraction voltage, and since that voltage is the difference of the extraction pulse voltage and the reverse bias voltage, the sensitivity to variations in the pulser output voltage is very high.

Because of drift in the pulse extraction voltage monitor fiber optic link, we have developed a procedure to calibrate the extraction pulser in situ, using the Injector beam current, and the DC bias and extraction pulser charge voltages. These voltages utilize a DC link, which has much less drift than the high-speed link; and the set point and readback voltage level can be compared for agreement.

In an ion diode, beam current is limited by the Child-Langmuir current limit. In this limit, emission from the ion source is governed by space charge flow and ion flow is determined by the scaling relation

$$ I = K_{gun} V^{3/2}, \tag{A1} $$

where $K_{gun}$ is a constant known as the gun perveance [141] and $V$ the extraction voltage. The gun perveance is determined only by the geometry of the diode, and

the mass and charge state of the ion. For a given ion species, and using modern

alumino-silicate-based solid-state ion sources, the emission is stable to the level

of 0.1%.

In this procedure, we measure the beam current, extraction charge voltage, and

bias voltage for a number of cases, and generate a series of linear fits to the

data:

$$V_{Gate} = \alpha V_{Bias} + \beta, \text{ for } I_B = \text{const.} \tag{A2}$$

The calibration constant is the slope of the line at the current of interest:

$$\alpha = \frac{\Delta V_{Gate}}{\Delta V_{Bias}}. \tag{A3}$$

The calibration constant $\alpha$ multiplied by the charge voltage is the empirical value

for the pulsed extraction voltage. The calibration constant may vary slightly from

time to time. The differences are attributed to residual drift in the fiber optic link.

In this way, the extraction voltage may be accurately determined by measuring

the bias voltage.

# APPENDIX B: Glossary

The following short glossary is intended to define some of the terms used in this thesis that non-specialist readers may not be familiar with. It is based on a glossary compiled by the Beams Division, Operations Department at Fermilab National Accelerator Laboratory (originally written by Jack Standeven and further edited by Wally Kissel).

## - A -

**Accelerator**:

Any machine used to impart large kinetic energies to charged particles such as electrons, protons, and atomic nuclei.

**Acceptance**:

The measure of the limiting aperture of a transport line, accelerator, or individual device; it defines how "large" a beam will fit without scraping. More technically acceptance is the phase-space volume within that the beam must lie in order to be transmitted through an optical system without losses. From an experimenters point of view acceptance is the phase-space volume intercepted by an experimenter's detector system. This is the complement of emittance.

**Aperture**:

A measure of the physical space available for beam to occupy in a device.

## - B -

**Beam**:

This is a slender unidirectional stream of particles or radiation.

**Beam brightness**:

The ratio of the beam current to the square of the beam emittance. For heavy ion fusion, high brightness (high current, low emittance) are desirable.

**Beam head**:

Refers to the early times of the beam pulse (when the beam current increases to reach its flattop value).

**Beam intensity**:

The average number of particles in a beam passing a given point during a certain time interval, given, for example, as the number of ions per pulse or ions per second.

**Beam line (transport line)**:

A series of focusing elements (electrostatic and/or magnetic) and vacuum pipe that carry a particle beam from one portion of the accelerator to another.

**Beam loss**:

A beam loss is any loss of particles due to any reason.

**Betatron oscillation**:

Betatron oscillations are the transverse oscillation of particles about the center of the beam line (for a linear accelerators) or about the equilibrium orbit (for circular accelerators).

**Beam tail**:

Refers to the late times of the beam pulse (when the beam current decreases back to zero).

**- C -**

**Cell**:

This refers to the smallest repeatable configuration of focusing elements.

**Centroid**:

Technically, the center of mass, which is used here to describe the center of a beam profile.

**Chromatic aberration**:

Beam spreading out due to different momentum particles being bent by the applied fields at different angles.

**Coasting beam**:

Beam which is not accelerated as it propagates in the beam line.

**Conditioning**:

Vacuum term. The process of running voltage in a beam line element (such as an electrostatic quadrupole) at a high level over a period of time to clean up the vacuum. The voltage is turned on at a low level and slowly raised over time to avoid sparking in the device that can spoil vacuum. By burning off these things the ability of the device to pump down to operating vacuum is greatly improved.

**Confinement**:

In order for significant thermonuclear energy production, the fuel must remain confined for a sufficiently long time (at both a high enough temperature and

271

density) so that a large number of nuclear fusion reactions will occur. For inertial confinement, this time is less than a nanosecond. For the magnetic confinement, this time ranges from seconds to an eventual goal of hours.

**- D -**

**Dipole**:

A device for deflecting the path of the beam. A magnetic dipole field bends the path charged particles (or beams of charged particles) with a force proportional to their velocity, the strength of the field, and the charge of the particles. An electric dipole field bends with a force proportional to the strength of the field and the charge of the particles.

**Divergence**:

This refers to the angle that the trajectory of each particle makes with the beam axis.

**Downstream**:

This is a relative term that corresponds to the direction that the ions travel in that portion of the accelerator.

**Driver**:

The term driver is the name given to the apparatus that produces the required laser or ion beams and which directs them at the fuel pellet in an inertial confinement fusion reactor chamber.

**Dynamics**:

This is the study of the motion of particles under the influence of forces. Dynamics deals with the causes of motion, as opposed to kinematics that deals with its geometric description.

**- E -**

**Electrostatic quadrupole**:

See Quadrupole

**Emittance**:

This refers to the area in phase space occupied by a particle beam. The units are mm mrad for transverse emittance and eV s for longitudinal emittance.

**Emittance scanner**:

Device used to measure the size of the phase space ellipse occupied by the beam, done by measuring the divergence of the beam at a number of points across the beam axis.

**Envelope (or beam envelope)**:

The boundary of the beam distribution in phase-space, used to describe the beam as a whole. In this thesis, the $2\times$ RMS convention is employed and definitions of the envelope parameters are given in Section - II.1.3 -.

**Extraction**:

The controlled removal of ions from the source that creates them.

## - F -

**Flattop**:

The portion of a waveform pulse (voltage, current) that remains at a constant maximum value.

## - H -

**HCX**:

High-Current Experiment (HCX) is a beam-transport experiment taking a driver-scale 2 MeV beam through a lattice of electrostatic and magnetic quadrupoles.

**Heavy ion fusion (HIF)**:

Refers to all aspects of the scientific effort geared towards producing electricity via the inertial fusion energy (IFE) concept, using a heavy ion beam as the driver.

## - I -

**ICF**:

Inertial Confinement Fusion (ICF) is the approach to controlled thermonuclear fusion which uses intense ion or laser beams to implode and ignite target pellets of deuterium-tritium fuel, whose inertia confines them for a sufficiently long time for a good "burn" to occur.

**IFE**:

Inertial Fusion Energy (IFE) is the name for the research program in the U.S. Department of Energy whose goal is to use the ICF approach to controlled thermonuclear fusion energy to commercial power production.

**Induction linac**:

Induction linac is the name given to a type of linear accelerator which accelerates charged particles by using the electric field produced by a rapidly-changing magnetic field strength in a ferrromagnetic core. Induction linacs are useful wherever relatively large (> 1 kiloamp) beam currents must be accelerated.

**Injection**:

The process of putting a beam of particles into an accelerator.

**Injector**:

The ion source and first stage of acceleration up to 1-2 MeV is the injector of a driver.

**Intensity**:

Number of particles in the beam.

**- L -**

**Lattice**:

The periodic relative arrangement of quadrupoles and drift spaces in an accelerator.

**Linac**:

Linear accelerator.

**- M -**

**Magnetic quadrupole**:

See Quadrupole.

**Matching**:

The process of tailoring the envelope parameters of a beam to the acceptance of a device.

**MFE**:

Magnetic Fusion Energy (MFE) is the approach to controlled thermonuclear energy which uses magnetic fields to confine a hot, but rarefied thermonuclear fuel. A tokamak is an example of a device that operates upon the principles of magnetic confinement.

**- P -**

**Perveance**:

A measure of the ratio of space-charge potential energy to kinetic energy. See (Eq. I-4) for a formal definition.

**Phase advance**:

A measure of the stage of the betatron oscillation at some point in the accelerator.

**Phase space**:

A six-dimensional space consisting of a particle's position (x, y, and z) and divergence (x′, y′, and z′). Phase space is generally represented in two dimensions by plotting position on the horizontal axis and the corresponding divergence on the vertical axis.

**- Q -**

**Quadrupole**:

A quadrupole is the name given to a force field produced by four individual poles, two positive and two negative. Quadrupoles may use either electric or magnetic fields. Quadrupole fields are often used to focus and help transport charged particle beams in accelerators. For heavy-ion fusion accelerators, electrostatic quadrupoles are typically employed for low-energy transport (< 20 MeV), and magnetic quadrupoles are used at higher energies. Quadrupole is often used to refer to the mechanical hardware that produces the quadrupole field.

**- R -**

**RMS**:

Root-mean-squared. The root-mean-squared of a distribution is defined by (Eq. II-26) and (Eq. II-27).

**- S -**

**Secondary particles**:

Those particles that are produced by hitting a target with the primary ion beam from the accelerator.

**Space charge**:

A radially defocusing force caused by mutual electrostatic repulsion between ions within an accelerator.

**Space-charge-dominated beams**:

A beam of charged particles is said to be space-charge dominated when the effective electrical force of repulsion of the like charges is stronger than the

pressure associated with the internal temperature of the beam. Usually, this concept applies to non-relativistic ion beams, since the repulsive space-charge force is normally almost completely canceled by the attractive self-magnetic force in relativistic electron beams.

**Step motor**:

This is a motor that rotates a small specific amount in response to an encoded bit of information. It allows beam-line elements to be moved precise distances.

**Strong focusing**:

A system for focusing charged particles in that the particles pass alternately through non-uniform electric or magnetic fields having gradients of opposite sign.

**- T -**

**Tokamak**:

A tokamak is the Russian name given to a large, doughnut-shaped fusion device that is surrounded by electrical coils which produce intense magnetic fields to confine a hot, D-T fuel plasma.

**- U -**

**Upstream**:

This is a relative term indicating the direction opposite to the ions' normal direction.

**- W -**

**Water resistor**:

The water resistor are the plastic tubes, running along the accelerating column of the injector, which are used to control the potential drop among the column

electrodes. The resistance of the tubes is controlled by Low Conductivity Water (LCW) flowing through them. On the HCX, the LCW is a solution of sodium sulfate.

**Waveform**:

A current or voltage (electrical signal) considered as a function of time.